Creep Deformation and Thermal Aging of Random Glass-Mat Polypropylene Composite

by

Aaron Chi Kwan Law

A Thesis
Presented to University of Waterloo
in the fulfilment of the
thesis requirement for the degree of
Master of Applied Science
in
Mechanical Engineering

Waterloo, Ontario, Canada, 2007

DECLARATION

I hereby declared that I am the sole author of this thesis. This is a true copy of the thesis, including any required final revisions, as accepted by my examiners.

I understand that my thesis may be made electronically available to the public.

ABSTRACT

The current research is part of a wider experimental program on creep modeling of glass mat reinforced polypropylene composites which are increasingly being used in molding automotive parts. This specific study is focused on the dimensional and thermal stability of chopped fibre mat and long fibre mat composites. The objective of the study is two-fold. First, to characterize *in-situ* the micro-failure mechanisms associated with damage accumulation during creep at room temperature and at service temperature (80°C) for stresses up to 67% of the ultimate tensile strength. Second, to characterize the effects of prolonged exposure at elevated temperature on the crystallinity and chemical degradation of the polypropylene matrix.

In the first part of the investigation, micro-failure mechanisms including fibre-matrix interface, matrix yielding and cracking during the creep process have been captured *in-situ* using reflection microscopy. Specimens with 12 mm gauge length were mounted onto a Minimat tensile tester. The applied stress levels of interest were 33% and 67% of the ultimate tensile strength (UTS) at room temperature (RT) and high temperature (HT), respectively. It was found that the deformation mechanisms do not change with temperature but creep in the chopped fibre material is substantially higher than that in the long-fibre. Creep deformation is typically associated with multiple transverse crack initiation at the fibre-matrix interface, crack crazing and rapid coalescence of the small cracks leading to abrupt fracture. Debonding of the fibres is usually detected at the loading stage of the test but fibre breakage is minimal even at high temperature. The change in creep strain at room temperature is similar for both composites but creep strains are highly sensitive to the fibre-mat type at higher temperature. Long-fibre mat structures offer greater creep resistance. Micro-indentations on the matrix-rich regions showed elongation along the loading direction but shear yielding (distortion of indentations) was not noticeable. Using scanning electron microscopy (SEM), the fibre pullout was observed to be pronounced thus suggesting poor adhesion at the fibre-matrix interface.

In the second part of this study, the effects of elevated temperature aging on the microstructural changes of isotactic polypropylene matrix in a composite have been studied using wide-angle X-ray scattering (WAXS) and Fourier-transform infrared spectroscopy (FTIR). The objective was to quantify small and slow changes in crystallinity due to thermal aging. To minimize sample variability, polypropylene resin was extracted from the molded composite plaque. Changes in crystallinity level and crystalline form were detected using WAXS after prolonged aging at 90 and 140 °C. FTIR was utilized to monitor *in-situ* crystallinity changes and to detect oxidation products due to thermal decomposition. The level of crystallinity was monitored by changes in the absorbance ratio of A_{997}/A_{973} and A_{841}/A_{973}; the former ratio was found to be more sensitive for detecting crystallinity changes. Aging at 140°C resulted in oxidation. The kinetics of secondary crystallization for the aging conditions studied was characterized using Avrami plots.

ACKNOWLEDGEMENTS

I wish to extend my sincere gratitude to Dr. Pearl Sullivan and Dr. Leonardo Simon for their insight, patience and guidance throughout this work. Also thanks to Mr. Andy Barber and Mr. Tom Gawel for test equipments setup; Dr. Yuquan Ding for technical assistance on the electron microscopy.

I am thankful to Dr. Xinran Xiao from the Materials Processing Lab, General Motors Corporation, Warren, Michigan for providing technical advices and raw materials for testing.

Special thanks to Jack Tang, Prasad Dasappa, Jonathan Mui, Paula Kruger, Zena Ng, Anthony Shin, Dominik Jürgen-Lohmann and Jason Kuo for laboratory support.

Last but not least, I gratefully acknowledge the financial supports from: the Center for Automotive Materials and Manufacturing (CAMM), a program established by the Ontario Research Development Challenge Fund (ORDCF); General Motors Canada; the Natural Science and Engineering Research Council Canada (NSERC); and the Department of Mechanical and Mechatronics Engineering, University of Waterloo.

DEDICATION

May the present work inspire those interested in polymer research to pursue knowledge in this field. My love and thanks are extended to my family and friends for their support and encouragements.

CONTRIBUTIONS TO THE LITERATURE

Poster presentations:

Event: **Institute of Polymer Research** - University of Waterloo (May 2007)

Title: *Characterization of Microscale Deformations due to Creep in Glass-Mat Thermoplastic (GMT) Composites at Elevated Temperature*

Authors: Aaron Law, Leonardo Simon, Pearl Lee-Sullivan

Event: **Canadian Materials Science Conference** – McMaster University (June 2007)

Title: *Effects of Thermal Aging on Isotactic Polypropylene (iPP) Crystallinity and Chemical Structure*

Authors: Aaron Law, Leonardo Simon, Pearl Lee-Sullivan

Publications:

Newsletter – **Society of Plastic Engineers** – November 2006 Issue – Feature article section: SPEC-TECH-CLE

Title: *Automotive Applications – Glass Mat Thermoplastic Composite*

Author: Aaron Law

Journal Paper – **Polymer Engineering and Science** (in print)

Title: *Effects of Thermal Aging on Isotactic Polypropylene Crystallinity*

Authors: Aaron Law, Leonardo Simon, Pearl Lee-Sullivan

Paper in preparation:

Title: *In-situ Observations of Deformation Mechanisms during Creep in Chopped and Continuous Glass-mat Reinforced Polypropylene*

Authors: Aaron Law, Pearl Lee-Sullivan, Leonardo Simon

TABLE OF CONTENTS

LIST OF FIGURES

LIST OF TABLES

NOMENCLATURES

GMT – Glass-Mat Thermoplastics

PMC – Polymer Matrix Composite

UTS – Ultimate Tensile Strength

RT – Room Temperature

HT – High Temperature at 80 °C

RT – UTS – Ultimate Tensile Strength measured in Room Temperature

HT – UTS - Ultimate Tensile Strength measured in High Temperature

SEM – Scanning Electron Microscopy

WAXS – Wide Angle X-ray Scattering

SAXS – Small Angle X-ray Scattering

FTIR – Fourier Transform Infrared Spectroscopy

IR – Infrared

DSC – Differential Scanning Calorimetry

DMA – Dynamic Mechanical Analysis

GPC – Gel Permeation Chromatography

TGA – Thermogravimetric Analysis

iPP – Isotactic Polypropylene

PP – Polypropylene

SAN- Styrene Acrylonitrile

PVC – Polyvinylchloride

PBT – Polybutylene Terephthalate

HDPE – High Density Polyethylene

LDPE – Low Density Polyethylene

D100 – Chopped-fibre composite

G100 – Long-continuous fibre composite

1.0 Introduction

1.1 Glass-mat Thermoplastics

The development of lower cost, lightweight materials with excellent performance capabilities is a key factor in advancing manufacturing technologies. Metallic materials have traditionally been used in mainstream engineering applications but they are increasingly being substituted with plastics. Glass mat reinforced thermoplastic (GMT) has increasingly been used over the past decade due to its well known high strength-to-weight ratio and cost-effectiveness as compared to metallic materials. The mechanical properties of the engineering plastics are further improved by relatively low cost fibre reinforcements. The technical accomplishments of this type of polymer matrix composite (PMC) material are primarily involved in interdisciplinary combination of plastics engineering, materials science and engineering mechanics.

There are two processing methods to fabricate the commercially used GMT materials: melt impregnation and slurry deposition. The two methods result in different fibre architectures, thus significantly affecting mechanical properties. Melt impregnation is the dominating method of fabricating semi-finished GMT sheets. Glass fibre mat are prepared ahead of time with a separate process, as the needling operation of the glass fibre strands strongly influences the flow characteristics of the material. The glass fibre mat will then be transferred to the laminator where the thermoplastic film overlay, molten extrudate and the preformed glass fibre mat will be sandwiched together. The outer layer of the thermoplastic film will melt in the oven with applied pressure to improve the wetting of the fibres. The GMT is then cooled and cut to size according to customers' specification [1].

The other type of fabrication process is the slurry deposition process. Based on paper-making technology, chopped fibres are mixed with polymeric powder and water to form the slurry. The slurry will then pass through the vacuum filter to remove most of the

water, and then dried and consolidated in a double belt press, similar to the heating stage of the melt impregnation process.

The processing time of the GMT materials is rapid through stamping or high speed compression molding, depending on the types of polymer being used. Blanks are cut from the preformed semi-finished GMT sheets from the supplier, where they are heated individually, and stacked up to the proper geometry of final part to form the charge. The charge is then transferred to the mold and pressed to the final shape. The component is removed from the mold as soon as it has solidified enough to be removed. Compared to injection molding, the cycle time is relatively short, thus increasing the production rate, which is favourable for mass production environments such as in the automotive industry.

The properties of GMT material are also strongly affected by its composition and processing. Material compositions differ mainly in terms of fibre architecture such as random short fibres or swirled fibre mats, as well as the weight percentage of the fibres. The heating/cooling conditions, pressure, flow rate and flow length are among the processing variables that will affect the microstructure of GMT material, thus affecting the mechanical properties [1].

1.2 Applications and General Properties

With its lighter weight compared to common metallic materials such as steel or aluminum, GMT materials have successfully become the preferable alternatives of the semi-structural components, where there are constant loads applied to the part and the surface finish is not critical. The most popular automotive applications include front ends, seat frames, door modules, battery trays, under body shields, instrument panel structure and inner structure of tailgate. Due to the geometry complexity, compressive molding with GMT materials can be performed in one forming operation, which is theoretically not possible with sheet metal structure. The cost of the production will be reduced due to fewer process steps required. Depending on the applications, other types of thermoplastics can be used as the matrices of the GMT such as styrene acrylonitrile (SAN), polyvinylchloride (PVC), polybutylene terephthalate (PBT), high density polyethylene (HDPE) and nylon-6 [2]. Polypropylene (PP) accounts for most of the products that are commercially available due to its cost and operating conditions that is suitable for automotive applications. For demanding applications such as aerospace engineering, other types of thermoplastic with better thermal, chemical resistant and higher service temperature should be used. Other applications of GMT include pallets, shipping containers, blower housings, helmets and door skins [1].

Compared to metallic materials, components made from GMT materials are not subjected to high constant mechanical load due to its viscoelastic behaviour which is strongly dependent on the operating time and temperature. The interaction between the glass fibre mat and the matrix provides high energy absorption during failure, thus improving the impact strength. For commercial type of GMT, based on polypropylene matrix and glass fibre reinforcements, the tensile modulus is 4 – 8 GPa and tensile strength is 40 – 100 MPa [1]. The reported values are governed by structural parameters such as fibre content, distribution, orientation, length, matrix crystallinity and molecular orientation. Also, due to the viscoelastic behaviour of the polymer materials, time and temperature effect will also play important roles when characterizing the properties of the GMT materials. A challenge in property characterization is the large scatter in data due to the

randomness of glass fibre distribution orientation and inhomogeneous microstructure of the GMT material.

1.3 Motivation of Research Work

Although GMT material has been largely utilized in the automotive industry in semi-structural applications, their long-term mechanical behaviour and dimensional stability such as creep at elevated temperature have yet to be properly characterized. When a vehicle is stationary under the direct sunlight, the temperature of the vehicle components will rise to over 80°C, where the GMT material experiences thermal aging, greatly affecting the material's performance.

An extensive research program aimed at experimental characterization and constitutive modeling of creep in GMT materials reinforced with chopped fibre and long fibre mat is currently in progress. This specific study is only part of the program and is focused on two main areas. First, to characterize *in-situ* matrix and interfacial deformation and failure during creep using optical microscopy. Miniature size polypropylene/glass fibre GMT specimens are loaded in a microtensile instrument at elevated temperature. While most of the creep deformation is viscoelastic, creep-related cracking mechanisms are permanent/plastic as the propagated cracks do not recover when the load is released. Images on microstructural changes during progressive creep deformation will help explain the long term creep response of the two different GMT composites with different fibre lengths and mat structure. The results of this work will enhance our understanding of micro-scale failure mechanisms responsible for changes in the creep strain rate and eventual failure.

The other focus of research work is capturing the changes in polypropylene crystallinity and stability due to thermal aging. The changes between the amorphous and crystalline fraction of a semi-crystalline polymer, isotactic PP in this case, induced by accelerated aging at temperatures about 80°C, will alter the mechanical properties of the material [3]. Fourier transform-infrared (FTIR) spectroscopy and differential scanning calorimetry (DSC) were used to detect the crystallinity changes of the PP matrix, while other technique such as wide angle X-ray scattering (WAXS) was also applied to complement our observations. FTIR spectroscopy measures the vibrational energy levels of molecules

and under appropriate circumstance it is capable of indicating when the polymer material changes the morphology from the amorphous to the crystalline phase during aging [4]. With the online scanning ability, the changes in the crystallinity index, determined from the intensity of FTIR absorbance spectra provide the insight of how crystallinity changes at different time frames, in order to predict the stability of the GMT materials [5]. Correlated with the DSC analysis, the heat of fusion is measured with respect to the 100% crystalline material to determine the overall crystallinity index between the sample before and after aging [6]. Melting point detected from DSC will also help confirm if there are any changes on the lamellar thickness or spherulite structure [7].

The experimental studies in this work will provide greater insight into the physical and chemical changes during long-term creep in random mat composites at elevated temperature. The results will improve our general understanding of the relationship between changes in physical and chemical structure and durability of these polymeric-based materials under increasingly higher loading stress loading. The developed constitutive models can then be utilized with more confidence when the model users desire to push the design envelope for thinner components that can sustain higher service temperatures.

1.4 Objectives of Research Study

This work is part of a larger experimental program aimed at characterizing the creep response of random glass-mat thermoplastic composites (GMT). GMT materials, which have polypropylene matrices, are increasingly being used to manufacture semi-structural components for automotive applications. The service temperature for such components can reach as high as 80°C. An inherent difficulty in characterizing GMT materials is the large data scatter due to the random distribution of the glass-fibre reinforcements. Therefore, relatively large changes in the mechanical properties of the polypropylene matrix due to long-term thermal exposure may not be detectable. In order to gain greater confidence in designing with these new materials, it is necessary to determine if the material is significantly affected by creep loading and thermal aging during its service life.

The current work has two main objectives:

- To investigate the deformation mechanisms under creep loading; and
- To characterize the effects of thermal aging on the crystallinity level and chemical degradation of polypropylene matrix at different temperature levels.

To achieve the first objective, a miniature tensile tester mounted inside a heating chamber is used to perform creep testing at different temperatures. During creep loading, a microscope with camera attachments is used to capture *in-situ*, images of micro-failure mechanisms as the specimen elongates. SEM is used to verify the detail of deformations at a higher magnification. To study chemical degradation due to thermal aging, the WAXS technique is used to determine crystal type transformation while FTIR is used to detect chemical changes in crystallinity or in oxidative breakdown. DSC is also used to measure crystallinity level, as well as the properties such as melting and glass transition temperature.

1.5 Scope of Work

There are two main parts in this research study:

- To measure microscopic level creep deformation of composite due to combined stresses and temperatures:
    - *In-situ* imaging of creep deformation
    - Identify the deformation mechanism causing progressive failure (at the matrix interface or fibre components)
    - To correspond changes in creep strain with progressive failure behaviour

- To characterize the effects of thermal aging (long-term exposure) on the isotactic polypropylene matrix phase of a GMT:
    - Crystallinity changes, secondary crystallization
    - Degradation, formation of oxidation products

A number of assumptions have been made in this study. First, the properties of the mat materials are isotropic, due to random orientation of the fibre-glass [8]. Second, the size effects of the specimen, such as the thickness of the as-received composite plaques, are negligible since the deformation analysis is focused on one planar surface. Hence, as the images of micro-failure are captured, they are assumed to be typical and representative of the overall progressive failure mode for the GMT. This assumption is verified by randomly examining other regions of the specimen surface.

1.6 Structure of the Thesis

The structure of this thesis consists of five chapters. The first chapter will introduce the characteristics of glass-matted thermoplastic (GMT) with polypropylene matrix, its usage and sectors in the world of different materials; the motivation, objective and scope of this research will also be given. The second chapter will provide some background information about the different aspects such as aging, crystallinity and creep, with different characterization techniques and a literature review on related works that were done by other investigators. The third chapter will focus on the sample preparation procedures, experimental details, as well as methods and equipments that were used in this study. The fourth chapter will discuss the results and findings in detail with the supporting figures and tables. Finally, this thesis will conclude with summaries of the major findings from this work that could to provide further understanding of the behaviour of the material of interest.

2.0 Background and Literature Review

2.1 Creep Deformation

2.1.1 Viscoelasticity and Creep in Thermoplastic Composites

Polymeric materials are well known to exhibit viscoelastic behaviour. While the polymeric materials are under deformation, they exhibit both elastic and viscous responses. When the load is applied to the viscoelastic material, instantaneous strain of the material results due to the elastic response, followed by gradually increase of strain and plateaus over time due to the viscous response. Therefore, viscoelasticity is a time-dependent property and it is strongly related to the applied stress level and strain rate.

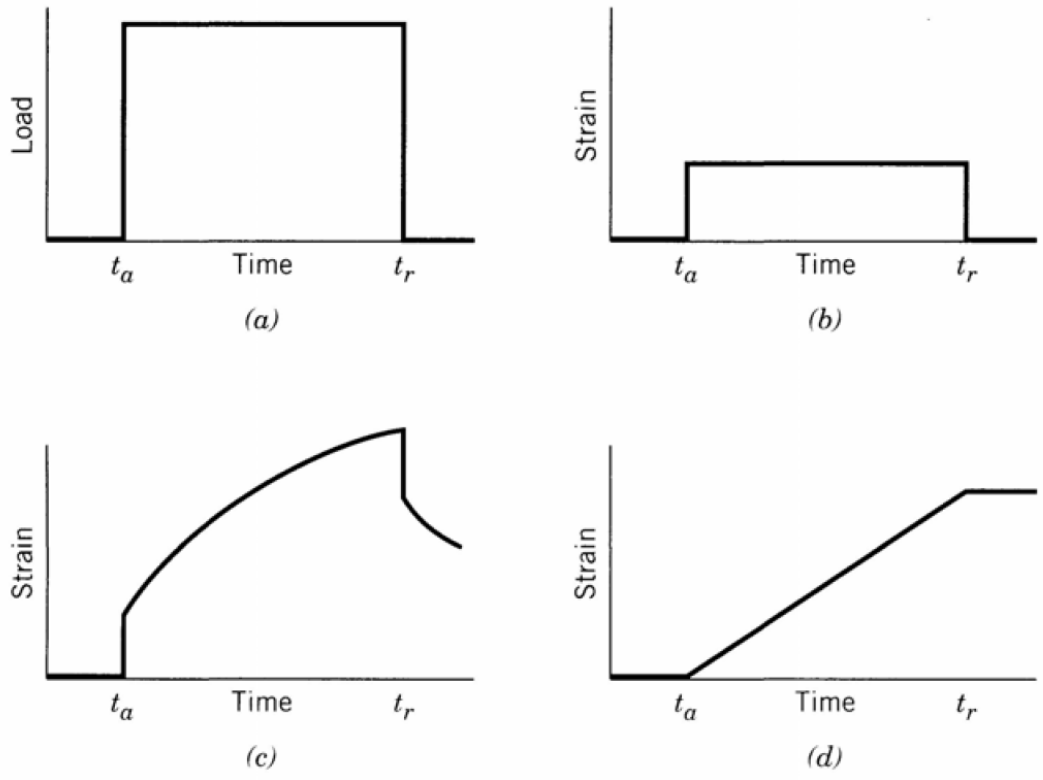

Figure 2-1: a) Instantaneous loading profile applied at t_a and released at t_r and the strain profiles for b) elastic, C) viscoelastic and d) viscous material responses [9].

When thermoplastic composites experience creep, as the constant load applied over a period of time, the stress-strain curve for the material can be separated in to two distinct regions, viscoelastic and viscoplastic behaviours.

The total strain during creep consists of the sum of two major elements which can be characterized in the following equation:

$$\varepsilon(t) = \varepsilon_{ve}(t) + \varepsilon_{vp}(t) \tag{1}$$

where $\varepsilon_{ve}(t)$ and $\varepsilon_{vp}(t)$ represent the viscoelastic and viscoplastic strain respectively which includes the elastic responses and time-dependent variables. For creep recovery, another governing equation is used:

$$\varepsilon_r(t) = \varepsilon_{ve}(t) + \varepsilon_{pl} \tag{2}$$

where $\varepsilon_{ve}(t)$ refers to the reversible slip of macromolecular chains, and $\varepsilon_{vp}(t)$ is the irreversible slip of macromolecular chains. However, $\varepsilon_{vp}(t)$ in eq. (1) will soon become ε_{pl} in eq. (2), as the plastic strain remains constant (not time-dependent) during recovery [10].

The creep profile plotted in total strain as a function of time is shown in Figure 2-2 with three stages of elongation. The first stage refers to primary creep. Deformation takes place during this period and the resistance to creep increases. In the second stage, a gradual increase of strain in a nearly constant rate refers to secondary creep. In the third stage, refers to tertiary creep, the creep rate increases and leads to final fracture.

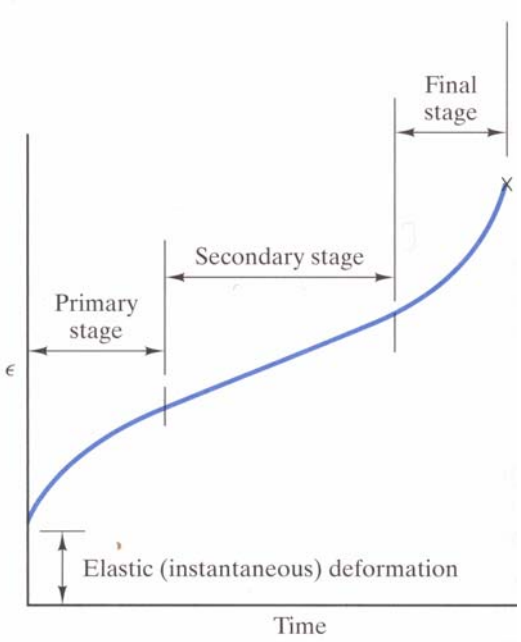

Figure 2-2: Creep profile with different stages [Redrawn from 11].

2.1.2 Composite Failure Mechanisms

It is difficult to predict the strength of the fibre reinforced composite materials due to the random nature of failure, different failures modes (fibre, matrix or interface), local failure initiation and the associated stress field determined by the fibre packing. Although GMT composites have randomly oriented fibres in entangled mat structures, it is useful to briefly review the factors causing failure in unidirectional composite materials. Figure 2-3 shows the different failure behaviours that are controlled by the relative values of matrix and fibre strains ($\hat{\varepsilon}_m$, $\hat{\varepsilon}_f$) and volume fraction of fibre (V_f) [12] for unidirectional composites loaded along the fibre direction.

Figure 2-3a shows the failure of the composite fails when the fibres fail. This will happen at high values of V_f and if $\hat{\varepsilon}_m$ is greater than $\hat{\varepsilon}_f$. When the composite is under load, if the strain of the matrix is higher than that of the fibres, most of the load will be carried by the fibres. Once the fibres break, the matrix cannot withstand the extra load. This results in failure of the composite due to fibre fracture. Figure 2-3b shows the

similar failure behaviour with low V_f, resulting multiple fibre facture prior to matrix failure. The failure behaviour will change if $\hat{\varepsilon}_f$ is greater than $\hat{\varepsilon}_m$ or if V_f is low. Figure 2-3c shows the failure of the composite that occurs when the matrix fails. This is the reverse of the case seen in Figure 2-3a and b. As the fibres have a higher load carrying capability, the matrix fails when the composite will hold the load until the fibres fail. With high V_f, multiple matrix fracture may result prior to the failure, as shown in Figure 2-3d [12].

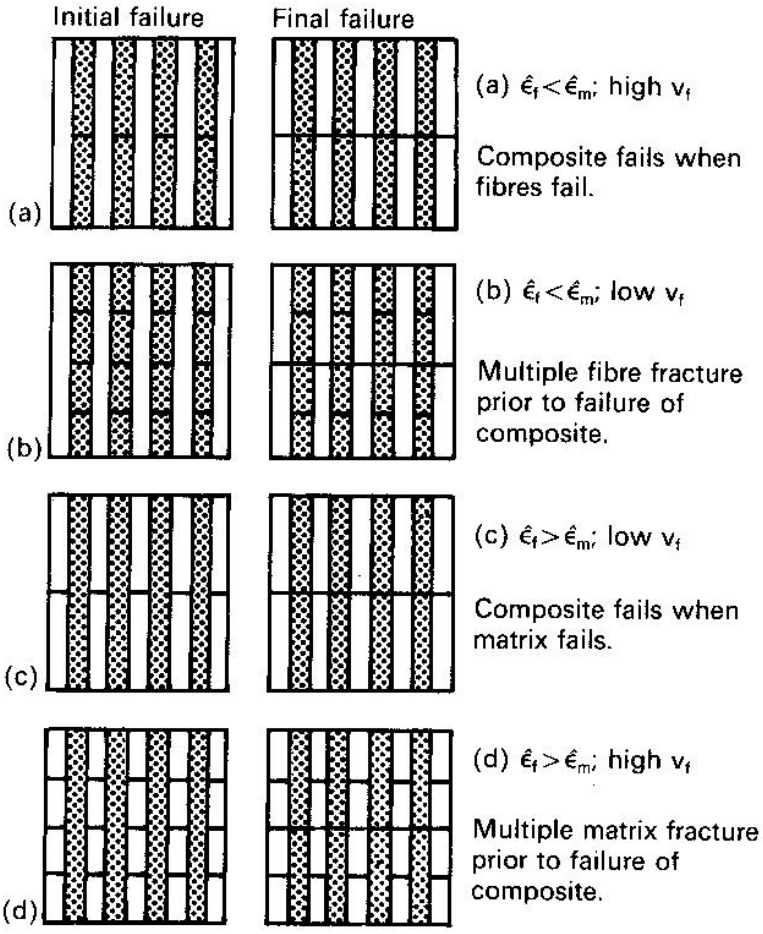

Figure 2-3: Composite failure modes with relative values of fibre and matrix failure strains ($\hat{\varepsilon}_m$, $\hat{\varepsilon}_f$), and fibre volume fraction (V_f) [12].

In this study of GMT composites, the failure modes are indeed more complex and final failure is most likely a combination due to the accumulation of two or more of the modes

shown in Figure 2-3, depending on the local volume fraction of local region. Moreover, the random orientation of fibres adds other modes not shown in the figure such as matrix crazing, shear yielding and shear stresses along the fibre-matrix interface. Consequently, while the characteristics of the "local" region affects failure initiation, the entire failure process is three-dimensional as it progresses through the thickness.

2.1.3 Literature Review on Microscale Creep Deformation

The popularity of GMT materials is increasing significantly over the decades due to its high strength-to-weight ratio and the ease of manufacturing complex shaped parts with compression molding. However, the long-term engineering properties of the polypropylene-based glass fibre reinforced composite are not fully known. There is significant interest about the impact properties of such material, and with the increasing interest to understand the deformation mechanisms under long-term creep, where the parts are under a constant load over its service life, with the thermal effects between room and elevated temperature at 80 °C. Common approaches for characterizing the deformation mechanisms under load are to conduct microscopy on the specimen surface and acoustic emission studies at the temperature level of interest. There are already ample studies of deformation mechanisms in polypropylene-base fibre glass reinforced composite material using microscopy [13-17] and acoustic emission [18-21] during loading of the samples.

Although the deformation mechanisms of the polypropylene-based fibre-glass mat reinforced materials has been studied by other investigators, there are variations between the studies with different ways for sample preparations, fibre treatments, different temperature levels, loading conditions and durations.

2.1.3.1 Microscale Deformations

Hugo *et al.* studied creep damage of the isotactic polypropylene matrix and short glass fibres at different stress levels and temperatures [13]. Figure 2-4 shows an image of

unreinforced isotactic polypropylene. Crazes, are regions of very localized yielding, which lead to the formation of small and interconnected microvoids to grow and coalesce to crack formation [22], develop as an initial form of damage in the thermoplastic matrix, and later open up to become transverse cracks perpendicular to the stress direction. With the standard adhesion glass fibre reinforcement, as shown in Figure 2-5, crazes initiate from the interface of the fibre and matrix regardless of the orientation of the glass fibres which, in this case are parallel to the applied stress direction. Figure 2-6 shows the sample under creep with 20 wt% fibre content. Joining of the crazes initiated at the fibre and matrix interface comprise a large extent of plastic strain, and eventually lead to the final fracture of the sample. Hugo *et al*. also compared the standard adhesion composite to the elevated adhesion composite. An elevated adhesion composite gives a better bonding between the fibre and matrix material. Figure 2-7 shows the deformation of the elevated adhesion composite. The mechanism of non-recoverable creep of iPP remains unchanged because the crazes developed from fibre and matrix interface are still predominant. However, it reduced the crazes development quantitatively due to the improved bonding of fibres.

In summary Hugo *et al.* suggested the mechanical behaviour is governed by the matrix phase and there is a matrix-dependent difference in the matrix and fibre interaction at different temperature levels as the non-recoverable flow of the matrix is very low even above the glass transition temperature. Therefore, the reinforcing effect of fibre with standard or elevated adhesion has no difference when creeping at low temperatures (up to 40°C). At high temperatures (typically above 50°C), the well bound fibres reduce the matrix flow, where the fibre and matrix load transfer is efficient, thus the creep of composite reduced. There are counter effects of the glass fibre reinforcements. The glass fibre can act as reinforcing element to improve mechanical properties, while all the fibre ends and interfaces are the potential initiators of crazes [13].

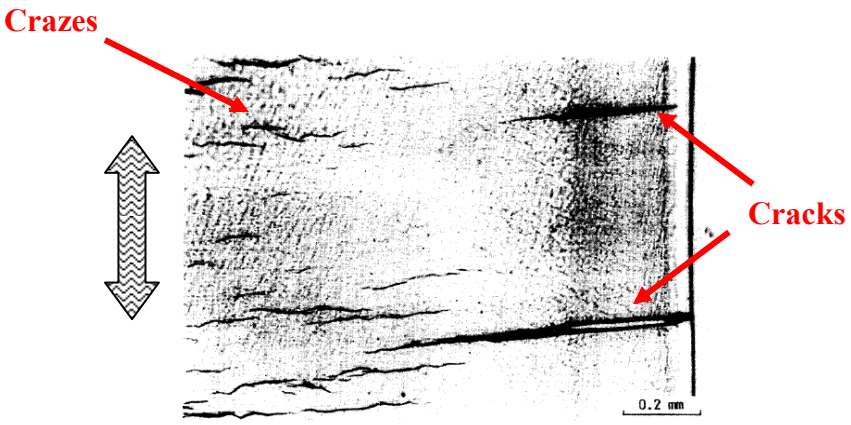

Figure 2-4: Unreinforced iPP at 80°C and 3 MPa after 2400 hours with low creep rate [13].

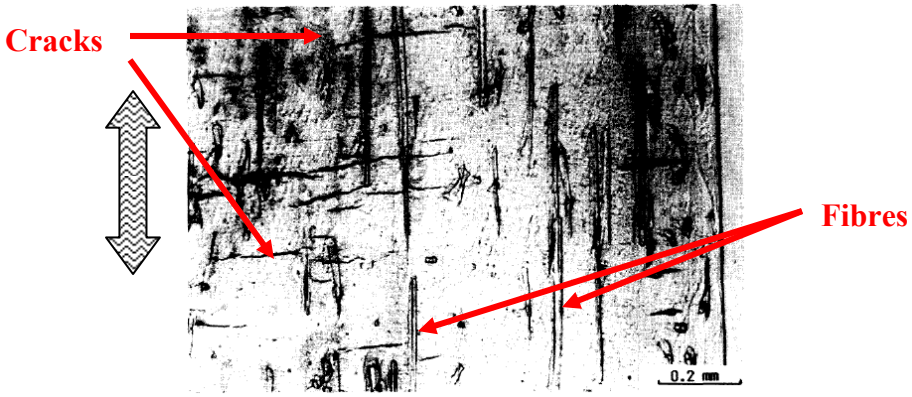

Figure 2-5: Reinforced iPP with 5 wt% standard adhesion fibres at 80°C and 3 MPa after 5200h at low creep rate [13].

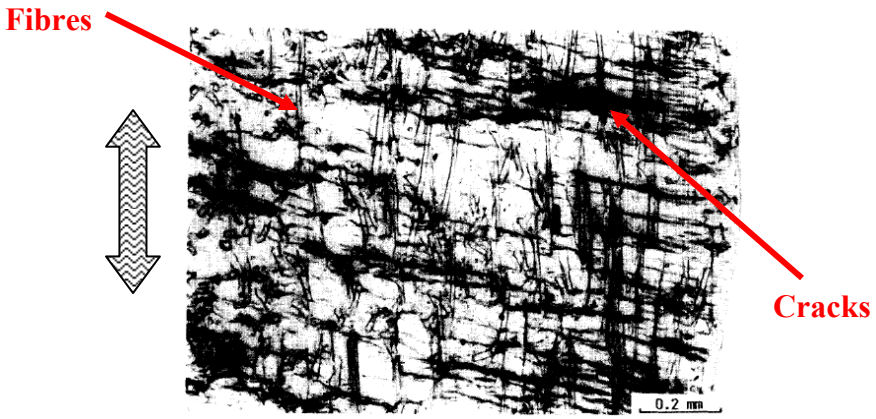

Figure 2-6: Reinforced iPP with 20 wt% standard adhesion fibres at 80°C and 6 MPa after 26h at high creep rate [13].

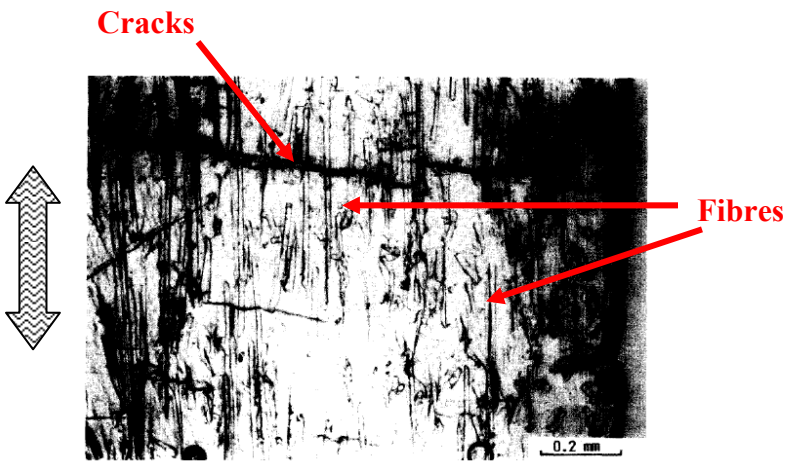

Figure 2-7: Reinforced iPP with 20 wt% elevated adhesion fibres at 80°C and 9 MPa after 5700h at low creep rate [13].

Lindhagen and Berglund also studied the damage mechanism at the microscopic level of the glass fibre reinforced polypropylene. The authors used thin notched sheets of swirled mat continuous fibre bundles and short single fibres [14]. By looking at the swirled mat samples, the transverse fibre bundles are more prone to debond under loading when compared to transverse single fibres. The fibre bundles initiate the damage due to existing debonding indicating by the shadows prior to the notch as shown in Figure 2-8. Other researchers also found that simultaneous debonding and plastic matrix deformation are the initiators of the damages [15]. Debondings propagate along fibres and coalesce through the thickness of the specimen to form microcracks which then leads to fracture with fibre pullout.

In the short fibre material, where the material has single fibres instead of the fibre bundles as found in the swirled mat material, fibres are evenly distributed throughout the material. Debonding of the materials is the initiator of the damage. Figure 2-9 shows the specimen is appearing darker throughout the material volume due to the evenly distributed single fibres. The diagonal crack growth as shown in Figure 2-9 indicated a region of the lower material strength, but the investigator did not mention the reason why the lower material strength region lies diagonally along the sample [14].

The study from Lindhagen and Berglund summarized the differences between the single fibre and the fibre bundles in the material: fibre bundles oriented transverse to the

direction of load act as the initiators of damage due to poor bonding of the individual fibres within the fibre bundles and the individual fibres tend to separate easily compared to the single fibre materials. The longitudinal crossing fibre bundles effectively stop a growing crack from the transverse oriented fibre bundles for further propagation. The crack propagations are forced to deviate to other crack formation zones, resulting in a larger damage zone. However, the short fibre material exhibits a more uniform fibre dispersion and the crack propagation is unhindered by crossing single fibres, resulting in a smaller damage zone compared to the swirled mat materials [14].

Ericson and Berglund also studied the deformation and fracture of the reinforced polypropylene with two structurally different GMT materials [16]. The investigators also studied the mechanical behaviour between the discretely dispersed in-plane random fibres compared to continuous looped bundles of fibre. The study showed that the material with discretely dispersed fibred has higher values of tensile creep modulus, tensile strength, elongation at fracture and work of fracture. The findings correlated to the result obtained by Lindhagen and Berglund.

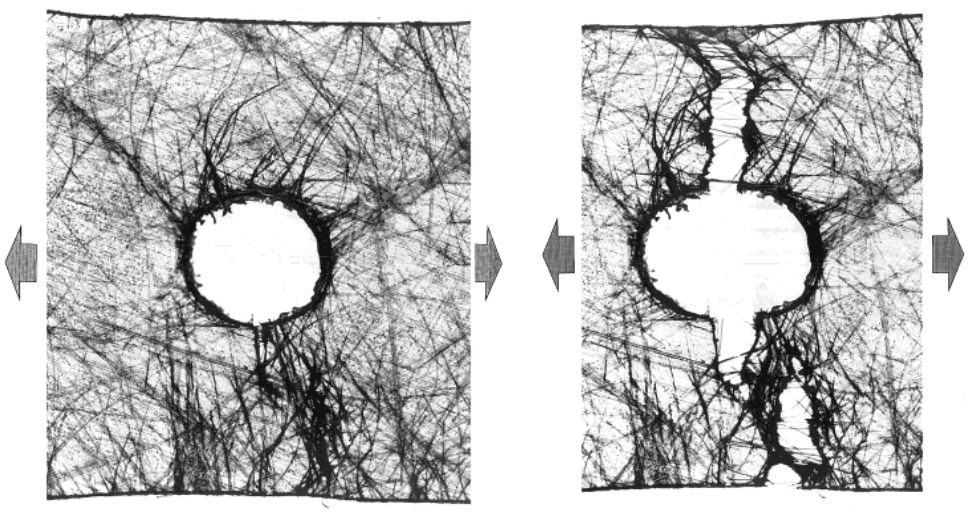

Figure 2-8: Swirled glass looped continuous mat reinforced polypropylene with notch at different state of damage [14].

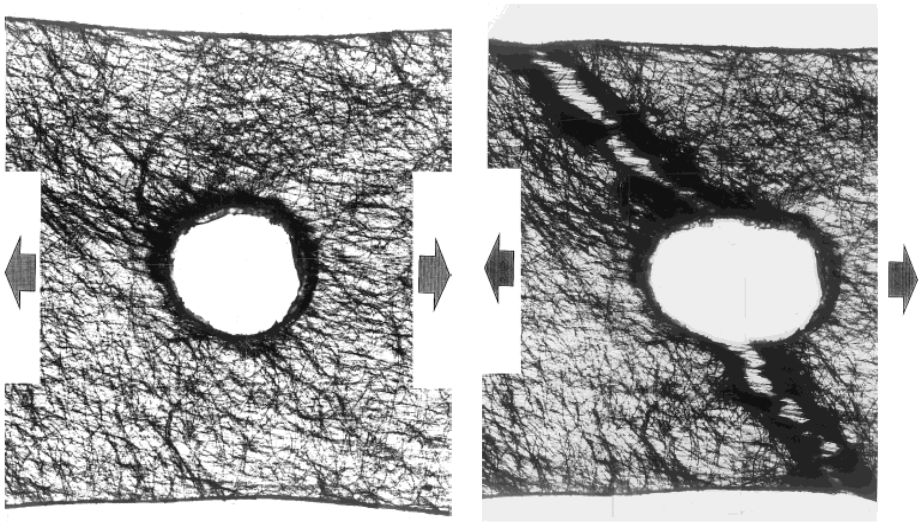

Figure 2-9: Short fibre reinforced polypropylene with notch at different state of damage [14].

Zebarjad *et al.* investigated the deformation mechanism with the injection molded specimen according to ASTM D 638 [17]. This study also compared the effect of adhesion between the standard fibres and the silane-treated fibres. It is found that the yield stress, modulus of elasticity and elongation at break are superior in the silane-treated fibres than the untreated fibres, as the primary function of fibre-matrix interface is to transmit stress from the viscoelastic polymer matrix to the high strength fibres. Figure 2-10 shows the difference of the fibre surface between the treated and untreated fibres. The silane-treated fibres have a rough surface, indicating strong adhesion to the polypropylene matrix, resulting in a good interface for the stress transmission between the matrix and the fibres. In Figure 2-11, the investigators found that the crazes are developed from the interface and the ends of the glass fibre, which is similar to the results found by Hugo *et al.* in Figure 2-5. The ends of the fibre are the preferred place for craze initiation due to stress concentrations resulting from weak bonding to the matrix. This phenomenon can be seen clearly in Figure 2-12. If there is a strong adhesion at the interface the crazes grow transversely which will eventually break the fibres as shown in Figure 2-12. With further stretching of the specimen Zebarjad *et al.* also found the crazes touch each other and grow in the matrix. These results are similar to those shown in Figure 2-6 by Hugo *et al.* Zebarjad *et al.* also concluded from their study that there is no

significant influence of interfacial adhesion on the craze thickening mechanism as the original crazes thicken after some craze extension caused by energy input.

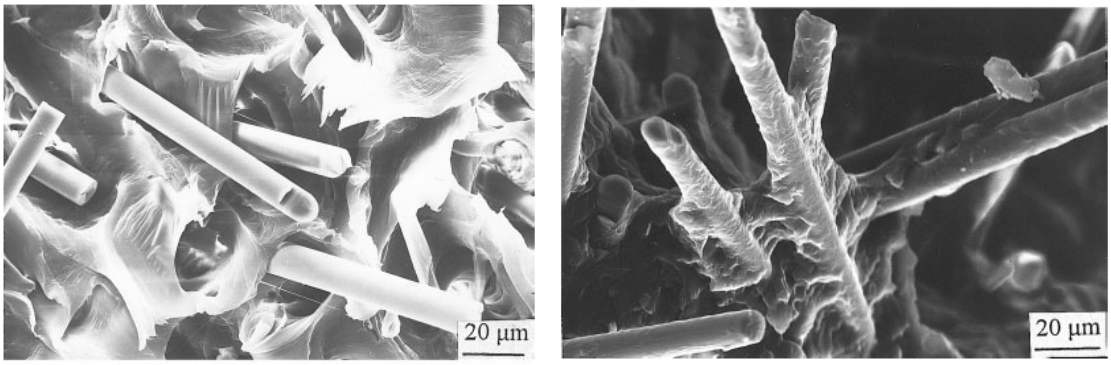

Figure 2-10: Fracture surface of PP reinforced with 20 wt%: (left) standard glass fibres, (right) treated glass fibres [17].

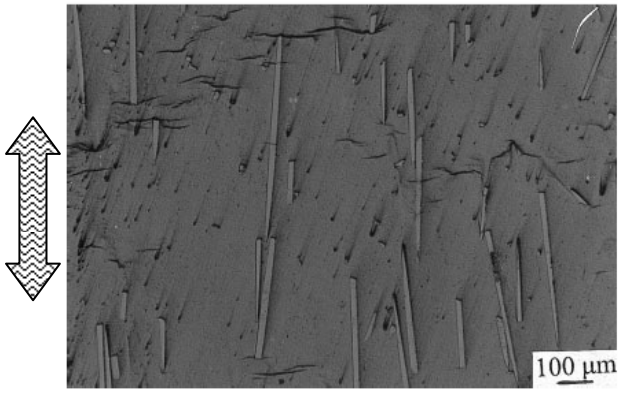

Figure 2-11: Optical microscopy of polished surface of tensile specimen with 20 wt% treated glass fibre with vertical loading direction [17].

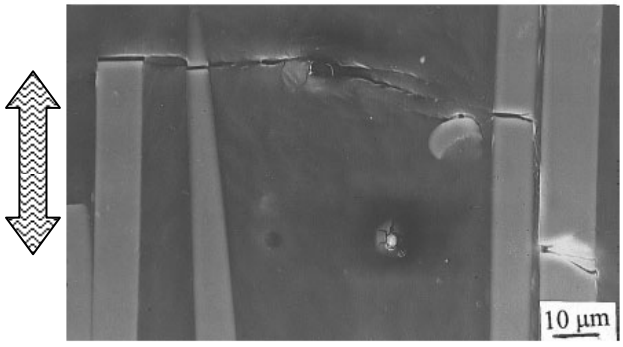

Figure 2-12: SEM micrographs of tensile specimen with treated fibres with vertical loading direction [17].

Another study by Zebarjad using three and four-point bending test on the notched specimens to study the fracture behaviour of polypropylene glass fibre composite found that fracture toughness increases with glass fibre content, as the composite leads to more ductile behaviour [18]. Investigating the polished surface of the damaged zone under the cross-polarized light microscopy, illustrated that shear yielding is not observed with during the fracture of the specimen. There is no evidence of birefringence in the composite.

Zhao *et al.* studied the fracture propagation energy between the different types of glass-mat structure, continuous fibre-bundle mats and continuous single-fibre mats [19]. The GMT with fibre-bundle mat structure with untreated polypropylene matrix resulted the longest fracture propagation time in the Izod impact test at room temperature, which showed extensive fibre debonding, pullout and bridging at the fracture surface in Figure 2-13a compared to GMT with single-fibre mat structure in Figure 2-13b. The results showed the facture propagation energy of the single-fibre GMT is lower than that of the fibre-bundle GMT. The investigators in this study have also suggested the present of voids resulted from poor fibre-matrix adhesion, causing decrease in tensile and flexural properties but the slight increase in impact properties.

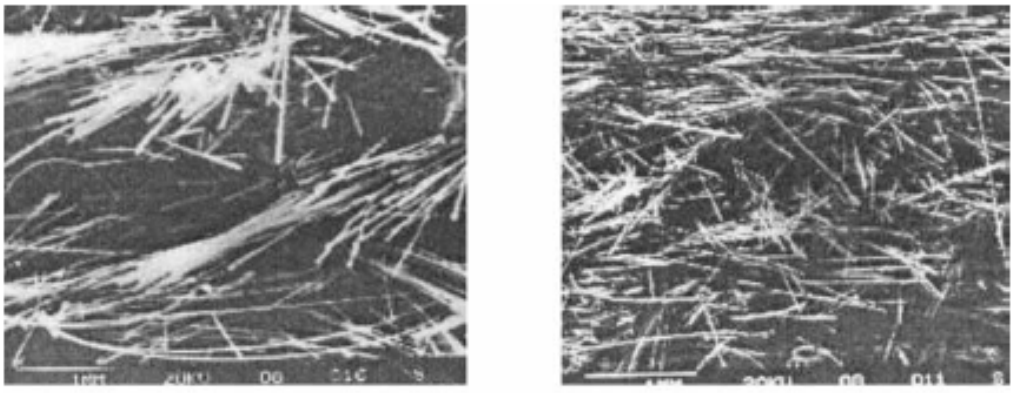

Figure 2-13: SEM images of the fracture surface from the Izod impact test for a) fibre-bundled mat and b) single-fibre mat GMT [19].

2.1.3.2 Acoustic Emission

Acoustic emission technique has been employed by numerous investigators to study the fracture mechanism of composite materials [10,15]. It is a high sensitivity and non-destructive technique for detecting active microscopic events such as different types of deformation mechanism in a material. Acoustic emission occurs due to transient elastic waves which are generated when there is a rapid release of energy from localized sources within a material [20]. The advantages of such technique provide a passive monitoring without requiring full volumetric scanning and it is not necessary to focus on the exact location of where the events are happening. During loading of a fibre-reinforced composite material, the events such as fibre breakage and debonding along the specimen may happen prior to the final fracture. By capturing the stress wave generated from the deformation, the data can be used to characterize the different deformation events.

Although the acoustic emission technique has not been used in this study, however, the investigations that were done using acoustic emission provide further insight of understand the fracture mechanisms and failure behaviours of the composite materials.

Aside from studying the fracture and deformation at the microscopic level, Karger-Kocsis *et al.* employed acoustic emission and infrared thermographic on the compact tension notched specimens to study the failure behaviour of composite materials with different structures [15]. With the same fibre content, it was found that the hot-pressed continuous glass fibre mat reinforced polypropylene (GMT) is superior to injection-molded long glass fibre reinforced polypropylene (LGF) when fracture toughness and energy are considered under both static and dynamic conditions. Figure 2-14 shows the load-displacement behaviour of the composite with different structures. The fracture behaviour of LGF can be characterized into four distinct regions, compared to two distinct regions for the GMT material. Figure 2-15 shows the distribution of matrix and fibre-related fracture behaviour. For LGF materials, the dominating facture mechanisms are debonding and fibre pull-out, which correlates to Figure 2-14 in region II and III. The overall distribution of the fracture mechanisms is fairly even. This correlates to

Lindhagen and Berglund's [14] suggestion that the composite with single fibres gives a more uniform material structure than one with fibre bundles.

By comparing the acoustic emission amplitude data for GMT and LGF material, the distribution of the facture mechanisms are different. Initiations of the facture shown in region I of GMT material in Figure 2-14 are due to matrix deformation and debonding, according to Figure 2-15. As in region II of GMT material, acoustic emission amplitude also shows that roving splitting up, fibre pull out and fracture of the roving result in the final fracture of the GMT material. Because GMT induces a more complex failure mode than LGF composite, GMT results in a higher toughness.

The difference between the damage zones for LGF and GMT is illustrated in Figure 2-16. Karger-Kocsis *et al.* suggested that GMT has a higher damage tolerance due to local deformation of the glass fibre mat. The local deformation creates stress release and redistribution processes, developing a large and steadily damaged zone. The energy dissipation in the GMT is far superior to LGF where the fracture mechanisms are mostly fibre-related such as debonding, pull out and fibre fracture (swirl mat versus long single fibres). This study concludes that the energy-related toughness of GMT is higher than LGF for the same reinforcement content.

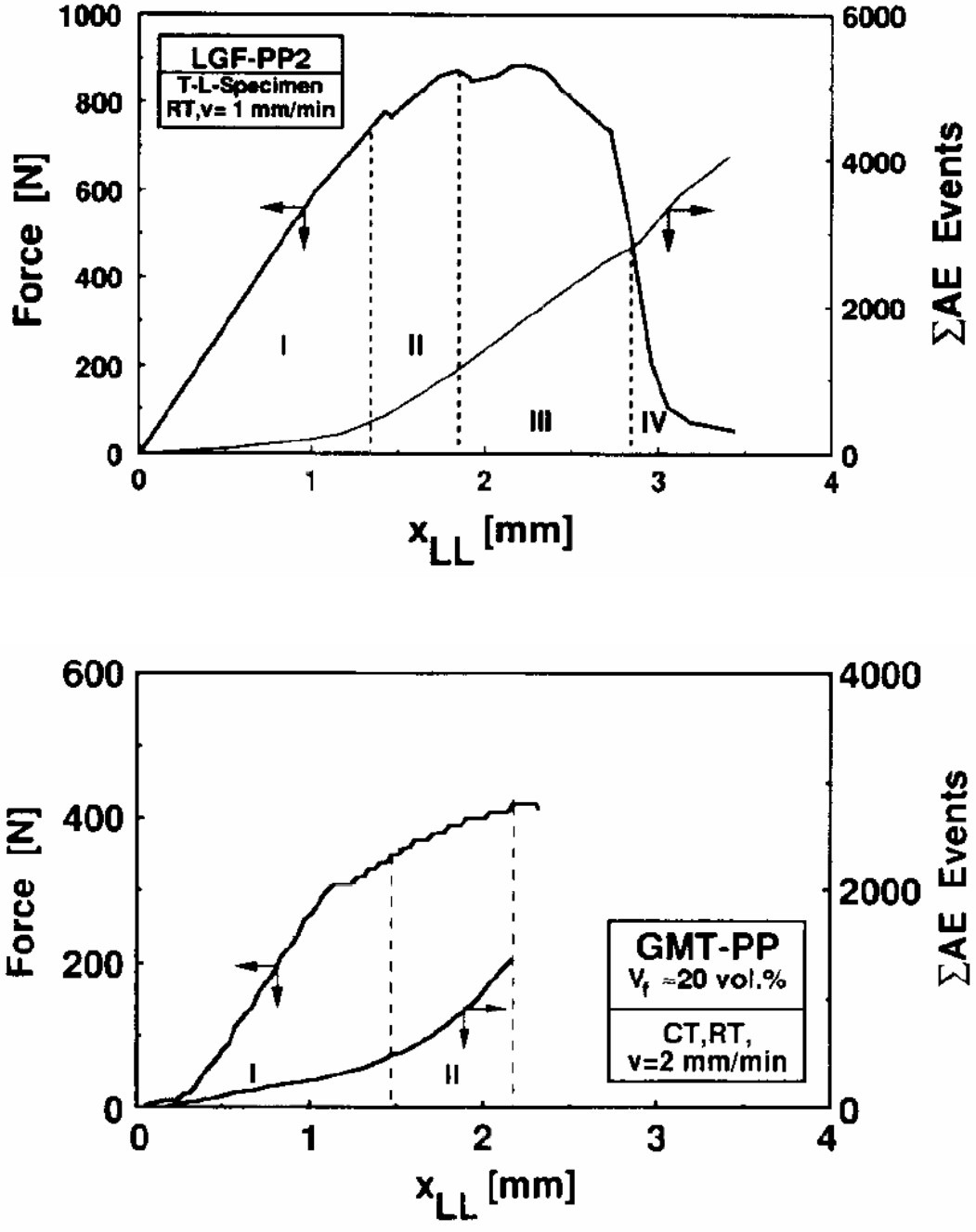

Figure 2-14: Curve of load-displacement and cumulative acoustic emission events (count) of compact tension specimen for LGF (top) and GMT (bottom) materials (Redrawn from [15]).

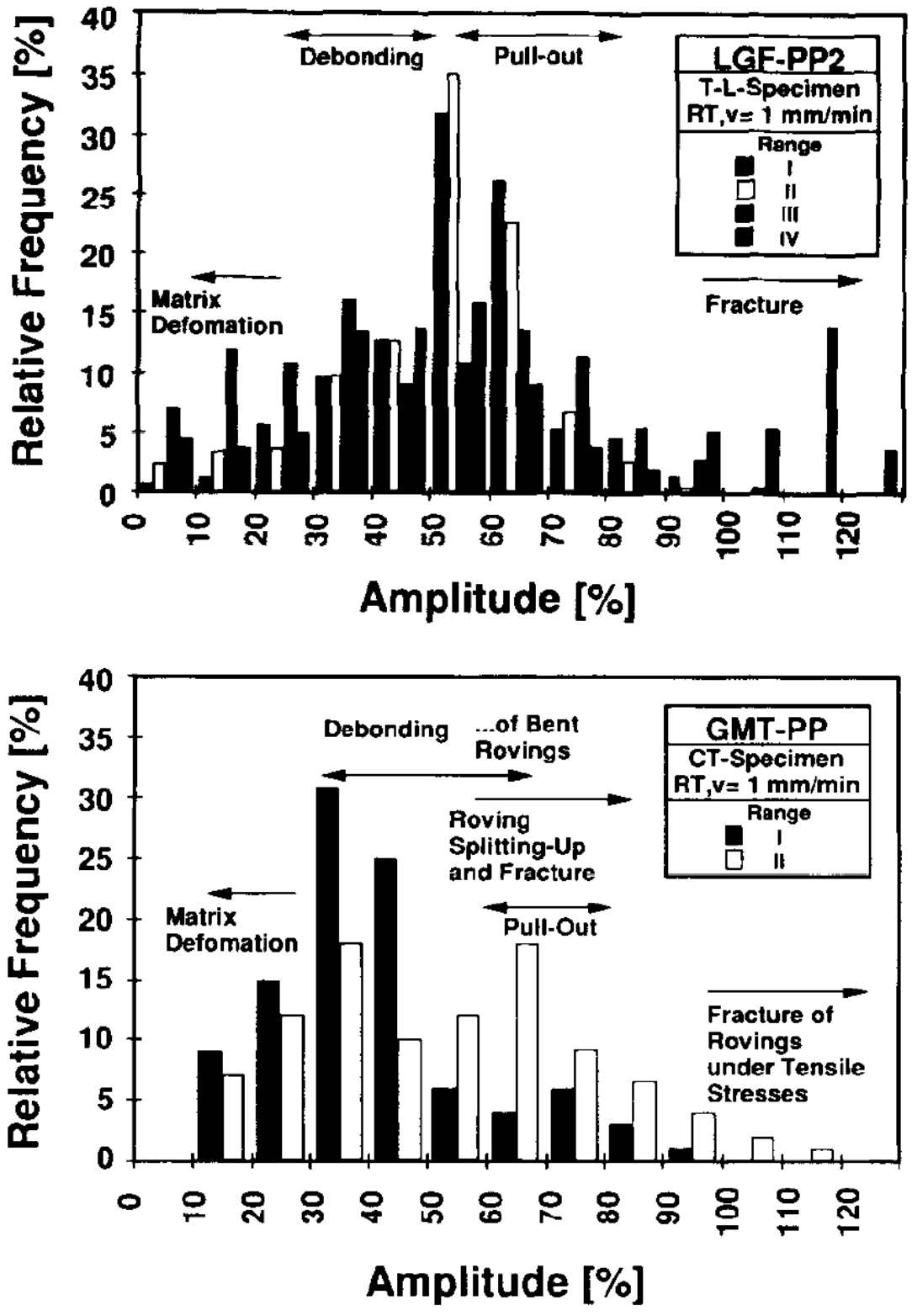

Figure 2-15: Comparison of acoustic emission amplitude in selected sections of loading curve of LGF (top) and GMT (bottom) materials [15].

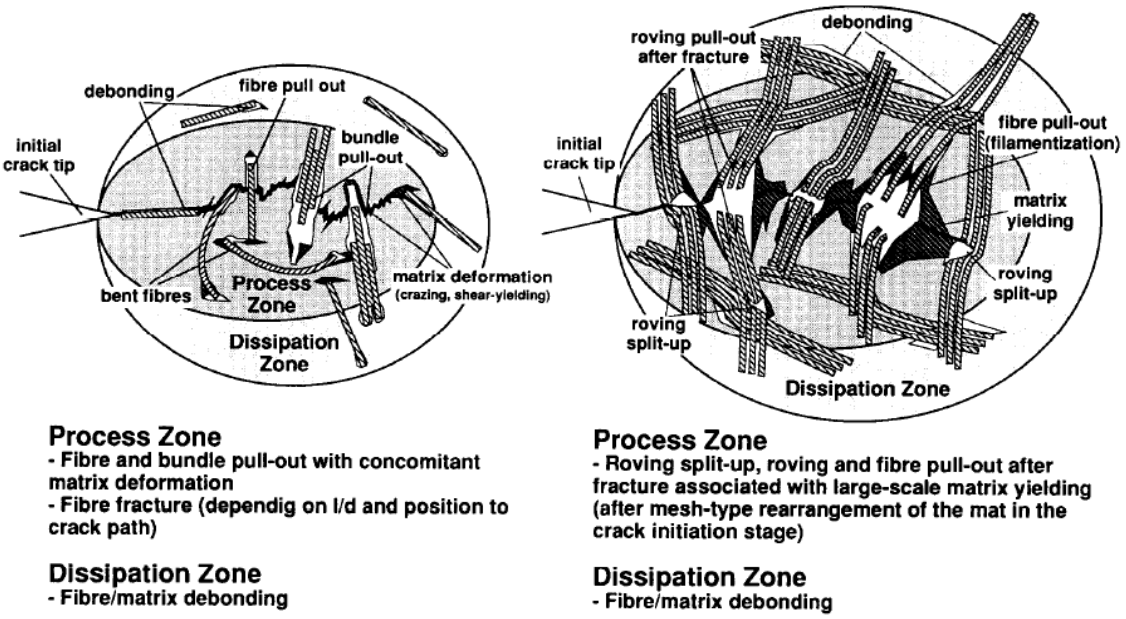

Figure 2-16: Damage zone schematic between the failure mode in LGF (left) and GMT (right) [15].

Ségard *et al.* also employed the technique of acoustic emission to identify the linear and non-linear damages during creep and recovery tests [10]. They specified the amplitude range of different deformation mechanisms, where 33-45 dB: microscracks of matrix; 46-58 dB: microcracks growth; 59 -68 dB: fracture of interface; 69-86 dB: Fibre/matrix friction, fibre pull-out; and 87-100 dB: fracture of fibres [21]. The microcracking of the matrix, in the range of 33-45 dB has the highest participation rate at 76 and 79% of the total number of damage events for both untreated and treated fibre respectively.

2.2 Crystallinity and Thermal Aging

2.2.1 Crystallinity in Polypropylene

The crystallinity of polypropylene determines its mechanical properties. Most of the commercial polypropylene materials have a crystallinity level between low density polyethylene (LDPE) and high density polyethylene (HDPE). There are three types of crystal lattice structures in polypropylene materials, α-, β- and γ-. The monoclinic α-phase crystals is usually the dominant type, with β- and γ-phase crystals formed by imposed orientation and elevated pressure during processing of materials, respectively. The typical densities are 0.936 g/cm^3 for the crystalline phase and 0.855 g/cm^3 for the amorphous phase at 20 °C. The typical values for degree of crystallinity of commercial samples are between 60 and 80%. Tacticity of the polypropylene samples also related to the crystallinity levels. Commercial PP samples usually have a high tacticity of 90% or more. They are highly isotactic and contain only a small amount of atactic material. The isotactic material is partially crystalline with sufficient packing efficiency and a high degree of lateral order [23].

The common techniques used to determine the degree of crystallinity, or the fraction of crystalline phase in the sample, are X-ray diffraction, density measurements and differential thermal analysis. In this study, the wide-angle X-ray diffraction (WAXS) technique was used to quantify the change in crystallinity levels due to effects of thermal aging. Figure 2-17 shows the intensity as a function of 2θ of the WAXS pattern for different crystal types of the polypropylene material. Infrared spectroscopy was also employed in this study to detect the *in-situ* crystallinity changes over the course of aging, as well as the detection of the chemical degradation.

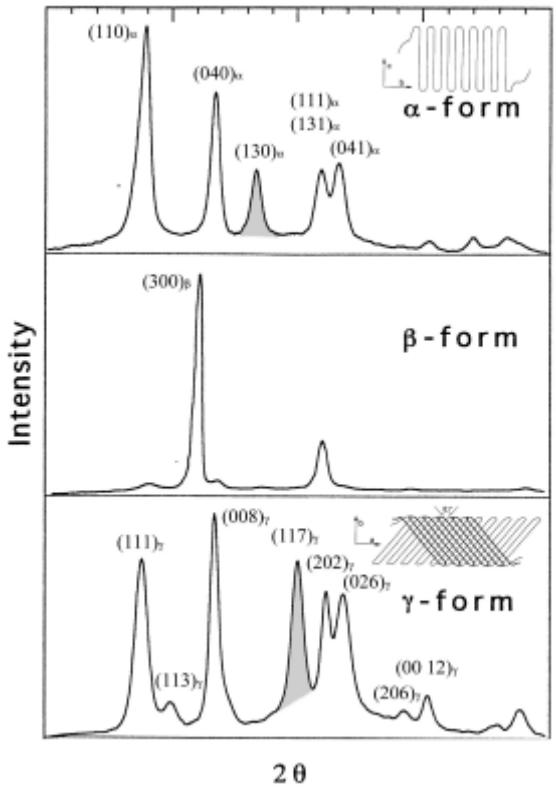

Figure 2-17: WAXS-pattern of different crystal phases and their crystal structures. (Courtesy F. Auriemma and C. DeRose, Naples University) [24].

2.2.2 Thermal Aging of Semi-crystalline Polymers

Semi-crystalline polymer, such as polypropylene, consists of crystalline and amorphous phases. During processing of the material, the molten state is rapidly cooled to solid state of parts with different shape, in order to improve the cycle time of the process. However, due to the rapid quenching of the material during processing, there is insufficient time for the molecular chains in amorphous phase to flow into crystal lattice. The chains are frozen with reduced mobility and the material results a lower crystallinity level.

Semi-crystalline polymers exhibit thermal aging effect at above the glass transition temperature. Heat energy due to aging unfreezes the molecular chains in the amorphous phase resulting increased in mobility. This allows the amorphous chains to fold with the existing crystal or formation of the new crystals, thus increasing the crystallinity of the

materials. With the increase in crystallinity with high tacticity, the mechanical properties such as stiffness of the material increases [23]. However, excessive aging over time results in chain scissions due to oxidative attacks [3]. The reduction in length of the molecular chains promotes higher mobility to fold into crystal lattices, but it also degrades the mechanical properties significantly.

Therefore, it is very important to understand how thermal aging affects the crystallinity changes and oxidative degradation of the polypropylene materials, through the polymer characterization techniques.

2.2.3 Polymer Characterization Techniques

The techniques that are used in this study for polymer characterization are wide-angle x-ray scattering (WAXS), Fourier transform infrared spectroscopy (FTIR) and differential scanning calorimetry (DSC). Each of these techniques will characterize different properties of the polypropylene sample, but may result in the same trends; such as the increase or decrease of the crystallinity level, which is one of the major interests in this study. Thermogravimetric analysis (TGA) and gel permeation chromatography (GPC) techniques were also used to determine the supportive data such as information on the additives and molecular weight distribution of the samples, respectively.

The results from WAXS will provide information on the amount of crystallinity and different forms of crystal type, (α, β and γ) within the sample. The profile of the intensity at different 2θ angles will also dictate the crystallinity level through the mathematical post-processing of the recorded data.

The results from FTIR will provide information on the changes of the crystallinity level and the detection of any oxidation product developed during thermal aging. The intensity of the absorbance ratios are use as an index to determine the increases and decreases of crystallinity. Carbonyl groups and hydroxyl groups are the oxidation products that will

be detected at unique ranges of the spectrum if developed in the samples over the course of aging.

The results from DSC will provide information on the transition and melting temperatures of the samples. The crystallinity can also be determined from the area of the endothermic peaks divided by the reference enthalpy for the 100% crystalline samples. Also, the profile of the DSC data can also determine the uniqueness of the crystalline structures.

The results from TGA will provide information on the weight fraction of the fibre in the composite samples. The weight loss curve measured from TGA will also allow characterization of the degradation behaviour of the composite at elevated temperatures. The weight loss curve will show the degradation of additives, provided there is a sufficient amount of the additive present. By referring to the oxidation temperature range of the additives, materials like carbon black, which is know to degrade between 500 to 750 °C [25], can be detected by looking for drops in the weight loss curve within the oxidation temperature range.

The results from GPC will provide the information on the number average and weight average of the molecular weight. The molecular weight distribution data, determined from the calibration plot and elution profile, will provide the information on the distribution of the molecular chains of different sizes.

The polymer characterization techniques mentioned above will discuss further in the following sections in this chapter.

2.2.4 Wide-Angle X-Ray Scattering

X-ray diffraction is a powerful, non-destructive analytical technique that is used to reveal the crystallographic structure, chemical composition, physical properties. It can also be used to identify materials by comparing them to a known crystal structure by measuring

the scattered intensity of the x-ray beam. There are different types of scattering techniques such as small angle x-ray scattering (SAXS), x-ray reflectivity and wide angle x-ray scattering (WAXS) [26].

The underlying principle of WAXS is the diffraction of the incident rays such as the visible light passing through a glass slide, where scratch lines in the glass plate serve as the light scattering centre with typical spacing of 1 μm. For x-ray diffraction, the same principle applies but in the sub-nanometer scale where the atoms are the scattering center and the crystal structure acts as the scratch line. X-radiation has been used as the incident rays with wavelength of 0.1 nm. Because the size of the atoms and ions are on the order of 0.1 nm, x-ray diffraction is capable of characterizing crystalline structure by treating the stacks of crystal planes as the parallel scratch lines [26].

The Bragg equation demonstrates the relationship as follows:

$$n\lambda = 2d \sin\theta \tag{3}$$

where n is the integer number of radiation wavelengths and θ is the scattering angle (°) or Bragg angle. d is referred to interplanar spacing in nanometres (nm), which is the distance between the adjacent crystal planes as a function of the Miller indices for the plane which depend on structure of the unit cell. The angle 2θ is the diffraction angle that will be measured experimentally.

The experiments in this study were done with a diffractometer and the schematic is shown in Figure 2-18. The intensity of the diffracted bream is monitored by the detector. The recorded diffraction pattern can be used to identify the materials by comparing against a database of known diffraction patterns for different materials.

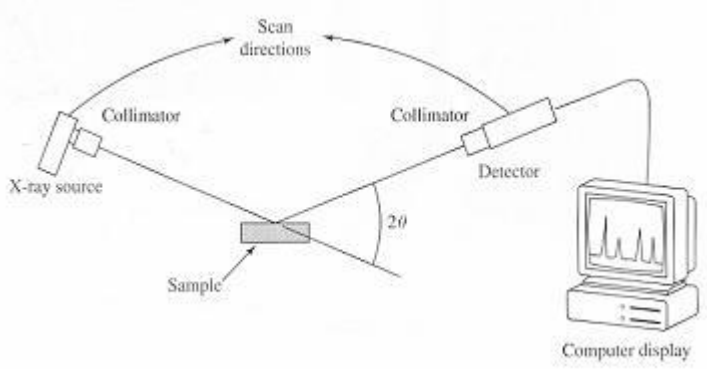

Figure 2-18: Schematic of an X-ray diffractometer [26].

In this study the recorded diffraction pattern for the polypropylene samples will be used to determine the crystallinity levels after post-processing with mathematical software. The techniques used for crystallinity level determination will be discussed in the following chapter.

2.2.5 Fourier Transform Infrared Spectroscopy

FTIR is a non-destructive analytical method that is used to identify the presence of the functional groups in a molecule, to confirm the identity of a pure compound or to detect the presence of specific impurities. It generates the result in the form of qualitative analyses such as composition for identifying reagents and quantitative analyses such as concentration comparisons of a known sample.

In both organic and inorganic materials the chemical bonds in the molecule will vibrate uniquely. Bending and stretching will occur at various frequencies depending on the elements and the types of bonds. The frequencies of these vibrations are in the same range as the infrared frequencies of electromagnetic radiation. Thermal excitation occurs when they are exposed to the infra-red (IR) portion of the electromagnetic spectrum. The infra-red light of energy is absorbed by the molecule, resulting in vibrations within the molecule jumping from the ground state to the excited state. By monitoring the absorbance of a range of wavelengths or frequencies of an infra-red light as it is

transmitted through or reflected from a sample, a characteristic infra-red spectrum can be obtained.

By obtaining the infra-red absorption spectrum, the materials can be identified by looking at the composition of the function groups or cross referencing to the spectrum library.

The mathematical relationships of the intensity of IR spectrum are as follows [27]:

Transmittance:
$$T = \frac{P}{P_o} \times 100\% \tag{4}$$

Absorbance:
$$A = \log\left(\frac{1}{T}\right) = \log\left(\frac{P_o}{P}\right) = abc \tag{5}$$

where P_o = Intensity of incident radiation

P = Intensity of transmitted radiation

a = the absorptivity of the component at a particular wavelength ($M^{-1}cm^{-1}$)

b = path length of the sample (cm)

c = concentration of the component (M)

Excited molecular movements can be classified as stretching or bending vibrations. Stretching can be classified into symmetric and asymmetric stretching, while bending can be referred to deformation and sub-classified into scissoring, wagging, twisting and rocking as shown in Figure 2-19.

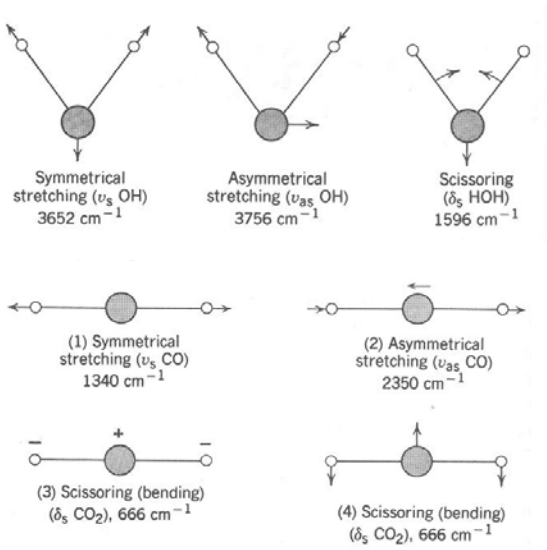

Figure 2-19: Fundamental vibration modes, stretching and bending, symmetric and asymmetric [28].

The infrared fundamental region is in the range of wavenumber (frequency) of 4000 to 400 cm^{-1}. Figure 2-20 shows the general absorption band covers a wide range of organic compounds of the fundamental vibration modes, by limiting the discussion to molecules containing only the elements: carbon, hydrogen, nitrogen and oxygen.

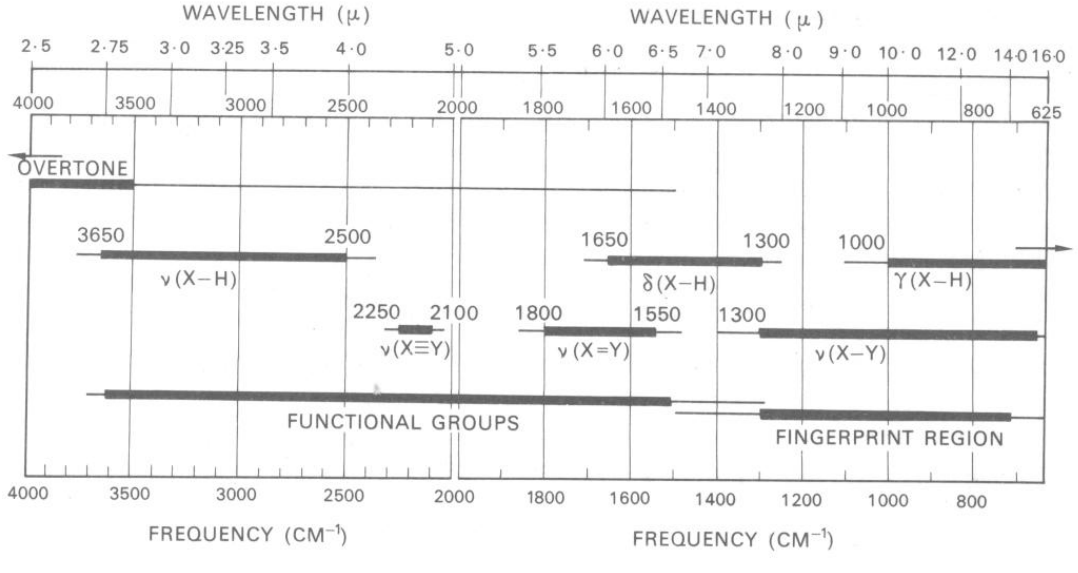

Figure 2-20: The infrared fundamental region. ν = stretching, δ= in-plane bending, γ=out-of-plane bending. X and Y represent different atoms for bonding [29].

The typical applications of the FTIR spectroscopy are the materials evaluation, identification, failure analysis and quality control screening. IR spectroscopy can offer information about the polymer matrix composite (PMC) materials on both qualitative and quantitative levels. Most of the PMC materials are optically opaque due to their composition. However, they have significant spectral "windows" in the infrared range, through which the polymer matrix can be identified by the characteristic absorption. The reinforcing materials in the composite will scatter the absorption due to reduced energy throughput and cause spectral distortions, which will make it harder to identify the matrix. Another application will be finding out how thermal effects affect the crystallinity of polypropylene matrix glass fibre reinforced composite materials. The crystallinity index was determined by analysis of the FTIR absorbance spectra by applying Lambert and Beer's law to the selected peaks. The FTIR spectroscopy technique is chosen for this application as it is a suitable apparatus to *in-situ* monitoring the evolution of crystallinity during the thermal effects to the PMC materials [5]. However, for the field of interest, we will only be investigating in the polymer matrix of the composite.

The samples can be prepared in solid, liquid and gas form in order to obtain the infrared spectra [28]. In this study, all the samples that are examined are in a solid state. Solids are usually examined as a mull, a pressed disk, or as a deposited glassy film. The deposited film technique is particularly useful for obtaining spectra of resins and plastics, while care must be taken to free the sample of solvent by vacuum treatment or gentle heating.

There are different types of FTIR analyses and they are mainly classified in two categories: transmission spectroscopy and reflection spectroscopy. Transmission spectroscopy is the most simple and basic sampling technique where the infrared radiation is passed through a sample and the transmitted radiation is measured. Reflection spectroscopy will employ samples that are thick, opaque, highly reflective, or otherwise unsuitable for transmission analysis. There are three main categories for this technique and they are specular reflectance, internal reflectance and diffuse reflectance.

They depend on different applications as the reflected radiation is measured rather than the transmitted radiation.

2.2.6 Differential Scanning Calorimetry

Differential scanning calorimetry is a thermo-analytical technique which measures the energy required to heat a sample and a reference as a function of temperature. The most common applications of the DSC include evaluating the sample purity and studying polymer curing in industrial settings.

The basic principle of this technique is to maintain the same temperature between the reference and the sample. When the sample reaches a temperature close to the melting point, extra heat is required for the solid sample to melt into a molten stage in order to maintain the same temperature level as the reference. The recorded data from the DSC is the heat flux, either increased or decreased, in milliwatts (mW) as a function of time or temperature.

Both exothermic and endothermic processes can be observed from the DSC data. An example of an exothermic process is the crystallization of thermoplastic materials, while exothermic processes include phase transitions and melting of samples. Figure 2-21 shows some common features that may be observed from DSC data, showing exothermic process upwards, as the heat flow decreases with increase in the y-axis.

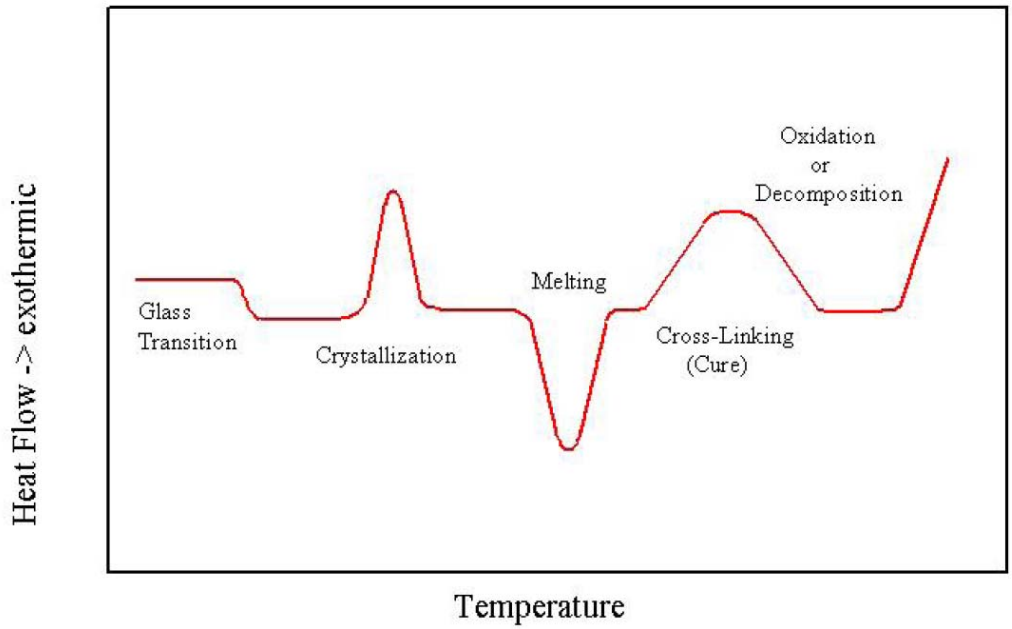

Figure 2-21: Schematic of DSC curve [30].

The data recorded from DSC can also be used to calculate enthalpies by integrating the area under the curve within a range of temperature. Enthalpy calculated from the integration of the heat flow profile is useful for determine the crystallinity of the sample by comparing it to the enthalpy of a known reference having 100% crystalline structure. In this study the technique of dividing the integral of the melting endotherm of the polypropylene sample by the reference for a 100% crystalline polypropylene material was extensively used to determine the crystallinity changes due to the effects of thermal aging.

The crystallinity, X_c, determined from the DSC analysis can be calculated as [31]:

$$X_c = \frac{\Delta H_M}{\Delta H_o} \tag{6}$$

where ΔH_M is the measured melting enthalpy and ΔH_o is the melting enthalpy of a 100% crystalline polypropylene at equilibrium melting point at 165.0 J/g [32].

Glass transition temperature can be determined from the DSC data recorded at a relatively fast scanning rate in order to detect the step change of the endothermic process which changes from a glassy state to a semi-crystalline phase. The melting temperature can also be determined from the DSC data by locating the temperature where the melting endotherm peak occurs.

2.2.7 Gel Permeation Chromatography

Gel permeation chromatography (GPC) is a technique used to separation, purification, and analysis of mixtures of substances based on the differences in molecular size. Molecular weight distribution is determined by separating the particles based on the elution volume. This technique is often applied to macromolecular complexes such as industrial polymers for molecular weight determination [33]. GPC provides the first (M_n), second (M_w) and third (M_z) degree of molecular weight. The main system components consist of the pump, injector, columns, various types of detectors such as refractive index and the data acquisition system.

The basic principle of GPC is the measurement of the retention time of the mobile phase as it travels through the stationary porous phase depending on the size of the particles. The mobile phase consists of the mixture of the solvent and polymer particles. The solvent used in the mobile phase depends of the type of polymer particles. Due to the size differences of the particles, the small particles diffuse inside the pores of the stationary phase, while the large particles cannot diffuse inside the pores, resulting in less interaction time with the stationary phase. The difference in retention time, as the time required for a fraction of the polymer particles travel through the columns, will result the broadening of the molecular weight distribution [34].

With the above parameters setup and controlled properly, the elution profiles and calibration plot can be generated from GPC, as shown in Figure 2-22.

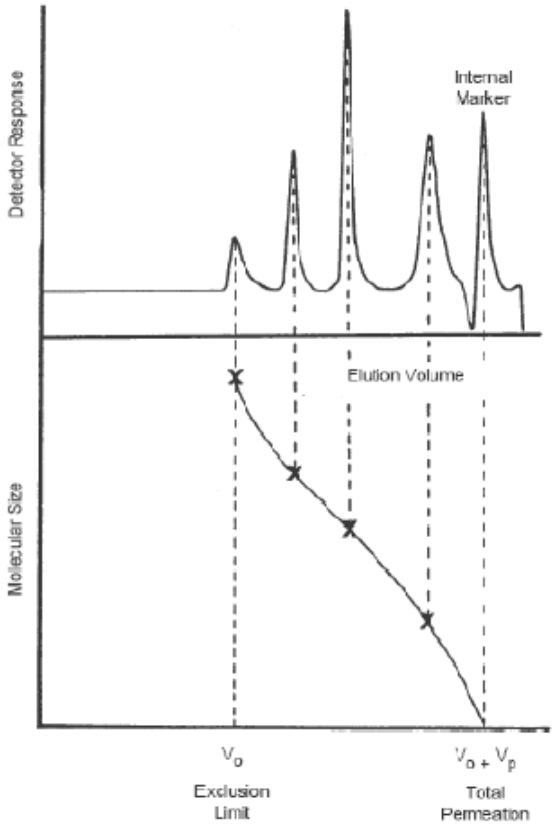

Figure 2-22: Examples of elution profile and calibration plot [34].

The elution plot in Figure 2-22 measures the response of the detector in voltage (mV) as a function of time, which is the measurement of time it takes for the mobile phase to travel through the porous stationary phase while a quantity of the particles are converted to measure of voltage. With the constant injection flow rate and the elution profile of a known reference polymer, a calibration plot of the molecular weight as a function of the retention volume (mL) can be obtained. By simple mathematical operations and replotting the data, the molecular weight distribution curve can be generated in volume fraction as a function of the molecular weight.

There are different average values of the molecular weight such as weight average (M_w), number average (M_n), viscosity average (M_v) and Z average (M_z). In this study, M_w and M_n will be the major interest, and they can be calculated in the following equation in weighted mean:

$$\overline{M_x} = \frac{\sum C_i M_i^n}{\sum C_i M_i^{n-1}} \tag{7}$$

where M_x is the average value of interest either M_n (for n = 1) or M_w (for n=2), Mi is the molecular weight and C_i is the number of chains of molecule i, respectively. The polydispersity index (PDI), defined as M_w divided by M_n, determines the dispersity of the molecular chains with different molecular weights. A smaller PDI, implies a narrow distribution of the molecular weight with high uniformity of similar size chains of a polymer sample.

2.2.8 Literature Review on iPP Physical Aging and Crystallinity

Isotactic polypropylene (iPP) is used extensively as a matrix material in thermoplastic composites due to its excellent mechanical properties and relatively low cost. Since the long-term engineering properties of iPP are intrinsically linked with the polymer microstructure, there is significant interest in understanding the effects of aging, particularly due to prolonged exposure at service temperatures. A common approach for characterizing aging response in a more practical time frame is to conduct accelerated aging tests at temperatures above the expected service limits. There are already ample reports of physical and chemical changes in polypropylene including secondary crystallization [3, 35-37] and degradation due to oxidation [38-42] caused by the thermal aging process.

Most of the reported studies thermally age samples in an oven in air, with [36, 40, 41] or without ambient light (UV irradiation) [3, 35, 37-39, 41]. The temperature levels studied ranged from sub-freezing to room temperature and up to 150°C for different time periods. The most common analytical techniques were differential scanning calorimetry (DSC), wide-angle X-ray scattering (WAXS), Fourier-transform infrared spectroscopy (FTIR) and gel permeation chromatography (GPC). Although the aging behaviour of iPP has been widely studied, it is not easy to correlate the different sets of data due to the

differences in processing morphologies (solidification rates) and additives (carbon-black and/or anti-oxidant), as well as aging conditions.

2.2.8.1 Change in Molecular Structure

The stability of polypropylene depends on the impurities present within the material. Mathur and Mathur [42] employed infrared (IR) spectroscopy to detect and quantify the presences of impurities. They found that the formation of the oxygenated and unsaturated groups induced by chemical reactions affect the ultimate properties of the polymer and alkoxy radicals deteriorate the properties of polyolefins.

Wyzgoski [38] used infrared transmittance to detect the formation of the oxidation products of polypropylene specimens aged at 90°C by dissolved polypropylene off the surface of the tensile bar. There was particular interest at the absorbance wavenumber 1708 cm^{-1}, normalized with 974 cm^{-1}, which accounted for the C=O vibration commonly associated with hydrocarbon oxidation products such as acids, aldehydes or ketones. The normalized infrared absorbance increased after aging for about 240 hours, indicating oxidation was occurring on the surface after aging for 200 hours.

Gugumus [43] also used FTIR spectroscopy to monitor the formation of the carbonyl groups (C=O) and hydroperoxides (POOH) during oven aging of unstabilized polypropylene at 80°C. Absorbance bands at 1714 and 3400 cm^{-1} were used to account for the formation of the carbonyl groups and hydroperoxides respectively. Figure 2-23 shows the absorption intensity changes over various aging periods. The author examined the kinetics of the thermal oxidation as functions of aging time, sample thickness, sample preparation and different polymer grades. It was found that the formation of the functional groups did not fit perfectly to the power law. Figure 2-24 shows that the associated hydroperoxides show a tendency to reach the plateau values while the associated carbonyl groups increase linearly with aging time until sample becomes brittle, and varies between different sample thickness.

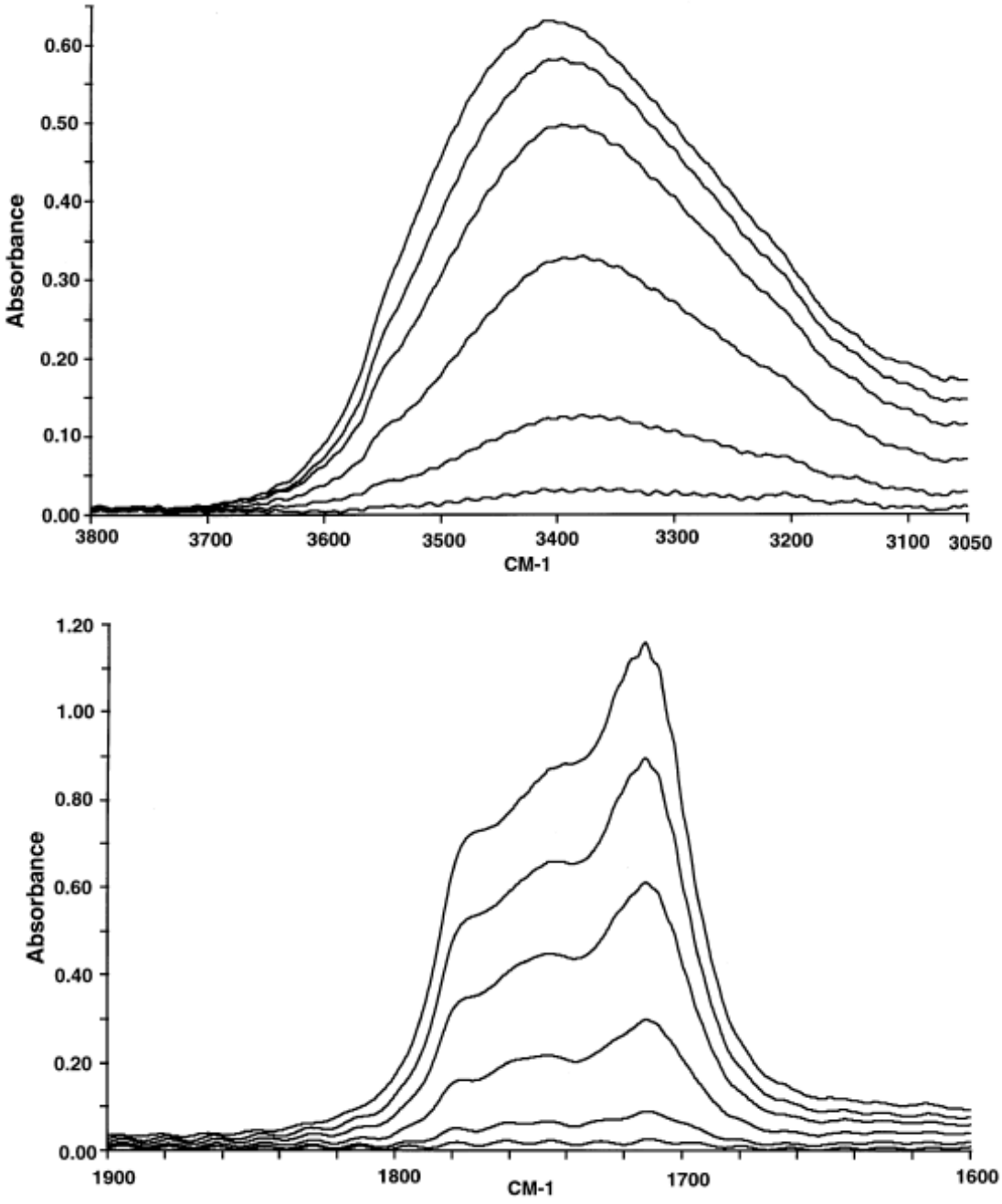

Figure 2-23: Change in IR absorbance of a PP film on thermal oxidation at 80 °C.

Aging times (hrs): 303, 327, 353, 378, 400, 428 [43].

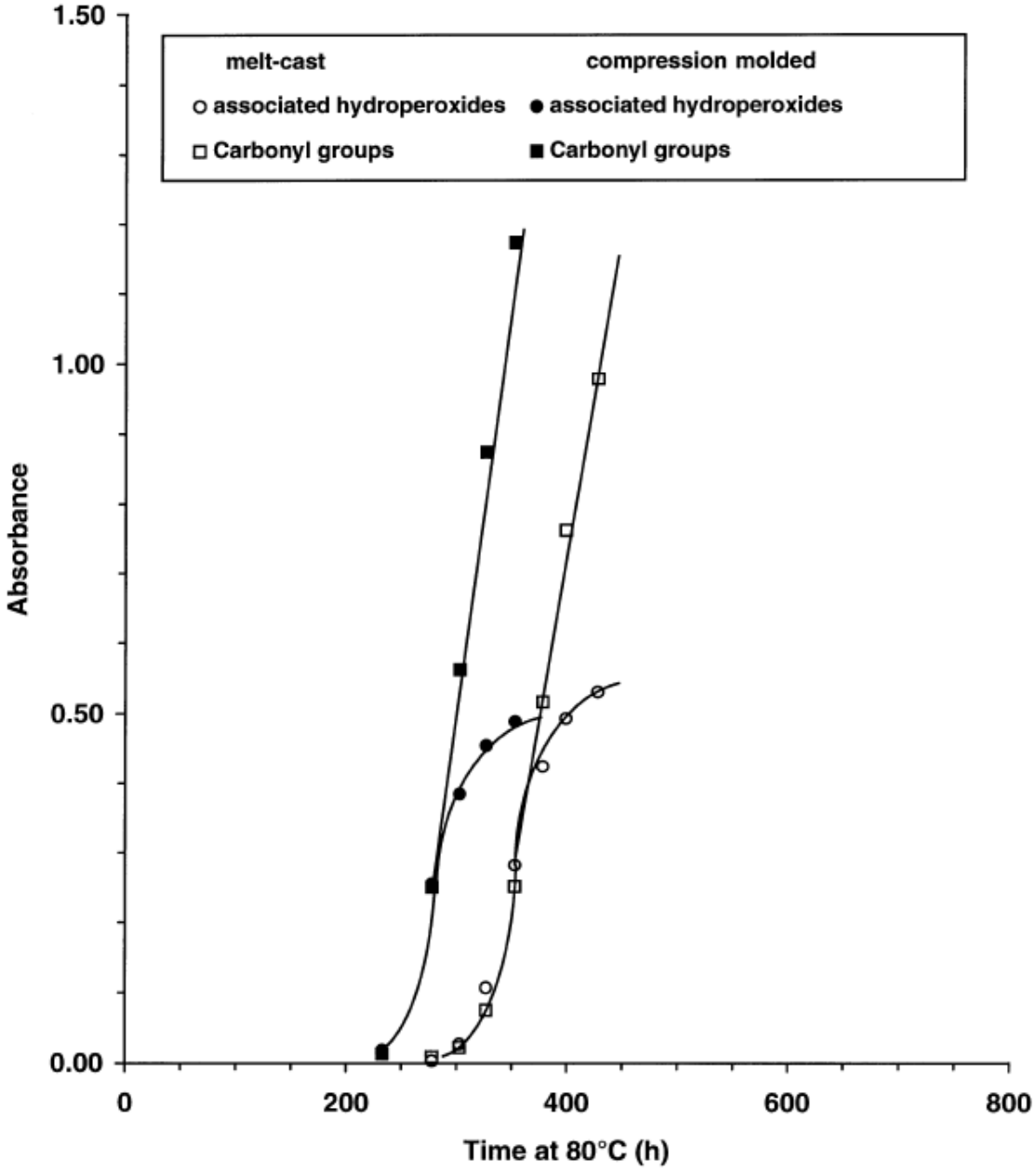

Figure 2-24: Comparison of IR absorbance for carbonyl groups (1714 cm^{-1}) and hydroperoxides (3400 cm^{-1}) aged at 80 °C for mold-cast and compression-molded materials [43].

Larena, Jiménez de Ochoa and Domínguez [40] studied the photo-degradation of long glass fibre reinforced polypropylene. Although photo/UV degradation is outside the scope of this literature review, there is certain important information provided from this study. Photo-oxidation effects are more intense compared to thermal-oxidation, therefore

the intensity changes with exposure time should not be used as a reference to thermal-oxidation effects. They also employ FTIR to detect the oxidation products from radiation effects. Carbonyl and hydroxyl groups will appear at wavenumber from 1900-1500 cm^{-1} and 3800-3000 cm^{-1} region respectively, as shown in Figure 2-25.

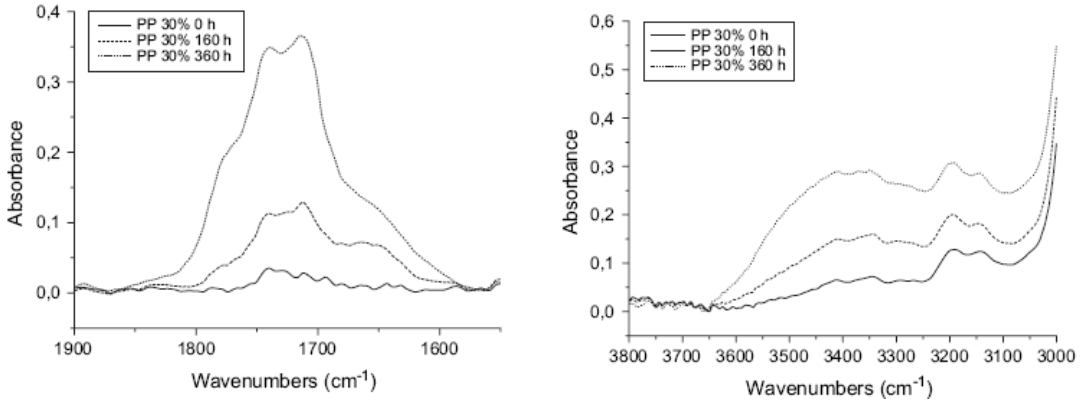

Figure 2-25: IR intensities for carbonyl (left) and hydroxyl groups due to photo-oxidation [40].

Rjeb *et al.* [41] also characterized aging under ambient atmospheric conditions with FTIR spectroscopy. From the new isotactic sample that was used in the study, the presence of oxygen was found at the corresponding wavenumber of 1168cm^{-1}, incorporated into the chain in the form of C-O-C, even before the material was aged. When aging without the exposure to the sun, the investigator further broke down the oxidation products in the carbonyl group such as ketones conjugated to alkenes, nonconjugated ketones, aldehydes, esters, acids, peresters and peracids. However, the closeness of the absorption bands impeded the quantitative analyses of the individual oxidation products. It was observed that the intensity of methylene (CH_2) decreases with the increase of C-O, suggesting that the methylene (CH_2) was the favourable oxidation site.

2.2.8.2 Change in Crystallinity

The degree of crystallinity is closely related to isotacticity and density. Polypropylene with high isotacticity, has the methyl side groups on the same side of the backbone with the same stereoregularity, thus enhancing its ability to crystallize in the helical form. With the chains that aligned properly in the crystalline phase, the density of the crystalline regions will be higher compared to the amorphous regions with the chains in less ordered form.

Martynov and Valegzhanina [39] studied the heat-aging effects of polypropylene back in 1965. Aging in air was performed in 150 °C, where they found the crystallinity and size of microcrystal increased at the initial period of aging, and then decreased slightly as time prolonged until breakdown by formation of micro-cracks developing to macro-cracks, as shown in Figure 2-26. This was because the heating from aging increased the chain mobility, resulting in partial crystallization and formation of new supermolecular structures. However, at the same instance, oxidation took place causing molecular ruptures, which resulted in a competing process between crystallization and oxidation breakdown.

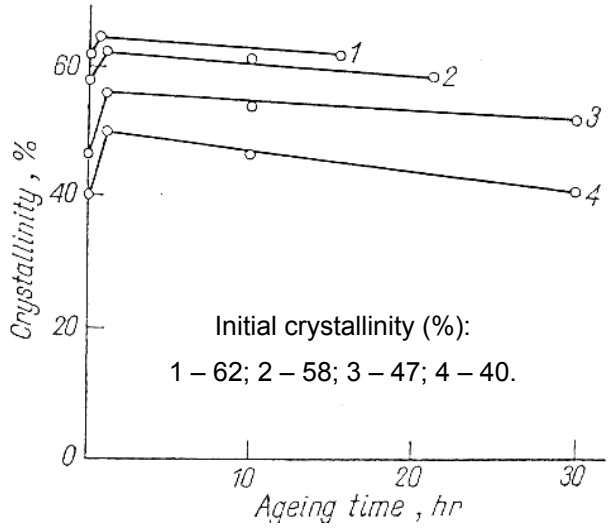

Figure 2-26: Variation of PP crystallinity aging at 150 °C in air [redrawn from 39].

Mathur and Mathur [42] reported that the crystallinity, in terms of isotacticity and density, increased with aging time. This was due to the low molecular weight chains attaining a more ordered form in the matrix during aging.

Wyzgoski reported [38] that the crystallinity index measured by IR reflectance directly from the polypropylene surface was slightly higher than IR transmittance obtained from removing the material from the surface by toluene immersion, as shown in Figure 2-27. The results indicated that aging increased the surface crystallinity but not homogeneously, thus oxidation degradation did not necessarily make polypropylene more prone to crystallization. Oxidation, however, allowed recrystallization of tie molecules from the broken chain, thus maintaining a constant degree of crystallinity.

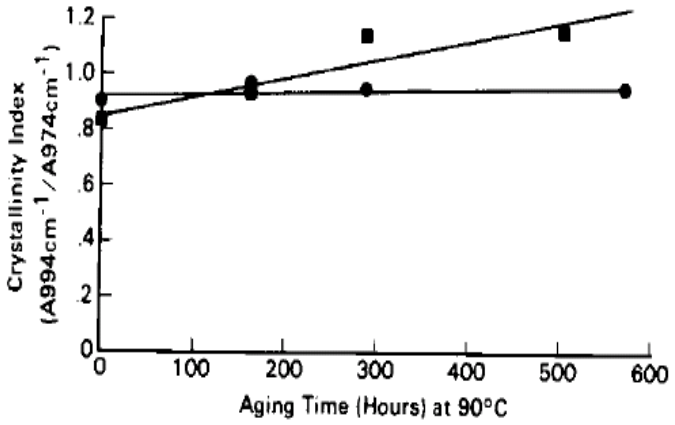

Figure 2-27: Crystallinity index as function of aging time for (■) IR reflectance and (●) IR transmission aging at 90 °C [38].

An extensively aged specimen revealed no change in the crystal structure of the α form by X-ray diffraction and no change on the surface detected by electron microscopy. However, the degree of crystallinity was increased with aging as found by IR and DSC.

Dudić *et al.* [3] characterized the secondary crystallization of isotactic polypropylene using DSC and density measurements on specimens aged at 60 °C in oxygen and annealed at 140 °C in an inert atmosphere. The Avrami relation is given as:

$$X_V(t) = 1 - e^{-Kt^n} \tag{8}$$

where X_v is volume crystallinity, K is the characteristic constant, t is the time of crystal growth and n is the Avrami exponent. The Avrami exponent can also be treated as a measure of secondary crystallization ability. Figure 2-28 shows the Avrami plot for unaged samples with different cooling rates. The sample quenched from melt in ice-water resulted in the highest slope of the Avrami plots, suggesting it had the highest secondary crystallizability because of the low crystallinity of quenching. With slower cooling rates, the potential for secondary crystallization was reduced, as there was more time for the chains to align themselves during solidification.

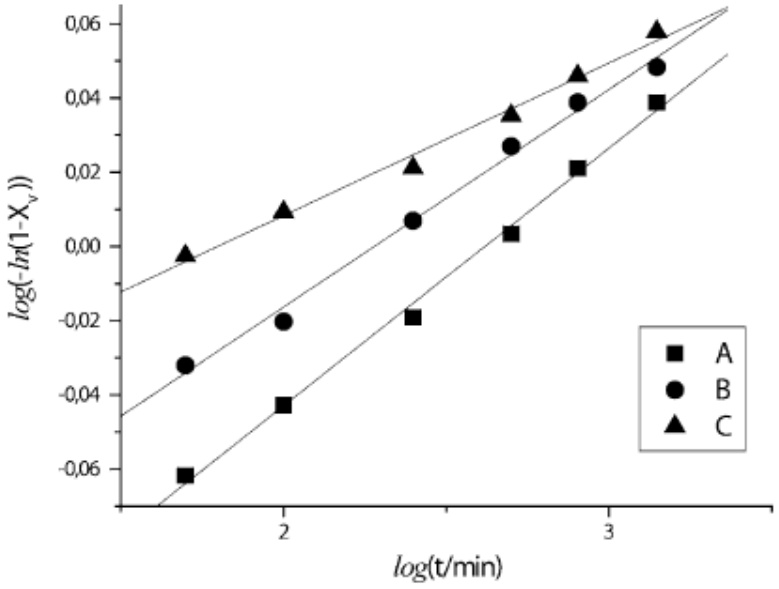

Figure 2-28: Avrami plots for unaged samples quenched in (A) ice-water, (B) air and in (C) mold [3].

Figure 2-29 shows the Avrami exponents as the function of the aging time at 140°C. The chain mobility in the amorphous phase was reduced due to free volume contraction during structural relaxation in physical aging. From the sample quenched in ice-water, the chain mobility was reduced, thus thickening of the crystalline lamellae was more

difficult and a lower melting temperature was determined from DSC. The sample with cooling from the mold has the most time for the crystallization process during slow solidification, thus the effect of annealing to secondary crystallization are negligible. However, the sample cooled in the air was favourable for high temperature secondary crystallization due to oxidative chain scissions. The broken chains with higher mobility allowed crystallization on the existing lamellae, which thickened the lamellae, thus increasing the melting temperature as confirmed by DSC.

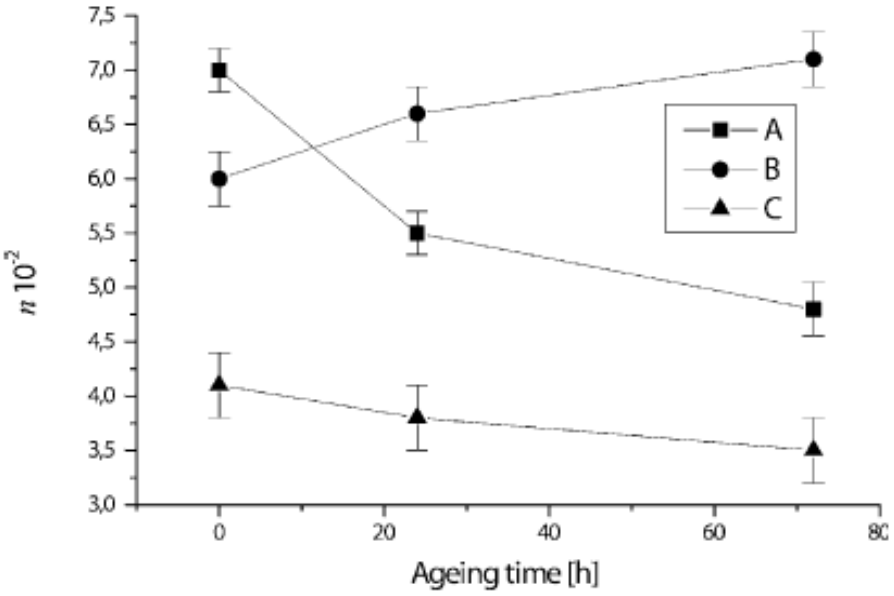

Figure 2-29: Avrami exponents of samples aged at 140 °C in (A) ice-water, (B) air and in (C) mold [3].

Aside from the secondary crystallization, Dudić *et al.* [3] also suggested that there was a decrease in crystallinity as aging prolonged. This was found in the samples cooled by ice-water or air due to the degradation of the lamellae, probably at the crystallite borders. However, for the sample slowly cooled from the mold, the crystallinity increased with aging time due to a large number of taut tie molecules, which was liable to oxidative chain scissions resulting in reorganization of the crystal phase and relief of the strained lamellae.

Larena, Jiménez de Ochoa and Domínguez [40] studied the photo-degradation of fibre-glass reinforced polypropylene. The authors stated that chemical degradation increased crystallinity in the sample. Chain scission, caused by degradation, segregated the entangled molecular segments and the crosslinked segments in the amorphous regions in order to rearrange. This process was referred to as chemi-crystallization, which was different from secondary crystallization. The latter case was referred to as the thermal activation of molecules with increased mobility, crystallizing without molecular size changes.

Groff *et al.* [44] also detected a slight increase in crystallinity in the study of the polypropylene pipes during aging in air at 135°C and water at 95°C. IR, DSC and x-ray diffraction analyses all showed an increase of crystallinity during the initial stage of aging due to secondary crystallization. The investigator also employed the small angle light scattering method (SALS) to determine the size of the spherulite dimension from the morphological structure.

Kotek *et al.* [45] studied the transformation of crystal structure during annealing at different temperatures and times. Four crystalline forms have been described and they are: monoclinic α, trigonal β, orthorhombic γ modifications and the smectic form in small irregular crystallites. The investigators concentrated on the β-phase formation, which was induced by crystallization in shear fields, temperature gradients and nucleators. The presence of the β-phase crystals provided the material with enhanced toughness but with lower stiffness and yield stress. To predict the long-term stability of the β-phase material, the investigators studied how the transformation of the crystalline structure under aging at 80, 110 and 140°C related to the structural behaviour of isotactic polypropylene. From the result of the X-ray diffraction, it was found that β-phase crystals formed in a nucleated sample. The fraction of the β-phase decreases dramatically with increasing annealing temperature and duration. The lateral size of both α and β-phase crystals increased with anneal time, but α-phase crystals appear in sizes around three times smaller than the β-phase crystals. Because the overall crystallinity remained constant, or

slightly increased when annealing at 104°C, it was implied a β to α-transformation during annealing of the sample, thus affecting the mechanical properties.

The temperature does have an effect on physical aging of the isotactic polypropylene. Agarwal and Shcultz [37] studied physical aging effects at 0°C and room temperature. The crystallinity and conformation orders remained the same, confirmed by X-ray scattering and FTIR respectively. The loss tangent from DMA showed the β to α-transition at about 10°C, which reduced with prolonged aging due to the shrinkage of the non-crystallite regions as the mobile phase transformed into a more constrained phase. The decrease of chain mobility occurred through the β-type relaxation, where the motion of the segments of the chain backbone was restricted over the course of aging. Compared to α-type chains, the change in loss tangent was invariant over the course of aging, ensuring the drop of β-type did not affect the α-relaxation type motions in the crystalline regions.

Guadagno *et al.* [46] studied the physical aging of the syndiotactic polypropylene at room temperature. By employing WAXS to determine the crystalline fraction and sorption at low activity, an impermeable intermediate phase was discovered. Over the aging period of 30 days, the fraction of the crystalline phase and intermediate phase increased by 7% and 33% respectively. The increase of the crystalline phase was due to secondary crystallization at room temperature, which was higher than the quenching temperature of the test sample, thus repairing the small and defective crystals that melted at a lower temperature. Figure 2-30 shows the DSC analyses of the aging of syndiotactic polypropylene, exhibiting a decrease in melting temperature with increased aging time. Also, there were small endothermic peaks present in all samples in the 50°C range, as shown in Figure 2-30. The increased enthalpy represents the upper glass transition or disordering of the intermediate phase.

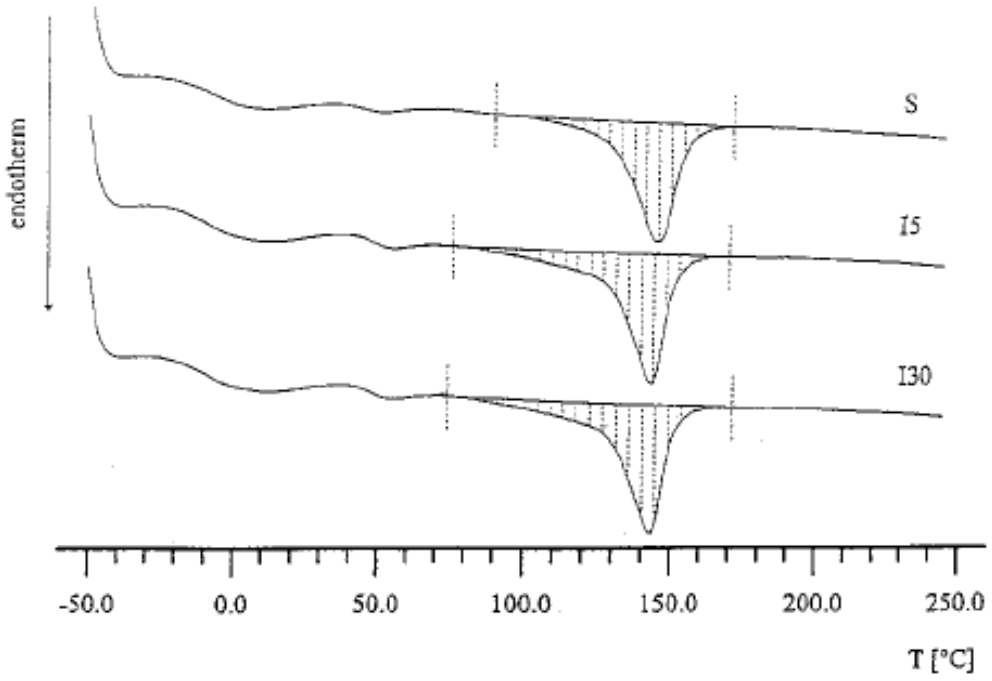

Figure 2-30: DSC curves for sample after quenched in ice-water (S), stored for 5 days (I5) and 30 days (I30) in room temperature [46].

2.2.8.3 Environmental Effects

Groff *el al.* [44] studied the aging of commercial polypropylene pipes aging at 135°C in air and 95°C in water for up to 3000 and 4000 hours respectively. This study was significantly different from the other studies due to the effects of the high moisture content. The aging effects in circulating water at 95°C were less severe than aging in air at 135°C due to the lower temperature and the practical absence of oxygen.

Agarwal and Shcultz [37] studied aging at room temperature in air and vacuum environment. The yield stress and elastic modules were the same whether aging in air or vacuum. Thus, it was proven that the effects from diffusion of moisture in air were not as significant as the aging effects.

3.0 Materials and Experimental Methods

3.1 Materials

The material studied in this work is a polypropylene based random glass-fibre mat composite produced by Quadrant Plastic Composites. Two different types of materials have been chosen for this study, and the commercial model numbers are D100-F40-F1 and G100-F40-F6. The material specifications of each can be found in the Appendix A. Both types of material typically have 40% fibre-weight content, with the only difference being fibre length. D100 series material consists of chopped fibres that are 25 to 70 mm in length, while the G100 series material consists of long continuous fibres. The materials were pre-fabricated into composite plaques with the dimensions of 390 x 390 mm^2 by Polywheels Manufacturing Ltd. via the compression molding process discussed in the previous chapter. The test plaques have a nominal thickness of 3 mm with slight variations between the D100 and G100 series materials. Figure 3-1 shows the fibre dispersion of the different types of materials captured using a stereomicroscope. D100 series material with the chopped fibres shows relatively shorter fibre lengths and extra fibre ends compared to the G100 series material. The indentation process on the D100 series material was more difficult due to the wider spread of fibres and less matrix area to target for indentation.

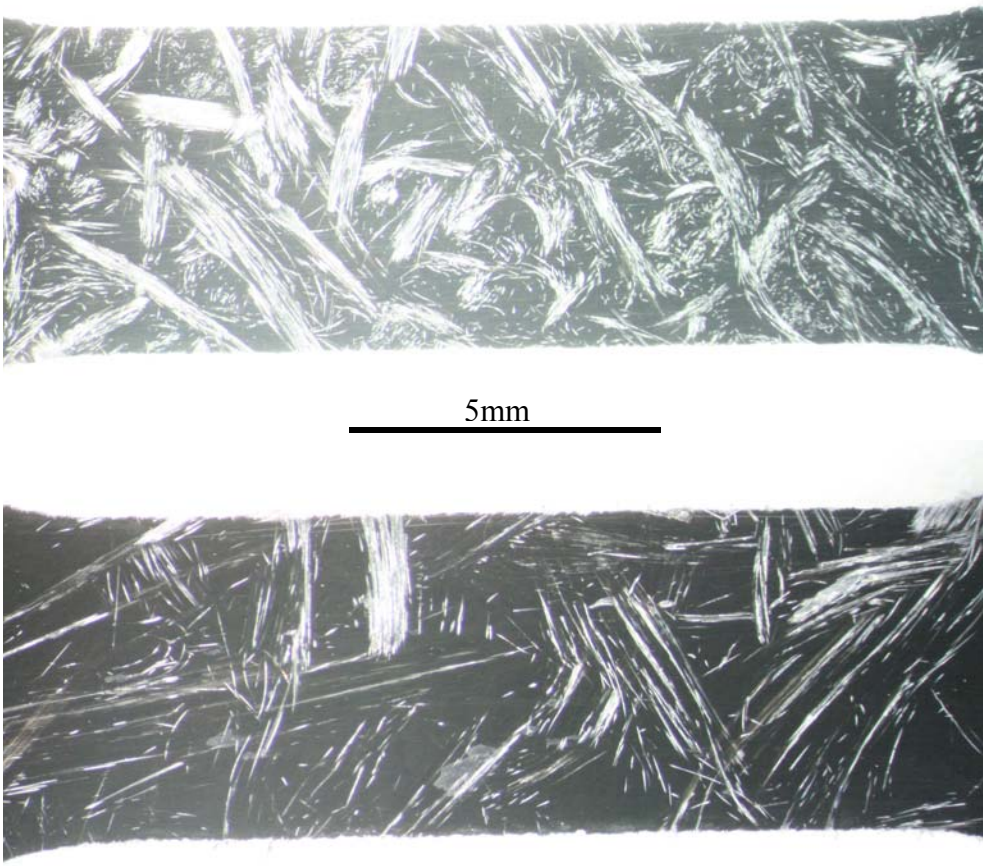

Figure 3-1: Fibre dispersion for D100 (top) and G100 GMT at 10x magnification.

Information on additives in the polypropylene matrix is valuable for characterizing the matrix behaviour under thermal aging, as they will greatly affect the properties. Due to confidentiality issues with Quadrant Plastic Composites, however, the type of additives cannot be disclosed. However, some information was obtained through personal communication with a technical representative from Quadrant Plastic Composites. It was confirmed that the polypropylene matrix for both D100 and G100 series materials are homo-polypropylene grade, which contains carbon black and stabilizers [47]. The average molecular weights of the extracted polypropylene sample are shown in Table 3-1 measured from Gel Permeation Chromatography (GPC) with high temperature filtration technique performed by Jordi FLP Laboratory and the report is shown in Appendix C.

Table 3-1: Molecular weights for extracted samples.

	M_n (Kg/mol)	M_w (Kg/mol)	PDI (M_w/M_n)
Sample #1	46.3	108.6	2.4
Sample #2	46.6	106.3	2.3
Sample #3	41.4	102.4	2.5

The sample preparations in this study were different for the various types of analysis. This included the testing of extracted fibre-free polypropylene samples and the polished miniature tensile creep specimens. The details of sample preparation will be discussed in this chapter.

Using ASTM standard methods for dynamic mechanical analysis (DMA) results obtained from other investigators [8,48] and differential scanning calorimetry (DSC), the average glass transition temperature of the extracted fibre-free polypropylene was found to be within the 4-5 °C range. The melting temperature was 160 °C using DSC at a scanning rate of 10 °C/min.

3.2 Methods for In-situ Creep Deformation

3.2.1 Tensile Creep Specimen Preparation

Molded plaques of about 3 mm thickness were cut with a water jet to manufacture specimens in accordance to ASTM D-1708 standard for testing tensile properties of plastics using micro-tensile specimens. However, a slight modification to the gripping portion of the specimen was necessary due to equipment constraints. Figure 3-2 shows the dimensions of the creep specimens that were used in this study. The thickness of the specimen was the same as the as-received thickness.

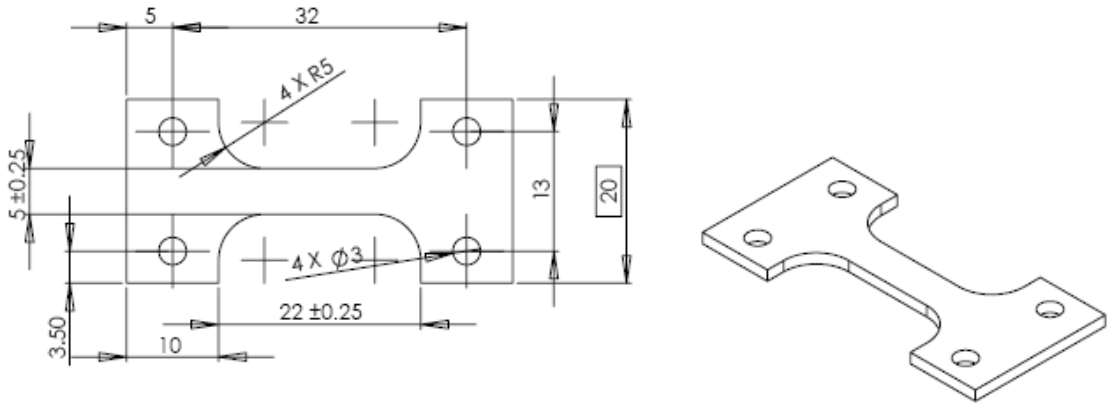

Figure 3-2: Detailed drawing of specimen with dimensions in mm.

The creep specimens were polished prior to testing in order to distinguish more easily between the glass fibres and the matrix phase. The fixture shown in Figure 3-3 is machined from aluminum block and holds onto the specimens during polishing. The initial step in this 3-stage process uses a hand grinder and 4 different grit sizes (240, 320, 400 and 600) of sand paper with running water to reduce the surface roughness on the cut specimen. It is then followed by the second stage of polishing using Struers DP-Mol woven 100% wool cloth with abrasive Struers DiaPro-Mol diamond solution for 3 minutes. The final step of polishing uses the Struers DP-Nap short synthetic nap with cerium oxide abrasive for 2 minutes to bring the final surface roughness to about 3 μm. Figure 3-3 on the right shows the comparison of the specimens before and after polishing.

The polished specimen results in a glossy surface due to low surface roughness, which effectively improves the details of the fibres and the matrix phase under the microscope with the camera.

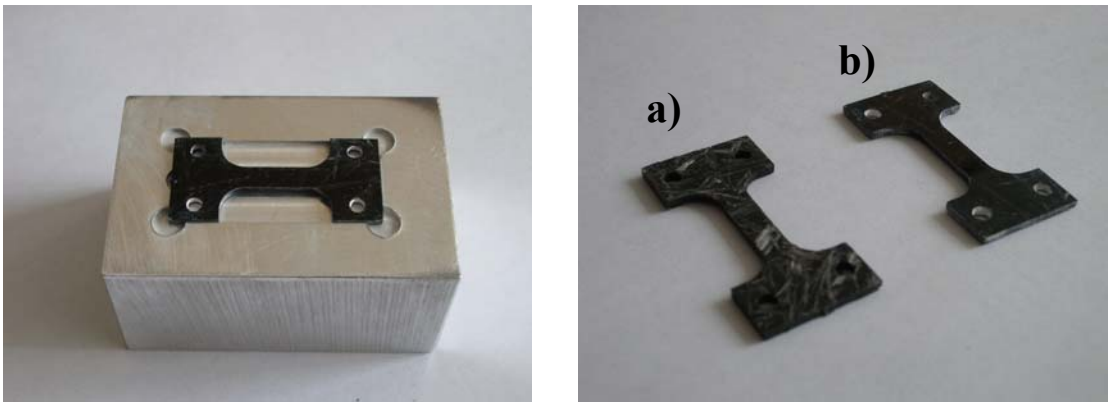

Figure 3-3: Polishing fixture (left) and the comparison of specimens (a) before and (b) after polishing.

Indentations were then marked on the polished specimen surface prior to creep testing by using a Vicker's hardness micro-indenter (LECO MHT-200) at 500 g for 15 s dwelling time. The indented area is about 200 x 200 μm^2 on the polished surface, specifically on the matrix area which is free of fibres. The indentations will help characterize any deformation and movement of the matrix phase, which will be discussed further in Chapter 4.

3.2.2 Apparatus for Creep Testing

The major apparatus for the creep study were the optical microscope and microtensile stage with the environmental chamber. The setup is shown in Figure 3-4. The creep specimen was observed under an Olympus BX-41M optical microscope in bright field reflection mode. The miniature tensile stage was placed directly underneath the objective lens to capture the *in-situ* creep deformation mechanism, and images were taken at different intervals during the creep tests for analysis.

Figure 3-4: Apparatus set up with Minimat underneath the microscope.

A Minimat 2000 miniature tensile machine installed with a 1000 N load cell was used for creep testing at ambient temperature in an uncontrolled environment, while an environmental chamber, as shown in Figure 3-5 was used for elevated temperature experiments at 80±2 °C.

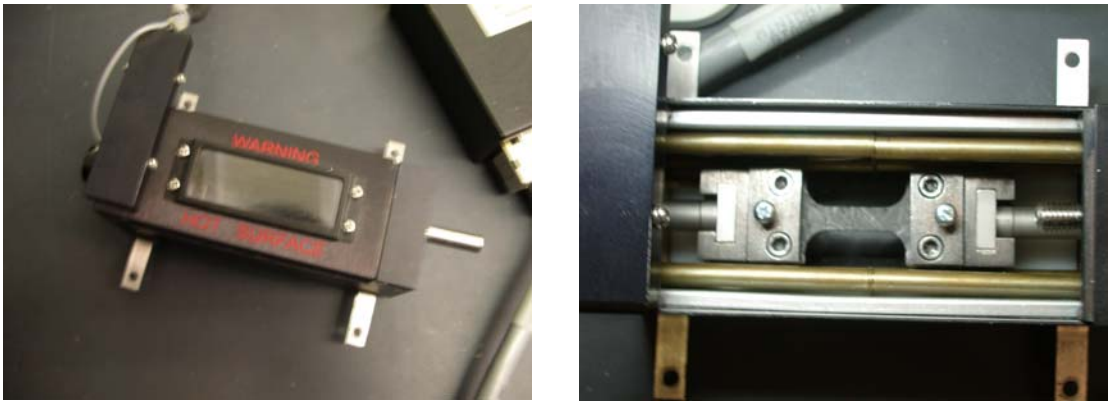

Figure 3-5: Environmental chamber (left) with specimen inside the environmental chamber.

To improve the clarity of the *in-situ* creep images, the original cover of the environmental chamber could not be used, and a new cover was customized built for this study. Figure 3-6 shows the comparison of the covers. The customized cover was bent into shape with aluminum sheet metal. A silicon cookie baking sheet was used as the insulation material

to prevent heat lost during high temperature creep testing. The customized cover uses a counter-sink design due to the short focal length between the objective lens and the surface of the specimen There is a small open slot on the customized cover which eliminated reflection as usually experience with a glass slide. The size of the open slot was kept to a minimal to avoid excess amount of heat loss. Temperature calibration has been done with the customized cover to ensure the temperature can be maintained consistently. Figure 3-7 shows a close-up view of the setup during creep testing at elevated temperature, with the objective lens looking through the open slot to capture *in-situ* creep images.

Figure 3-6: Original and customized environmental chamber cover.

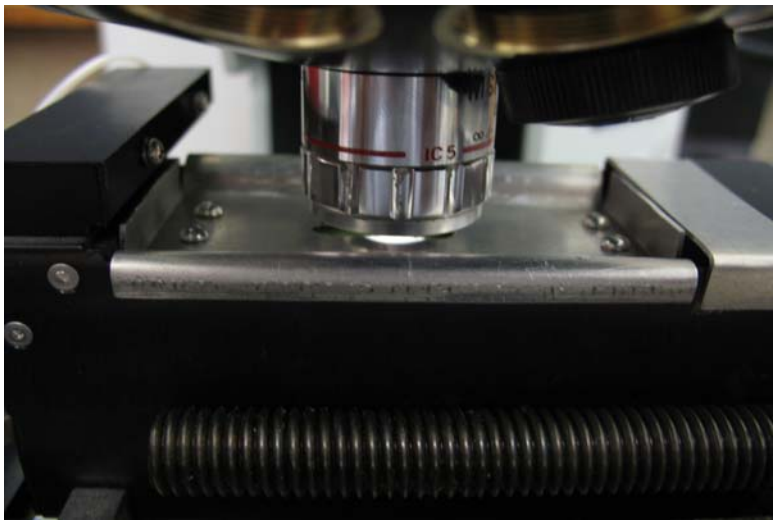

Figure 3-7: Close-up view of apparatus (creep test in-progress).

3.2.3 Creep Testing Parameters

The stress levels used for creep testing were 33% and 67% of the ultimate tensile strength (UTS) of the material at room temperature and elevated temperature. An Instron model 1331 material testing machine mounted with environmental chamber model 3119 was used to determine the UTS at elevated temperature, while the UTS at room temperature was obtained from earlier reports from the research group [8,48]. Since the Minimat 2000 was not built for creep testing purposes, there were certain restrictions on the setup of the testing parameters through the computer interface. It was not possible to apply instantaneous loading of the creep specimen, as the crosshead would rotate at high speed to match the preset value of the force required. The machine tends to overshoot the preset value and the force would be too high causing the specimen to break at the start of the test. To overcome this issue of overshooting, the machine was set to a constant strain rate of 1 mm/min. This allows more time for the machine to compare the real time and preset value of required force, and adjust accordingly. After the force has reached the preset value, the machine holds the force for creep test to begin. The motor adjusts the crosshead movement to accommodate the viscoelastic behaviour of the material, in order to maintain the preset value of the force. The strain was measured using the crosshead movement of the miniature tensile machine.

3.2.4 Image Acquisition and Modification

The images for this *in-situ* creep study are captured with a commercial type digital camera Canon® Power Shot A620 digital camera with 7.1 mega pixels and 4x optical zoom. The digital camera is attached to the eyepiece of the Olympus microscope with an adapter kit to capture the images during creep tests. With the 4x optical zoom from the camera looking through the 50x of total magnification of the microscope, the overall magnification of the captured images is about 200x.

The camera was pre-set to the following setting in order to capture the deformation images with high details. Shutter speed priority mode is set to control the exposure time manually at 1/50 second to ensure the images captured with sufficient lighting. Aperture

is set to be auto in order to compensate for the shutter speed, and the ISO rating was set to high sensitivity. Macro setting has been used to prevent auto focusing, and the images are brought to steady focus by the microscope stage to reduce variability between images.

Images captured from the digital camera are shown in Figure 3-8 and they were processed using Microsoft® Photo Editor. The option of 'auto balance' enhances the picture quality by adjusting the brightness, contrast and gamma automatically to give distinct differentiation between the fibre and matrix phase. The processed images with higher contrast facilitate the analysis visually, which allows the detection of deformation mechanisms easier.

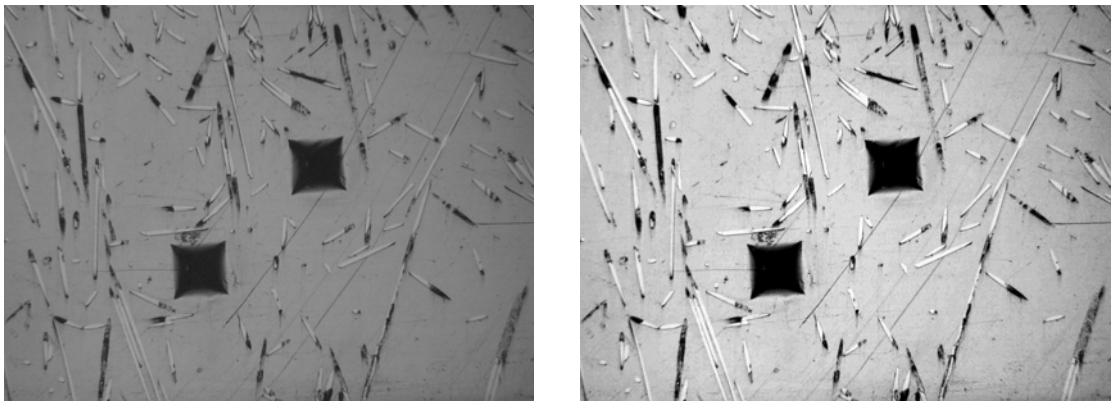

Figure 3-8: Examples of micrographs before (left) and after (right) image modifications.

3.2.5 Scanning Electron Microscopy Parameters

Details of cracks, fibre-matrix interface, and fibre surfaces were observed using a Jeol JSM-6460 field emission scanning electron microscope. The samples were plated with gold in order to avoid the charge build-up on the sample surface during the analysis. The magnification of the images ranged from about 20x up to 1500x.

3.3 Methods for Characterization of Crystallinity and Thermal Aging

3.3.1 Polypropylene Thin Film Preparation

A random chopped fibre GMT composite commercially known as Quadrant Plastics D100 series glass mat reinforcement series was chosen for this study. The composite has a nominal fibre-weight fraction of 40%. For more accurate analysis of the crystallinity changes in the polypropylene matrix due to thermal aging, the thermoplastic matrix resin was extracted from composite samples for this study.

About 2 g of composite sample wrapped in a steel meshed (0.031 mm^2 openings, mesh size) envelope was placed in a round flask with a condenser mounted on top. The flask containing xylene was boiled at 140°C for 7 hours. The polypropylene was recovered by precipitating in ethanol followed by filtration. The extracted polypropylene was dried in vacuum then pressed into films of up to 100 μm thick by hot pressing at 180°C under 4500 psi and holding for 3 minutes, and then stored at room temperature. To erase the thermo history, the film was heat up to melt at 180°C, then cooled to solid state from melt at two different solidification rates:

- controlled cooling film sample (FC) – at 10°C per minute using a forced convection oven
- quenched film sample (FQ) – rapid cooling in ice-water at 0°C.

3.3.2 Apparatus and Aging Parameters

Two sets of samples with different solidification rates were aged in air at 90 and 140°C for 12 days. A relatively high aging temperature at 140 °C selected for the analysis was to confirm if there were any significant changes might occur compared to aging at 90 °C. The effects of aging were characterized in two ways. First, the film samples were aged in air in an oven and then analyzed using WAXS to compare the crystallinity changes before and after aging. The second technique consisted of progressive FTIR scanning of

the iPP film aged in air in a heated sample holder. The FTIR monitored *in-situ* crystallinity and oxidation changes over the 12 days of aging.

3.3.3 Differential Scanning Calorimetry Parameters

The DSC analysis was carried out on a TA Instruments DSC 2920 with a refrigerated cooling system. Samples were cut from the two differently solidified thin films and encapsulated in non-hermetic aluminum pans. The sample weights were kept at approximately 10 mg, heating from 25 to 180 °C at a rate of 10 °C/min in nitrogen purge gas in most of the analyses. To determine the glass transition of the extracted polypropylene samples, various heating rates (20 to 40 °C/min) and temperatures (from -70 °C to melt) have been used to capture the step change of the recorded data.

3.3.4 Wide Angle X-ray Scattering Parameters

WAXS measurements were carried out with a Bruker AXS D8 Advance X-ray diffractometer operating with Cu Kα source. The equipment was operated in ambient temperature at 40 kV and 30 mA with a 2 mm slit opening. The scanning range was fixed for 2θ from 10 to 24° with increments of 0.05°/step at 1 sec/step. Three specimens of each sample were measured. The crystallinity determined from the WAXS data was in accordance to a procedure proposed by Lima *et al.* [31]. X-ray measurements on the pure glass fibre obtained by burn-off test showed no significant crystalline peaks confirming the amorphous property of the glass fibre. Therefore, this validated the assumption that any changes to crystallinity levels during thermal aging were only due to the thermoplastic matrix phase.

3.3.4.1 Post-processing of WAXS Data Using Origin®

The data collected from the WAXS measurements went through post-processing using mathematical software, Origin ®. The post-processing technique has followed the methodology that was used my Lima *et al.* [31] to determine the crystallinity content in the sample. The peak with the lowest amplitude and largest width, called the amorphous-

halo, accounts for the amorphous phase of the sample. The other peaks with relatively high magnitude account for the peaks for crystalline phase. The location of the peaks corresponding to the different types of crystalline phase in the polypropylene sample is described in section 4.2.

Figure 3-9 shows the screenshot of the processed WAXS data using Origin ®. By performing the operation of 'fit multiple peaks - Gaussian', the overall WAXS data will break down into six individual peaks as shown in Figure 3-9. The black line is the raw data collected from WAXS, and the red line is the post-processed data, made up from the superposition of the 6 individual peaks. As it can be seen in Figure 3-9, the post-processed data (red-line) closely resembles the raw data (black-line). The percentage crystallinity of the sample is calculated by dividing the crystalline peaks area over the total area under the entire curve. Figure 3-10 graphically shows the data after the mathematical post-processing with the crystalline and amorphous phases separated.

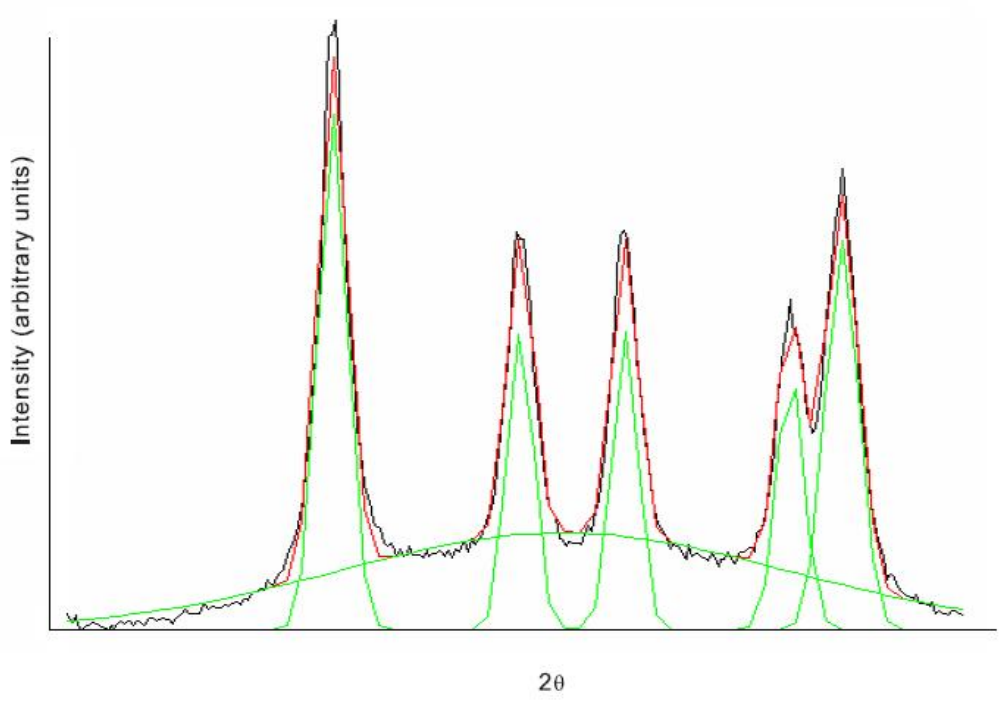

Figure 3-9: Peaks fitting of WAXS data.

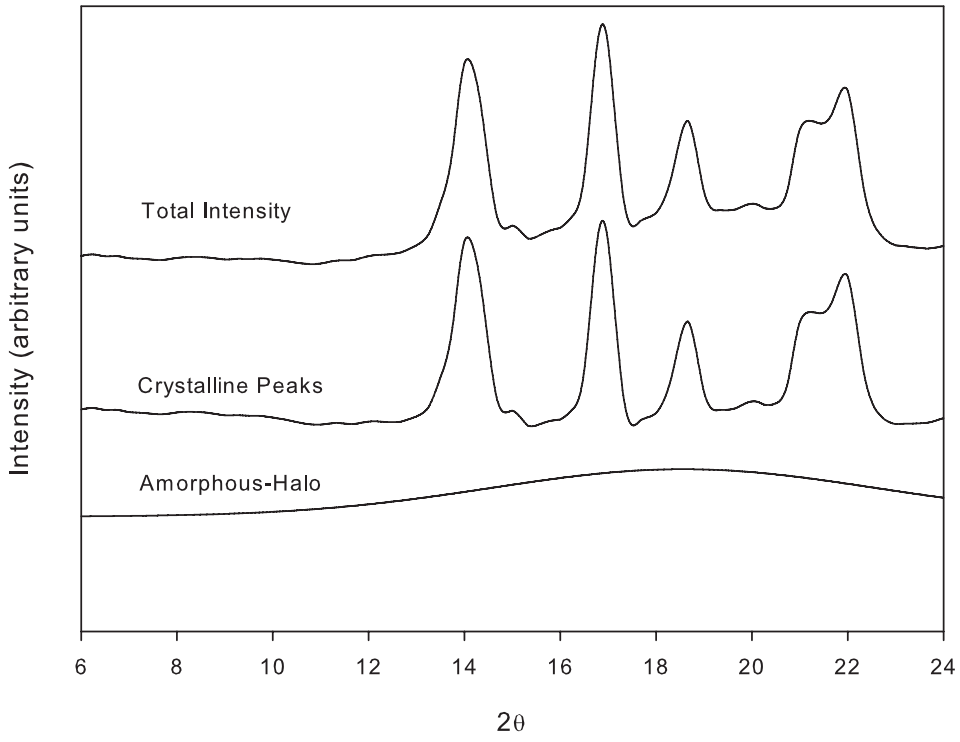

Figure 3-10: Post-processed WAXS data showing the crystalline peaks and amorphous-halo.

3.3.5 Fourier Transform Infrared Spectroscopy parameters

FTIR spectroscopy measurements were carried out with a Bruker Optics Tensor 27 FTIR spectrometer. The equipment was operated in transmission mode with 64 scans per sampling at a resolution of 1 cm^{-1} in the wavenumber range between 4000 to 400 cm^{-1}. Internal calibration was done automatically by using a polystyrene film. Spectra were filtered using software to remove the atmospheric effects such as carbon dioxide and the moisture in the air. The crystallinity levels determined from the FTIR spectra were based on the absorbance intensity ratio of certain peaks.

3.3.6 Gel Permeation Chromatography Parameters

Molecular weight measurements were conducted by Jordi FLP Laboratory on 3 extracted samples obtained from 3 different D100 composite plaques. Employing Gel Permeation Chromatography (GPC) technique, the samples were dissolved in trichlorobenzene and

filtered using a high temperature filtration system. The samples were then run in duplicate in the same solvent. The GPC test was run at a flow rate of 1.2 mL/min on a Jordi DVB mixed bed column, 500 x 10 mm (ID) at 145 °C. Injection size was 200 μL of a 2.5 mg/mL solution. A set of polystyrene standards with a concentration of 0.5 mg/mL were used with an injection size of 100 μL. The samples were monitored at a sensitivity of 8 and a scale factor of 64 using the Waters 150-C instrument.

3.3.7 Thermogravimetric Analysis Parameters

Thermogravimetric Analysis was carried out with a TA Instrument SDT 2960. The equipment was operated at a heating rate of 10 °C/min from 40 to 900 °C purging with air. Different forms of sample and pure fibres were used in order to determine if there were changes in quantity of the additives due to different forms of sample preparation, such as the extracted polypropylene thin film samples. The weights of the sample were between 5 to 10 mg.

4.0 Results and Discussions

4.1 Creep Deformation

4.1.1 Creep Instrument Limitations

The main objective for using the Minimat 2000 miniature tensile tester is to enable the *in-situ* imaging of progressive damage accumulation during creep deformation. It is a suitable setup since the load can be conveniently calibrated and a microscopic lens can be mounted directly above the creep specimen to capture micro-failure mechanisms associated with damage accumulation during the creep process at both room and elevated temperatures. However, the Minimat instrument has some inherent limitations due to its size and design.

In the Minimat tester, the creep displacement in the small specimen is measured from the cross-head travel which is then converted to strain by dividing by the gauge length of 12.0 mm. As illustrated in Figure 4-1, however, the tester cannot apply the load instantaneously to reach the set stress level but is actually loading at 1 mm/min. Figure 4-2 shows the example of loading the sample at 20 MPa in stress and strain as a function of time. The cross-head measures a specimen elongated about 2.3% strain before creep actually begins. The existence of a "ramp-up displacement" was validated by testing steel specimens shown in Figure 4-1. The steel tests also showed that the load application ramp, although not instantaneous, had good repeatability. A key difference between the ramp-up curves is the existence of a "toe region" in the GMT material which is characteristic of compliant thin materials. Accordingly, a displacement correction of 2.3 % is necessary for tests at 20 MPa, the dotted line shown in Figure 4-2. The resulting instantaneous net strain in this case is the secondary creep strain minus the correction (2.65% – 2.3%) or 0.35%.

To verify the accuracy of this correction, the creep curve from testing a larger tensile specimen on a rigid frame [49] designed to apply instantaneous loading to 20 MPa is compared with the Minimat test curve in Figure 4-3. The larger tensile creep strain was

measured using a strain gauge. It is seen that the initial creep strains (with time) are nearly identical in both curves.

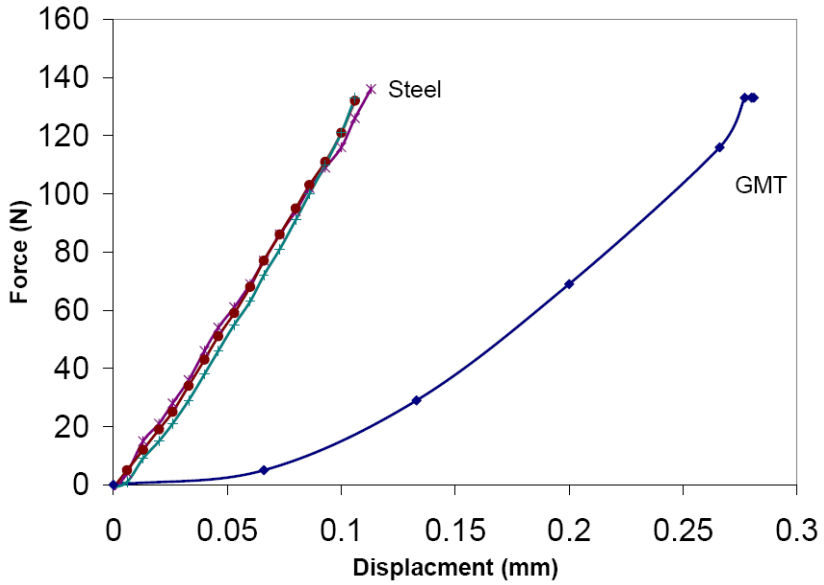

Figure 4-1: Comparison of force versus displacement profiles during application load in the Minimat for steel (3 samples) and GMT material.

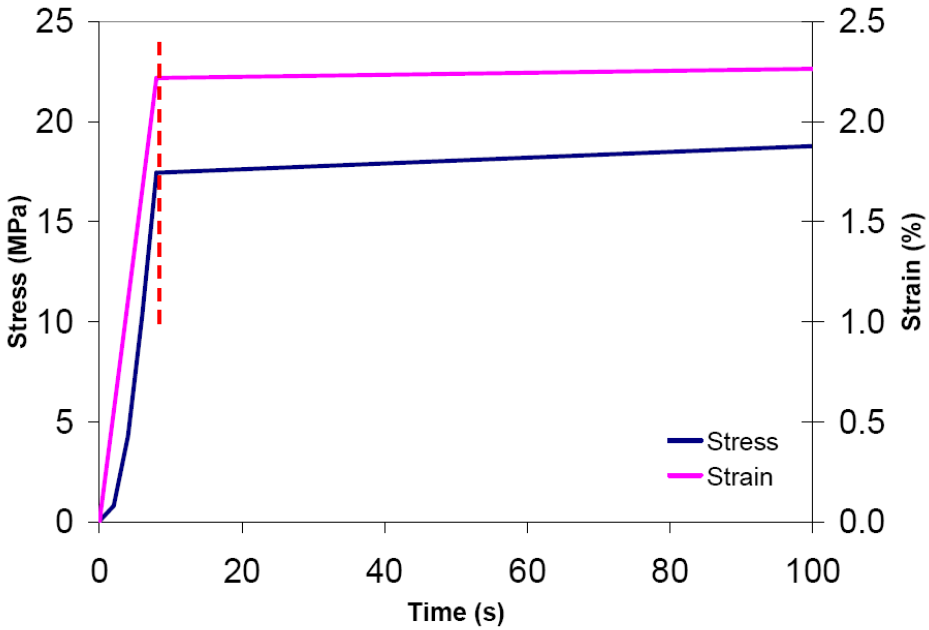

Figure 4-2: Typical stress and "corrected" strain profiles during GMT. specimen loading to 20 MPa.

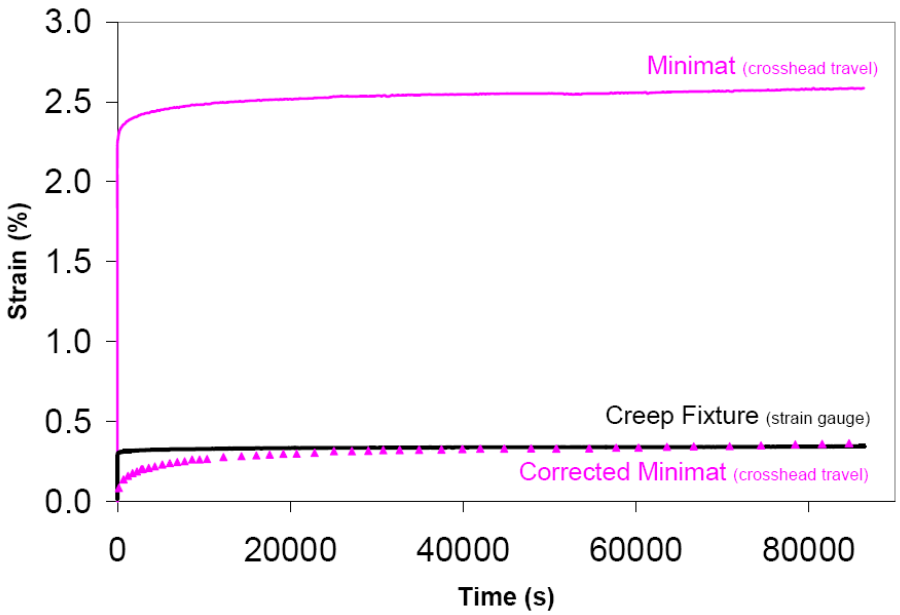

Figure 4-3: Comparison of corrected Minimat strain measurement with results from creep fixture with instantaneous loading capability [50].

Despite this limitation, the current test setup meets our requirement for *in-situ* imaging and comparison of creep data as long as the corrected strains are used consistently in the analysis.

4.1.2 Ultimate Tensile Strength

Tensile tests were performed at 80 °C, the anticipated service temperature for GMT composites, to compare the ultimate tensile strength (UTS) with data obtained previously [8] at room temperature. The tests were performed at 5 mm/min loading rate using specimen size prepared in accordance with ASTM D638. As shown in Figure 4-4 , the UTS for D100 and G100 materials dropped by 57% and 31%, respectively, at 80 °C as compared with room temperature. It is noted that the UTS plotted is the average of 5 replicates for each type of material. Raw data for these tests can be found in the Appendix D. The stress-strain curves for both types of materials tested at room temperature are compared with results at 80 °C in Figure 4-5 . The figure also indicates the two stress levels, 33% and 67% UTS, that were used in this creep study.

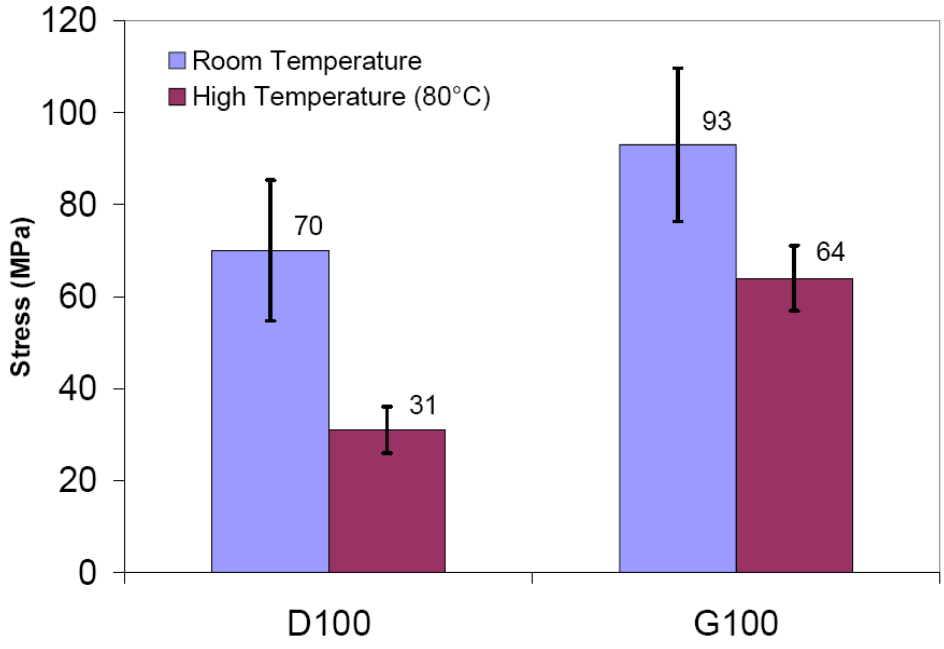

Figure 4-4: Comparison of UTS at room temperature and 80 °C for chopped (D100) and long-fibres (G100) GMT.

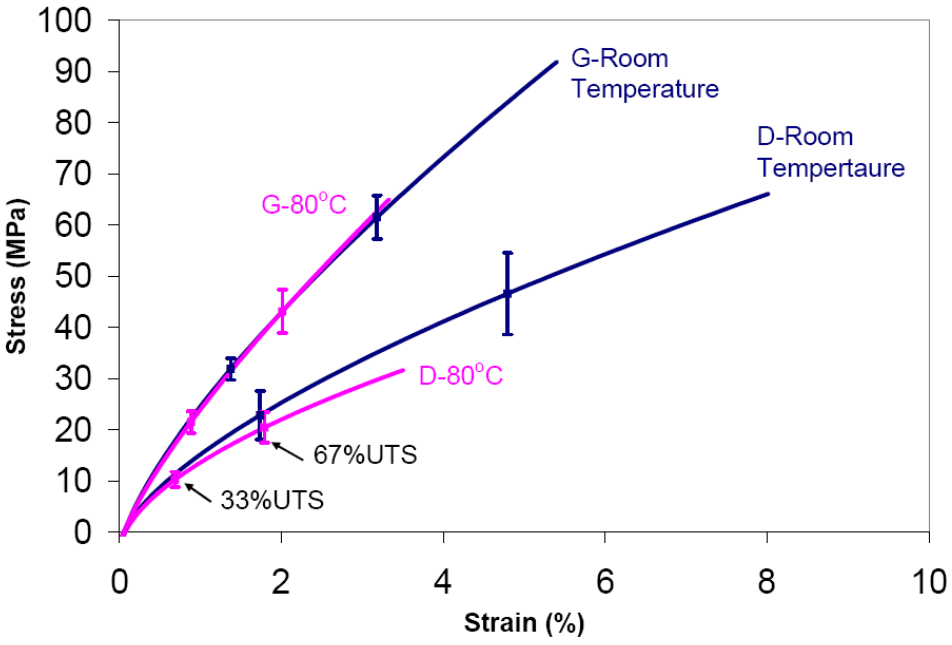

Figure 4-5: Stress-strain curves for both GMT materials at room temperature (RT) and at 80 °C (HT).

4.1.3 Investigation of Surface Polishing Effects

Damage progression in the GMT materials during creep can be influenced by the initial surface properties of the specimens. Specifically, a potential source of specimen damage is fibre pullout or fibre breakage during specimen polishing. As all the creep specimens had to be polished to obtain clear images, a set of preliminary tests were conducted to determine to what effect, if any, polishing would have on the mechanical properties. The tests involved two stages of mechanical pre-conditioning.

4.1.3.1 Pre-conditioning

Pre-conditioning can introduce a consistent level of plastic deformation in all the specimens [51]. The two-stage pre-conditioning procedures were as follows:

- First stage: initial condition at about 50% of UTS at room temperature for 5 minutes
- Second stage: 15% of UTS at room temperature for 30 seconds creep and recovery repeated for 10 cycles.

Figure 4-6 shows the creep response of the 2 samples of D100 chopped-fibre composite after first stage conditioning at 30 MPa for 5 minutes. It is clear that the first stage of conditioning had minimal effect on the instantaneous creep strain as well as the time-dependent creep behaviour. In the second stage where both the specimens are subjected to 10 cycles of the creep and recovery at 15% UTS, Figure 4-7, the strain levels remain stable during subsequent creep testing. This verifies that specimen homogeneity after pre-conditioning. Strain at recovery during the cyclic testing was not recorded due to the limitations of the instrument. The drop of strain values at the start of all the second stage conditioning shown in Figure 4-7 was due to machine overshooting the applied load while attempting to meet the pre-set stress level.

Similarly, the first stage conditioning of the G100 long-fibre composite at a higher load of 40 MPa is given in Figure 4-8. Since the second stage conditioning results are similar to that for the chopped fibre composite, the result is not shown here.

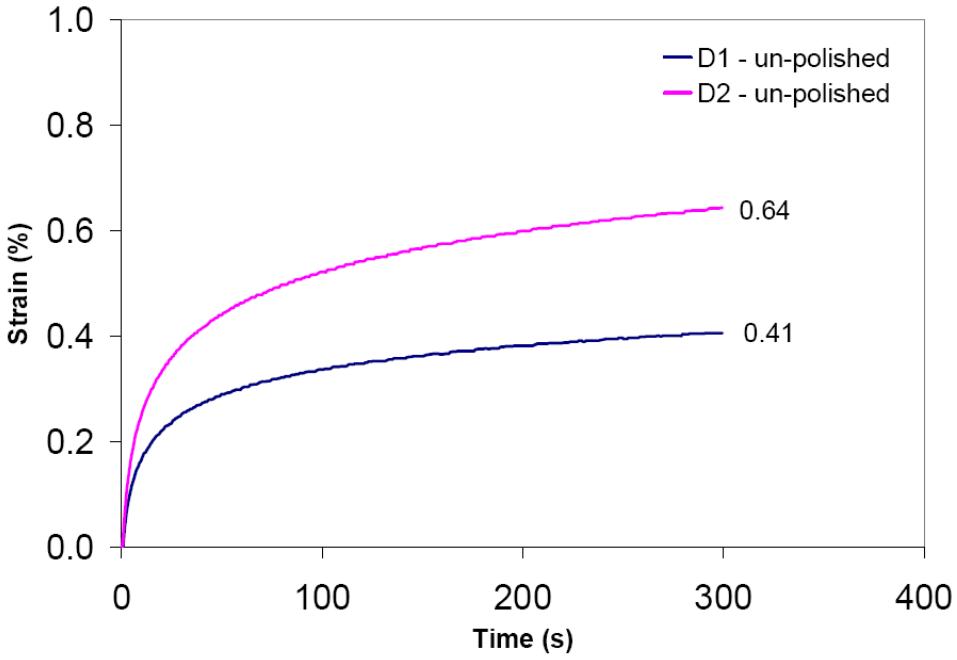

Figure 4-6: First stage conditioning of chopped-fibre (D100) specimens at 30 MPa for 5 minutes.

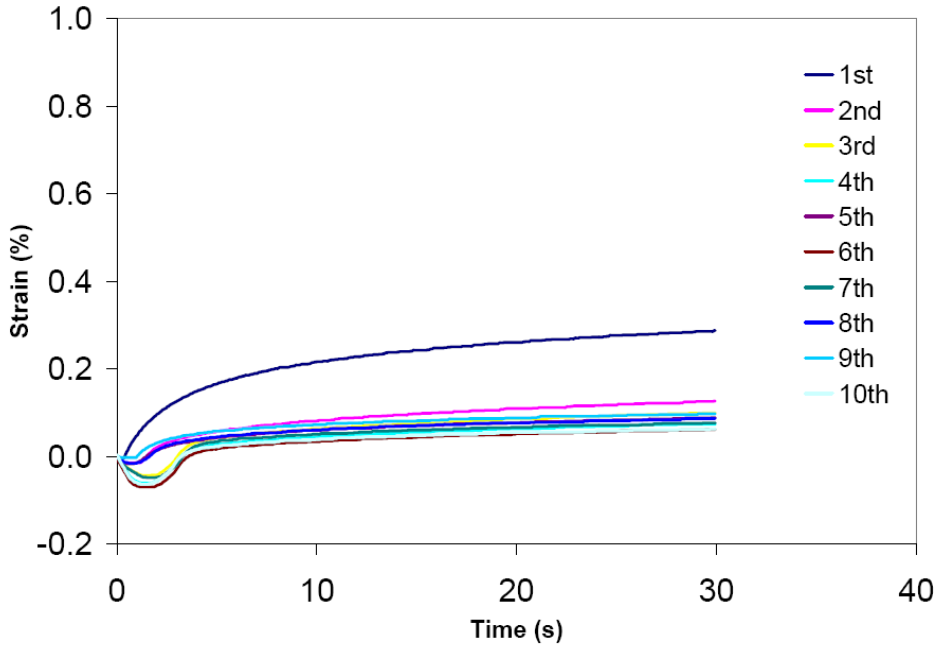

Figure 4-7: Second stage conditioning of chopped-fibre (D2) specimens at 10 MPa for 30 s creep and recovery for 10 cycles.

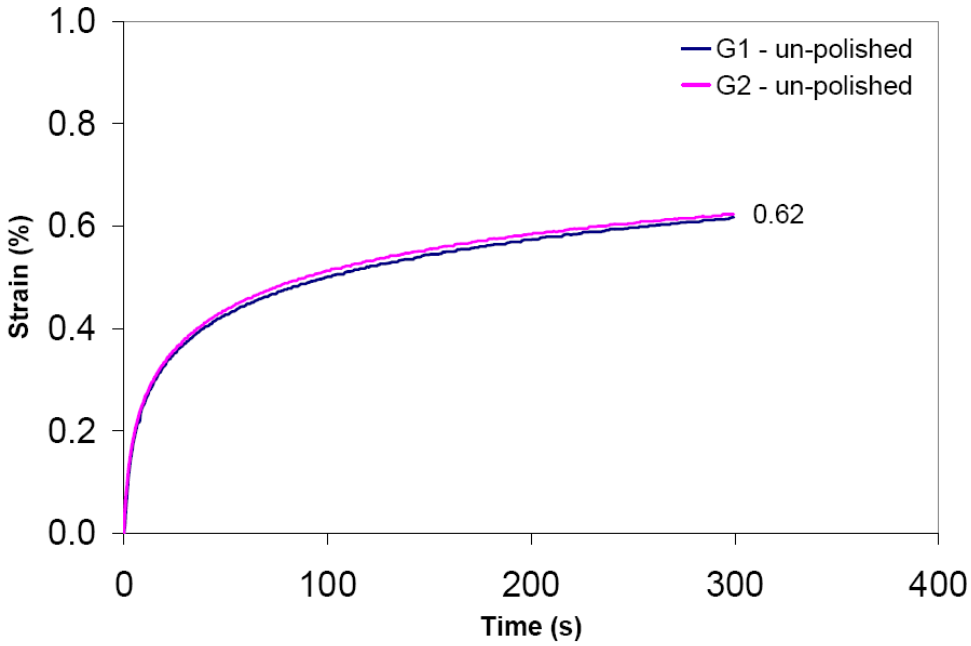

Figure 4-8: First stage conditioning of long-fibre (G100) specimens at 40 MPa for 5 minutes.

4.1.3.2 Effect of Polishing

To investigate the effects of polishing, one of the pre-conditioned specimens was polished to remove about 50 to 100 μm of material from one side. Since the average diameter of the glass fibres is between 15 and 20 μm, it is possible that polishing may break several fibre clusters (about 4 to 7 fibres) throughout the specimen surface. To investigate the effects of polishing on creep data, creep tests were performed on polished and un-polished samples for comparison.

Figure 4-9 compares room temperature creep results between the polished and un-polished samples for the chopped-fibre D100 composite at 10 MPa for about 1 day. Although the creep strains are slightly different between the two samples, the polished sample (D2) resulted in a lower creep strain compared to the un-polished sample (D1) under the identical pre-conditioning and creep testing procedures. It is noted that the very small fluctuations observed in the measured strains are characteristic responses of the Minimat tensile machine and data acquisition system when the creep loading is

relatively low. Nevertheless, it is evident that polishing has negligible effect on overall creep response for chopped fibre materials.

Figure 4-10 shows the creep behaviour between the polished and un-polished G100 long-fibre composite specimens at 20 MPa for up to one day. The creep strain for the polished specimen (G2) reported in Figure 4-10 decreases compared to the un-polished specimen (G1), while the creep behaviour were almost identical at the first stage conditioning process shown in Figure 4-8. This is also evident that polishing has negligible effect on creep response of the long-continuous fibre materials.

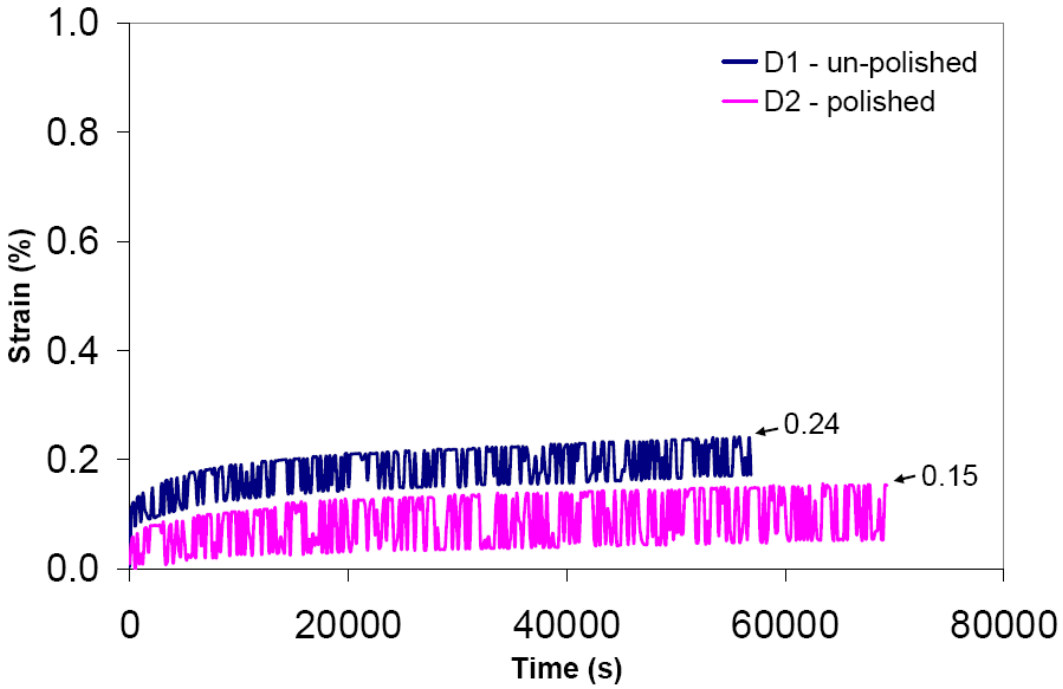

Figure 4-9: Creep strain comparison between polished and un-polished chopped-fibre (D100) specimens at 10 MPa in room temperature (specimens 1 and 2 are the same as in Figure 4-6).

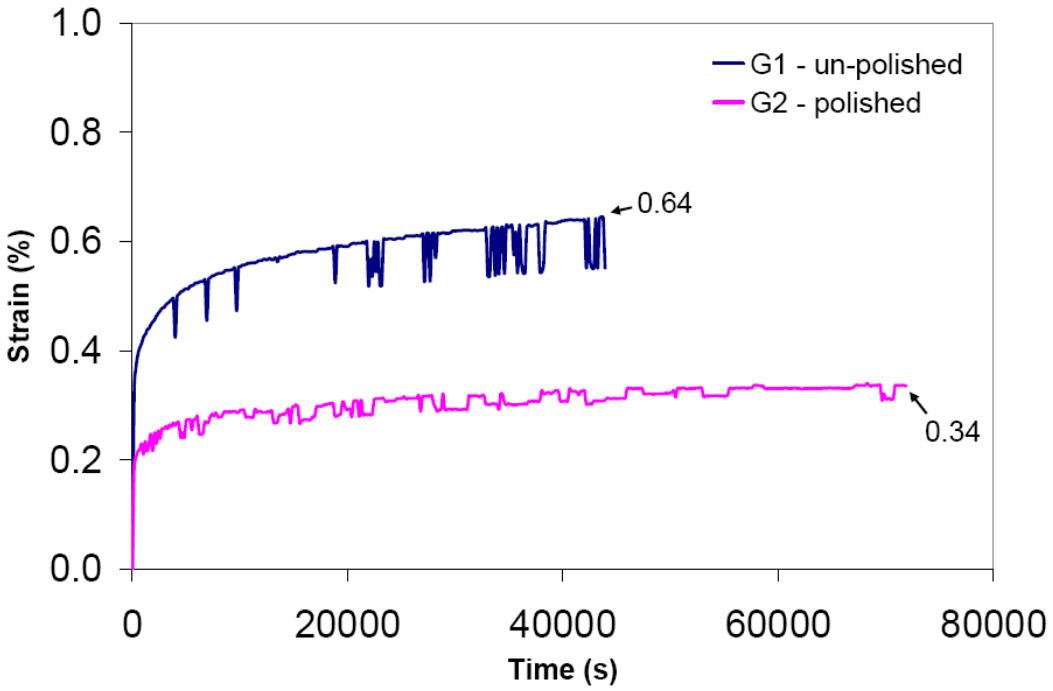

Figure 4-10: Creep strain comparison between polished and un-polished long-fibre (G100) specimens at 20 MPa in room temperature (specimens 1 and 2 are the same as in Figure 4-8).

From the above analyses, it can be concluded that sample preparation procedures used in this work had minimal effect on creep properties of both composite materials.

4.1.4 Damage Accumulation at Micro-scale

Both D100 and G100 materials were observed under the microscope for the *in-situ* creep deformation analysis. As discussed earlier, instantaneous loading of the specimens could not be achieved due to limitations of the instrument. All the specimens were loaded with the creep rate of 1mm/min. The loading direction was horizontal to all the images shown in this study. To standardize the testing procedures, the stress level that were chosen from the experiments were 33% and 67% of the UTS. However, the UTS was dependent to the temperature levels. The UTS measured at room temperature (RT-UTS) and at high temperature (HT-UTS) were reported and discussed in section 4.1.2 and shown in Figure 4-4. Indentations have been marked on the specimens to detect the deformation on the matrix phase of the material, and it will be discussed in details in the following section. To improve the clarity of the results, Tables 4-1 and 4-2 were attached at the end of this section to summarize figure numbers to the testing conditions, measured creep strains and the major findings. The 'Δ strain' reported in Table 4-1 is the change between the 'instantaneous strain' and 'end of test strain' (data points have been enlarged in the figures of the creep profile) of a particular sample with the micrographs shown in this study. The 'creep rate', also reported in Table 4-1, is the rate of change in strain over the change in time in the secondary creep region described in section 2.1.1. The creep test data of all the specimens tested are shown in Appendix E.

Table 4-1: Summary of strain measurements.

GMT	Creep strain data	Stress Level (MPa)	% UTS	Temperature (°C)	Instantaneous strain (%)	End of test strain (%)	Δ strain (%)	Creep rate (% 10^{-6} s^{-1})
D	Figure 4-11	23	33	23 (RT)	0.08	0.37	0.29	1.0 ± 0.1
D	Figure 4-11	47	67	23 (RT)	0.65	1.63	0.98	5.5 ± 0.7
G	Figure 4-14	31	33	23 (RT)	0.27	0.51	0.24	1.0 ± 0.5
G	Figure 4-14	62	67	23 (RT)	0.55	1.37	0.82	4.3 ± 1.1
D	Figure 4-17	10	33	80 (HT)	0.08	0.34	0.26	1.6 ± 0.4
D	Figure 4-17	21	67	80 (HT)	0.82	4.35**	3.53	51.3 ± 16.7
G	Figure 4-20	21	33	80 (HT)	0.43	0.86	0.43	1.6 ± 0.4
G	Figure 4-20	43	67	80 (HT)	0.81	3.36**	2.55	28.8 ± 10.6

Table 4-2: Summary of micrograph parameters.

GMT	Micrograph	Stress Level (MPa)	% UTS	Temperature (°C)	Fibre Debonding	Transverse Cracking	Fibre Breakage	No. of Specimen	Specimen Failure
D	Figure 4-12	23	33	23 (RT)	Minimal	Minimal	No	2	No
D	Figure 4-13	47	67	23 (RT)	Yes	No	No	2	No
G	Figure 4-15	31	33	23 (RT)	Minimal	No	No	2	No
G	Figure 4-16	62	67	23 (RT)	Yes	Yes	No	3	No
D	Figure 4-18	10	33	80 (HT)	Minimal	No	No	2	No
D	Figure 4-19	21	67	80 (HT)	Yes	Yes	No	3	3
G	Figure 4-21	21	33	80 (HT)	Minimal	No	No	2	No
G	Figure 4-22	43	67	80 (HT)	Yes	Yes	No	4	1

4.1.4.1 Creep Deformation at Room Temperature

The creep curves plotted in strain as a function of time for D100 chopped-fibre composite samples loaded at 33% and 67% UTS in room temperature are shown in Figure 4-11. When loaded at 33% UTS at room temperature, the data shows an instantaneous creep strain of 0.08% and increases gradually to about 0.37%. The change in strain is 0.29%, with the creep rate of about 1×10^{-6} % / s after 1 day of creep. Figure 4-12a and b shows the typical micrographs before and after 1 day of creep at 33% of the RT-UTS. A comparison of both micrographs shows no significant deformation at the surface at this relatively low stress level and room temperature. The area circled in Figure 4-12a and b shows the bridging of two fibre ends which could be the initiation of a transverse crack.

However, after one day of creep at 67% UTS in room temperature, the creep strain has increased by as much as 0.98%. Upon increasing stress from 33% to 67% of the RT-UTS, the creep rate has increased more than 5 times at 5.5×10^{-6} % / s. Figure 4-13a and b shows the typical micrographs for creep at 67% of the RT-UTS. Fibre-matrix debonding was detected during creep at this stress level and there were also clear signs of crack bridging between the interfaces of the matrix and fibres, as shown in the circled area on the left of Figure 4-13. The circled debonded fibres appear black on the micrograph as they were disjointed from the matrix and no longer lie on the plane of focus. The initiation of debonding can also be detected by the appearance of a bright outline around the fibre. Debonding, however, happened during the ramp-up loading period when the load was applied after 1 minute creep, while crack bridging developed slowly over the duration of creep.

Figure 4-14 shows the creep curve of the G100 long-continuous fibre composite samples. When loaded at 33% UTS at room temperature, the change in creep strain from time $t = 0$ s to 1 day of creep was 0.24%, which was lower than the chopped fibres at 0.29%. However, the measured creep rates show similar results for the long continuous fibre (1.0×10^{-6} % / s) as well as the chopped fibre (1.0×10^{-6} % / s). This suggested that creep rates at room temperature are not strongly influence by the mat reinforcement

structure. The micrographs in Figure 4-15a and b show no significant deformation after 1 day of creep at 33% of the RT-UTS at the relatively low stress level. By focusing on Figure 4-15a and b, however, there were some tiny black spots emerging on the specimen surface after 1 day of creep. The black spots tended to appear with debonding failure, where the fibres were perpendicular to the observed material surface. Due to the relatively low stress level at 33% of the RT-UTS, no bridging of cracks was detected on the specimen surface.

When the stress was increased to about 67% of the RT-UTS for the G100 series long-fibre composite, Figure 4-14 shows the creep strain has increased from the start of the creep at 0.55% to 1.37% after loading for 1 day during the untangling and yielding of the fibres and matrix phase. The creep rate has increased by more than 4 times after one day, which is more than double the strain at 33% of the RT-UTS stress level. Micrographs in Figure 4-16a and b show that cracks initiated quickly from the fibre-matrix interface within 1 minute of loading and grew transversely to the load direction, as shown in Figure 4-16c. Also in Figure 4-16c, it is observed that the surface of the specimen became uneven, as the fibres that were partially embedded below the specimen surface emerge with time. The damage region appeared to be larger than that observed for the D100 chopped fibres. This observation is consistent with reports by Karger-Kocsis *et al.* [15] that the long-continuous fibre material has a larger process zone associated with large scale matrix yielding, due to the tangled long continuous fibres. The current observations are consistent with earlier reports [8] of non-linear creep for this long-fibre GMT material.

4.1.4.2 Creep Deformation at 80°C

Typical creep curve of D100 series chopped-fibre specimens loaded at 33% of the HT-UTS at 80°C is shown in Figure 4-17. The data shows a creep rate of 1.6×10^{-6} % / s after 1 day of creep. The micrographs in Figure 4-18a and b, show that creep deformation is minimal even after one day of loading.

When the chopped-fibre specimen loaded at 67% of the HT-UTS at 80 °C, the creep profile in Figure 4-17 shows the creep strain increased dramatically from 2.22% to 3.32% after 6 and 12 hours of creep, respectively. The average creep rate of the chopped-fibre specimens tested under the same condition at 67% of the HT-UTS at high temperature is 51.3×10^{-6} % / s. The images in Figure 4-19a to d at 67% of the HT-UTS show relatively more severe deformation of the matrix at high temperature, and all the test specimens were failed prior to 1 day of creep. The surface of the polished specimen became progressively more uneven with increasing exposure time to 80°C. Before creep loading, the matrix appeared as a uniform bright background, but with increasing time, the matrix deformation becomes non-uniform due to pockets of localized matrix yielding. The emergence of various "intensities from grey to black" in the background suggests that there are different levels of deformation resulting on the surface of the sample. Such changes on the surface topology may be associated with changes inside the sample, possibly because of formulation of internal cracks or voids. Further investigation is needed to provide evidence for such deformation mechanism.

In addition to matrix yielding, the other deformation mechanisms such as debonding and transverse cracks initiated at the fibre-matrix interface were also appeared as they did in the room temperature tests. From the *in-situ* creep micrographs shown in Figure 4-19, there is a clear propagation pattern of the cracks. The circled area on the right in Figure 4-19b shows cracks that resulted from creep for 6 hours at elevated temperature. The cracks circled in Figure 4-19b appear to be the same size in Figure 4-19c, even after 12 hours of creep. By comparing the circled areas on the left of Figure 4-19b and c, it is possible to see that more cracks appeared and grown with time. It is evident that the fracture mechanism was not that of a single crack or even a handful of cracks, but rather a series of short transverse cracks across the matrix. The dominant failure mechanism was the initiation of multiples cracks which grew quickly to a certain size and stop, and then followed by the formation of new cracks developing in another region.

The steep increase in creep strain from 6 to 15 hours of creep in Figure 4-17 was clearly associated with two modes of failure:

- multiple transverse crack formation and limited growth
- matrix shear yielding.

The specimen in Figure 4-19 failed before 1 full day of creep. It fractured at about 16 hours as seen in the tertiary creep stage. Figure 4-19d shows the micrograph just prior to the abrupt failure at about 15 hours.

The G100 series continuous-fibre composite materials were also tested under the same parameters, 33% and 67% of the HT-UTS. The creep curve in Figure 4-20 shows the very slow and gradual creep strain increase for a period over 1 day, with a creep rate of 1.6×10^{-6} % / s. This corresponds well with Figure 4-21 which shows no significant deformation at 33% of the HT-UTS due to relatively low stress level.

For creep at 67% of the HT-UTS with continuous-fibre composite materials, 4 specimens were tested for this set of experiment and 1 of them failed prior to 1 day of creep. The specimen shown in Figure 4-20 failed at 4.36% strain after 10.5 hours of creep. The average creep rate for continuous-fibre materials creep at 67% of the HT-UTS was 28.8×10^{-6} % / s, which was about half of the creep rate for the chopped-fibre creep at 67% of the HT-UTS. Clearly, continuous-fibre mat composite offers higher creep resistance than chopped fibre composite at elevated temperature. The typical micrographs in Figure 4-22a to d show matrix yielding for the long-fibre composite was less pronounced than in the chopped fibre in Figure 4-19. The intensity of transverse crack formation and bridging is more apparent. At the higher load, the dominant mechanism for failure after more than 10 hours of creep is crack coalescence of a handful of relatively long matrix cracks. Crack bridging accelerated the creep strain - the strain reached 3.11% only after 9 hours of creep – to reach tertiary creep, as illustrated in Figure 4-20.

.

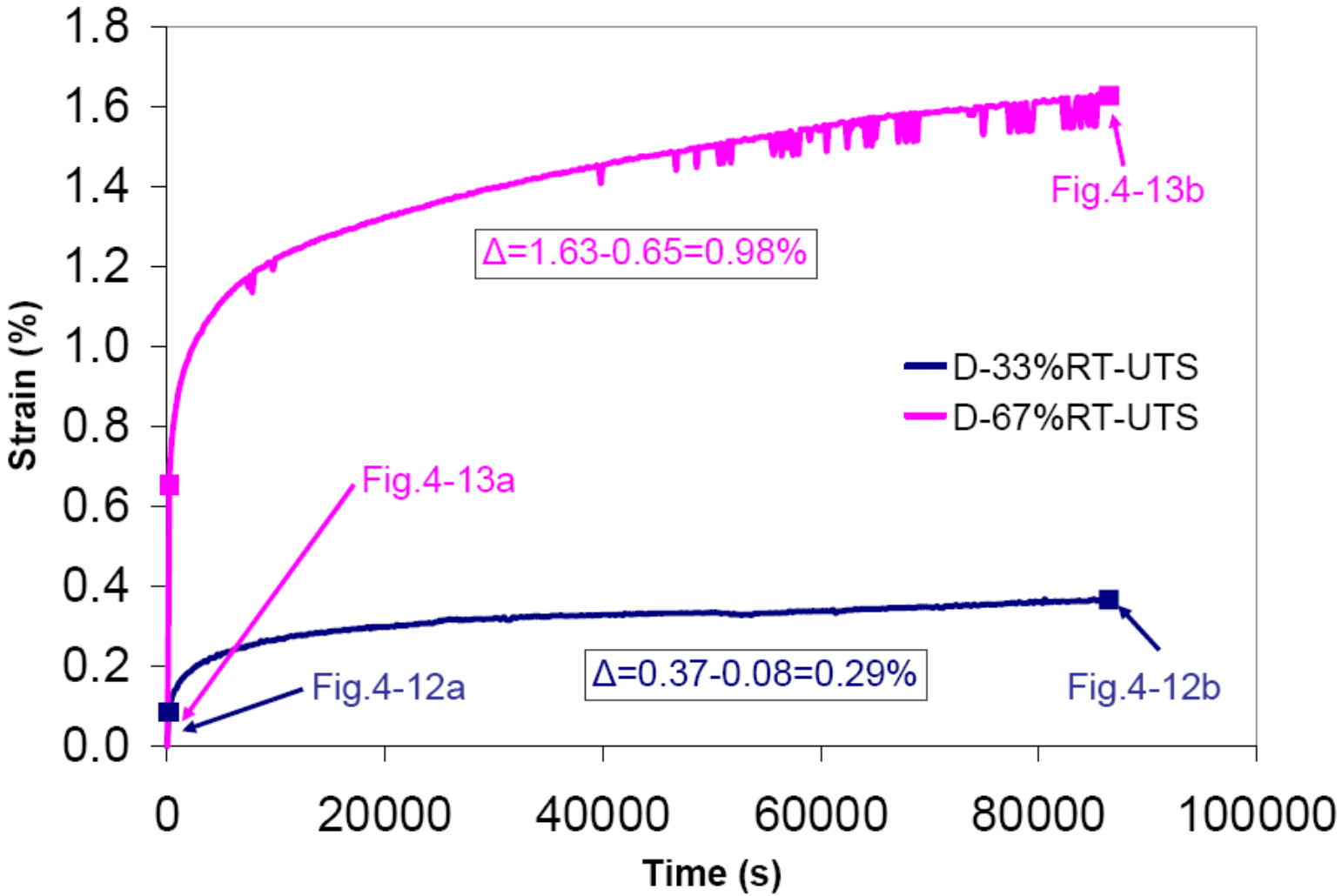

Figure 4-11: Creep strain profile of chopped-fibre (D100) samples in room temperature.

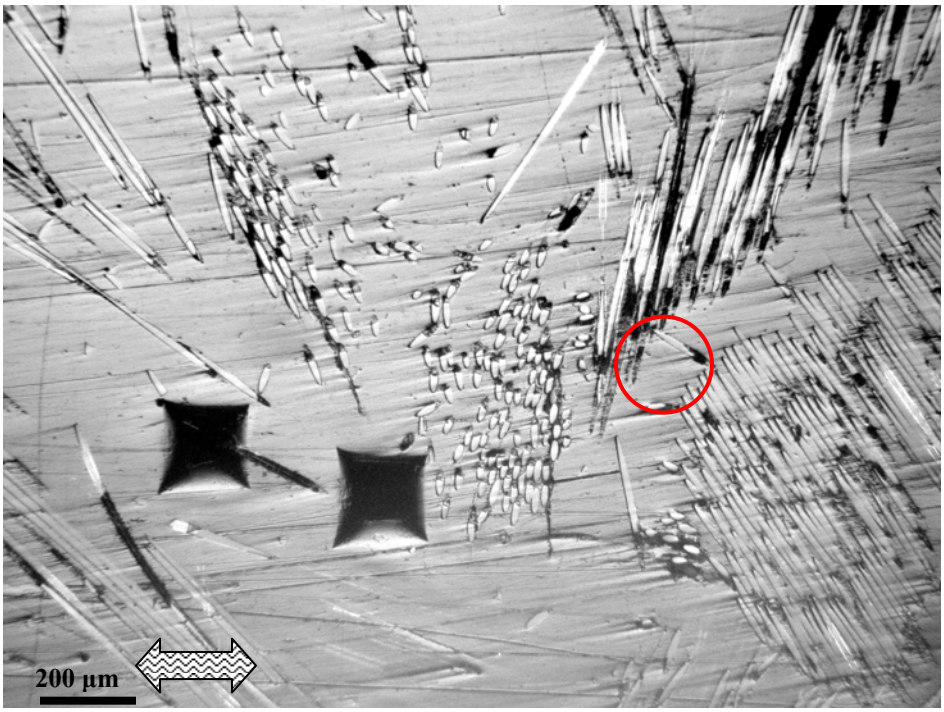

a)

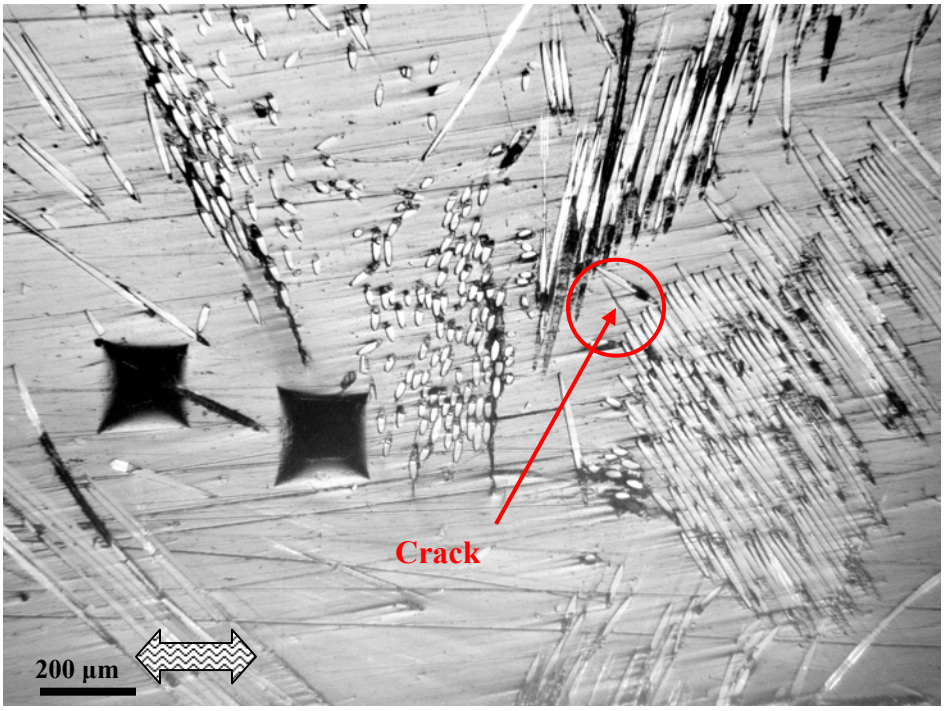

b)

Figure 4-12: Chopped-fibre (D100) at (a) no load; and (b) creep for 1 day at 33% RT-UTS.

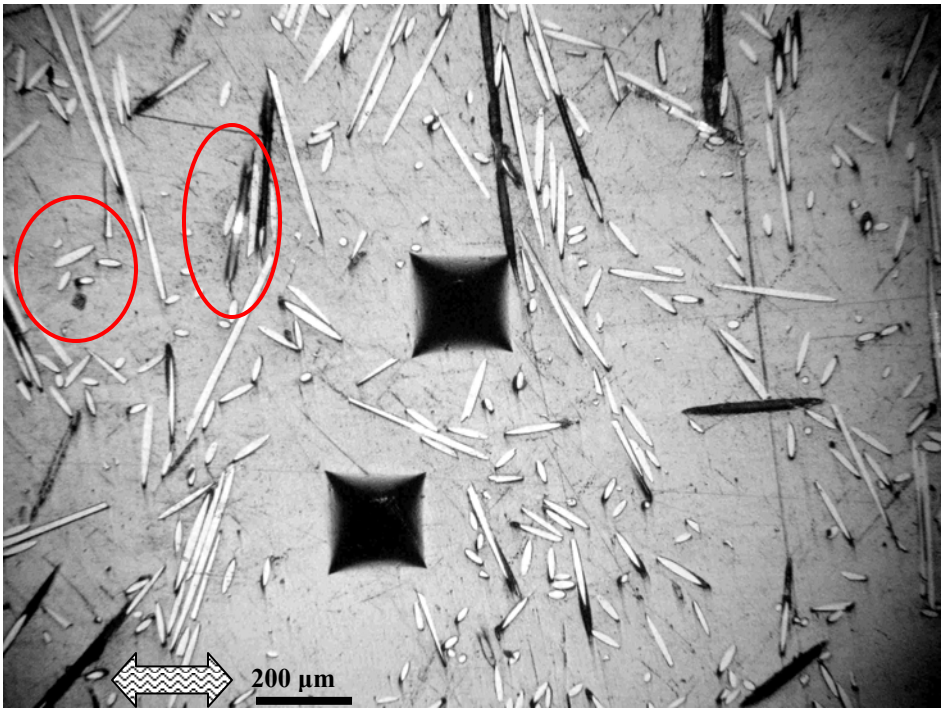

a)

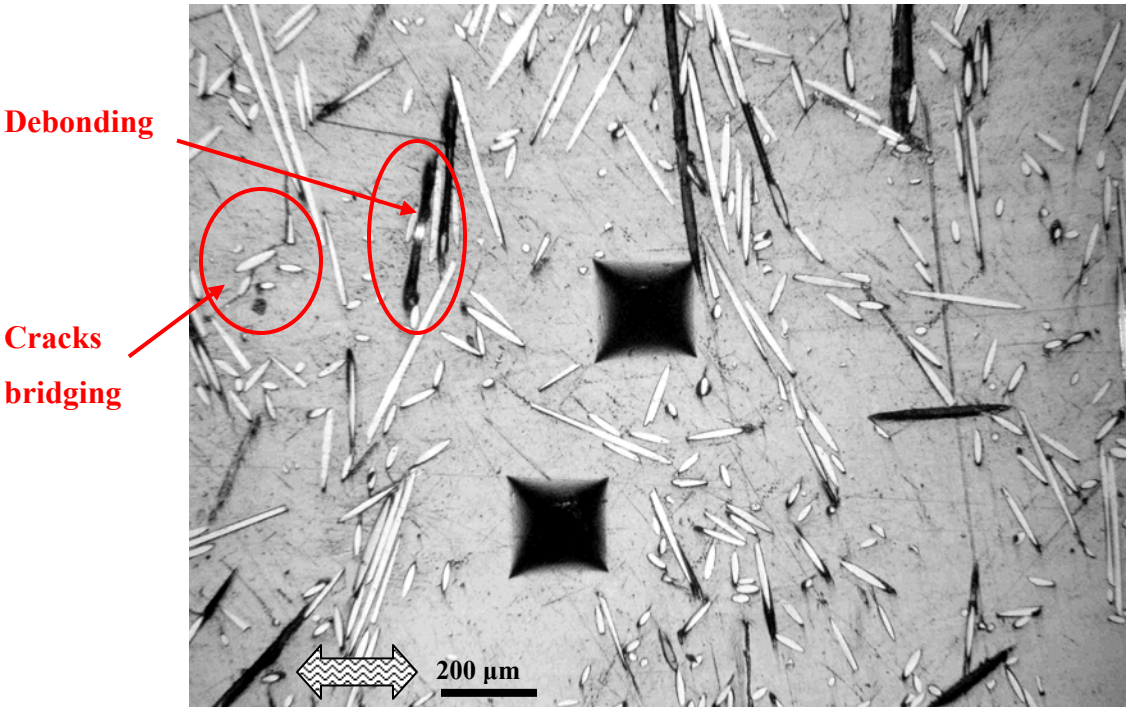

b)

Figure 4-13: Chopped-fibre (D100) at (a) no load; and (b) creep for 1 day at 67% RT-UTS.

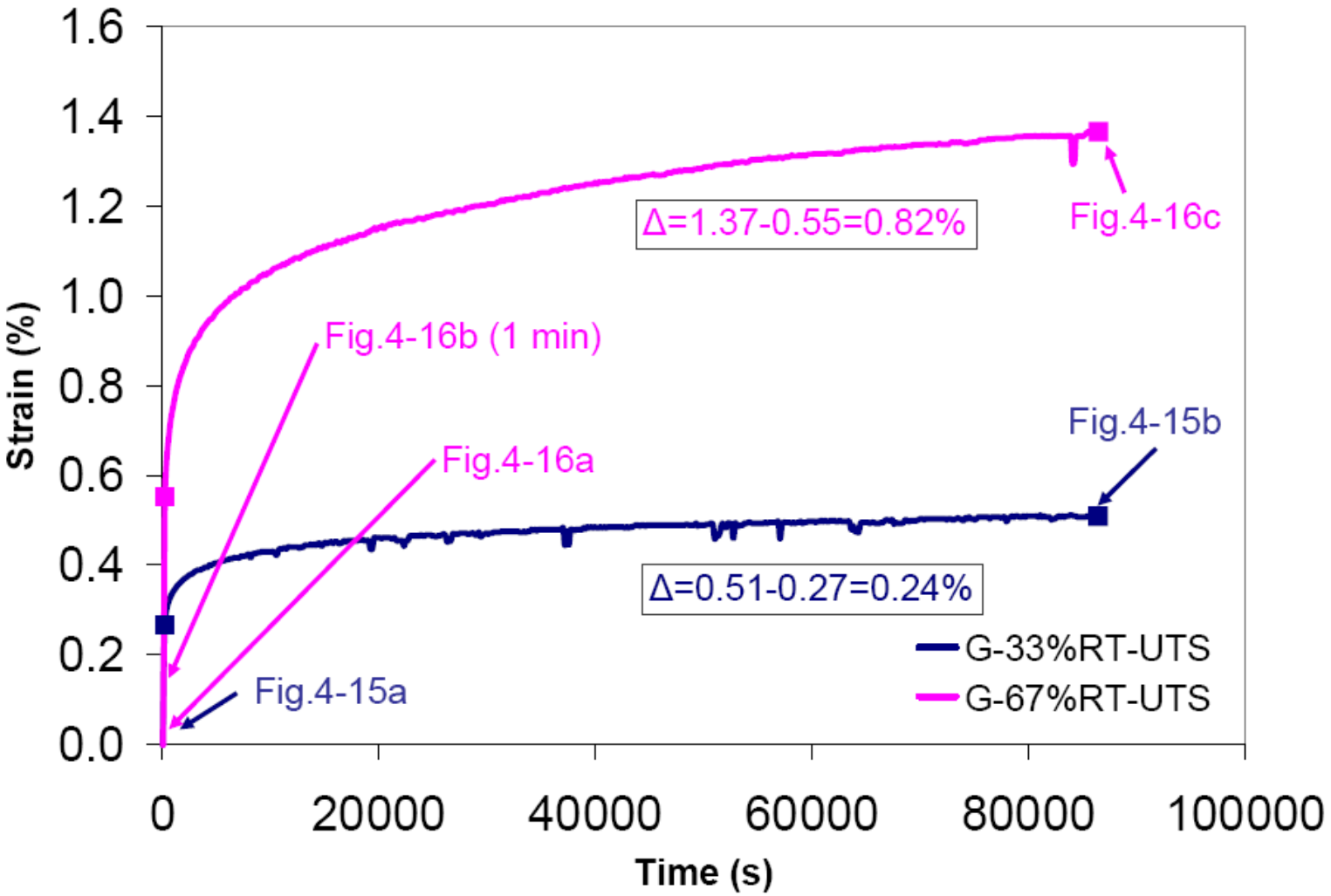

Figure 4-14: Creep strain profile for long-fibre (G100) samples in room temperature.

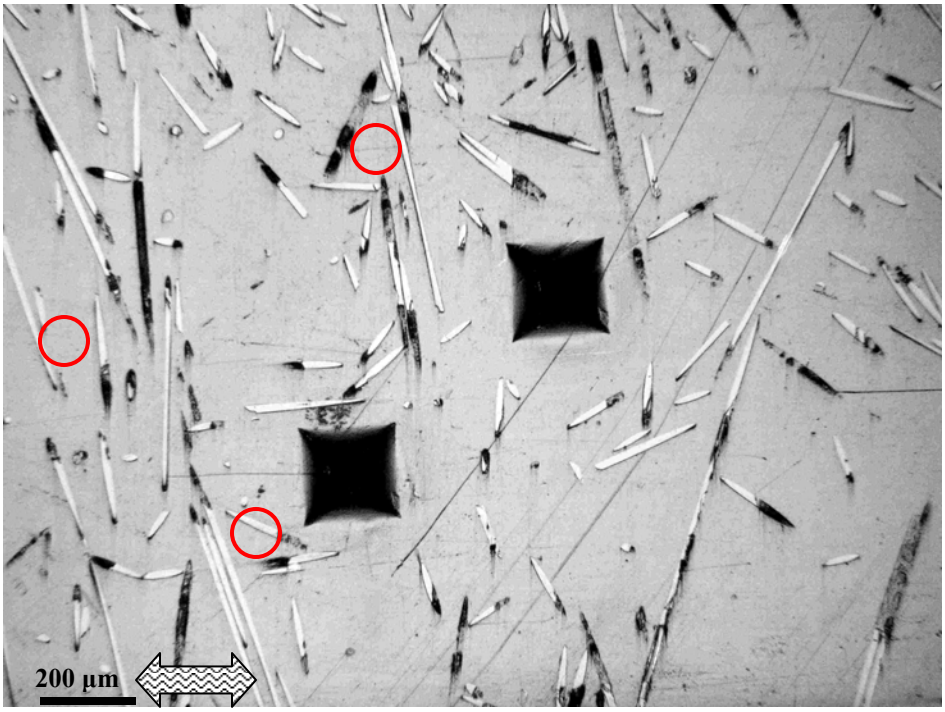

a)

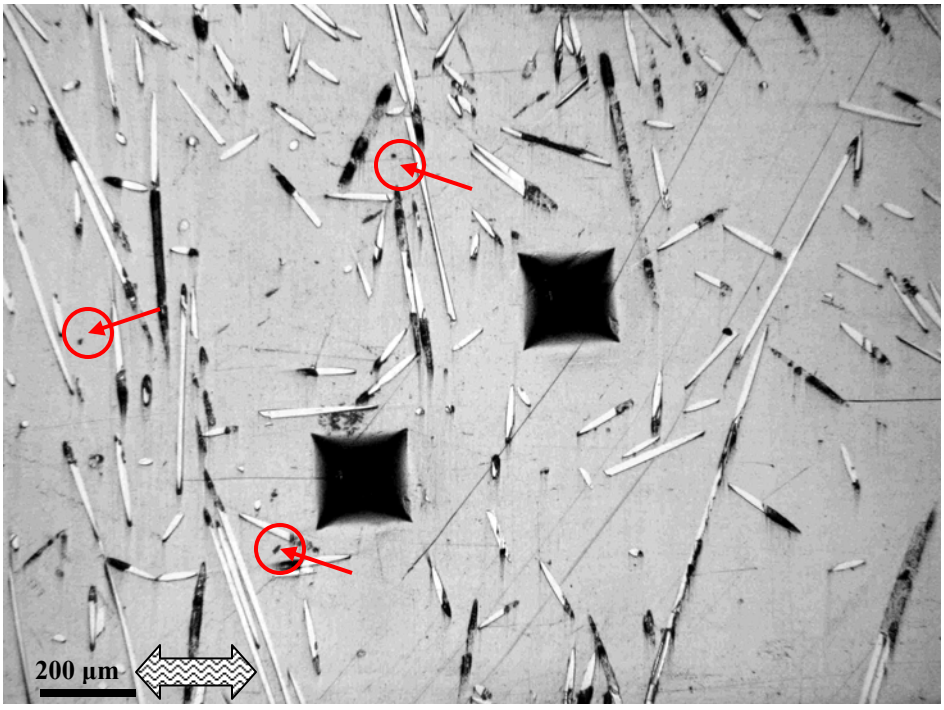

b)

Figure 4-15: Long-fibre (G100) at (a) no load; and (b) creep for 1 day at 33% RT-UTS. 'Black spots' appeared after creep for 1 day.

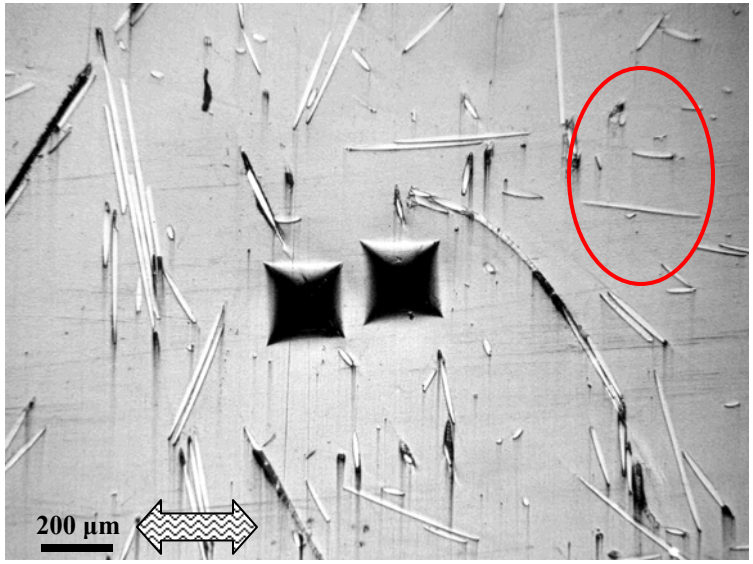

a)

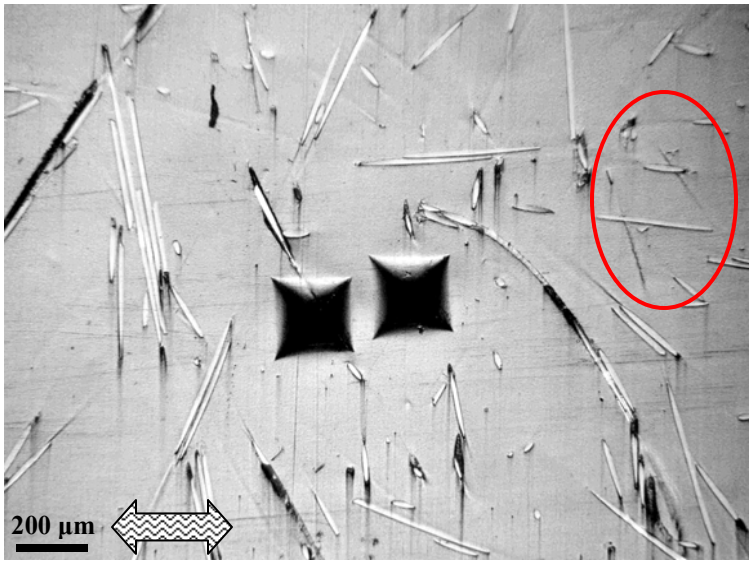

b)

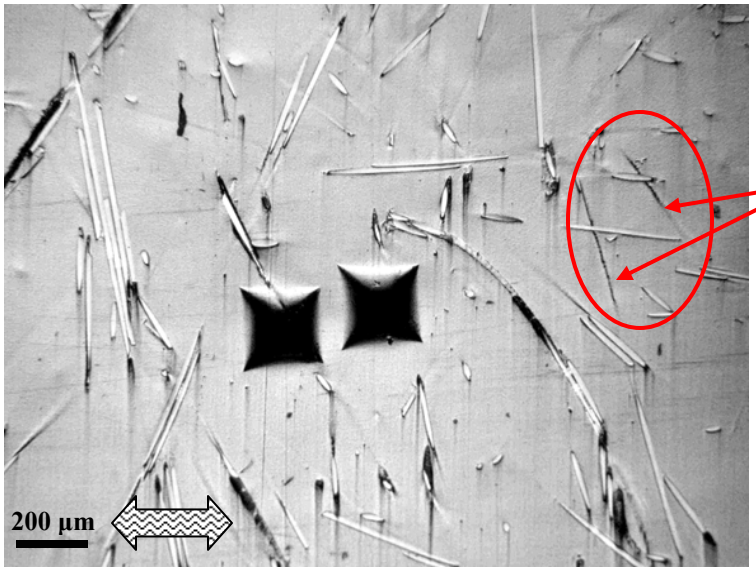

c)

Figure 4-16: Long-fibre (G100) at (a) no load; (b) creep for 1 minute; and c) creep for 1 day at 67% RT-UTS.

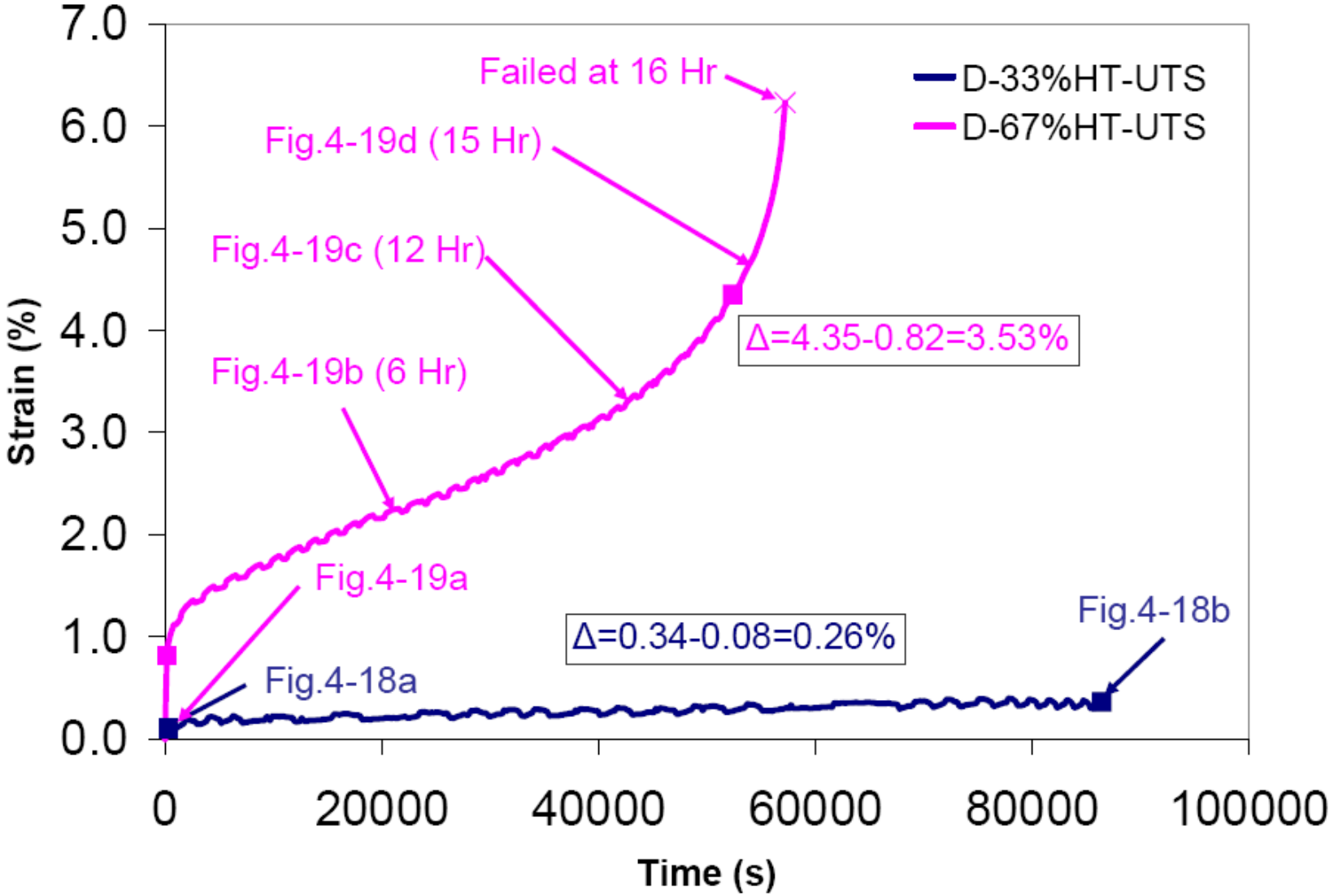

Figure 4-17: Creep strain profile of chopped-fibre (D100) samples in high temperature.

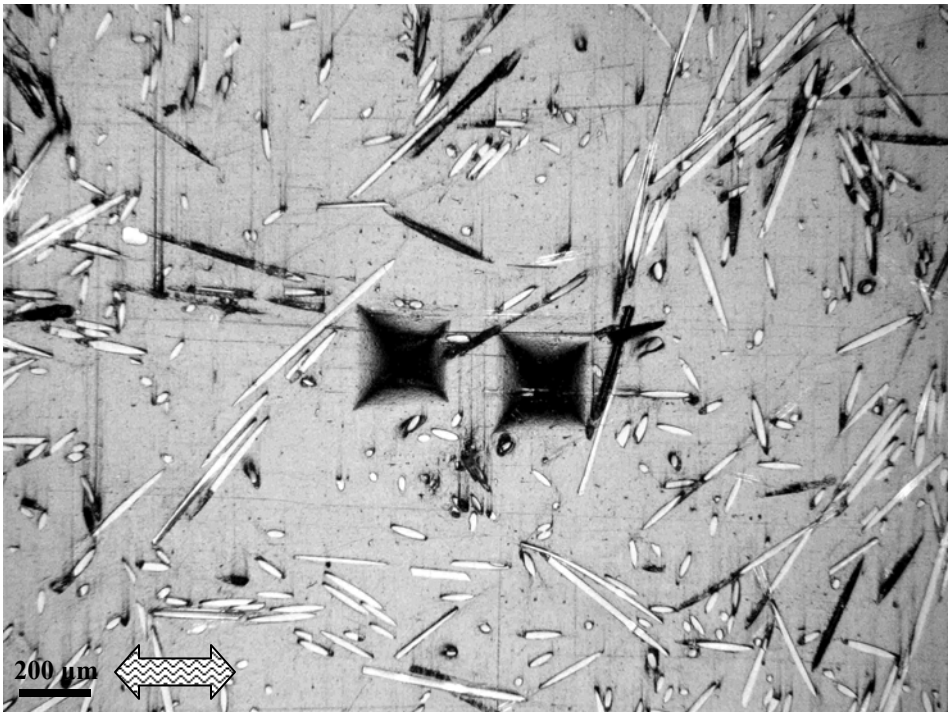

a)

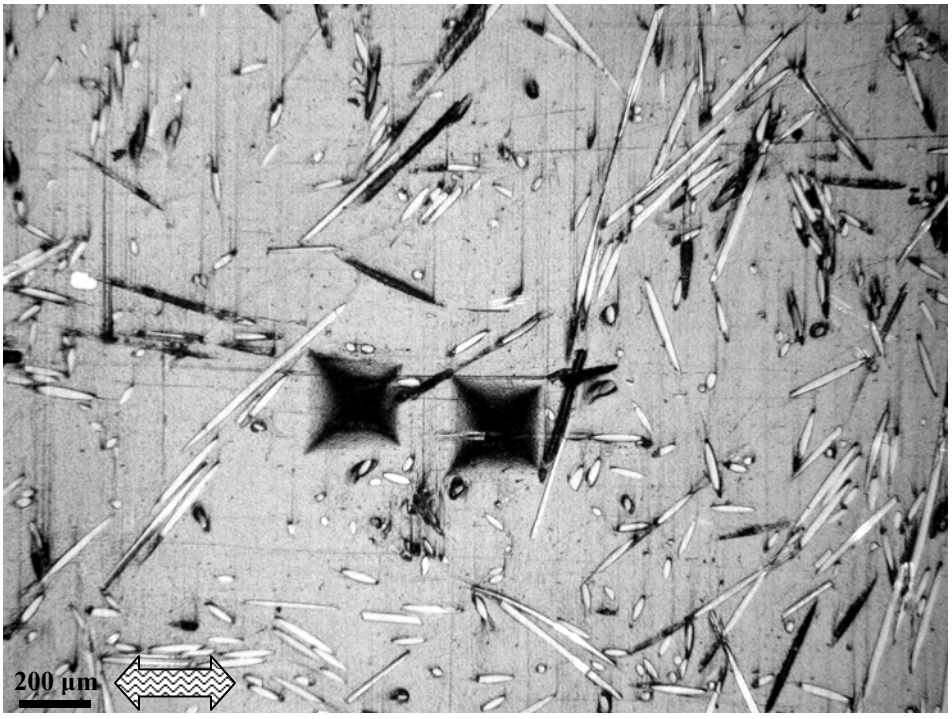

b)

Figure 4-18: Chopped-fibre (D100) at (a) no load; and (b) creep for 1 day at 33% HT-UTS.

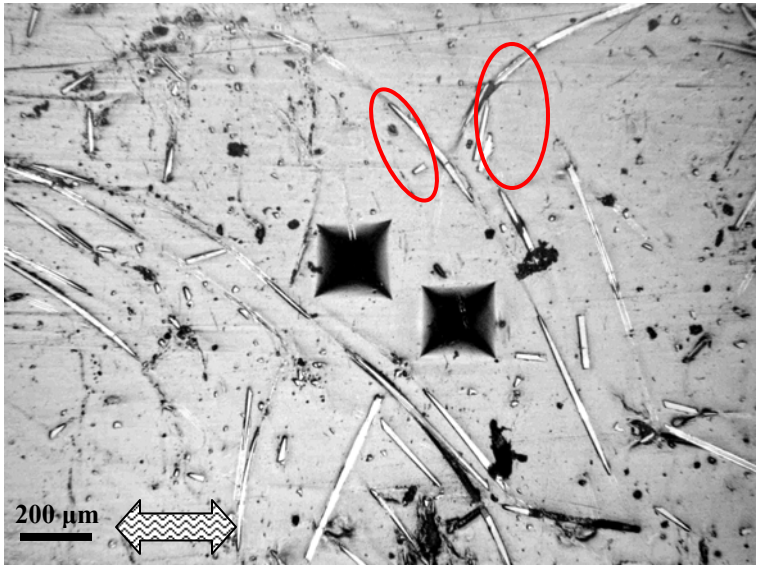

a)

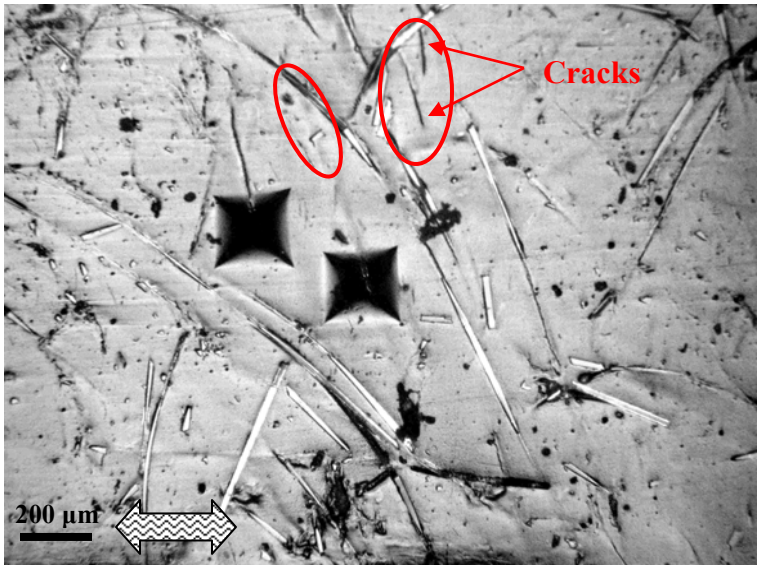

b)

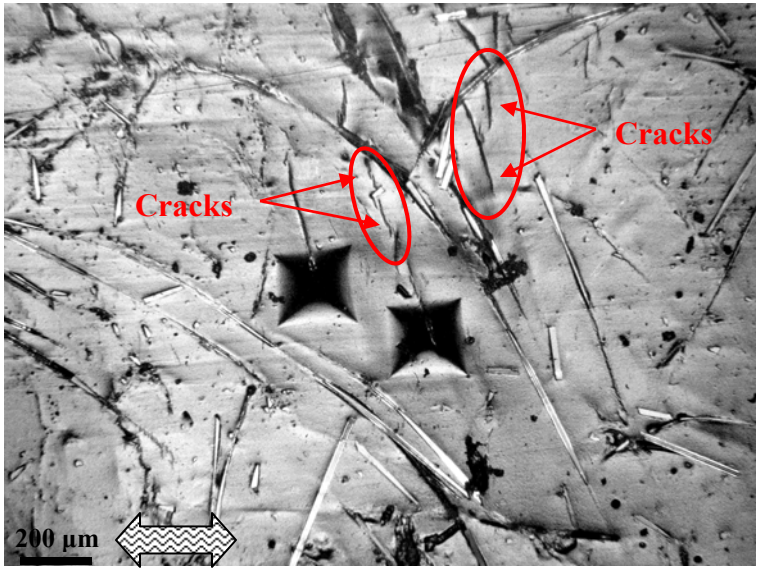

c)

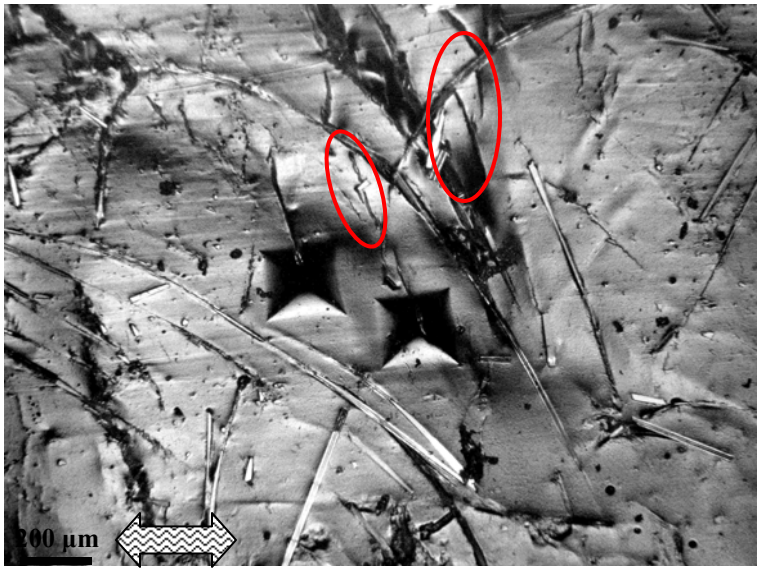

d)

Figure 4-19: Chopped-fibre (D100) at a) no load; creep for b) 6 hrs; c) 12 hrs; and d) 15hrs (prior to facture) at 67% HT-UTS.

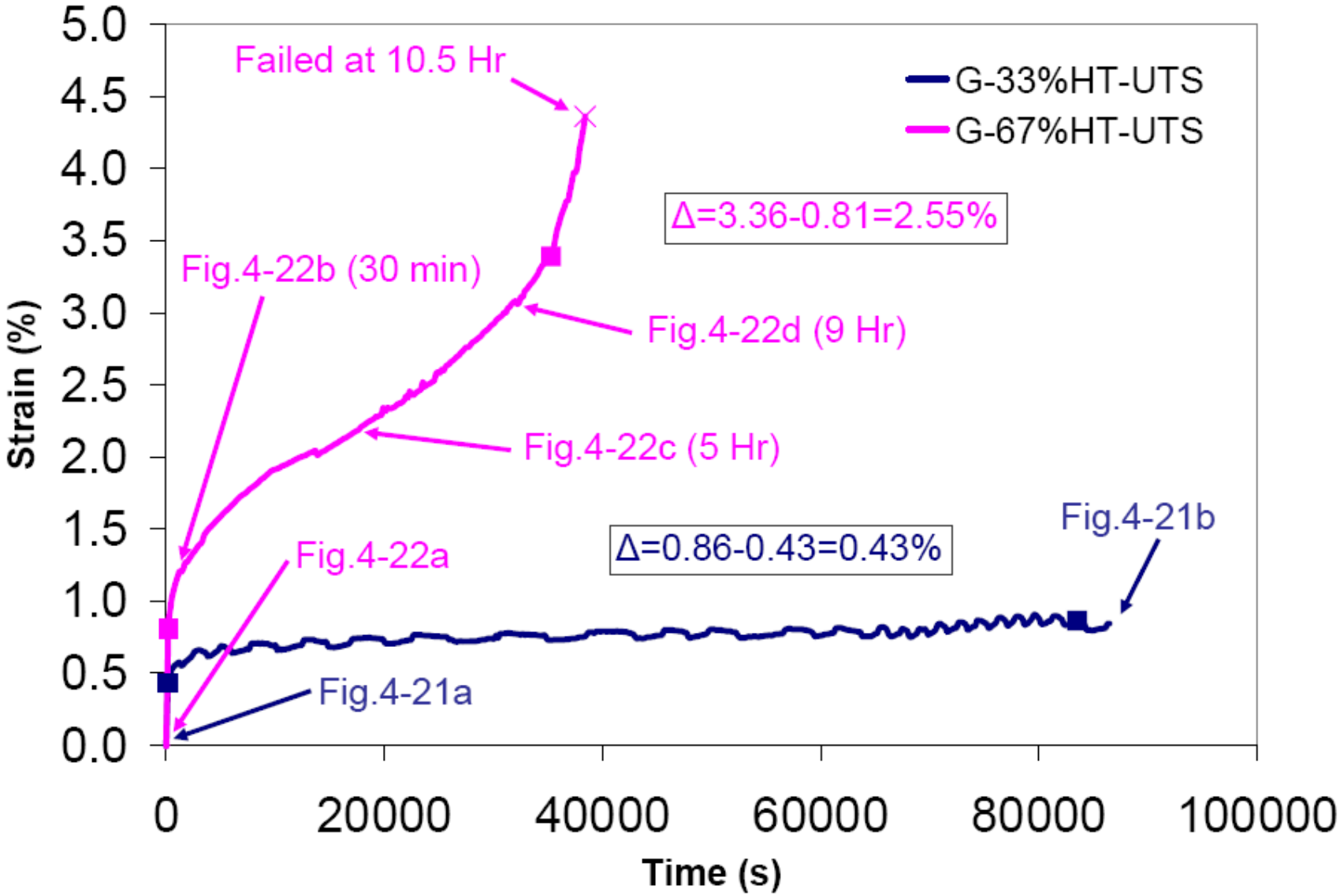

Figure 4-20: Creep strain profile for long-fibre (G100) samples in high temperature.

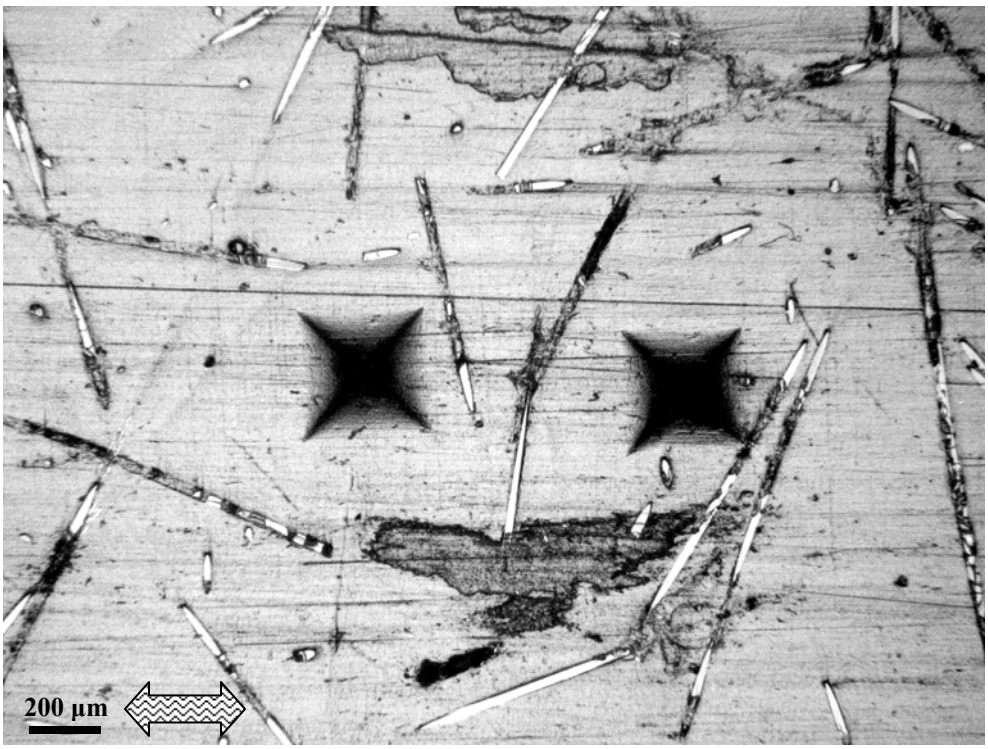

a)

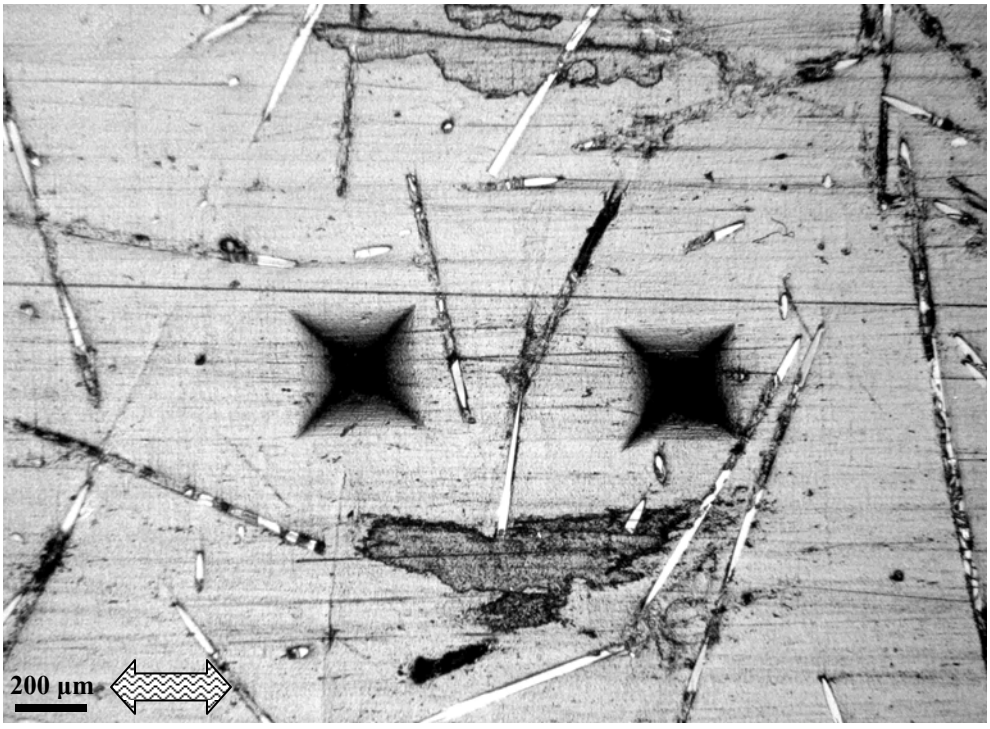

b)

Figure 4-21: Long-fibre (G100) at (a) no load; and (b) creep for 1 day at 33% HT-UTS.

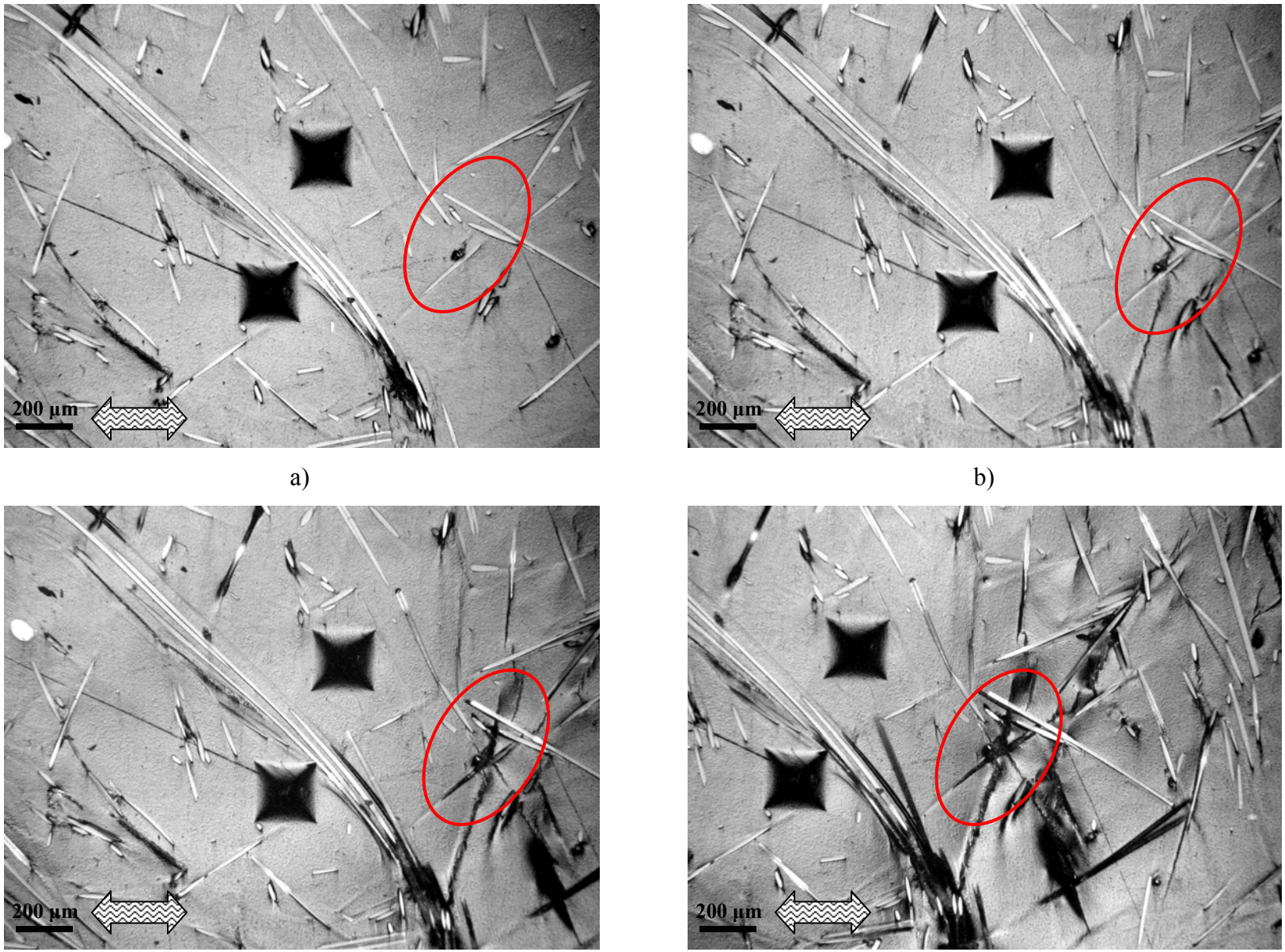

a) b)

c) d)

Figure 4-22: Long-fibre (G100) at a) no load; creep for b) 30 min; c) 5 hrs; and d) 9 hrs (prior to facture) at 67% HT-UTS.

4.1.5 Scanning Electron Microscope Fractography

Figure 4-23 shows the fracture surface of the D100 series chopped fibre composite specimen observed under the scanning electron microscopy. The presence of fibre bundles which have been pulled out of the polypropylene matrix was very pronounced. Clearly, the fibre-matrix interfacial bond (Figure 4-23b) was relatively weak as evidenced by the smooth and clean fibre surfaces at higher magnification. Similarly, the same characteristics were also found for the G100 series long fibre GMT in Figure 4-24.

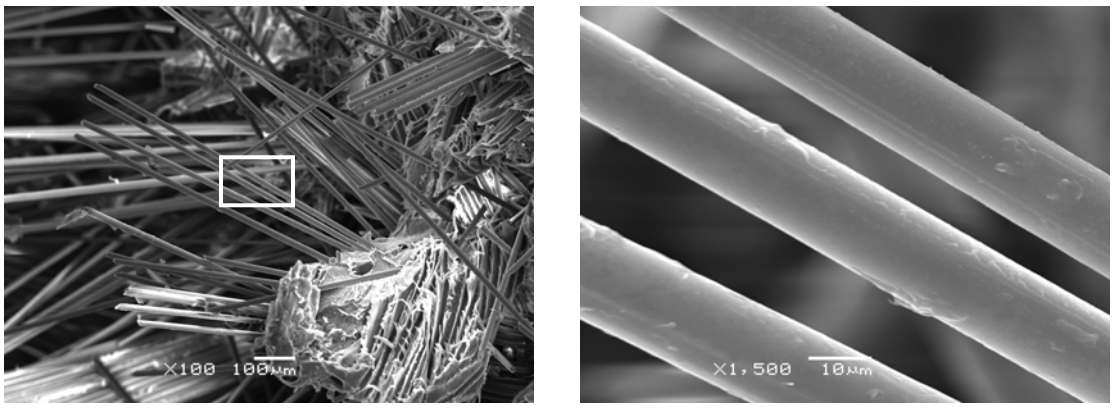

a) b)

Figure 4-23: Clean and smooth fracture surfaces of pulled out D100 chopped fibre.

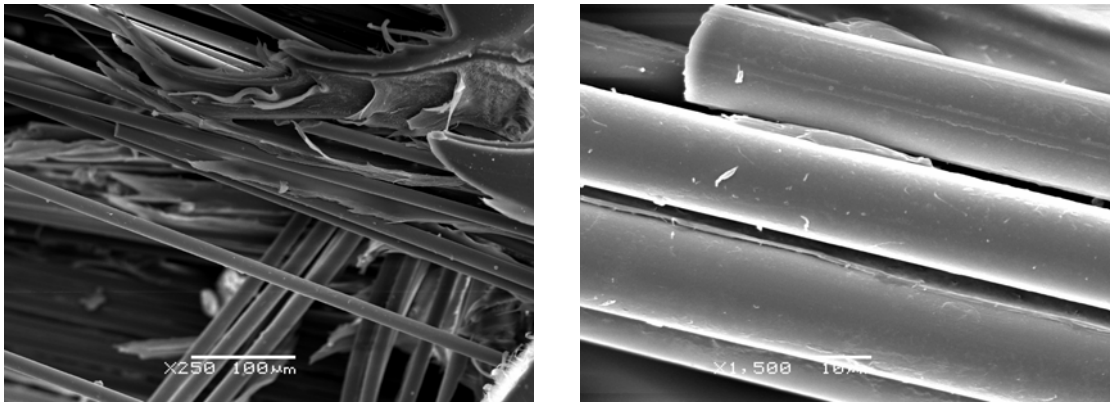

a) b)

Figure 4-24: Clean and smooth fracture surfaces of pulled out G100 long fibre.

It is useful to note that the earlier observation of tiny black spots appearing on the surface after creep for 1 day in Figure 4-15b were due to the debonding of the fibres which were perpendicular to the material surface. Figure 4-25 shows the SEM image of the 'black spot' after the creep, indicating the fibre end was oriented perpendicular to the polished surface.

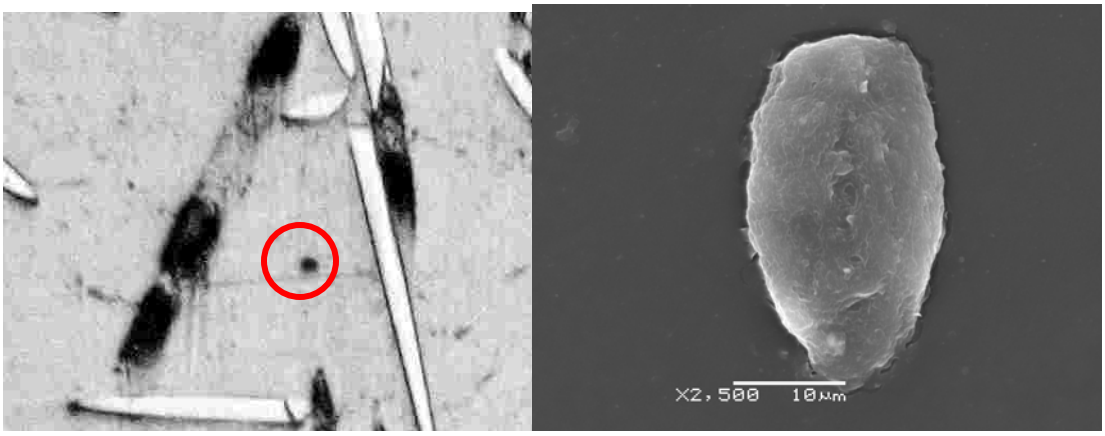

Figure 4-25: SEM image of the 'black spot' which is a glass fibre end.

4.1.6 Indentation Analysis

Micro-indentations were marked on a rich polypropylene matrix region on the specimen surface to act as "extensometers". The size of each indentation was about 200 by 200 µm. An image analysis software tool was used to measure the indentations after specified durations creep by counting the number of pixels in the image.

Table 4-3 provides the indentation measurements. All the indentations were slightly distorted due to the presence of randomly dispersed fibres. In this investigation only the specimens loaded at 67% RT-TUS and 67% HT-UTS have been studied since the creep deformation at lower stress levels were minimal. In Table 4-3, 'X1' (the distance along the horizontal x-axis), 'Y1' (the distance along the vertical y-axis) and 'D1' (the diagonal distance of the indentation) are the dimensions denoted to the left of the two indentations. Similarly, and 'X2', 'Y2' and 'D2' are denoted to the indentation on the right, the 'Dist'

is the distance between marked points of two indentations. The measurements of the indentations are illustrated in Figure 4-26 to Figure 4-29.

The strain for X1 and X2 increased with prolonged creep loading for both D100 and G100 series materials regardless of the temperature levels. The net strain increases were between 1.0% to 4.7% and along the x-axis, i.e., the loading direction, and there did not seem to be a difference between the two types of composites. Correspondingly, slight contractions along the y-axis of the indentations are seen. When the D1 (diagonal) values are compared for the two composites, there is no clear trend on the influence of temperature or fibre-reinforcement on matrix shear flow (45°). The Poisson's ratio calculated from the average change in strain values is about 0.30, compared to 0.25 found by the other investigator in the same research group [8].

To further investigate if the effect of temperature, Figure 4-30 shows the measurement of the indentations before and after the heating with no load applied to the long-continuous fibre specimen. From the results reported in Table 4-3, there was a change in 2.3% in strain between the two indentations, which correlated with the coefficient of thermal expansion that was found to be $9.004 \pm 3.02 \times 10^{-6}$ / °C by the investigator in the same group [8].

Overall, it can be concluded that the differences in deformation characteristics of the matrix phase between the D100 and G100 series materials are not apparent from indentation measurements. Although the creep strains measured from the indentation analysis reported in Table 4-3 are in the same order of magnitude as from the creep profiles in the previous section, however, there are no clear trends have been observed from the results. From the image analysis of the indentations, it is concluded that the largest matrix strain was observed along the loading direction, and minimal changes were detected along the transverse direction. This empirical data is consistent with the observed dominant failure mode, which is the coalescence of small transverse cracks developed along the matrix phase.

Table 4-3: Summary of micro-indentation measurements.

GMT	Micrograph	% UTS	Temperature (°C)		X1 (μm)	Y1 (μm)	D1 (μm)	X2 (μm)	Y2 (μm)	D2 (μm)	Dist (μm)
D	Figure 4-26a	67	23 (RT)	No load	208	222	298	213	223	301	312
D	Figure 4-26b	67	23 (RT)	Loaded	211	217	301	223	223	295	304
				Δ	1.4%	-2.3%	1.0%	4.7%	0.0%	-2.0%	-2.6%
G	Figure 4-27a	67	23 (RT)	No load	209	227	295	214	229	305	79
G	Figure 4-27b	67	23 (RT)	Loaded	216	227	307	218	229	311	75
				Δ	3.3%	0.0%	4.1%	1.9%	0.0%	2.0%	-5.1%
D	Figure 4-28a	67	80 (HT)	No load	209	198	293	203	192	288	87
D	Figure 4-28b	67	80 (HT)	Loaded	215	192	289	206	192	281	88
				Δ	2.9%	-3.0%	-1.4%	1.5%	0.0%	-2.4%	1.1%
G	Figure 4-29a	67	80 (HT)	No load	205	209	294	209	211	298	307
G	Figure 4-29b	67	80 (HT)	Loaded	213	209	297	211	209	299	309
				Δ	3.9%	0.0%	1.0%	1.0%	-0.9%	0.3%	0.7%
G	Figure 4-30a	n/a	23 (RT)	No load	217	215	300	213	213	303	300
G	Figure 4-30b	n/a	80 (HT)	No load	205	209	294	209	211	298	307
				Δ	-5.5%	-2.8%	-2.0%	-1.9%	-0.9%	-1.7%	2.3%

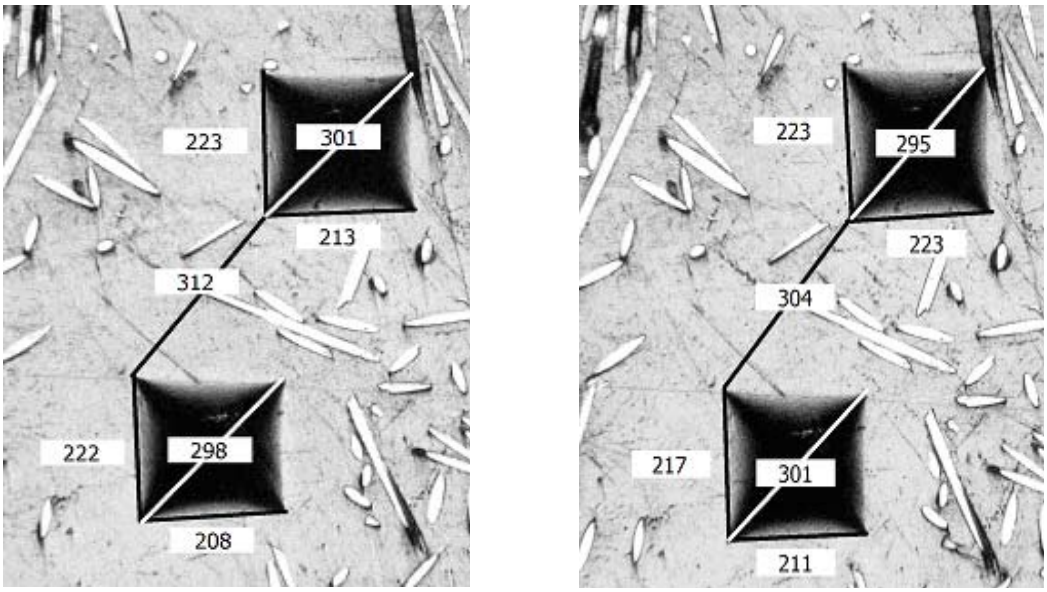

a) b)

Figure 4-26: Micrometer-based indentation measurements for D100 chopped-fibre sample at 67% RT-UTS with: a) no load; and b) creep for 1 day in room temperature.

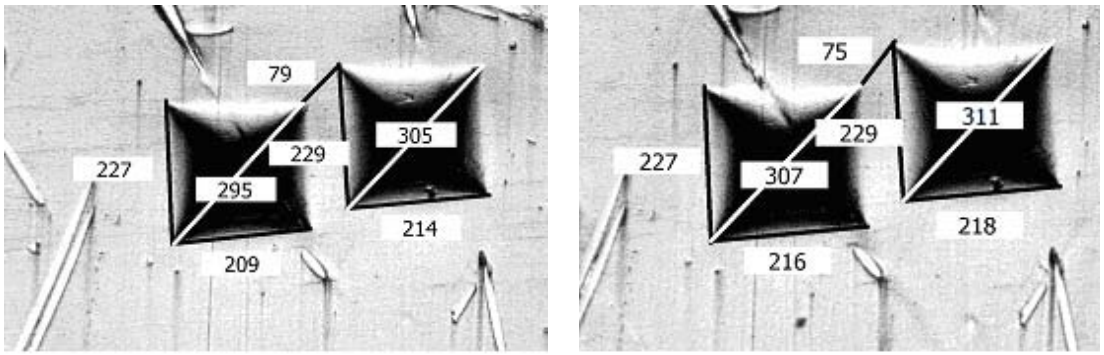

a) b)

Figure 4-27: Micrometer-based indentation measurements for G100 long-fibre sample at 67% RT-UTS with: a) no load; and b) creep for 1 day in room temperature.

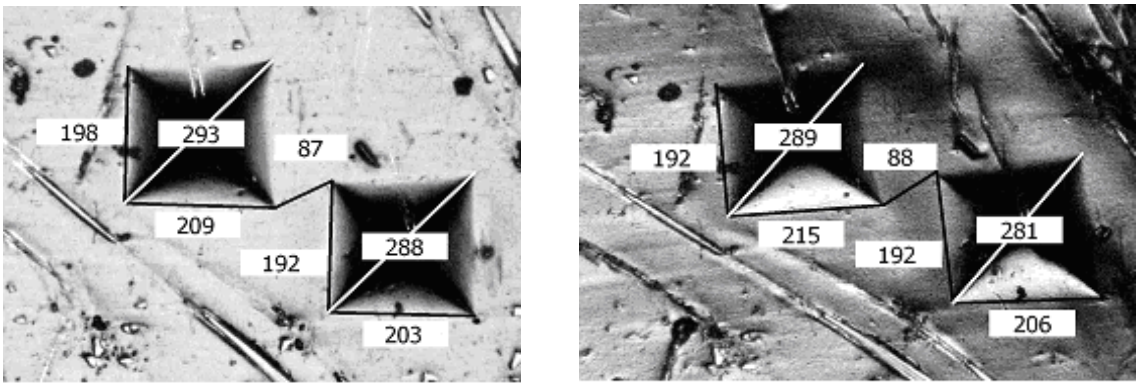

a) b)

Figure 4-28: Micrometer-based indentation measurements for D100 chopped-fibre sample at 67% HT-UTS with (a) no load; and (b) creep for 15 hrs at 80 °C.

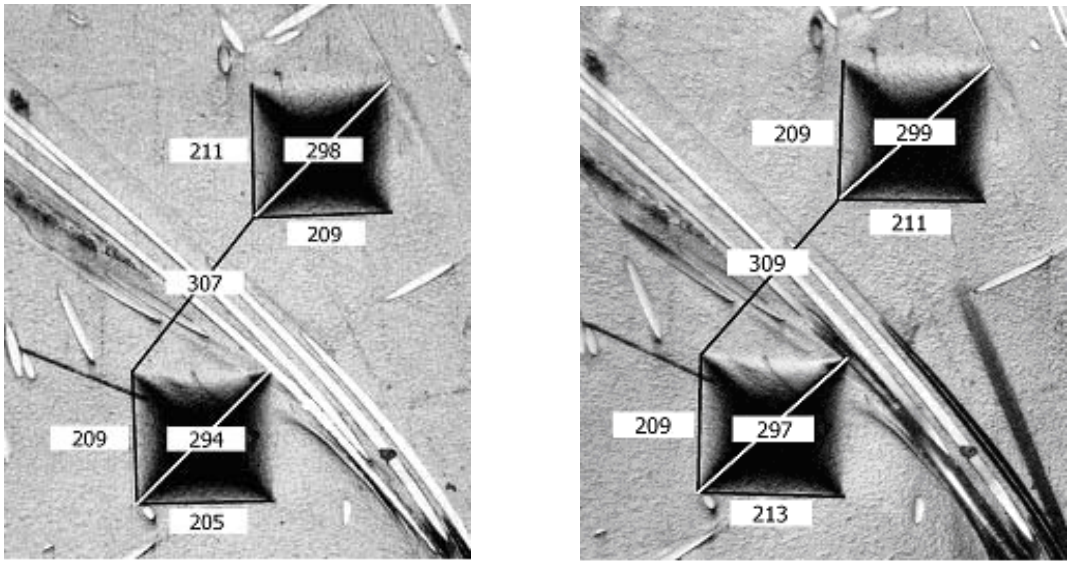

a) b)

Figure 4-29: Micrometer-based indentation measurements for G100 long-fibre sample at 67% HT-UTS with (a) no load; and (b) creep for 9 hrs at 80 °C.

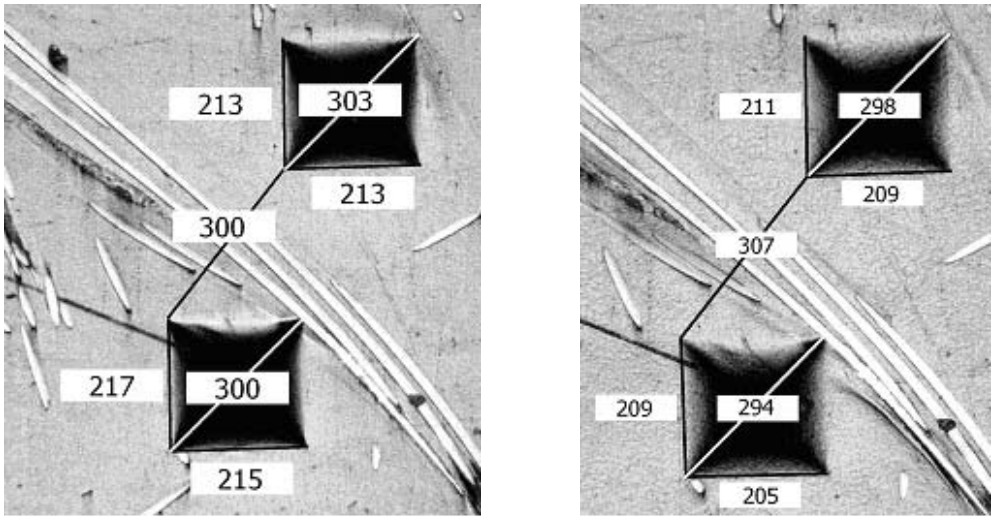

a) b)

Figure 4-30: Micrometer-based indentation measurements in G100 long-fibre sample at (a) room temperature; and (b) 80 °C exposed for 15 minutes.

4.2 Crystallinity and Thermal Aging

4.2.1 Thermogravimetric Analysis Results

Thermogravimetric analysis (TGA) was conducted by heating pure, extracted polypropylene and composite samples at a rate of 10 °C/min in order to study the weight-loss behaviour. The objective was to determine if there were any additives have been removed from the polypropylene extraction process. From the TGA data of the composite plaque shown in Figure 4-31, the onset of the drop in weight percentage happens at a higher temperature comparing to the extracted and pure polypropylene samples. This can be explained by presence of stabilizers in the as-received composite plaque. Stabilizers are additives that improve the thermal stability of polymers during its processing of life-time. The higher onset of thermal degradation observed here in the polypropylene extracted from the composite plaque is attributed to the presence of those additives. In the temperature range between 260 to 350 °C, there is a significant weight percentage drop about 60%. This is due to burn off of the matrix material. The remaining weight percentage at about 40% is the weight of the glass fibres.

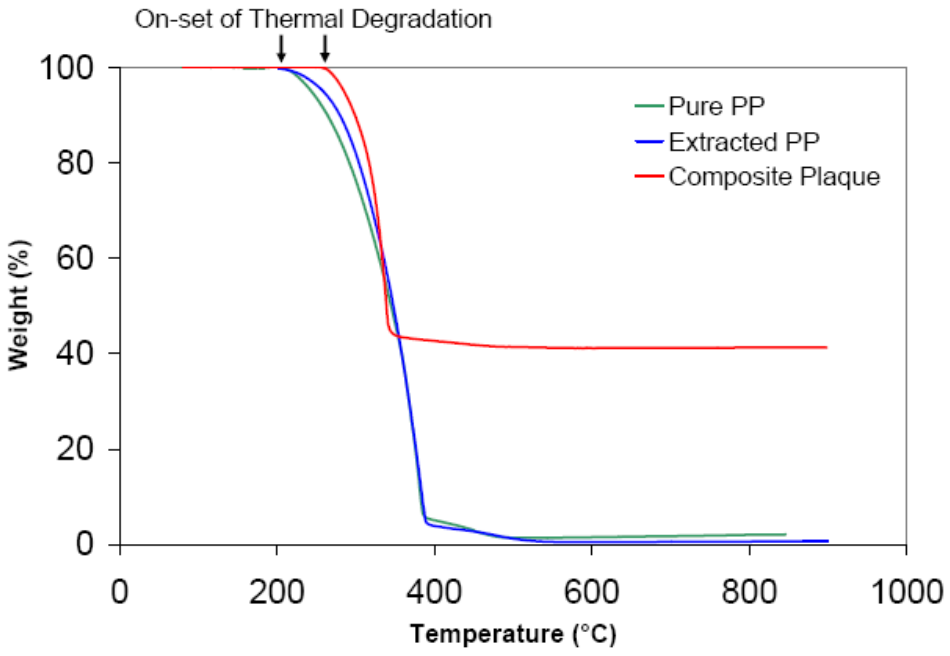

Figure 4-31: TGA data for samples in different forms.

Figure 4-31 also shows the weight drop profile for the extracted polypropylene sample. The extracted sample has an onset of the weight percentage drop which happens sooner than the composite plaque, and the extracted sample has burned off completely at about 400 °C. In order to confirm if the additives have been removed from the extraction process, TGA was also conducted to a known pure polypropylene sample for comparison. The resulting profile of the extracted polypropylene sample was almost identical to that of a known pure polypropylene sample - this verified that the extraction process removed nearly all of the stabilizer additives in the composite.

4.2.2 Wide Angle X-ray Scattering Results

The sample preparation procedures have been discussed in section 3.3.1. Table 4-4 describes the nomenclatures of the prepared samples for the study in crystallinity and thermal aging.

Table 4-4: Nomenclatures for prepared samples.

Sample Form	Solidification Rate	Treatment	Nomenclature
As-Received Plaque		Unaged	AR
Extracted iPP Film	**(i)Controlled Cooled (10°C/min)**	Unaged	FC-new
		Aged at 90°C	FC-90
		Aged at 140°C	FC-140
	(ii)Quenched (Ice-water at 0°C)	Unaged	FQ-new
		Aged at 90°C	FQ-90
		Aged at 140°C	FQ-140

Before aging the samples, a preliminary study was undertaken to verify the significance of extracted polypropylene film samples (FC and FQ) as a representative sample of the as-received molded composite plaque (AR). As seen in Figure 4-32, the peak locations for both samples are very similar although the as-received composite shows a small trace of the pseudo-hexagonal β-phase crystals which may be developed by compression molding due to the applied stress during crystallization [52]. The calculated crystallinity level of the composite plaque is 35% which is lower than the extracted films in the range of 45 to 48%.

Smectic phase polypropylene is a morphology between amorphous and crystalline phases [53]. It is formed when the sample is quenched at a relatively high cooling rate according to the X-ray observations of smectic phase by Ferrer-Balas *et al.* [54]. It is interesting that the smectic phase crystal was not detected in either sample investigated here, even for the FQ sample with the cooling rate that was significantly faster than the FC sample. This may be explained by the presence of residual amounts of carbon black [47] in the film sample after extraction, as even a minor amount of carbon black has been known to increase the rates of nucleation and crystallization significantly in the polypropylene [55]. Our results also differ from the observations by Busfield *et al.* [35] who reported the formation of a smectic phase when chilling the extrudate at 9°C and there was no carbon black additive in that work. DSC analysis, shown in the section 4.2.4, performed on our samples confirmed our WAXS results. It is reasonable then to assume that any changes during aging did not result from the smectic phase.

In Figure 4-32, the monoclinic α-phase crystals are clearly identified at 2θ = 13.9°, 16.6° 18.2° as well as the split peaks at 21.1° and 21.9° for both the FC and FQ samples. Moreover, there are no traces of either the β- and γ- phase crystals in the WAXS pattern in FC or FQ, infers that the monoclinic α-phase crystals are the dominant population. It can be seen in Figure 4-32 that the FQ sample resulted in lower initial crystallinity compared to the FC sample due to the larger area of the amorphous-halo. This is illustrated more clearly in Figure 4-33 for the FC samples aged at different temperatures, where the amorphous-halos are reduced significantly when aging at higher temperatures. The crystallinity for the controlled cooled and quenched samples were found to be 45% and 48%, respectively.

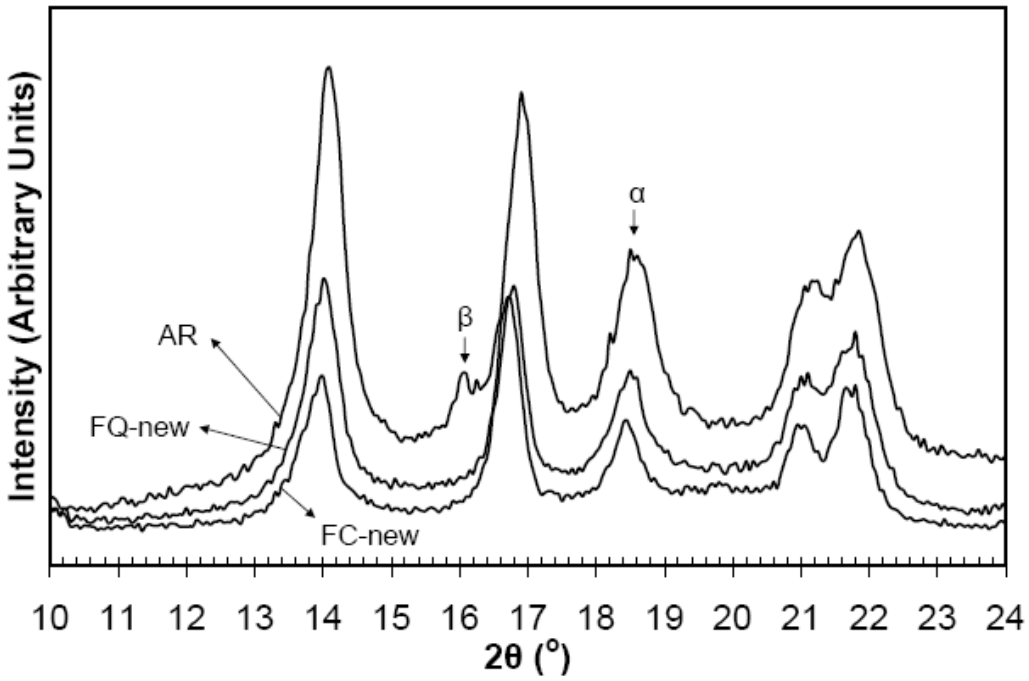

Figure 4-32: Comparison of WAXS patterns of extracted films and composite plaque.

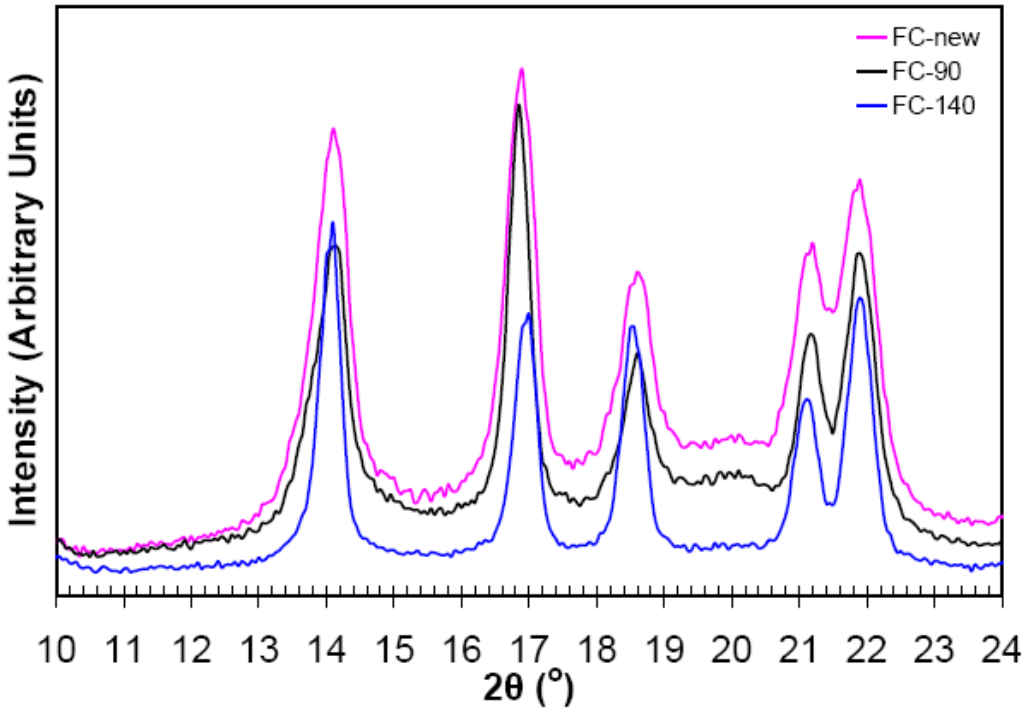

Figure 4-33: WAXS patterns for controlled cooled films (FC) in unaged and aged conditions.

Aside from the x-ray diffraction pattern of the smectic phase showed by Ferrer-Balas *et al.* [54], the split peaks at 2θ = 21.1° and 21.9° were less pronounced in the FQ sample. This is possibly due to freezing of the molecular chains as there was insufficient time to rearrange into proper α-phase crystals. This can be seen in Figure 4-34 for the FQ sample where the split peaks (indicated by an arrow) are more defined after aging at 140°C. For the sample aged at 90°C, however, did not show the presence of split peaks.

As shown in Table 4-5, aging at 140°C significantly increased the crystallinity of iPP regardless of the initial morphological state. It is also clear that aging at 90°C had a smaller effect on the crystallinity levels, with the increase in the FQ samples were slightly higher detected by WAXS.

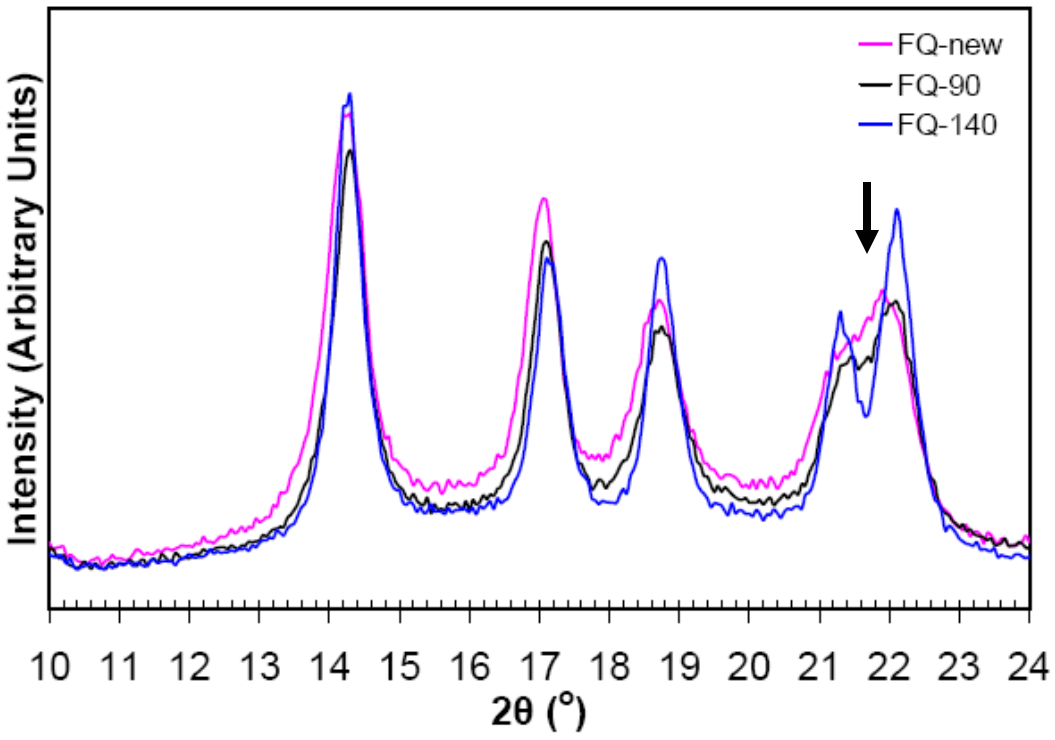

Figure 4-34: WAXS patterns for quenched films (FQ) in unaged and aged conditions.

Table 4-5: Crystallinity levels determined from WAXS.

	Unaged (%)	90°C Aged (%)	140°C Aged (%)
FC	48 ± 1	47 ± 1	58 ± 6
FQ	45 ± 1	50 ± 5	59 ± 10

4.2.3 Fourier Transform Infrared Spectroscopy Results

4.2.3.1 Evolution of FTIR Spectrum due to Aging

Progressive scanning using FTIR is a convenient non-destructive evaluation of the microstructural evolution during the aging process. When the sample is analyzed while mounted onto the heating stage for aging study, the progression of crystallinity changes and formation of oxidation products are captured *in-situ*. Figure 4-35 shows the full spectrum of the iPP material (FC-140 sample), with the evolutions of the oxidation products and crystallinity regions for 12 days of aging. For clearer illustration, Figure 4-36 shows the difference of the spectrum between the virgin and 12 days aged FC-140 sample. Table 4-6 shows the peak assignments [43, 56] that will be needed in this study.

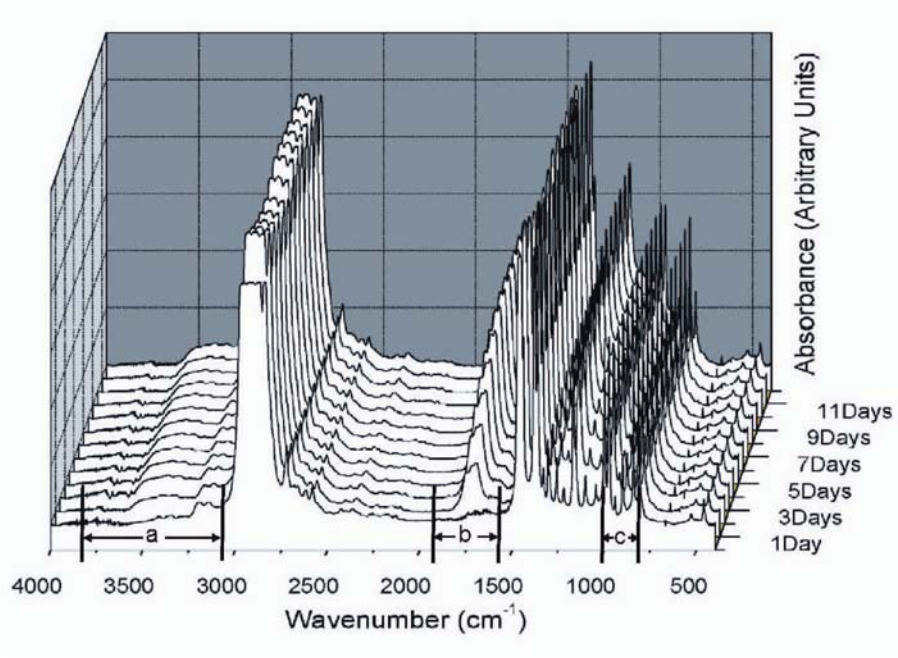

Figure 4-35: The evolution of FTIR spectra for FC-140 sample over the course of aging in 3D view with: a) region for hydroxyl group; b) region for carbonyl group; and c) region for crystallinity.

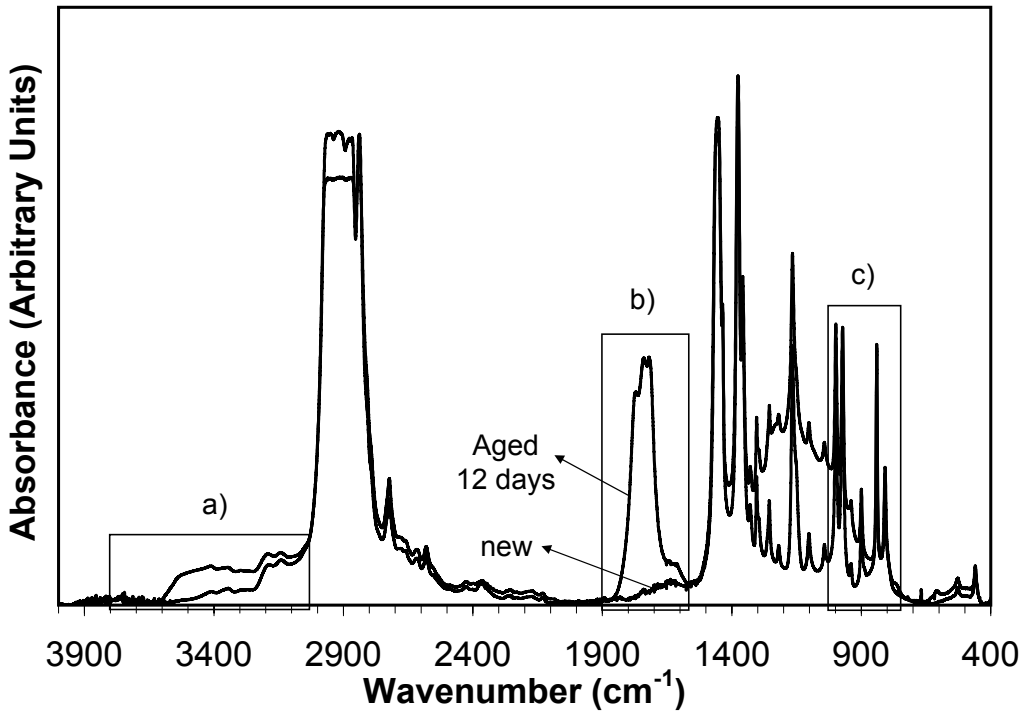

Figure 4-36: FTIR spectra for new and aged FC-140 specimen with :a) region for hydroxyl group; b) region for carbonyl group; and c) region for crystallinity.

Table 4-6: FTIR absorbance peak assignments.

Wavenumber (cm^{-1})	Vibrational Modes and Microstructure
3800-3050	Range for hydroxyl functional groups [43]
1900-1600	Range for carbonyl functional groups [43]
1646	C=C, vinyl groups [41]
1638	C=C, vinyl groups [41]
997	C-C stretching, CH_2, CH_3 rocking, helical (α crystalline) [56]
973	C-C stretching, CH_2, CH_3 rocking, amorphous [56]
841	C-C stretching, CH_2, CH_3 rocking, helical (α crystalline and mesophase) [56]

As seen in other reports [5, 38, 57], the crystallinity of iPP is determined from FTIR absorbance ratio. This ratio is calculated using the peaks in the region between 800 and

1050 cm^{-1} as shown in Figure 4-37. This figure contains the same data as in Figure 4-35. For sake of simplicity, the spectra of the new sample and the aged sample at 12 days, along with the other peaks in between, are shown in Figure 4-37. The bands at 997cm^{-1} and 841cm^{-1}, due to C-C stretching and CH_2, CH_3 rocking [56], was used for calculation of a ratio that can be correlated with crystallinity.

In this study, the crystallinity indices are plotted as a function of time in Figures 4-38 and 4-39 for films aged at 90 and 140°C, respectively. The results clearly show the crystallinity levels increasing for both aging temperature and morphologies. When aging at 140°C, the crystallinity level reached a plateau after 6 days. However, when aging at 90°C, it took at least 12 days to reach saturation and the changes are relatively smaller when compared to the overall crystallinity of the samples.

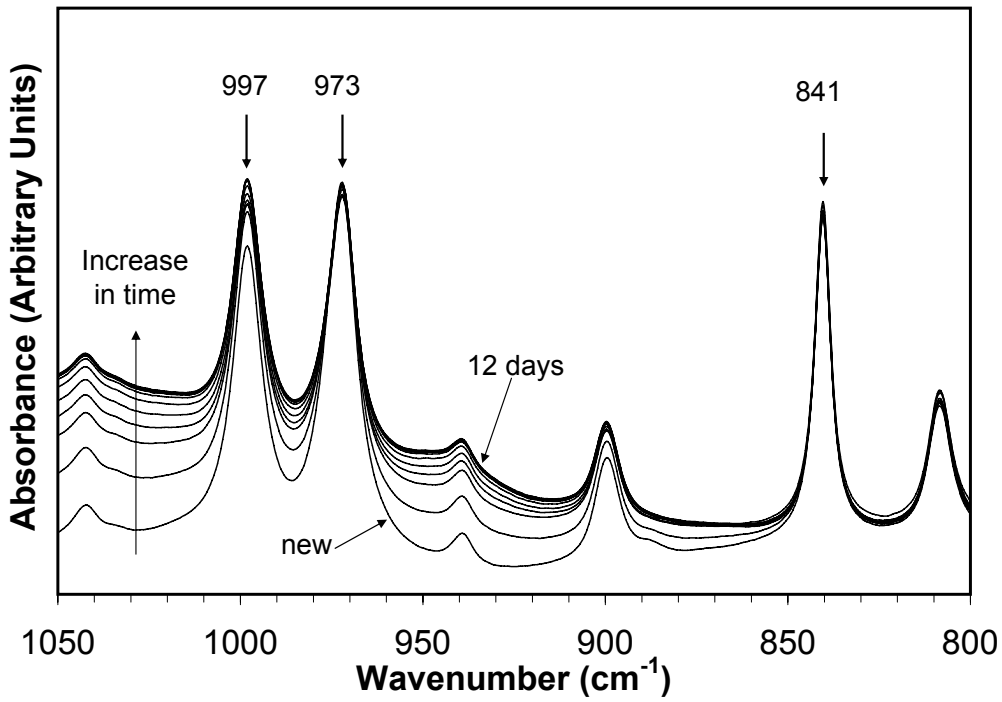

Figure 4-37: FTIR spectra of the crystallinity region (referred to in Figure 4-36c) for FC-140 aged for 12 days.

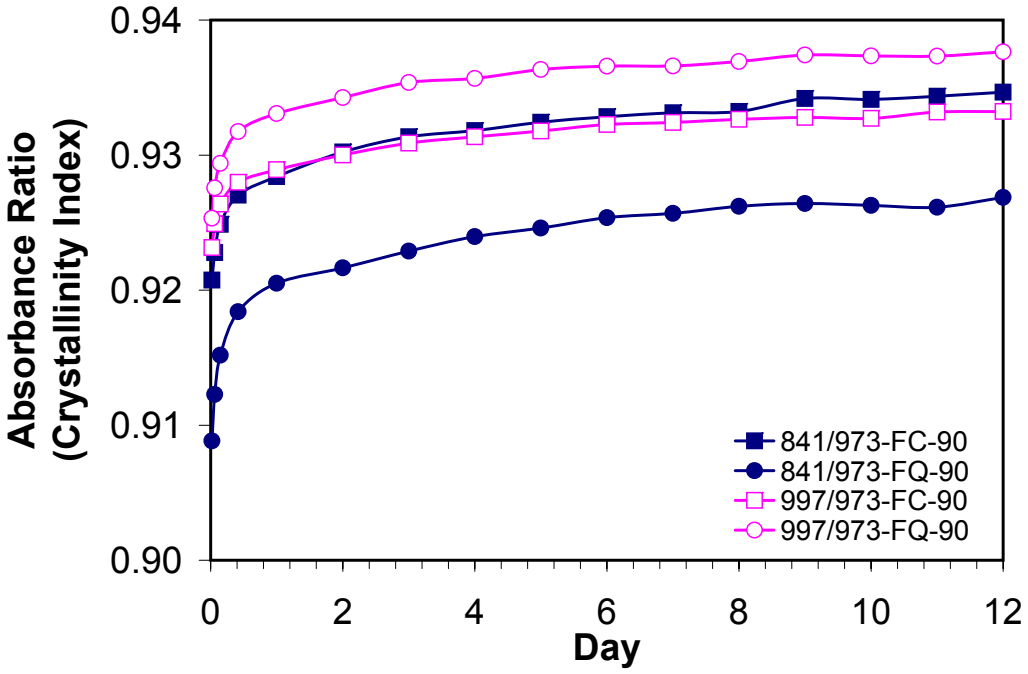

Figure 4-38: Progressive crystallinity index change at 90°C for 12 days.

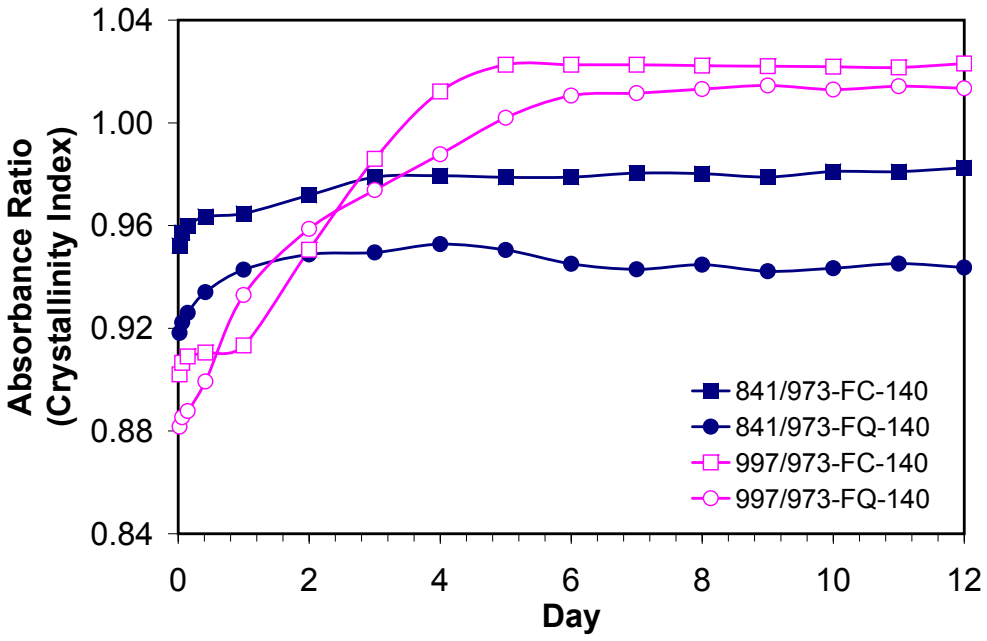

Figure 4-39: Progressive crystallinity index change at 140°C for 12 days.

In Figures 4-38 and 4-39, the two common approaches for determining crystallinity have been plotted namely, the absorbance ratios A_{997}/A_{973} [38, 57] and A_{841}/A_{973} [5]. The absorbance peak at 973 cm^{-1} is reported as the internal standard by Tadokoro *et al.* [58] as its intensity is relatively stable during the aging period and insensitive to the amorphous/crystalline structure change, as seen in Figure 4-37. Both ratios tend to be equally sensitive to 90°C aging detection. However, crystallinity increases when aging at 140°C was better detected using the A_{997}/A_{973} ratio due to the peak at 997 cm^{-1}, corresponding to the vibration of the helical structure of the α-phase crystalline as described in Table 4-6. The peak at 997 cm^{-1} grows progressively with aging compared to the peak at 841 cm^{-1} which is relatively stable throughout the aging period, as seen in Figure 4-37. The ratio of A_{997}/A_{973} is therefore more sensitive for detecting aging effects in iPP at elevated temperature. This is also verified by the present WAXS results that showed an increase of crystallinity after aging at both temperatures.

4.2.3.2 Oxidation Products Detection

There have been reports of severe oxidation in the iPP after aging at temperatures lower than 140°C [43]. Oxidative degradation is very much dependent on the composition of the polypropylene samples since additives such as anti-oxidants or stabilizers, where can dramatically reduce oxidation at high temperature. Figures 4-40 and 4-41 show the development of the functional groups, specifically carbonyl and hydroxyl, due to oxidation over the course of aging at 90 and 140°C for 12 days. No oxidation products were found in the sample aged at 90°C. The development of carbonyl groups at 140°C is more severe compared to the hydroxyl groups, where the carbonyl concentration increased up to 6 days of aging. The hydroxyl group concentration flattened after 2 days of aging. It was also observed that FQ samples aged at 90 and 140°C for 12 days exhibited similar behaviour as the FC samples.

FTIR spectroscopy can also detect the presence of vinyl groups (C=C bonds) formation corresponding to thermal degradation. This process is different from chain scission due to oxidation. Rjeb *et al.* [41] reported that vinyl groups appeared in 1646 and 1638 cm^{-1} for

polypropylene samples. However, there are no traces of chain scission due to formation of the vinyl groups over the course of aging shown in the FTIR spectra reported here.

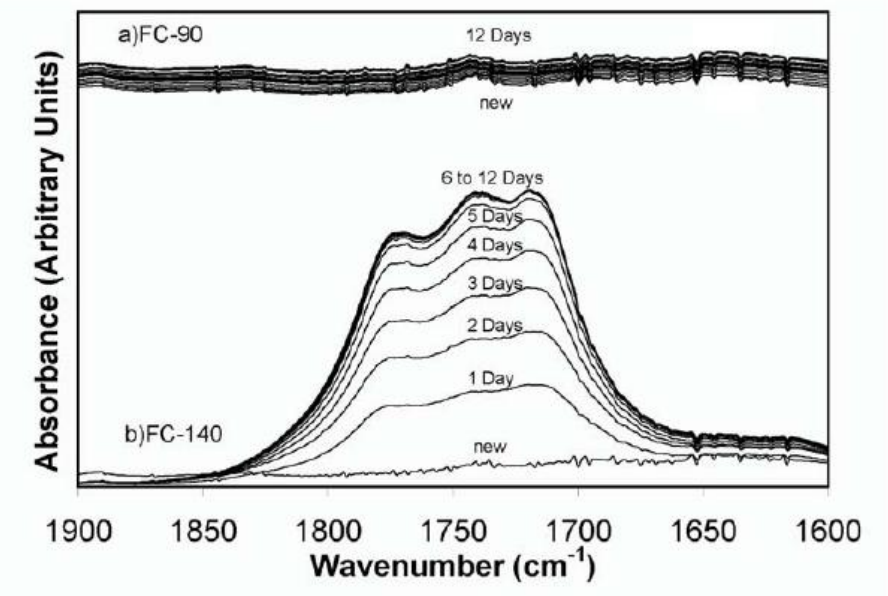

Figure 4-40: Progressive scanning of the carbonyl groups aging 12 days for: a)FC-90; and b) FC-140 samples (referred to in Figure 4-36b).

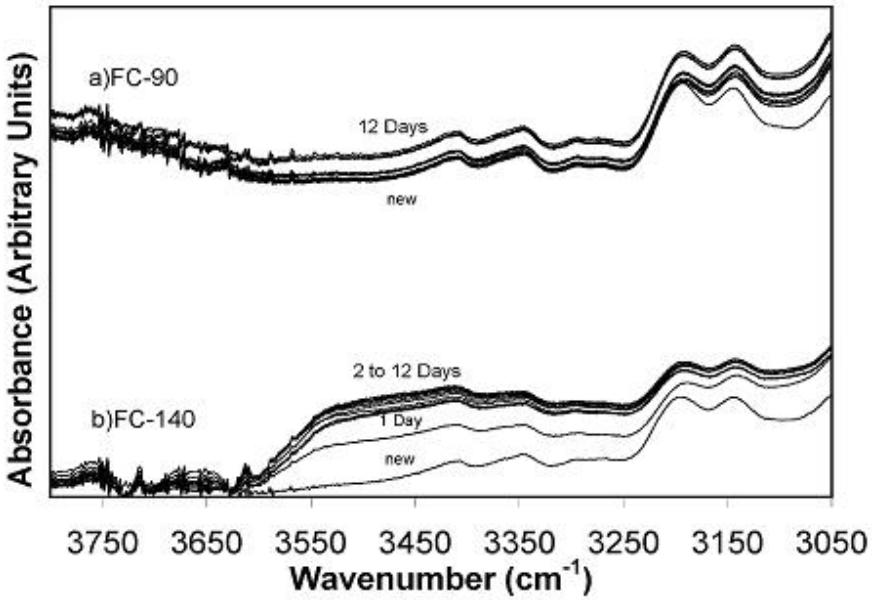

Figure 4-41: Progressive scanning of the hydroxyl groups aging 12 days for: a)FC-90; and b) FC-140 samples (referred to in Figure 4-36a).

4.2.4 Differential Scanning Calorimetry Results

4.2.4.1 Changes in Crystallinity and Melting Behaviour

Differential Scanning Calorimetry (DSC) was conducted to measure the glass transition temperature, onset and melting temperature and the degree of crystallinity. The enthalpy calculated from the heat flow profile can also be used to determine the crystallinity level changes between the unaged and aged samples. However, due to high scatter in the experiments, the data recorded from DSC was treated as supportive data for trend observations only.

Figure 4-42 shows the DSC curves for FC and FQ samples prior to thermal aging. The heat flow profile of the FQ sample shows an extra shoulder combined with the melting peak, which maybe due to the rapid quenching of the sample in ice-water. The fast cooling rate solidified the samples instantly, providing insufficient nucleation time and growth for all the crystals to form a perfect lattice structure. The imperfect crystals melt at a lower temperature than the prefect crystals, resulting in a shoulder in the melting peak for the FQ sample. By comparing to the FC samples, the slower cooling rate allows more time for crystal nucleation and growth to occur, forming a more uniform crystal structure.

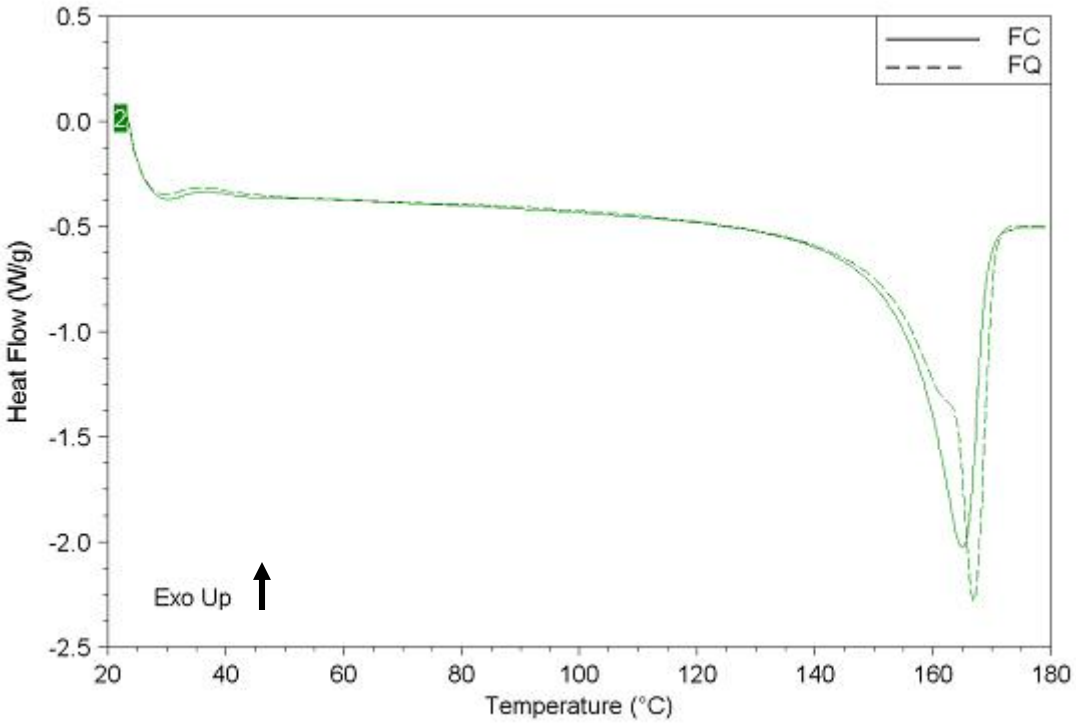

Figure 4-42: DSC data for unaged FC and FQ samples.

When the samples are undergoing thermal aging at elevated temperature, the heat energy introduces extra mobility of the chains. As the mobility of the chains increases during the aging process, the chains realign themselves from the amorphous phase to the crystalline structure. These phenomena are shown in Figures 4-43 and 4-44 for FC and FQ samples respectively.

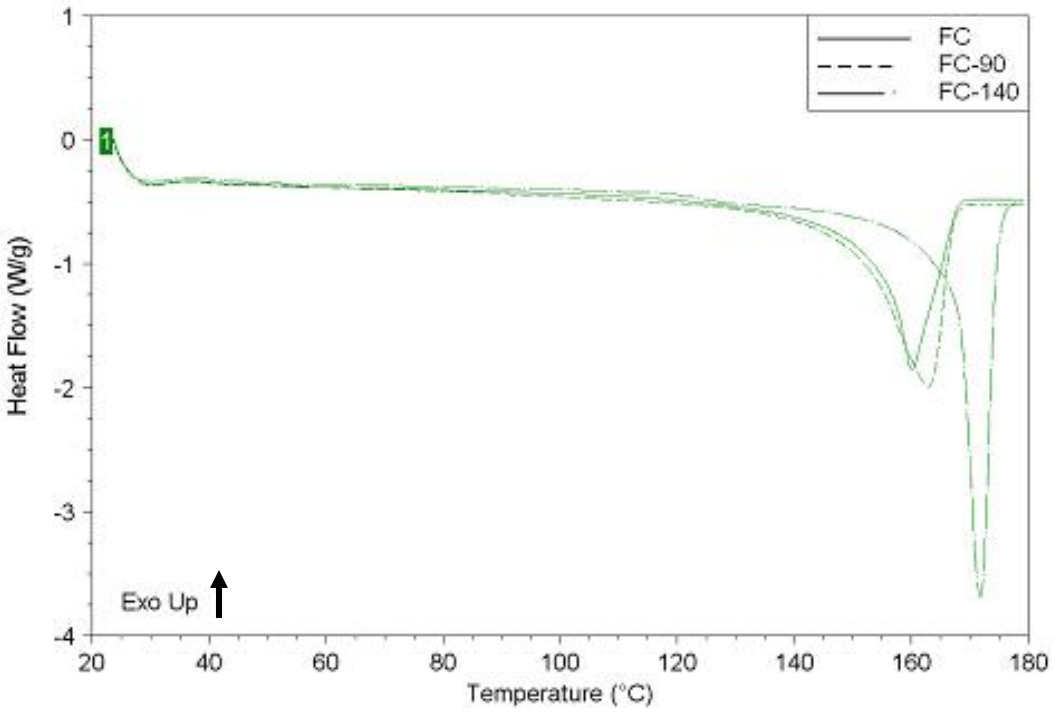

Figure 4-43: DSC data for unaged and aged FC samples.

In Figure 4-43 for the FC samples, the crystalline phase forms uniformly since there is sufficient time for nucleation and growth due to the slower cooling rate compared to FQ samples. There is only one type of crystalline population due to one melting peak appeared on the DSC curves. When the FC samples are aged at elevated temperature, increased chain mobility from the amorphous phase would fold itself into a crystalline structure, thus increasing the melting point of the samples as shown in Figure 4-43.

When aging at a higher temperature such as 140 °C, oxidation induced chain scission, proven from the FTIR analysis in the previous section, results in shorter chains with increased mobility compared to the longer chains. The heat flow profile for aging at 140 °C in Figure 4-43 shows a steeper melting peak with a highly uniform crystalline structure with an even higher melting point.

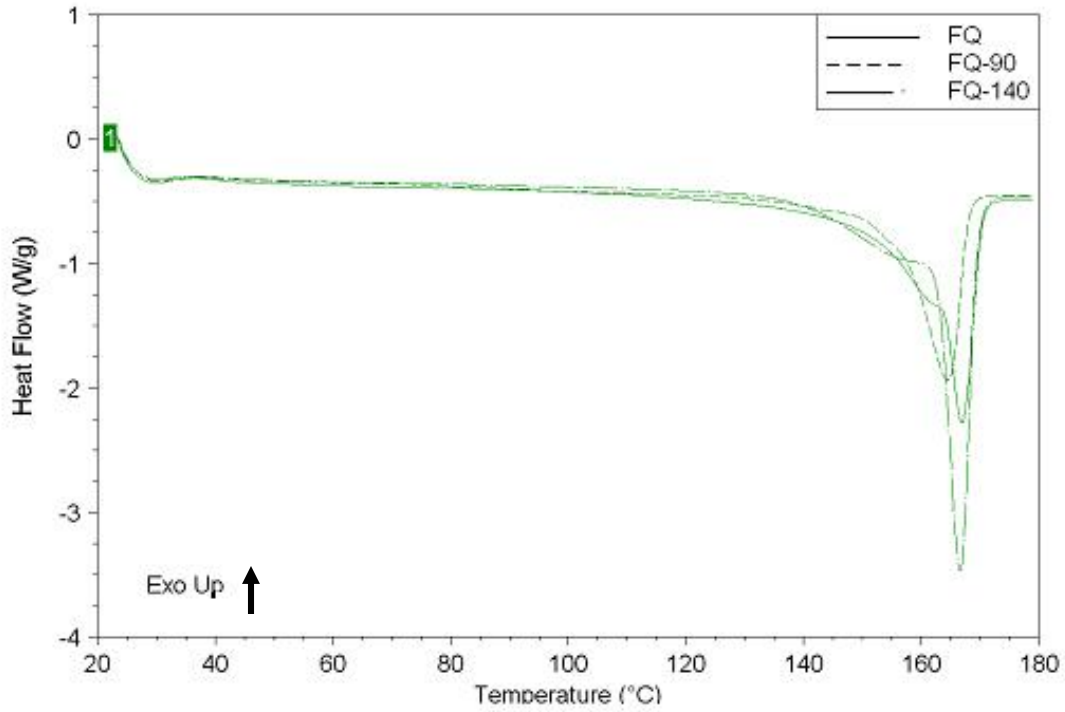

Figure 4-44: DSC data for unaged and aged FQ samples.

Figure 4-44 shows the DSC heat flow profiles for FQ samples with different aging conditions. Similar trends were observed from the FC samples in Figure 4-43 with slight differences. The crystallinity level increased over the course of aging for all aging conditions, but the melting points of the samples were in the same range.

By comparing the heat flow profile of the FQ and FQ-90 samples, the shoulder of the melting peak in the FQ-90 sample is smaller since aging at 90 °C provides increased chain mobility. This results in folding of the chains into more a uniform crystal lattice, similar to the situation in the FC samples.

It is important to point out that chain scission due to oxidation did not happen when aging at 90 °C, confirmed by FTIR analysis. While aging the FQ sample at 140 °C, due to the high temperature, oxidation chain scission happened more rapidly as the shorter chains folded into both the perfect as well as the imperfect crystalline phases. Therefore, the heat flow profile for FQ-140 in Figure 4-44 shows a discrete shoulder combined in the

melting peak implying another form of crystal population growth as well as the perfect crystals during aging at 140 °C.

Table 4-7 shows the crystallinity level measured from DSC with average of 3 measurements of each experiment. Crystallinity of the samples was increased by varying amount with subsequent aging. There was a slight increase in crystallinity for aging at 90 °C but a more significant increase for aging at 140 °C due to oxidative chain scission.

Table 4-7: Crystallinity levels determined from DSC.

	Unaged (%)	90°C Aged (%)	140°C Aged (%)
FC	69±3	76±1	84±3
FQ	67±5	62±1	76±6

Table 4-8 shows the melting and onset temperatures determined from the melting peak profile of the samples. ΔT is determined from the difference between the onset and melting temperatures. The lower the value of ΔT, the greater the uniformity in the crystal structure [59]. As mentioned before, the melting temperature increased for both FC and FQ samples over the course of aging due to increased chain mobility to fold into more a uniform crystal structure. The values for ΔT are similar for both FC and FQ samples aged at 90 °C, and changed significantly at a higher aging temperature. The FC samples showed a significant reduction in ΔT due to shorter chains resulting from oxidative chain scission to fold into a single-type uniformity crystalline structure. The FQ samples contained smaller crystals due to rapid quenching could have grown with the shorter chains produced by chain scission (oxidation). The presence of crystal domains of different size lamellae was likely to have produced the broad melting transition observed in samples aged at 140 °C.

Table 4-8: Melting and Onset temperature determined from DSC.

		Unaged	90°C	140°C
FC	$T_{Melting}$ (°C)	163±2	162±2	171±1
	T_{Onset} (°C)	154±2	152±4	167±1
	ΔT (°C)	8	10	4
FQ	$T_{Melting}$ (°C)	165±2	165±0	168±1
	T_{Onset} (°C)	150±2	149±1	146±5
	ΔT (°C)	15	16	23

4.2.4.2 Detection of Glass Transition

Differential scanning calorimetry (DSC) analysis was conducted to determine the glass transition of the extracted samples instead. Although dynamic mechanical analysis (DMA) is the preferred technique to determine the glass transition temperature, the extracted samples were in the form of a thin film, making the DMA technique impossible.

It was necessary to perform the DSC experiment at a relative high heating rate in order to detect the glass transition temperature due to the sensitivity of the DSC. Different trials of heating rate were done and it was found that the heating rate of 40 °C/min was adequate to detect the glass transition temperature in the film of the extracted sample. For easier detection of the glass transition, it would be preferable to have the samples containing a significant amount of the amorphous phase with respect to the crystalline phase. Special treatments have been done to the samples prior to the DSC analysis in order to facilitate the measurements. The sample was placed in the DSC pan and equilibrated to 180 °C and hold for 5 minutes to erase the thermal history. In order to obtain a sample with high amorphous content, the sample was taken out from DSC after the holding time and quenched in the ice-water to suppress the nucleation and growth of the crystalline phase. The sample stayed in the ice cold bath for about 5 minutes, and then put back into the DSC stage at 0 °C for continuous cooling to sub- zero temperature

level at -70 °C. When the temperature level was settled at -70 °C, the samples were heat up again at a rate of 40 °C/min from -50 °C to above the melting point.

However, due to the ice-water quenching process and the sample pan not being completely dry when put back into the sample stage, contamination from water droplets on the sample pan were detected by the DSC as shown in Figure 4-45. The profile of the heat flow was overlapped by the polypropylene sample, as well as the melting behaviour of the water droplets at about 0°C range.

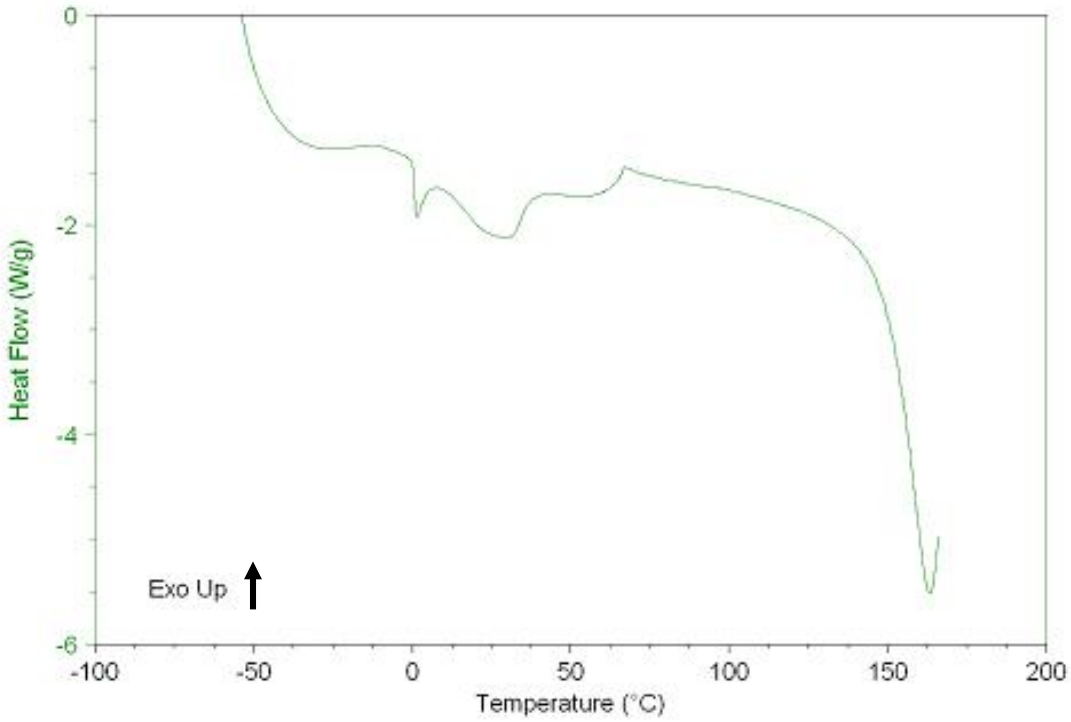

Figure 4-45: DSC data of sample with water contamination.

To overcome the contamination problem in the sample, quenching in the ice-water was replaced with cooling the sample with forced convection in a room temperature environment directly from melt. Although the cooling rate was not as fast as ice-water quenching, it gave a faster cooling rate compared to the controlled cooling that could be performed in the DSC stage.

Figure 4-46 shows the heat flow profile of the extracted sample measured from temperature range between -70 to 200 °C at 40 °C/min heating rate. To determine the glass transition temperature which happens at the shifting of the DSC curve, Figure 4-47 has plotted the change in slope of the enthalpy profile in Figure 4-46 as a function of time for better visualization. The glass transition temperature was measured by detecting the change in slope and was found at about 4 °C from the DSC analysis. This value was also obtained with DMA on the composite plaques samples in the range of 4 to 5 °C by other investigators in the laboratory [48,8].

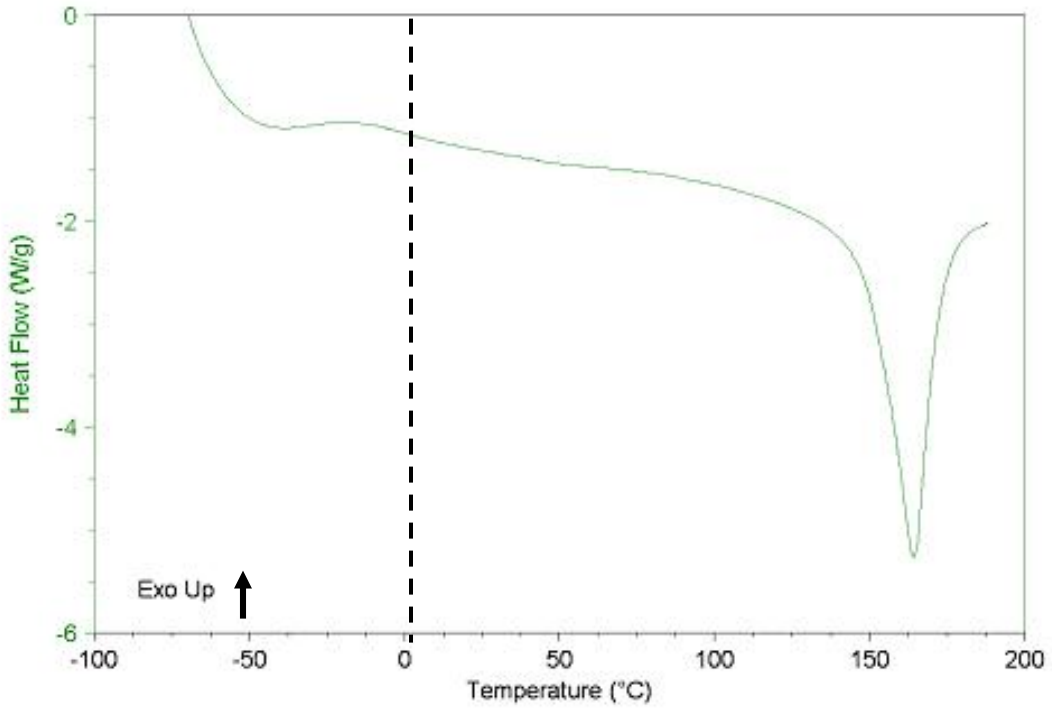

Figure 4-46: DSC data for determining glass transition temperature of the extracted pp sample.

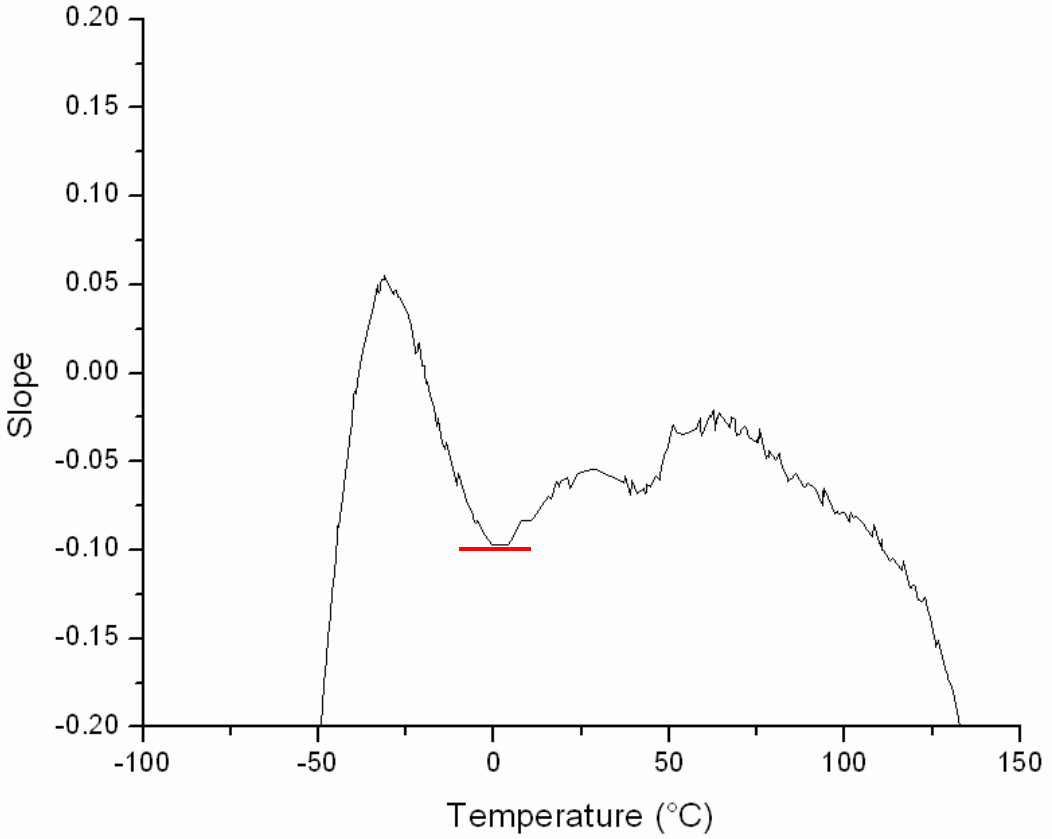

Figure 4-47: The derivative of the heat flow profile in Figure 4-46.

4.2.5 Kinetics of Thermal Aging

The effects of thermal aging on the rate of crystallinity can be quantified by the Avrami equation shown in eq. (8). The Avrami exponent depends on the type of nucleation and geometry of crystal growth, and it can also be an indicator of the ability of the materials to undergo secondary crystallization [3]. It is important to note that the slow and progressive changes of crystallinity in this study are due to thermal aging classified to be secondary crystallization, which can be interpreted in terms of an increase in lamellar thickness [60]. This process occurs without nucleation. Accordingly, the resulting Avrami exponents measured from secondary crystallization is significantly smaller compared to the primary crystallization where the material crystallized from molten state with nucleation.

The secondary crystallization process due to thermal aging was characterized using Avrami exponents, following the method used by Dudić *et al.* That group reported Avrami exponents were in the range about 3.5 to 7.0 × 10^{-2} when aged up to 3 days at 60°C for the polypropylene samples with different cooling rates and preparation processes [3].

The volumetric crystallinity (X_v) was obtained from FTIR measurements following the method used by Lamberti *et al.* [5]. The absorbance ratio was determined from the intensities of peak A_{997} and A_{973}. This ratio was calibrated with degree of crystallinity measured by DSC. Thus, the ratio A_{997}/A_{973} can be used to calculate the volumetric crystallinity since the density of the propylene crystal is constant. This can be correlated to Figure 4-38 and 39 of the crystallinity index measured from FTIR analysis.

By rearranging the Avrami equation (eq. (8)) to a linear form by using the law of logarithms, a plot of log $y = log(-Ln(1-X_v))$ as a function of $x = \log(t)$ in hour should allow determination of n, the Avrami exponent from the slope of the curve, according to equation $y = a + nx$.

Figure 4-48 shows the Avrami plot for aging at 90°C for 12 days, where the linear slopes represent the n value, the Avrami exponent. For aging at 90°C, the samples with different thermal histories showed a steady growth of crystallinity due to secondary crystallization. It is expected the FQ sample should have a higher n value (reported in Figure 4-48) compared to the slow cooling sample due to its higher amorphous content. When the Avrami exponent is less than unity, it implies that secondary crystallization occurred during the course of aging [61].

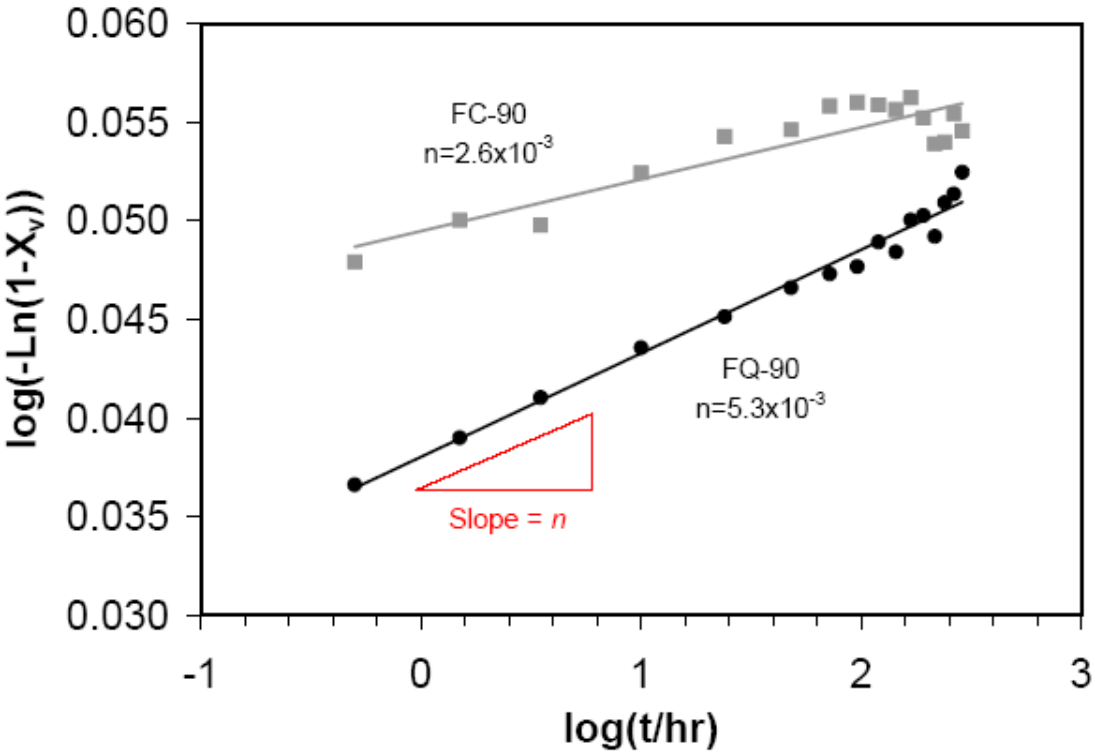

Figure 4-48: Avrami plot for aging at 90°C for 12 days (■ - FC; ● - FQ).

In contrast to Figure 4-48, Figure 4-49 shows the Avrami plot changed drastically for the samples aged at 140°C for 12 days. It is apparent that the kinetics of crystallization cannot be simply described by a single slope, commonly seen when applying the Avrami equation. The kinetics is represented by three stages, therefore resulting in three *n* values to describe crystallization upon long term aging at 140°C. At the initial stage, stage I, the samples undergo fairly slow secondary crystallization. After two days of aging, the crystallization rate increased dramatically. This is consistent with the observed FTIR patterns which showed oxidation at this time. The mechanism of oxidation involving formation of hydroxide or carbonyl groups also includes chain scission [3]. It is likely that oxidation occurred first in the amorphous domain instead of the crystalline domain. Therefore, chain scission in the amorphous domain would allow incremental mobility of certain chain segments leading to additional crystallization. The shorter chains free up entangled chains, thereby facilitating re-crystallization into other crystal forms [40].

The *n* value for FC sample in stage II is two orders of magnitude higher than at stage I, while the FQ sample increase is lower. In stage III, crystallization is complete as represented by negative slopes. This occurred after 6 days.

The study from Martynov and Valegzhanina [39] proposed that the competing processes of oxidation and secondary crystallization result in the termination of crystallization. The results in Figure 4-49 and the behaviour of crystallizations as characterized by the Avrami equation are consistent with the FTIR results shown in Figure 4-40b.

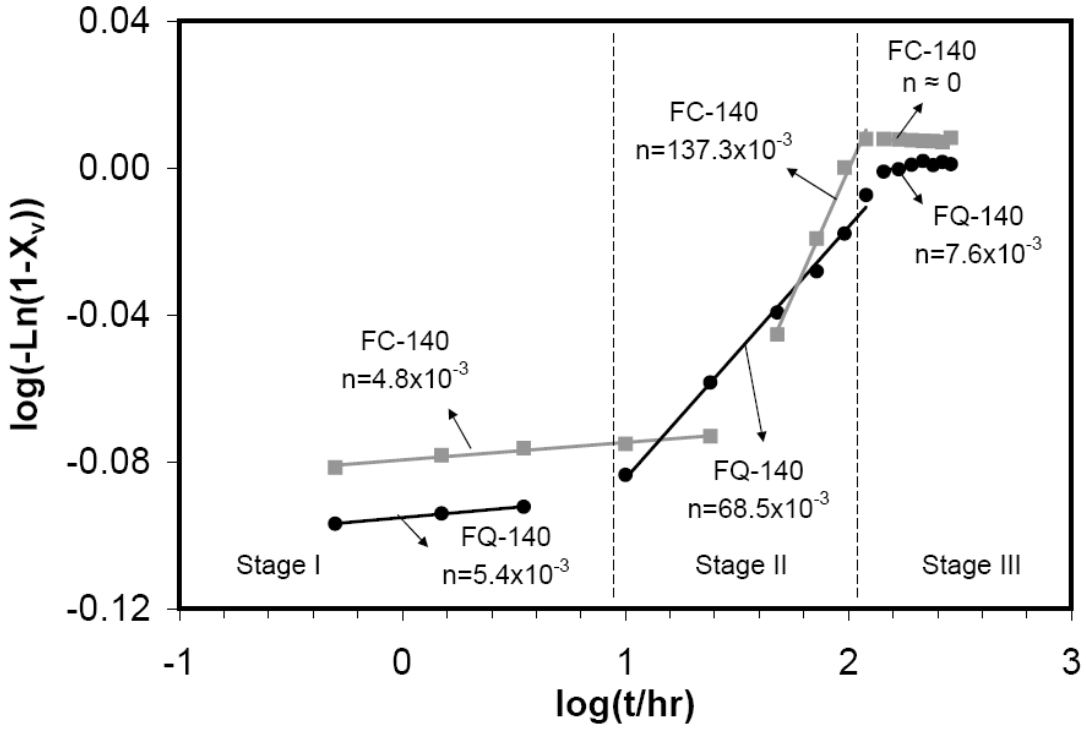

Figure 4-49: Avrami plot for aging at 140 °C for 12 days (■ - FC; ● - FQ).

It is important to note that the *n* values for samples aged at 90 °C reported in Figure 4-48, is of the same magnitude as stage I for samples aged at 140 °C, reported in Figure 4-49. This is strong evidence that the rate of secondary crystallization processes is similar regardless of the aging temperature as long as oxidation is negligible. Once oxidation commences, the rate of crystallization increased drastically, as seen from the *n* value changes between stages I and II for samples aged at 140 °C reported in Figure 4-49.

Another interesting observation in Figure 4-49 is the difference in profiles for samples with different thermal history. The onset of stage II for the FQ sample started earlier than the FC sample. This confirms that oxidation occurs more readily in the amorphous phase, which would be consistent with the results in Figures 4-40b and 4-41b in literature [36,62].

5.0 Conclusions

Based on creep testing of two types of glass-fibre mat composites, the following conclusions can be drawn:

- In comparing creep behaviour for tests performed at 33% and 67% ultimate tensile strength, the chopped fibre mat composite offers less resistance to creep than the long-fibre reinforced material at service temperature (80°C). This is due to matrix softening at the higher temperature since the creep rate for both materials is similar at room temperature. The higher resistance from the long-fibre mat is due to the tangled long fibre mat structure.

- The dominant failure mechanisms during the creep process are multiple matrix crack initiation and growth, and crack coalescence which leads to abrupt failure. *In-situ* micrographs show debonding upon first application of stress and followed by multiple matrix cracking. Debonding occurs at the fibre-matrix interface and matrix cracking is characterized by relatively short crack growth. The cracks developed during creep were transverse to the loading direction, and fibre breakage was minimal at all stress and temperature levels.

- Scanning electron microscopy shows a smooth fibre surface which indicates poor adhesion between the fibre and matrix phases. The poor adhesion is responsible for fibre debonding occuring extensively during secondary creep. Indentation marking on the matrix regions of all the samples did not show significant matrix shear yielding at the temperatures tested although the matrix elongation along the loading direction is evident.

In the work that characterized the thermal aging of films of polypropylene extracted from the chopped glass-fibre reinforced composite material, the following conclusions can be drawn:

- Thermal aging of the films for up to 12 days did not show any crystal phase transformation from WAXS measurements. Instead, the monoclinic α-phase was the dominant crystal population before and after aging. Crystallinity was found to increase upon aging at both 90 and 140°C by quantitative measurements using WAXS which clearly showed the amorphous-halo reducing in size after aging. *In-situ* scanning with FTIR showed an increase in crystallinity. At 140°C, however, the increased chain scission facilitated chain mobility resulting in higher crystallinity.

- The FTIR absorbance ratio A_{997}/A_{973} was a better indicator than A_{841}/A_{973} as it correlated well with the crystallinity changes of the iPP measured by WAXS. There was no trace of the formation of vinyl groups, when aging polypropylene at temperatures up to 140°C. This has been confirmed by *in-situ* scanning with FTIR.

- Avrami plots showed the temperature-dependence of the kinetics of secondary crystallization is not a simple relationship for the samples with different thermal histories studied. When aging at 90°C, the kinetics can be described by a single *n* value. However, at 140°C, there are three distinct stages where the second stage corresponds to significant oxidative chain scission which facilitated rapid secondary crystallization. This is consistent with the formation of oxidative products observed in FTIR. Before the onset of significant oxidation, the kinetics of secondary crystallization appears to be independent of the aging temperature.

References

1. L. A. Berglund and M. L. Ericson, *Glass Mat Reinforced Polypropylene. Ed.: J. Karger-Kocsis, in Polypropylene Structure, Blends and Composites Volume 3 - Composites,* Chapman & Hall, Cambridge (1995).
2. J. A. Brumann and N. Rauhupathi, *Azdel ® Composite Formable Fiber Reinforced Laminate. Ed.: A. K. Dhingra and R. B. Pipes in AIChE Symposium Series*, **78,** (217), 45 (1982).
3. D. Dudić, V. Djoković and D. Kostoski, *Polym. Test.,* **23,** 621 (2004).
4. K. Surya and N. Balaji, *Infrared Spectroscopy in Analysis of Polymer Crystallinity. Ed.: R. A. Meyers*, in Encyclopedia of Analytical Chemistry, John Wiley & Sons Ltd (2000).
5. G. Lamberti and V. Brucato, *J. Polym. Sci.: B Polym. Phy.,* **41,** 998 (2003).
6. T. H. Lee, F. Y. C. Boey and K. A. Khor, *Comp. Sci. Tech.*, **53,** 259 (1995).
7. E. P. Moore Jr., *Polypropylene Handbook*, Hanser Publisher, New York (1996).
8. P. Dasappa, *Constitutive modelling of creep in a low fibre random glass mat thermoplastic composite*, Master thesis, University of Waterloo, Waterloo (2006).
9. W. D. Callister, *Materials Science and Engineering – An Introduction*, John Wiley & Sons Inc., Toronto (1997).
10. E. Ségard, S. Benmedakhene, A. Laksimi and D. Laï, *Comp. Sci. Tech.*, **62**, 2029 (2002).
11. J. F. Shackelford, *Introduction to Materials Science for Engineers, section 6.5*, Pearson Prentice Hall, New Jersey (2005).
12. F. L. Matthews and R. D. Rawlings, *Composite materials: Engineering and science*, The Alden Press, Oxford (1999).
13. J. Hugo, M. Sova and J. Čižinský, *Comp. Struct.*, **24**, 133 (1993).
14. J. Lindhagen and L. Berglund, *J. App. Polym. Sci.*, **69**, 1319 (1998).
15. J. Karger-Kocsis, T. Harmia and T. Czigány, *Sci. Tech.*, **54**, 287 (1995).
16. M. Ericson and L. Berglund, *Comp. Sci. Tech.*, **43**, 269 (1992).
17. S. Zebarjad, R. Bagheri, S. Seyed Reihani and M. Forunchi, *J. App. Polym. Sci.*, **87**, 2171 (2003).

18. S. Zebarjad, *Materials and Design*, **24**, 531 (2003).
19. R. Zhao, X. Whou and G. Tai, *Polym. Comp.*, **23**, (6), 1026 (2002).
20. J. Matthews and D. Hay, *Acoustic Emission Evaluation in Acoustic Emission. Ed.: J Matthews*, Gordon and Breach Science Publishers, New York (1983).
21. E. Ségard, S. Benmedakhene, A. Laksimi and D. Laï, *Comp. Struct.*, **60**, 67 (2003).
22. W. Callister Jr., *Materials Science and Engineering An Introduction, section 16.8*, John Wiley & Sons Inc., Toronto (1996).
23. H. P, Frank, *Polypropylene*, Gordon and Breach, Science Publishers Inc., New York (1967).
24. F. P. T. J. van der Burgt, *Crystallization of isotactic polypropylene: The influence of stereo-defects*, Technische Universiteit Eindhoven, Eindhoven (2002).
25. *Comparative measurements of different types of carbon black with TGA*, ELASTOMER Volume **2**, Mettler-Toledo Collected Applications.
26. J. F. Shackelford, *Introduction to Materials Science for Engineers, section 3.7*, Pearson Prentice Hall, New Jersey (2005).
27. N. Alpert, W. Keiser and H Szymanski, *IR Theory and Practice of Infrared Spectroscopy*, Plenum Press, New York (1970).
28. R. Silverstein, G. Bassler and C. Morrill, *Spectrometric Identification of Organic Compounds, 5th ed*, John Wiley & Sons Inc., New York (1991).
29. F. Scheinmann, *An Introduction to Spectroscopic Methods for the Identification of Organic Compounds, Volume 1 – Nuclear Magnetic Resonance and Infrared Spectroscopy*, Pergamon Press Ltd, Oxford (1970).
30. TA Instruments manuals for MDSC-2920.
31. M. Lima, M. Zen Vasconcellos and D. Samios, *J. Polym. Sci. B Polym. Phys.,* **40**, 896 (2002).
32. J. E. Mark, *Polymer Data Handbook*, Oxford University Press, New York (1999).
33. H. Determann, *Gel chromatography – Gel Filtration, Gel Permeation and Molecular Sieves*, Springer-Verlag New York Inc., New York (1968).
34. Technical bulletin from Polymer Laboratories, http://www.polymerlabs.com, accessed on Nov 23, 2007.

35. W. K. Bursfield and C. S. Blake, *Polym.*, **21**, 35 (1980).
36. M. S. Rabello and J.R. White, *Polym.,* **38**, (26), 6379 (1997).
37. M. K. Agarwal and J. M. Schultz, *Polym. Eng. Sci.,* **21**, (12), 776 (1981).
38. M. J. Wyzgoski, *Appl. Polym. Sci.,* **26**, 1689 (1981).
39. M. A. Martynov, K. A. Valegzhanina, *Vysokomol. Soyed.,* **8**, (3), 376 (1966).
40. A. Larena, S. Jiménez de Ochoa and F. Domínguez, *Polym. Degrad. Stab.,* **91**, 940 (2006).
41. A. Rjeb, L. Tajounte, M. Chafik El Idrissi, S. Letarte, A. Adnot, D. Roy, Y. Claire, A. Périchaud and J. Kaloustian, *J. Appl. Polym. Sci.,* **77**, 1742 (2000).
42. A. B. Mathur and G. N. Mathur, *Polym.,* **23**, 54 (1982).
43. F. Gugumus, *Polym. Degrad. Stab.*, **62**, 235 (1998).
44. I. Groff, R. Franzese, L. D. Landro, M. R. Pagano and M. Genoni, *Polym. Test.*, **15**, 347 (1996).
45. J. Kotek, I. Kelnar, J. Baldrain and M. Raab, *European Polymer Journal*, **40**, 2731 (2004).
46. L. Guadagno, C. Fontanella, V. Vittoria and P. Longo, *J. Polym. Sci. B Polym. Phy.,* **37,** 173 (1999).
47. Private communication, Technical Center of Quadrant Plastics Composites, Germany (2007).
48. N. Zhou, *Constitutive modelling of creep in a short fibre random mat GMT Composite*, Master thesis, University of Waterloo, Waterloo (2006).
49. P. Dasappa, P. Lee-Sullivan, X. Xiao, P. Foss, *Tensile Creep of a Long-Fibre Glass Mat Thermoplastic (GMT) Composite Part I: Short-term tests,* submitted to *Polym. Comp.* under review.
50. Experimental data, courtesy of J. Mui, University of Waterloo, Waterloo (2006).
51. E. R. Thompson, *J. Comp. Mat.*, **5**, 235 (1971).
52. H. Dragaun, H. Hubeny and H. Muschik, *J. Polym. Sci. Polym. Phys.,* **15**, 1779 (1977).
53. G. Romano and R. Russo, *J. Marco. Sci. – Phys. B*, **37**, (6), 841 (1998).
54. D. Ferrer-Balas, M. L. Maspoch, A. B. Martinez and O. O. Santana, *Polym.*, **420**, 1697 (2001).

55. M. Mucha, J. Marszalek and A. Fidrych, *Polym*., **41**, 4137 (2000).
56. G. Parthasarthy, M. Sevegney and R. M. Kannan, *J. Polym. Sci. B Polym. Phys.*, **40**, 2539 (2002).
57. T. Huy, R. Adhikari, T. Lüpke, S. Henning and G. Michler, *J. Polym. Sci. B Polym. Phys.*, **42**, 4478 (2004).
58. H. Tadokoro, M. Kobayashi, M. Ukita, K. Yasufuku, S. Murahashi and T. Torii, *J. Chem. Phys.*, **4**, 1432 (1965).
59. C. Y. Yue and W. F. MSUYA, *J. of Materials Science Letters*, **9**, 985 (1990).
60. I. H. Hillier, *J. Polym. Sci. A*, **3**, 3067 (1965).
61. A. Peterlin, *Makromol. Chem.*, **74**, 107 (1964).
62. N. Kavafian, *J. Polym. Sci.*, **24**, 499 (1957).

Appendix A: Material Data Sheet

QUADRANT
PLASTIC COMPOSITES

Product Data Sheet

D100 F40 F1

D100 F40 F1 is a chopped fiber glass mat reinforced PP laminate with randomly oriented glass fibers. This product provides good flow properties, a very homogeneous fiber distribution and higher heat stabilization. It is commonly used for structural applications, like front-ends, seat back structures, door modules, battery trays, underbody shields and IP structures.

Properties		Standard	SI Units		Engl. Units	
Physical Properties						
Laminate Thickness*		Internal	4.8	mm	0.189	in
Area Weight*		Internal	5.8	kg/m^2	1.188	lb/ft^2
Fiber Content**		ISO 1172	40	%	40	%
Density (Laminate)*		ISO 1183	1.21	g/cm^3	0.0437	lb/in^3
Density (Molded)**		ISO 1183	1.22	g/cm^3	0.0441	lb/in^3
Mechanical Properties**						
Tensile Strength		ISO 527 / EN 13677	85	MPa	12329	psi
Tensile Elongation at Break		ISO 527 / EN 13677	2.5	%	2.5	%
Tensile Modulus		ISO 527 / EN 13677	5000	MPa	725	ksi
Flexural Strength		ISO 178 / EN 13677	140	MPa	20307	psi
Flexural Modulus		ISO 178 / EN 13677	5000	MPa	725	ksi
Impact Strength -	IZOD (4.0mm)	ISO 180/A	78	kJ/m^2	37	$ft*lb/in^2$
	IZOD (3.2mm)	ASTM D256 E	786	J/m	15	ft*lb(wt)/in
	Charpy (4.0mm)	ISO 179-1/2fn	85	kJ/m^2	40	$ft*lb/in^2$
Multiaxial Impact (4.0mm)						
Max. Load		ASTM D-3763	3423	N	770	lb(wt)
Energy @ Max. Load			17	J	13	ft*lb
Energy @ Failure			31	J	23	ft*lb
Max. Load		ISO 6603-2	5739	N	1280	lb(wt)
Energy @ Max. Load			16	J	12	ft*lb
Energy @ Failure			39	J	29	ft*lb
Processing Properties**						
Molding Shrinkage		ISO 2577	0.2 - 0.3	%	0.2 - 0.3	%
Special Properties**						
Heat Deflection Temperature		ISO 75-2	155	°C	311	°F
Coefficient of Thermal Expansion		EN ISO 11403-2	15 - 25	$10^{-6}/K$	15 - 25	$10^{-6}/K$
Burning Rate		ISO 3795 / FMVSS302	<10	mm/min	<0.4	in/min

1) - measured in longitudinal direction
2) - measured in transverse direction

* - Property was determined on the laminate
** - Property was determined on flat molded plaques

www.quadrantcomposites.com

Lenzburg, 04. August 2004

QUADRANT
PLASTIC COMPOSITES

Product Data Sheet

G100 F40 F6

G100 F40 F6 is a endless fiber glass mat reinforced PP laminate with randomly oriented glass fibers. This product provides good flow properties and low warpage tendency. It is commonly used for large semi-structural applications, like front-end, backrest.

Properties		Standard	SI Units		Engl. Units	
Physical Properties						
Laminate Thickness*		Internal	3.8	mm	0.150	in
Area Weight*		Internal	4.6	kg/m^2	0.942	lb/ft^2
Fiber Content**		ISO 1172	40	%	40	%
Density (Laminate)*		ISO 1183	1.21	g/cm^3	0.0437	lb/in^3
Density (Molded)**		ISO 1183	1.22	g/cm^3	0.0441	lb/in^3
Mechanical Properties**						
Tensile Strength		ISO 527 / EN 13677	75	MPa	10879	psi
Tensile Elongation at Break		ISO 527 / EN 13677	1.76	%	1.76	%
Tensile Modulus		ISO 527 / EN 13677	5780	MPa	838	ksi
Flexural Strength		ISO 178 / EN 13677	135	MPa	19582	psi
Flexural Modulus		ISO 178 / EN 13677	5775	MPa	838	ksi
Impact Strength -	IZOD (4.0mm)	ISO 180/A	64	kJ/m^2	30	ft*lb/in^2
	IZOD (3.2mm)	ASTM D256 E	650	J/m	12.18	ft*lb(wt)/in
	Charpy (4.0mm)	ISO 179-1/2fn	70	kJ/m^2	33	ft*lb/in^2
Multiaxial Impact (4.0mm)						
Max. Load		ASTM D-3763	3267	N	734	lb(wt)
Energy @ Max. Load			16	J	12	ft*lb
Energy @ Failure			27	J	20	ft*lb
Max. Load		ISO 6603-2	4811	N	1082	lb(wt)
Energy @ Max. Load			19	J	14	ft*lb
Energy @ Failure			43	J	32	ft*lb
Processing Properties**						
Molding Shrinkage		ISO 2577	0.15 - 0.25	%	0.15 - 0.25	%
Special Properties**						
Heat Deflection Temperature		ISO 75-2	155	°C	311	°F
Coefficient of Thermal Expansion		EN ISO 11403-2	25 - 28	10^{-6}/K	25 - 28	10^{-6}/K
Burning Rate		ISO 3795 / FMVSS302	3 - 4	mm/min	0.12-0.16	in/min

1) = measured in longitudinal direction
2) = measured in transverse direction

* = Property was determined on the laminate
** = Property was determined on flat molded plaques

Appendix B: Polishing Supply Details

Polishing Cloths / Poliertücher / Draps de polissage

All MD-Cloths are available in 200 mm dia., 250 mm dia. and 300 mm dia.
and all DP-/OP-Cloths are available in 200 mm dia., 250 mm dia., 300 mm dia. and 350 mm dia.

Alle MD-Tücher sind in 200 mm, 250 mm und 300 mm Durchmesser erhältlich.
Alle DP/OP-Tücher sind in 200 mm, 250 mm, 300 mm und 350 mm Durchmesser erhältlich.

Tous les draps MD sont disponibles en 200 mm de dia., 250 mm de dia. et 300 mm de dia. et tous les draps DP-/OP sont disponibles en 200 mm de dia., 250 mm de dia., 300 mm de dia. et 350 mm de dia.

Name Name Désig-nation	Composition Zusammensetzung Composition	Abrasive/Grain size Poliermittel/ Korngrösse Abrasif/Taille de grain	Application Anwendung Application
MD-Plan DP-Plan	Coated, woven polyester Gewebtes Polyester, beschichtet Toile polyester	Diamond / 15 - 3 µm Diamanten / 15 - 3 µm Diamant / 15 - 3 µm	Fine grinding of soft metals Pre-polishing of hard materials Feinschleifen weicher Metalle Vorpolieren von harten Materialien Prépolissage fin des métaux tendres Polissage grossier des matériaux durs
MD-Pan DP-Pan	Impregnated non-woven technical textile Nichtgewebtes technisches Textil, imprägniert Textile technique imprégné, non-tissé	Diamond / 15 - 3 µm Diamanten / 15 - 3 µm Diamant / 15 - 3 µm	Fine grinding of soft metals Pre-polishing of hard and brittle materials Feinschleifen weicher Metalle Vorpolieren von harten und spröden Materialien Prépolissage fin des métaux tendres Polissage grossier des matériaux durs et friables
MD-Dur DP-Dur	Satin woven natural silk Satingewebte Naturseide Soie naturelle tissée satin	Diamond / 15 - 1 µm Diamanten / 15 - 1 µm Diamant / 15 - 1 µm	Fine grinding and polishing of ferrous metals, non-ferrous metals, coatings and plastics Feinschleifen und Polieren von Eisen- und Nichteisenmetallen, Schichten und Kunststoffen Prépolissage fin et polissage des métaux ferreux, métaux non-ferreux, revêtements et plastiques
MD-Dac DP-Dac	Satin woven acetat Satingewebtes Azetat Acétate tissé satin	Diamond / 6 - 3 µm Diamanten / 6 - 3 µm Diamant / 6 - 3 µm	Universal polishing of all materials Universelles Poliertuch für alle Materialen Polissage universel de tous les matériaux
DP-Sat	Plain woven acetate Normal gewebtes Azetat Acétate normale-ment tissé	Diamond / 15 - 3 µm Diamanten / 15 - 3 µm Diamant / 15 - 3 µm	Fine grinding and polishing of ferrous metals, non-ferrous metals, coatings and plastics Feinschleifen und Polieren von Eisen- und Nichteisenmetallen, Schichten und Kunststoffen Prépolissage fin et polissage des métaux ferreux, métaux non-ferreux, revêtements et plastiques
MD-Mol DP-Mol	Taffeta woven 100% wool Taftgewebe, 100% Wolle Taffeta tissé 100% laine	Diamond / ≤ 3 µm Diamanten / ≤ 3 µm Diamant / ≤ 3 µm	Polishing of ferrous and non-ferrous metals and polymers Polieren von Eisen- und Nichteisenmetallen und Kunststoffen Polissage des métaux ferreux et non-ferreux et des polymères
OP-Nat	Woven wool felt Wollfilzgewebe Feutrine de laine tissée	Alumina / ≤ 9 µm Aluminiumoxid / ≤ 9µm Oxyde d'aluminium / ≤ 9µm	Polishing of ferrous metals Polieren von Eisenmetallen Polissage des métaux ferreux
OP-Felt	Thick felt Dicker Filz Feutrine épaisse	Alumina / ≤ 9 µm Aluminiumoxid / ≤ 9µm Oxyde d'aluminium / ≤ 9µm	Polishing of ferrous and non-ferrous metals Polieren von Eisen- und Nichteisenmetallen Polissage des métaux ferreux et non-ferreux
MD-Plus DP-Plus	Synthetic nap Synthetikflor Laine synthétique	Diamond / ≤ 3 µm Diamanten / ≤ 3 µm Diamant / ≤ 3 µm	One step polishing for sintered carbides and steels Einstufiges Polieren von Hartmetallen und Stählen Polissage en une étape des carbures frittés et des aciers
MD-Floc DP-Floc	Synthetic nap Synthetikflor Laine synthétique	Diamond, oxide polishing / ≤ 3 µm Diamanten, Oxidpolieren / ≤ 3 µm Diamant, polissage aux oxydes / ≤ 3 µm	Polishing of all materials Polieren aller Materialien Polissage de tous les matériaux
MD-Nap DP-Nap	Synthetic short nap Kurzer Synthetikflor Laine synthétique à poils raz	Diamond, oxide polishing / ≤ 1 µm Diamanten, Oxidpolieren / ≤ 1 µm Diamant, polissage aux oxydes / ≤ 1 µm	Final polishing of all materials Endpolieren aller Materialien Polissage final de tous les matériaux
OP-Chem MD-Chem	Porous neoprene Poröses Neopren Néoprène poreux	Oxide polishing / < 1µm Oxidpolieren / < 1 µm Polissage aux oxydes / <1 µm	Final polishing of all materials Endpolieren aller Materialien Polissage final de tous les matériaux

Struers

Struers A/S
Pederstrupvej 84
DK-2750 Ballerup, Denmark
Phone +45 44 600 800
Fax +45 44 600 801
struers@struers.dk

DEUTSCHLAND
Struers GmbH
Karl-Arnold-Strasse 13 B
D-47877 Willich
Telefon +49(02154) 486-0
Telefax +49(02154) 486-222
verkauf.struers@struers.de

ÖSTERREICH
Struers GmbH
Zweigniederlassung Österreich
Ginzkeyplatz 10
A-5020 Salzburg
Telefon +43 662 625 711
Telefax +43 662 625 711 78
stefan.lintschinger@struers.de

SCHWEIZ
Struers GmbH
Zweigniederlassung Schweiz
Weissenbrunnenstrasse 41
CH-8903 Birmensdorf
Telefon +41 44 777 63 07
Telefax +41 44 777 63 09
rudolf.weber@struers.de

CZECH REPUBLIC
Struers GmbH
Oceláŕská 799
CZ-190 00 Praha 9
Tel. +420 2 84 818 227
Fax +420 2 660 32 278
david.cernicky@struers.de

POLAND
Struers Sp. z o.o.
Oddział w Polsce
ul. Lirowa 27
PL-02-387 Warszawa
Tel. +48 22 824 52 80
Fax +48 22 882 06 43
grzegorz.uszynski@struers.de

HUNGARY
Struers GmbH
Magyarországi fióktelep
Puskás Tivadar u. 4
H-2040 Budaörs
Phone +36 (23) 428-742
Fax +36 (23) 428-741
zoltan.kiss@struers.de

SINGAPORE
Struers A/S
10 Eunos Road 8,
#12-06 North Lobby
Singapore Post Centre
Singapore 408600
Phone +65 6299 2268
Fax +65 6299 2661
struers.sg@struers.dk

THE NETHERLANDS
Struers GmbH Nederland
Electraweg 5
NL-3144 CB Maassluis
Tel. +31 (0) 10 599 72 09
Fax +31 (0) 10 599 72 01
glen.van.vugt@struers.de

FRANCE
Struers S.A.S.
370, rue du Marché Rollay
F- 94507 Champigny
sur Marne Cedex
Téléphone +33 1 5509 1430
Télécopie +33 1 5509 1449
struers@struers.fr

BELGIQUE
Struers S.A.S.
370, rue du Marché Rollay
F- 94507 Champigny
sur Marne Cedex
Téléphone +33 1 5509 1430
Télécopie +33 1 5509 1449
struers@struers.fr

USA and CANADA
Struers Inc.
24766 Detroit Road
Westlake, OH 44145-1598
Phone +1 440 871 0071
Fax +1 440 871 8188
info@struers.com

UNITED KINGDOM
Struers Ltd.
Erskine Ferry Road,
Old Kilpatrick
Glasgow, G60 5EU
Phone +44 1389 877 222
Fax +44 1389 877 600
info@struers.co.uk

JAPAN
Marumoto Struers K.K.
Takara 3rd Building
18-6, Higashi Ueno 1-chome
Taito-ku, Tokyo 110-0015,
Phone +81 3 5688 2914
Fax +81 3 5688 2927
struers@struers.co.jp

CHINA
Struers (Shanghai) Ltd.
Room 2705, Nanzheng Bldg.
580 Nanjing Road (W)
CN - Shanghai 200041
Phone +86 (21) 5228 8811
Fax +86 (21) 5228 8821
struers.cn@struers.dk

www.struers.com

01.05 / 40500063 (30 pcs) Printed in Denmark - 41

Appendix C: GPC Data Report

Table I.

Avg. Molecular Wt.

Sample ID	Run #	Mn	Avg.	Mw	Avg.	Mz	Avg.	Mw/Mn	Avg.
#1	1	46,046	46,321	108,622	108,631	186,918	186,564	2.36	2.35
	2	46,597		108,639		186,210		2.33	
#2	1	45,792	46,565	106,337	106,331	187,006	186,459	2.32	2.28
	2	47,337		106,325		185,911		2.25	
#3	1	40,697	41,390	102,280	102,376	179,370	179,283	2.51	2.47
	2	42,084		102,473		179,196		2.43	

Relative to polystyrene standards

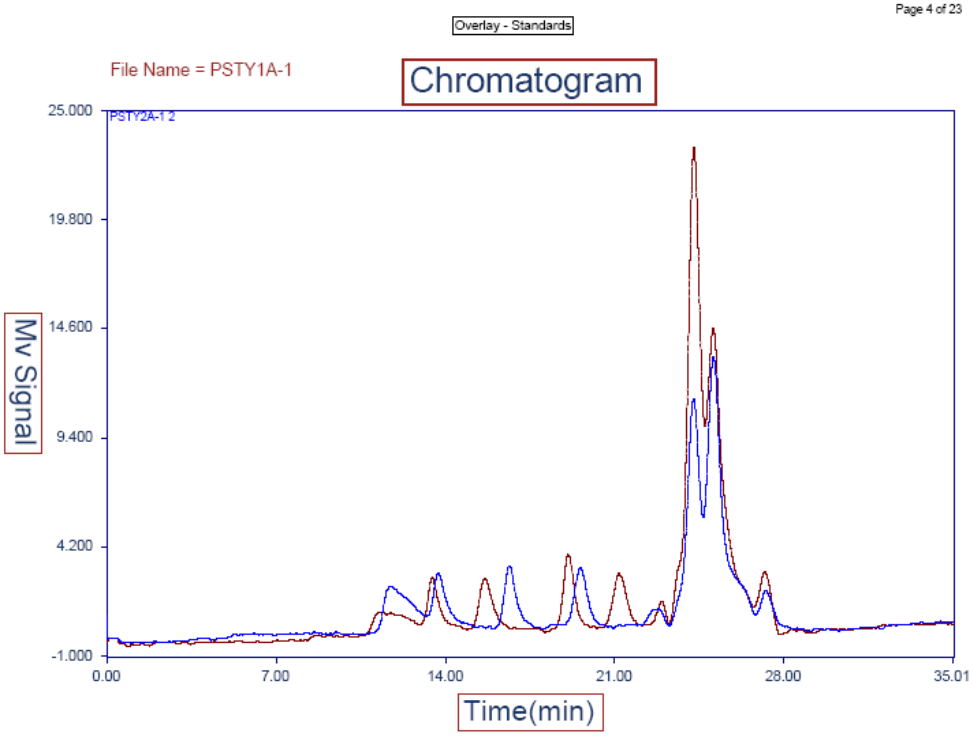

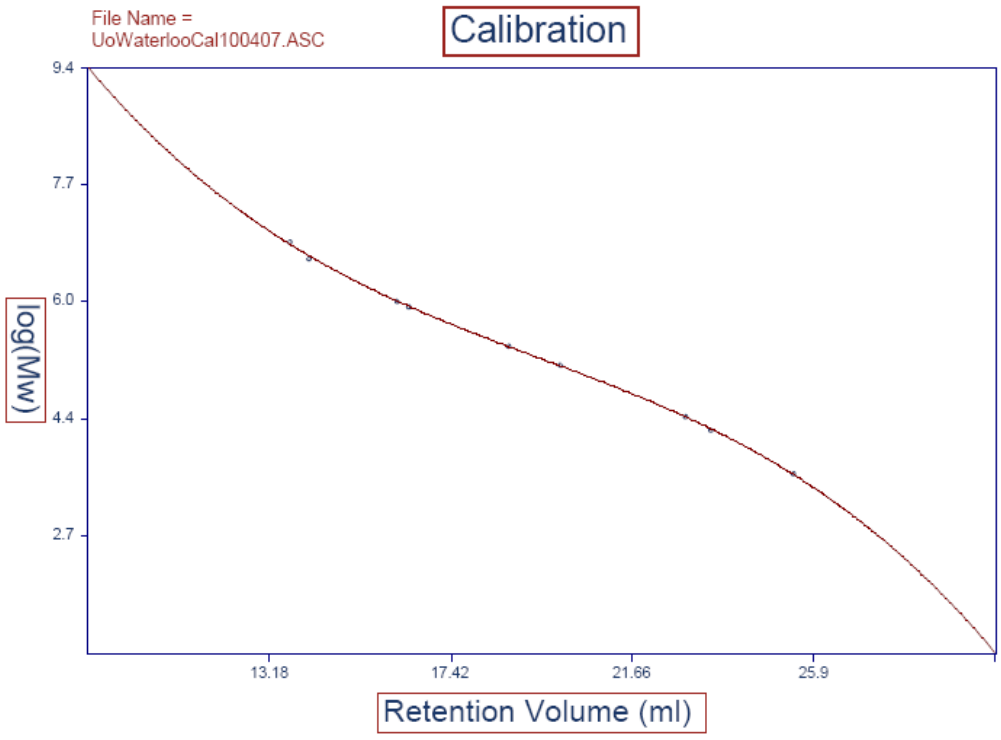
File Name =
UoWaterlooCal100407.ASC
Calibration
9.4
7.7
6.0
4.4
2.7
log(Mw)
13.18
17.42
21.66
25.9
Retention Volume (ml)

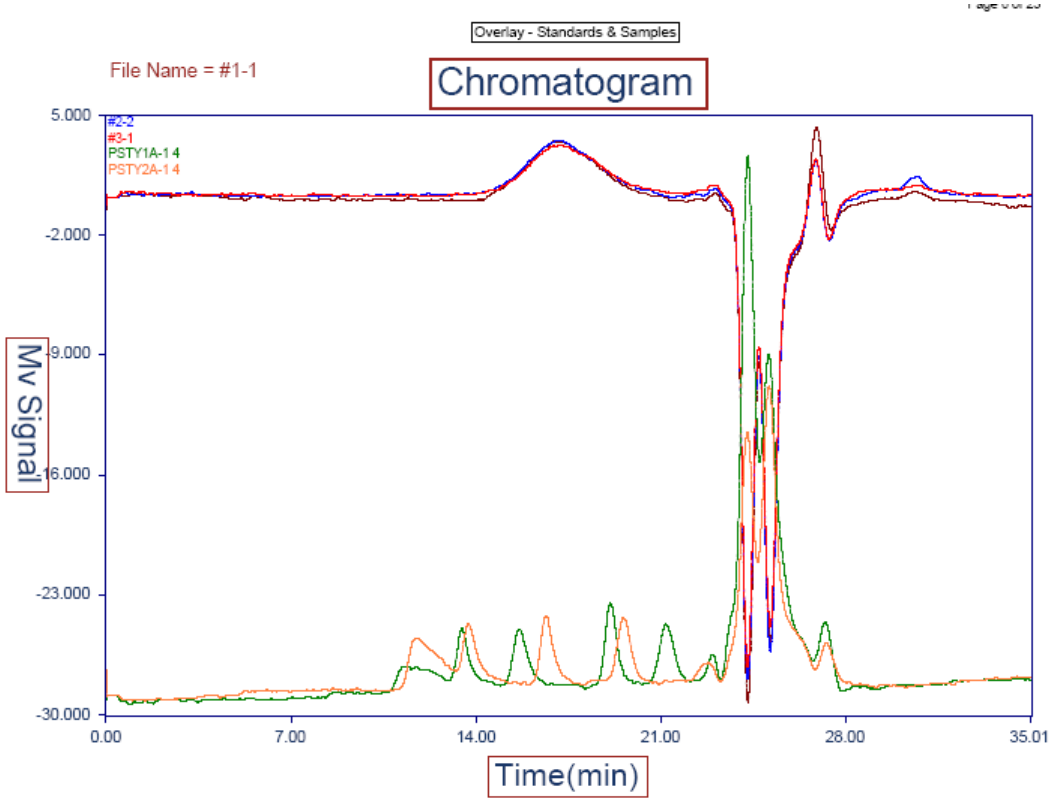
Overlay - Standards & Samples
File Name = #1-1
Chromatogram
#2-2
#3-1
PSTY1A-1 4
PSTY2A-1 4
5.000
-2.000
-9.000
-16.000
-23.000
-30.000
Mv Signal
0.00
7.00
14.00
21.00
28.00
35.01
Time(min)

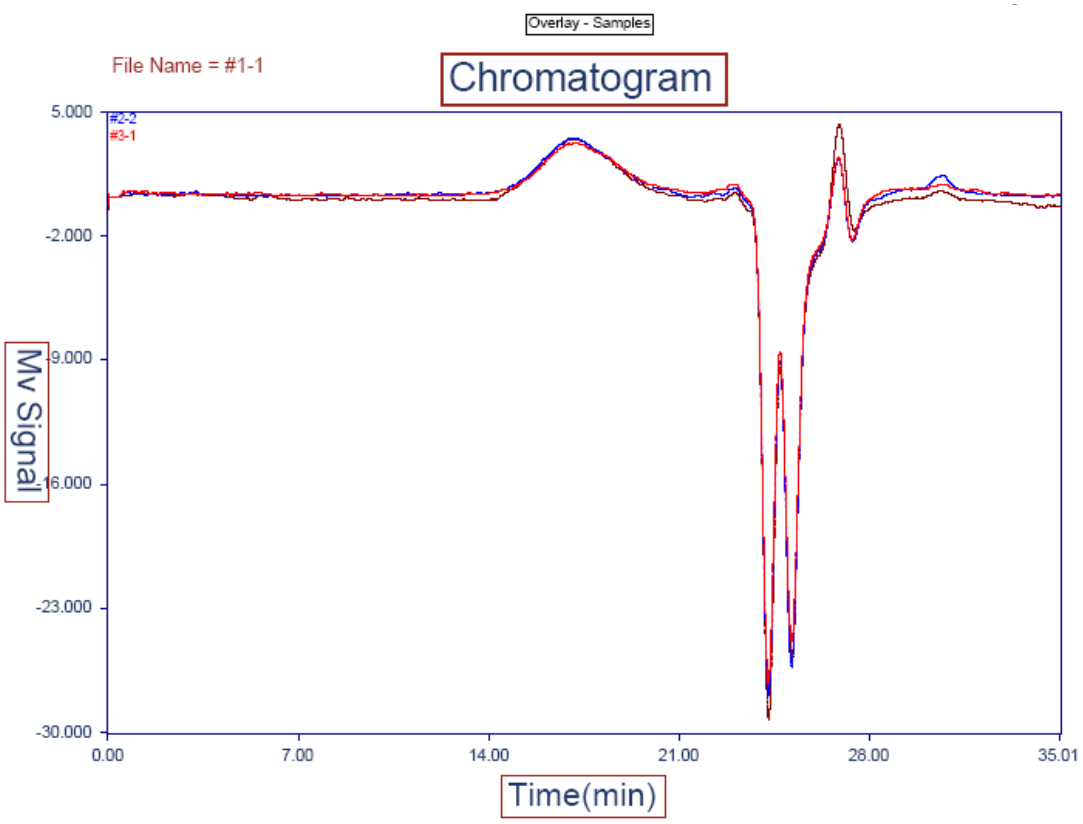
Overlay - Samples
File Name = #1-1
Chromatogram
#2-2
#3-1
5.000
-2.000
-9.000
-16.000
-23.000
-30.000
Mv Signal
0.00
7.00
14.00
21.00
28.00
35.01
Time(min)

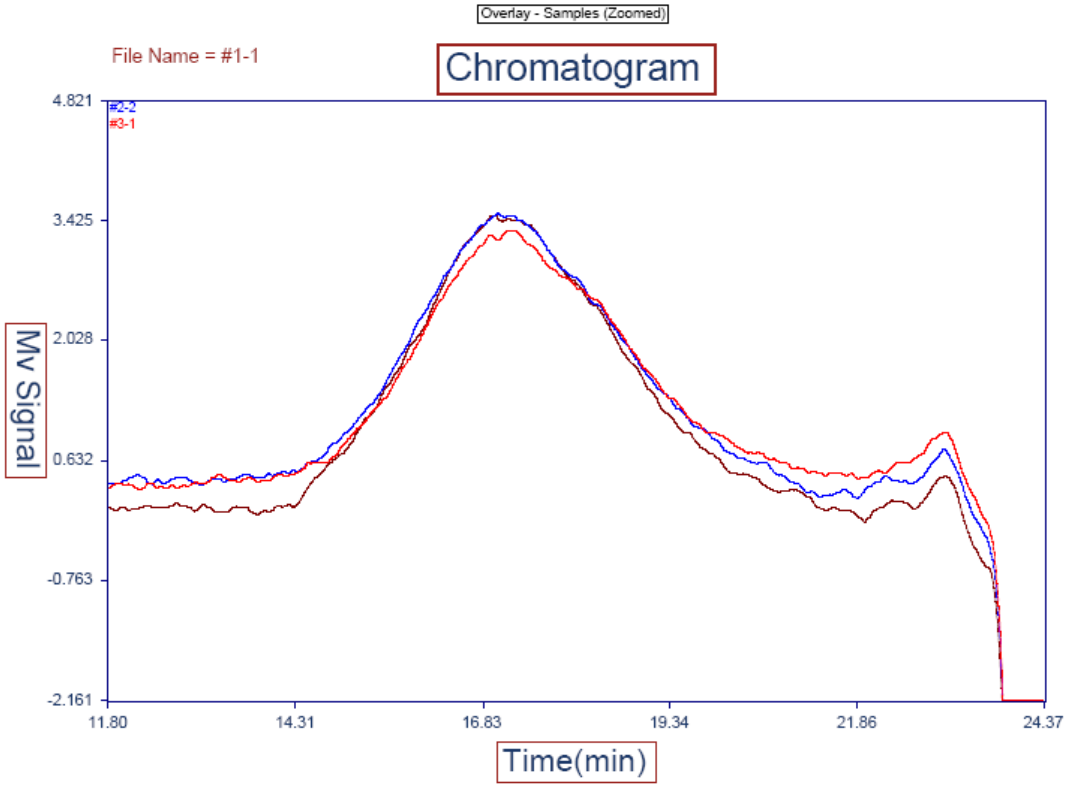
Overlay - Samples (Zoomed)
File Name = #1-1
Chromatogram
#2-2
#3-1
4.821
3.425
2.028
0.632
-0.763
-2.161
Mv Signal
11.80
14.31
16.83
19.34
21.86
24.37
Time(min)

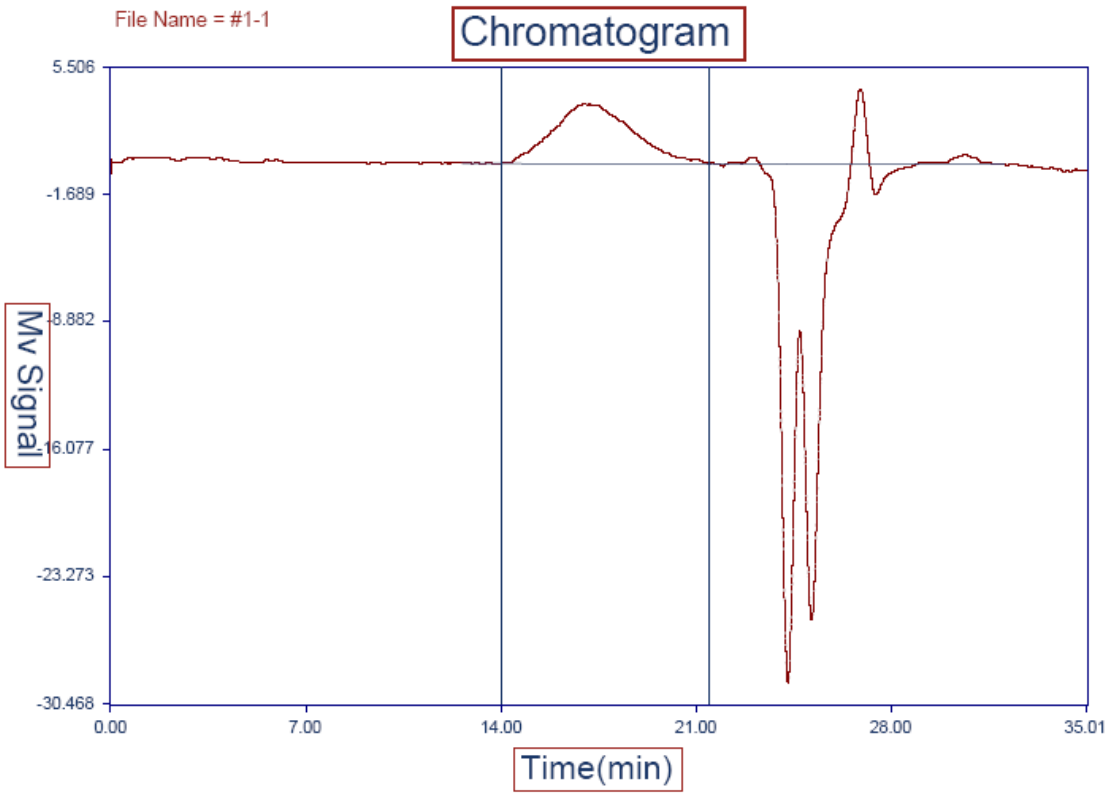
File Name = #1-1
Chromatogram
5.506
-1.689
-8.882
-16.077
-23.273
-30.468
Mv Signal
0.00
7.00
14.00
21.00
28.00
35.01
Time(min)

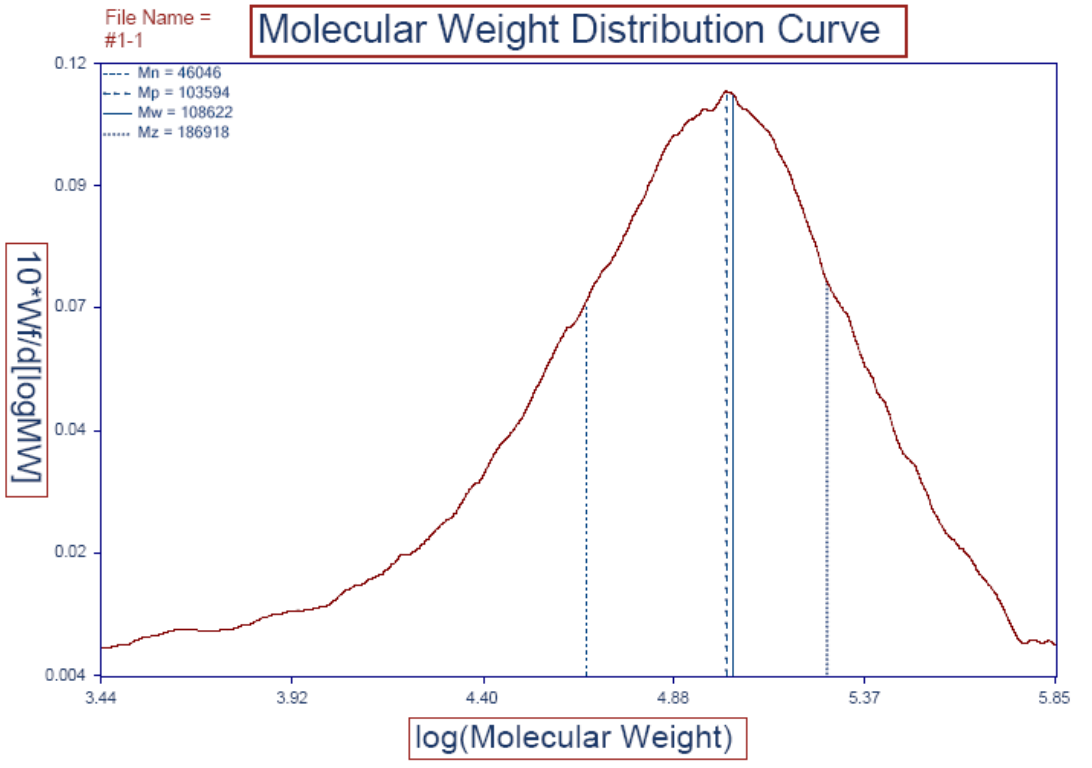
File Name = #1-1
Molecular Weight Distribution Curve
Mn = 46046
Mp = 103594
Mw = 108622
Mz = 186918
0.12
0.09
0.07
0.04
0.02
0.004
10*Wf/d[logMW]
3.44
3.92
4.40
4.88
5.37
5.85
log(Molecular Weight)

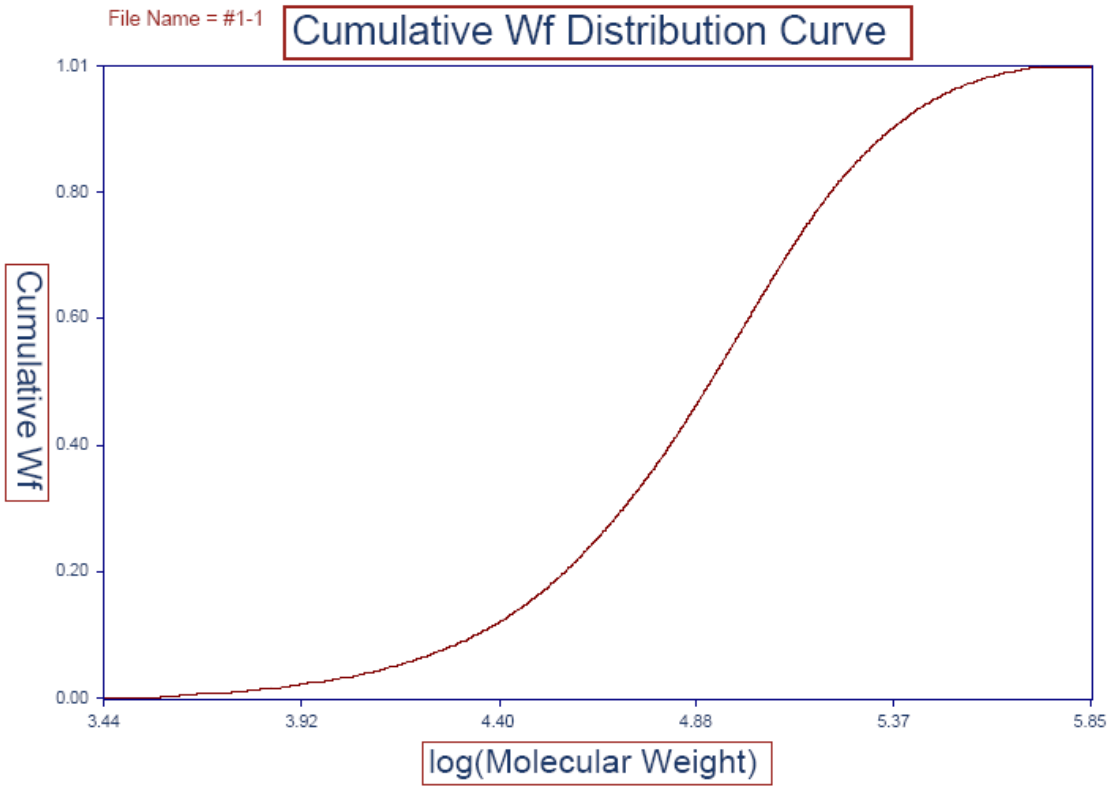

Summary of Molecular Weights

File Name = #1-1.ASC

Sample Name = Unknown

Calibration File Name = UoWaterlooCal100407.ASC

Number Average Molecular Weight (Mn) = 46046

Weight Average Molecular Weight (Mw) = 108622

Z Average Molecular Weight (Mz) = 186918

Peak Maximum Molecular Weight (Mp) = 103594

Polydispersity = 2.36

Peak Area = 6730

Integration Limits =

Left = 16.84

Right = 25.74

Mobile Phase = Trichlorobenzene

Detector = Refractive Index

Concentration = 2.5 mg/ml

Run Date = 10/3/2007 6:30:33 PM

Column = Jordi Gel DVB Mixed Bed 50cm x 10cm

Comments = None

Temperature = 145 ° C

Inj. Volume = 200 uL

Flow Rate = 1.2 ml/min

Summary of Molecular Weights

File Name = #1-3.ASC

Sample Name = Unknown

Calibration File Name = UoWaterlooCal100407.ASC

Number Average Molecular Weight (Mn) = 46597

Weight Average Molecular Weight (Mw) = 108639

Z Average Molecular Weight (Mz) = 186210

Peak Maximum Molecular Weight (Mp) = 104341

Polydispersity = 2.33

Peak Area = 7007

Integration Limits =

Left = 16.84

Right = 25.74

Mobile Phase = Trichlorobenzene

Detector = Refractive Index

Concentration = 2.5 mg/ml

Run Date = 10/3/2007 7:58:10 PM

Column = Jordi Gel DVB Mixed Bed 50cm x 10cm

Temperature = 145 ° C

Inj. Volume = 200 uL

Flow Rate = 1.2 ml/min

Comments = None

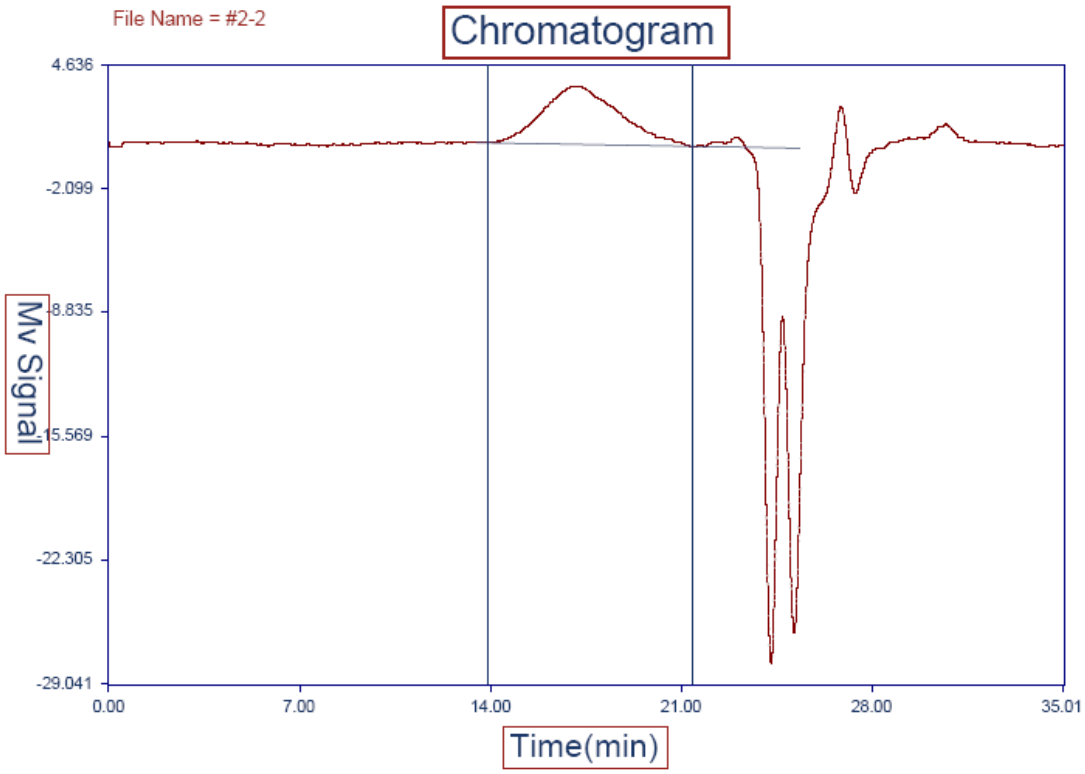

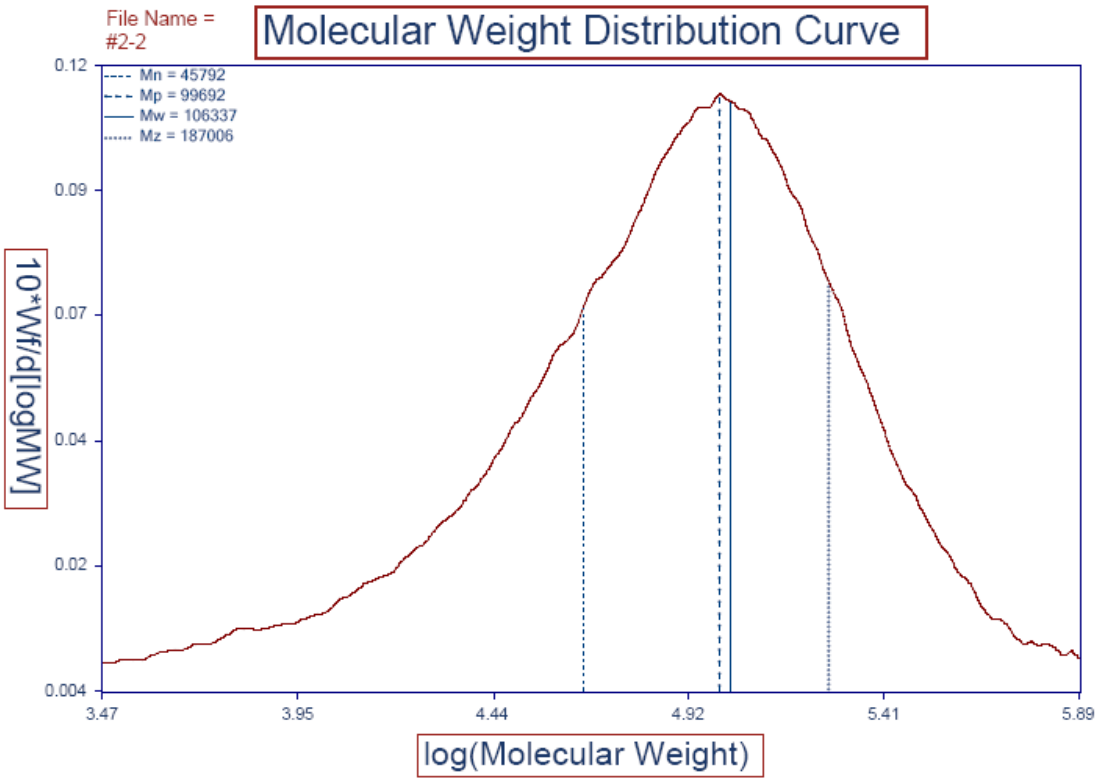
File Name =
#2-2
Molecular Weight Distribution Curve
Mn = 45792
Mp = 99692
Mw = 106337
Mz = 187006
10*Wf/d[logMW]
0.12
0.09
0.07
0.04
0.02
0.004
3.47
3.95
4.44
4.92
5.41
5.89
log(Molecular Weight)

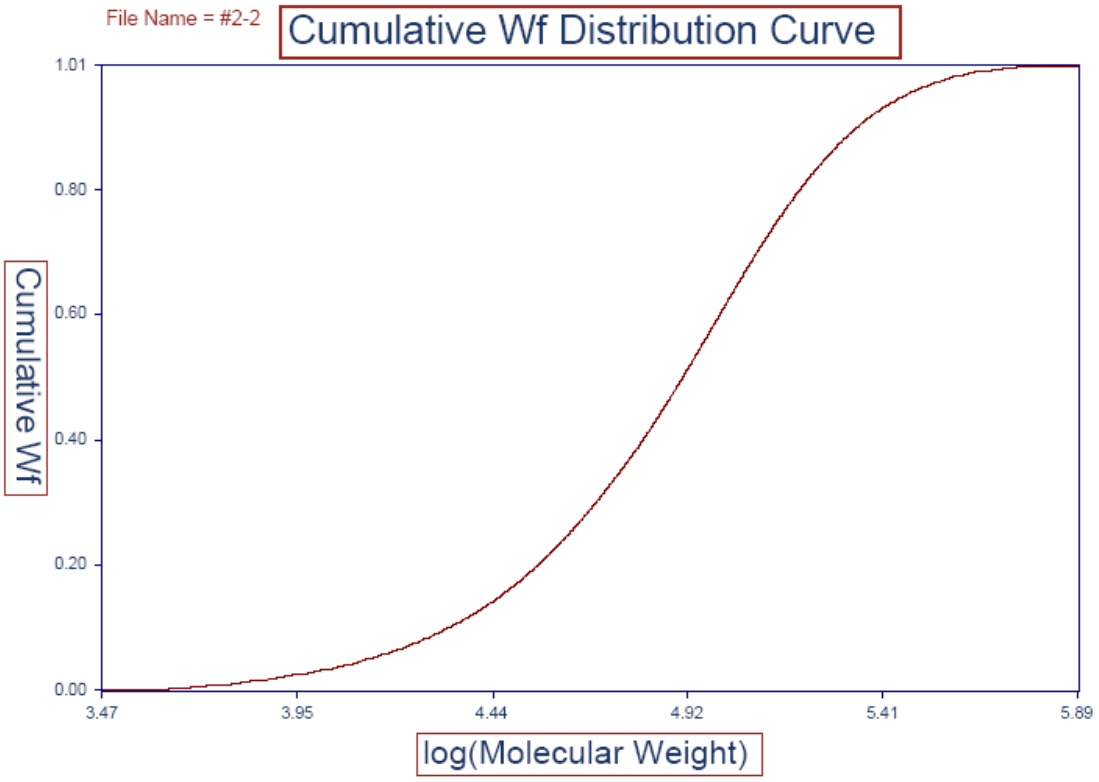
File Name = #2-2
Cumulative Wf Distribution Curve
Cumulative Wf
1.01
0.80
0.60
0.40
0.20
0.00
3.47
3.95
4.44
4.92
5.41
5.89
log(Molecular Weight)

Summary of Molecular Weights

File Name = #2-2.ASC
Sample Name = Unknown
Calibration File Name = UoWaterlooCal100407.ASC

Number Average Molecular Weight (Mn) = 45792
Weight Average Molecular Weight (Mw) = 106337
Z Average Molecular Weight (Mz) = 187006
Peak Maximum Molecular Weight (Mp) = 99692
Polydispersity = 2.32
Peak Area = 6165

Integration Limits =
Left = 16.67
Right = 25.67

Mobile Phase = Trichlorobenzene
Detector = Refractive Index
Concentration = 2.5 mg/ml
Run Date = 10/3/2007 9:25:47 PM
Column = Jordi Gel DVB Mixed Bed 50cm x 10cm

Temperature = 145 ° C
Inj. Volume = 200 uL
Flow Rate = 1.2 ml/min

Comments = None

Summary of Molecular Weights

File Name = #2-3
Sample Name = Unknown
Calibration File Name = UoWaterlooCal100407.ASC

Number Average Molecular Weight (Mn) = 47337
Weight Average Molecular Weight (Mw) = 106325
Z Average Molecular Weight (Mz) = 185911
Peak Maximum Molecular Weight (Mp) = 87532
Polydispersity = 2.25
Peak Area = 6383

Integration Limits =
Left = 16.67
Right = 25.67

Mobile Phase = Trichlorobenzene
Detector = Refractive Index
Concentration = 2.5 mg/ml
Run Date = 10/3/2007 10:09:36 PM
Column = Jordi Gel DVB Mixed Bed 50cm x 10cm

Temperature = 145 ° C
Inj. Volume = 200 uL
Flow Rate = 1.2 ml/min

Comments = None

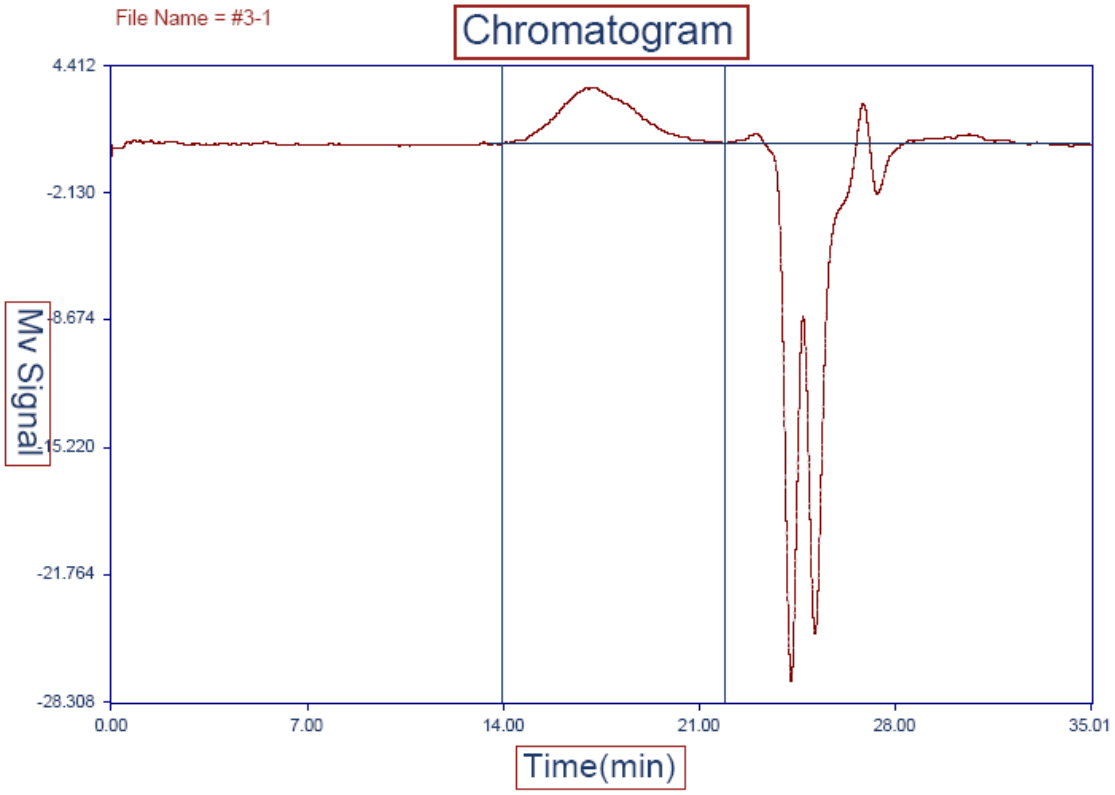
File Name = #3-1
Chromatogram
4.412
-2.130
-8.674
-15.220
-21.764
-28.308
Mv Signal
0.00
7.00
14.00
21.00
28.00
35.01
Time(min)

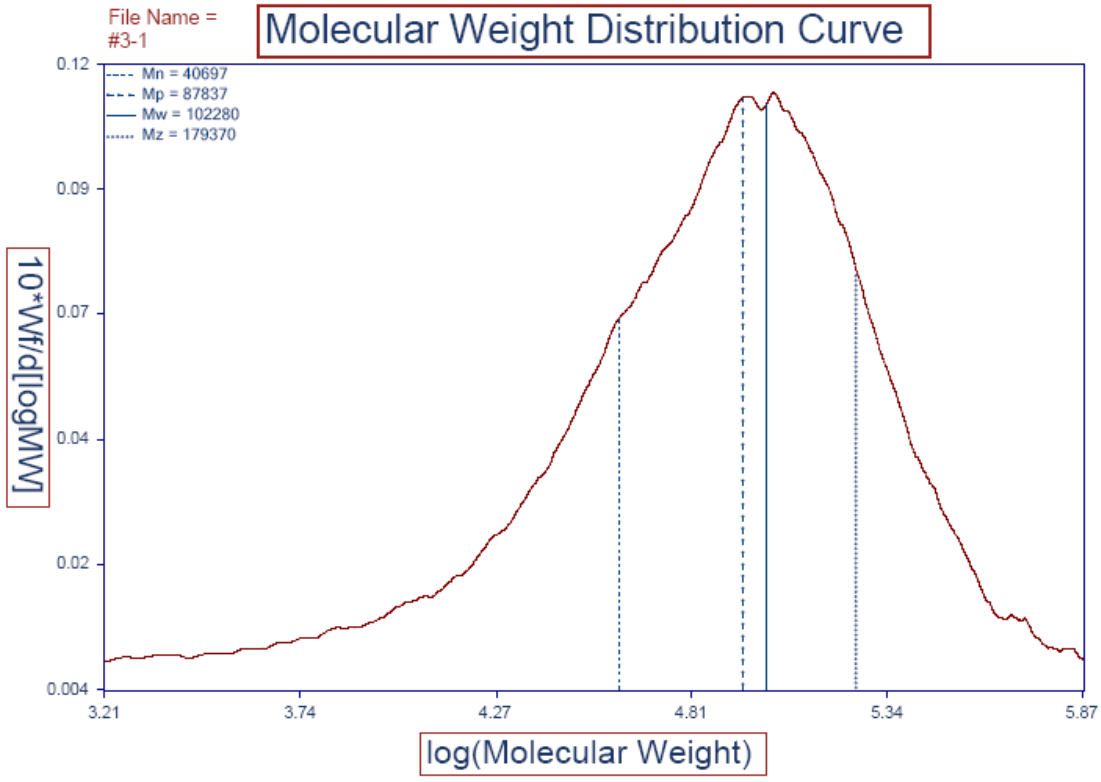
File Name = #3-1
Molecular Weight Distribution Curve
Mn = 40697
Mp = 87837
Mw = 102280
Mz = 179370
0.12
0.09
0.07
0.04
0.02
0.004
10*Wf/d[logMW]
3.21
3.74
4.27
4.81
5.34
5.87
log(Molecular Weight)

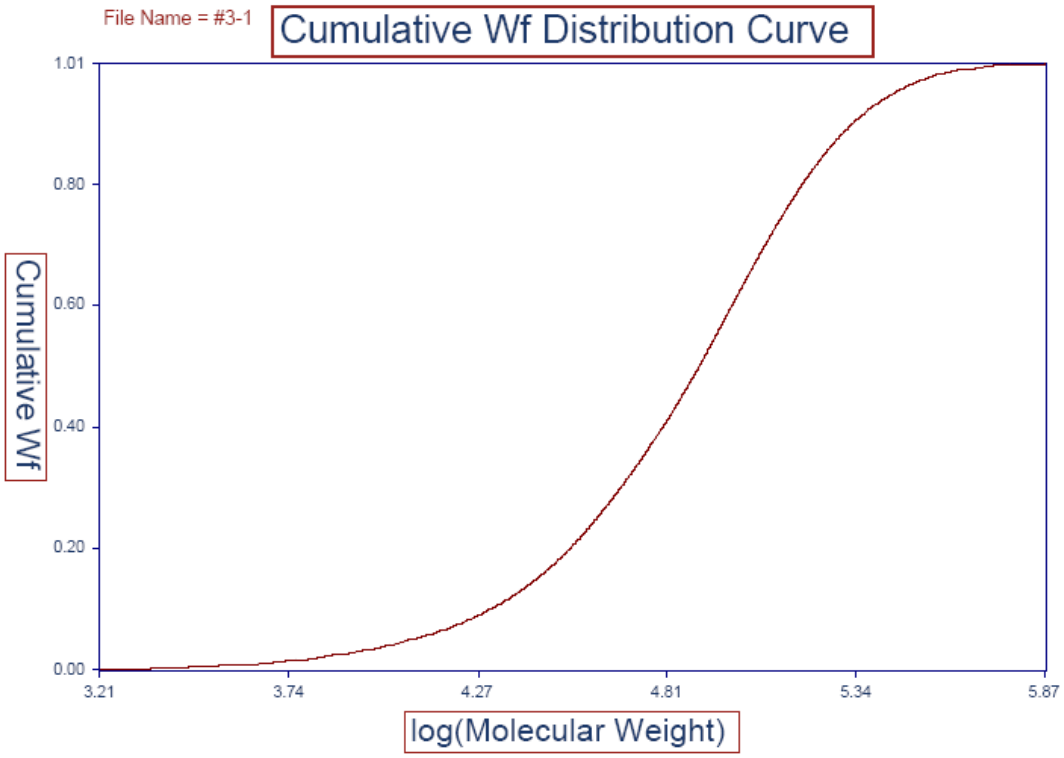

Summary of Molecular Weights

File Name = #3-1.ASC

Sample Name = Unknown

Calibration File Name = UoWaterlooCal100407.ASC

Number Average Molecular Weight (Mn) = 40697

Weight Average Molecular Weight (Mw) = 102280

Z Average Molecular Weight (Mz) = 179370

Peak Maximum Molecular Weight (Mp) = 87837

Polydispersity = 2.51

Peak Area = 5648

Integration Limits =

Left = 16.77

Right = 26.28

Mobile Phase = Trichlorobenzene

Detector = Refractive Index

Concentration = 2.5 mg/ml

Run Date = 10/3/2007 10:53:26 PM

Column = Jordi Gel DVB Mixed Bed 50cm x 10cm

Comments = None

Temperature = 145 ° C

Inj. Volume = 200 uL

Flow Rate = 1.2 ml/min

Summary of Molecular Weights

File Name = #3-2

Sample Name = Unknown

Calibration File Name = UoWaterlooCal100407.ASC

Number Average Molecular Weight (Mn) = 42084

Weight Average Molecular Weight (Mw) = 102473

Z Average Molecular Weight (Mz) = 179196

Peak Maximum Molecular Weight (Mp) = 89646

Polydispersity = 2.43

Peak Area = 5557

Integration Limits =

Left = 16.77

Right = 26.28

Mobile Phase = Trichlorobenzene

Detector = Refractive Index

Concentration = 2.5 mg/ml

Run Date = 10/3/2007 11:37:14 PM

Column = Jordi Gel DVB Mixed Bed 50cm x 10cm

Comments = None

Temperature = 145 ° C

Inj. Volume = 200 uL

Flow Rate = 1.2 ml/min

Appendix D: Tensile Test Data

D100 – Chopped fibre (80 °C)

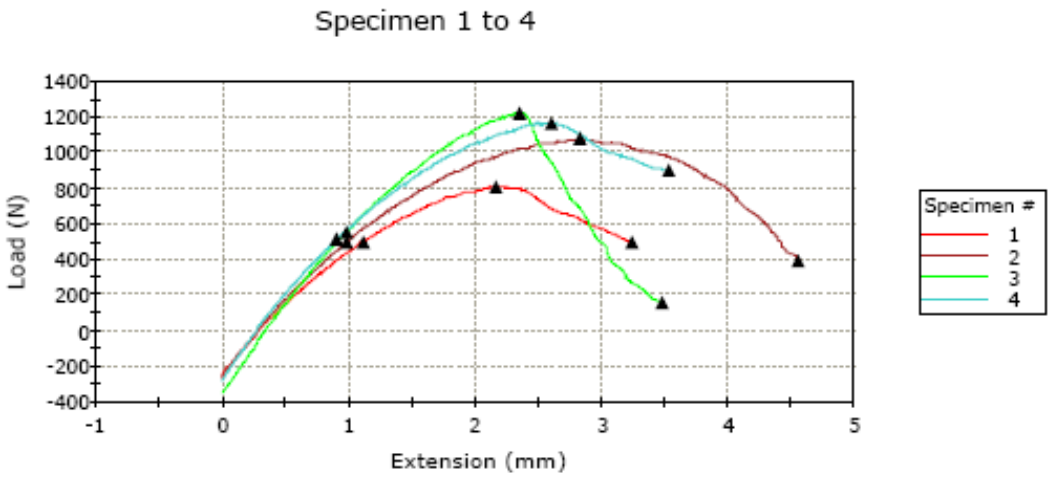

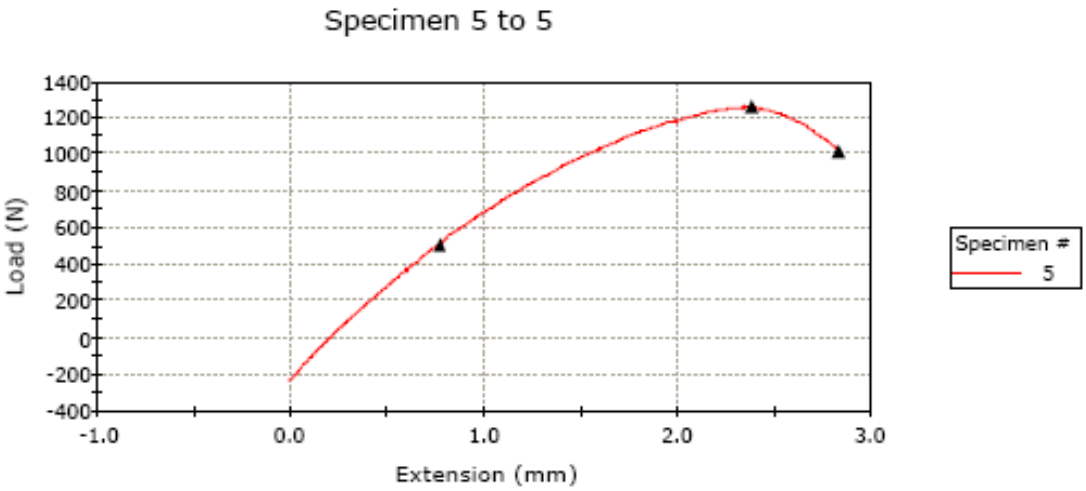

	Specimen label	Maximum Load (N)	Tensile stress at Maximum Load (MPa)	Tensile strain at Maximum Load (%)	Load at Break (Standard) (N)	Tensile stress at Break (Standard) (MPa)	Tensile strain at Break (Standard) (%)
1	1	807.89	22.26	54.29	494.55	13.62	46.68
2	2	1077.04	29.92	74.98	389.99	10.83	74.45
3	3	1224.78	33.82	30.82	158.86	4.39	7.44
4	4	1162.57	32.23	48.05	900.65	24.97	43.94
5	5	1266.77	34.92	52.81	1013.90	27.95	50.46
Coefficient of Variation		16.45050	16.47046	30.26945	60.42748	60.37229	53.90553
Maximum		1266.77	34.92	74.98	1013.90	27.95	74.45
Mean		1107.81	30.63	52.19	591.59	16.35	44.59
Median		1162.57	32.23	52.81	494.55	13.62	46.68
Minimum		807.89	22.26	30.82	158.86	4.39	7.44
Range		458.88	12.66	44.17	855.04	23.56	67.01
Standard Deviation		182.23999	5.04471	15.79809	357.48280	9.87242	24.03791
Mean + 1 SD		1290.05	35.67	67.99	949.07	26.22	68.63
Mean - 1 SD		925.57	25.58	36.39	234.11	6.48	20.55

	Tensile extension at Break (Standard) (mm)	Modulus (E-modulus) (MPa)	Tensile stress at Yield (Offset 0.2 %) (MPa)	Rate 1 (mm/min)
1	0.46678	50.97	13.76669	5.00000
2	0.74450	72.29	13.72865	5.00000
3	0.07436	105.98	15.18244	5.00000
4	0.43936	104.13	14.12417	5.00000
5	0.50463	101.62	13.99328	5.00000
Coefficient of Variation	53.90552	28.04770	4.20093	0.00000
Maximum	0.74450	105.98	15.18244	5.00000
Mean	0.44593	87.00	14.15905	5.00000
Median	0.46678	101.62	13.99328	5.00000
Minimum	0.07436	50.97	13.72865	5.00000
Range	0.67014	55.00	1.45379	0.00000
Standard Deviation	0.24038	24.40083	0.59481	0.00000
Mean + 1 SD	0.68631	111.40	14.75386	5.00000

	Tensile extension at Break (Standard) (mm)	Modulus (E-modulus) (MPa)	Tensile stress at Yield (Offset 0.2 %) (MPa)	Rate 1 (mm/min)
Mean - 1 SD	0.20555	62.60	13.56424	5.00000

	Comment
1	
2	
3	
4	
5	
Coefficient of Variation	
Maximum	
Mean	
Median	
Minimum	
Range	
Standard Deviation	
Mean + 1 SD	
Mean - 1 SD	

G-100 Long-Continuous Fibre (80 °C)

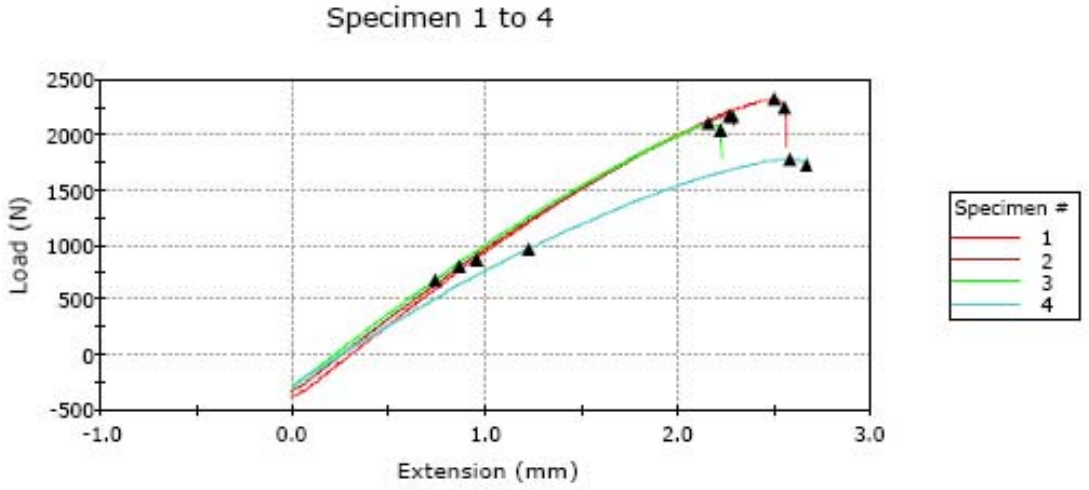

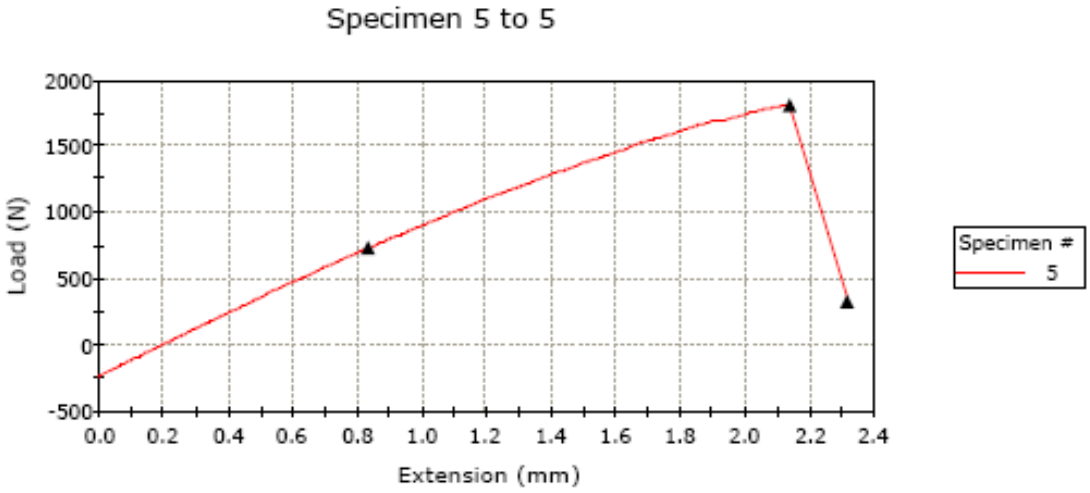

	Specimen label	Maximum Load (N)	Tensile stress at Maximum Load (MPa)	Tensile strain at Maximum Load (%)	Load at Break (Standard) (N)	Tensile stress at Break (Standard) (MPa)	Tensile strain at Break (Standard) (%)
1	1	2323.30	73.38	-9.44	2249.08	71.04	-8.90
2	2	2175.03	68.31	61.56	2169.50	68.14	63.39
3	3	2100.12	66.94	57.86	2044.77	65.18	61.60
4		1784.81	56.78	67.84	1735.28	55.20	74.02
5	5	1820.42	57.91	51.84	326.97	10.40	68.72
Coefficient of Variation		11.37235	10.99680	68.56830	46.61502	46.46390	66.18031
Maximum		2323.30	73.38	67.84	2249.08	71.04	74.02
Mean		2040.73	64.67	45.93	1705.12	53.99	51.77
Median		2100.12	66.94	57.86	2044.77	65.18	63.39
Minimum		1784.81	56.78	-9.44	326.97	10.40	-8.90
Range		538.49	16.60	77.28	1922.11	60.64	82.92
Standard Deviation		232.07945	7.11118	31.49382	794.84245	25.08692	34.25901
Mean + 1 SD		2272.81	71.78	77.42	2499.96	79.08	86.03
Mean - 1 SD		1808.66	57.55	14.44	910.28	28.91	17.51

	Tensile extension at Break (Standard) (mm)	Modulus (E-modulus) (MPa)	Tensile stress at Yield (Offset 0.2 %) (MPa)	Rate 1 (mm/min)
1	-0.08899	174.02	27.54666	5.00000
2	0.63388	157.89	25.19498	5.00000
3	0.61602	154.74	21.62137	5.00000
4	0.74023	143.42	30.68621	5.00000
5	0.68717	156.42	23.06464	5.00000
Coefficient of Variation	66.18031	6.96514	14.08222	0.00000
Maximum	0.74023	174.02	30.68621	5.00000
Mean	0.51766	157.30	25.62277	5.00000
Median	0.63388	156.42	25.19498	5.00000
Minimum	-0.08899	143.42	21.62137	5.00000
Range	0.82921	30.61	9.06484	0.00000
Standard Deviation	0.34259	10.95594	3.60826	0.00000
Mean + 1 SD	0.86025	168.25	29.23103	5.00000

	Tensile extension at Break (Standard) (mm)	Modulus (E-modulus) (MPa)	Tensile stress at Yield (Offset 0.2 %) (MPa)	Rate 1 (mm/min)
Mean - 1 SD	0.17507	146.34	22.01452	5.00000

	Comment
1	
2	
3	
4	
5	
Coefficient of Variation	
Maximum	
Mean	
Median	
Minimum	
Range	
Standard Deviation	
Mean + 1 SD	
Mean - 1 SD	

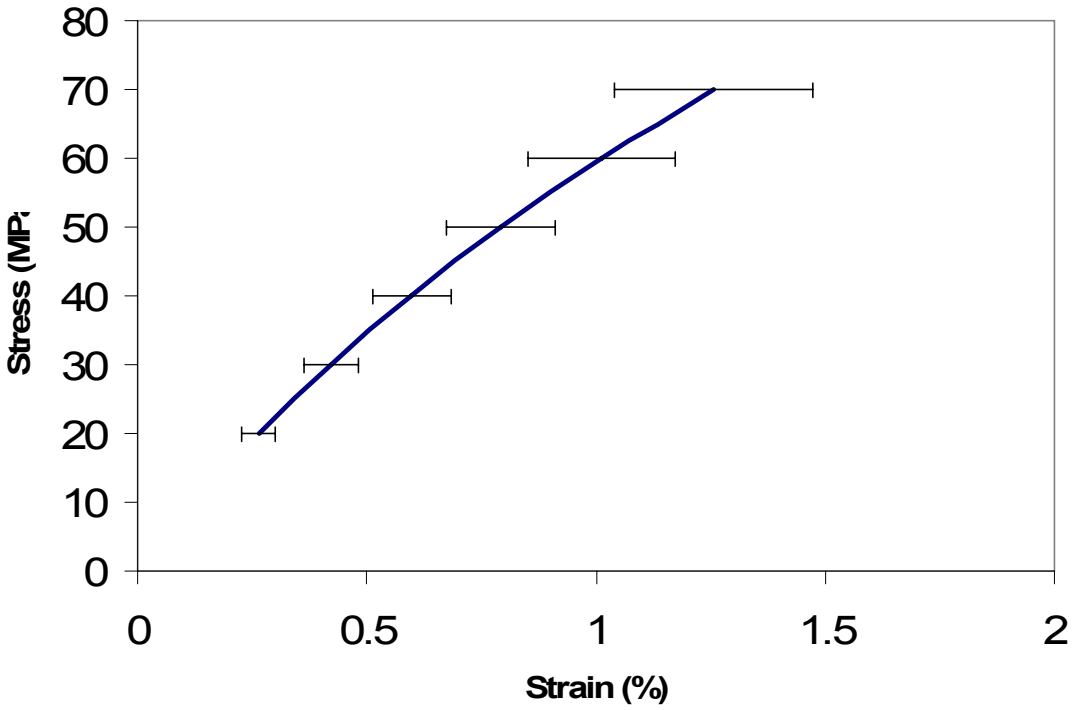

Average stress-strain behaviour for G100 measured with extensometer

(Courtesy of P. Dasappa)

Appendix E: Creep Test Data

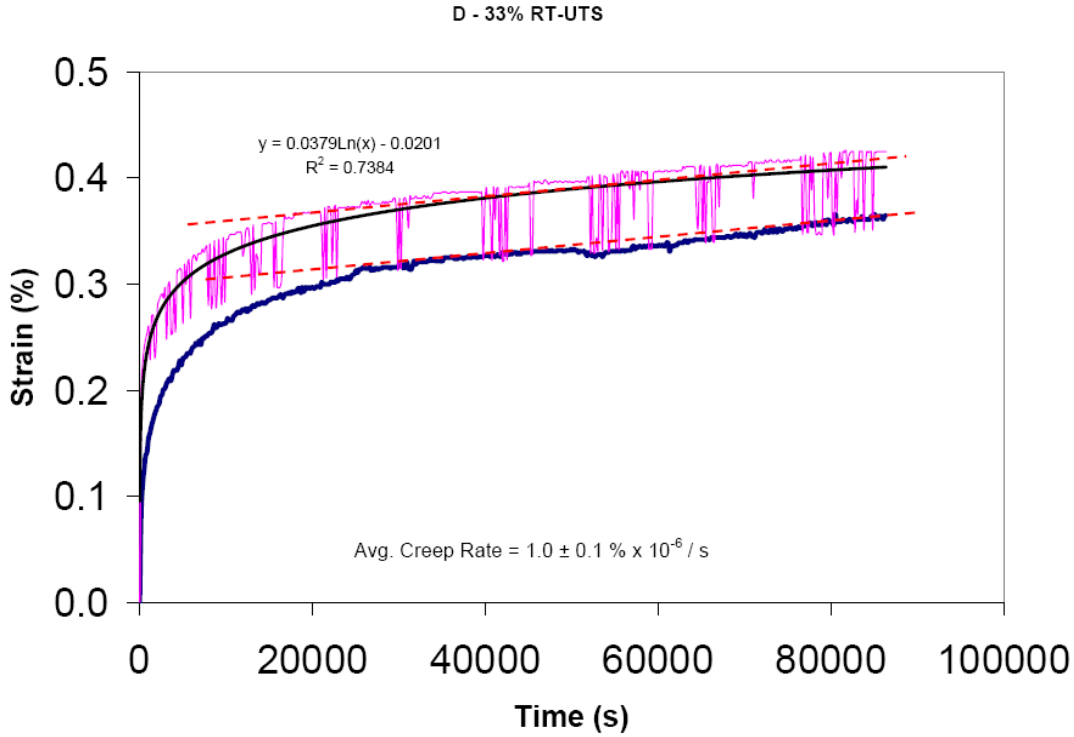

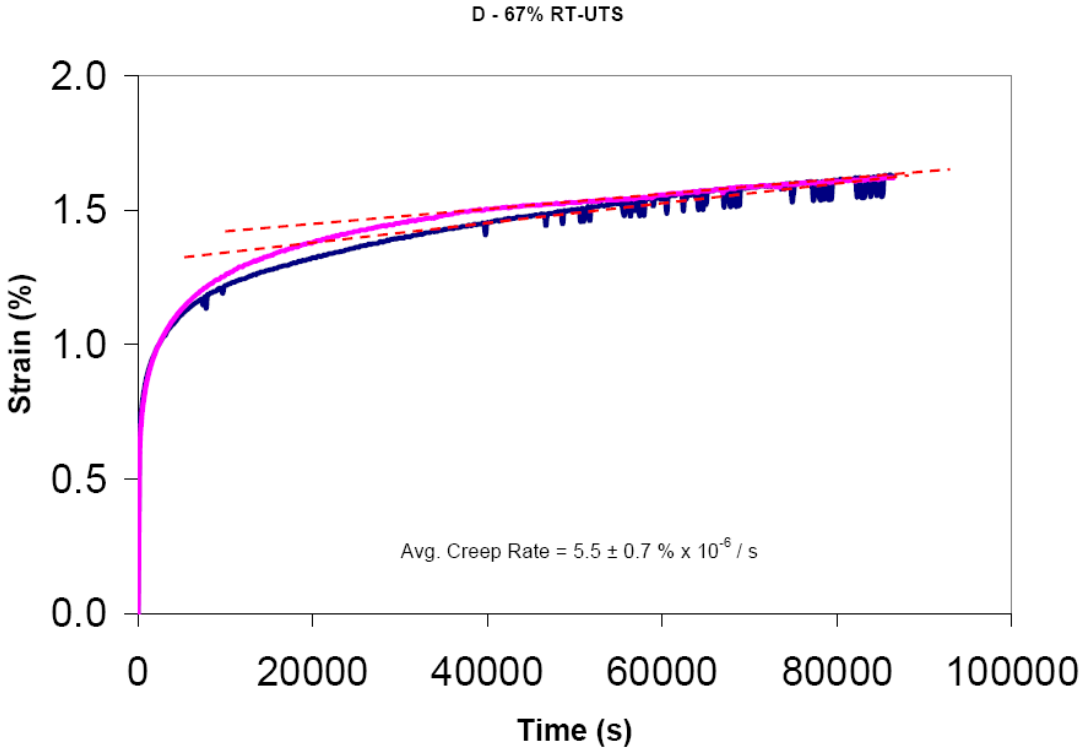

G - 33% RT-UTS

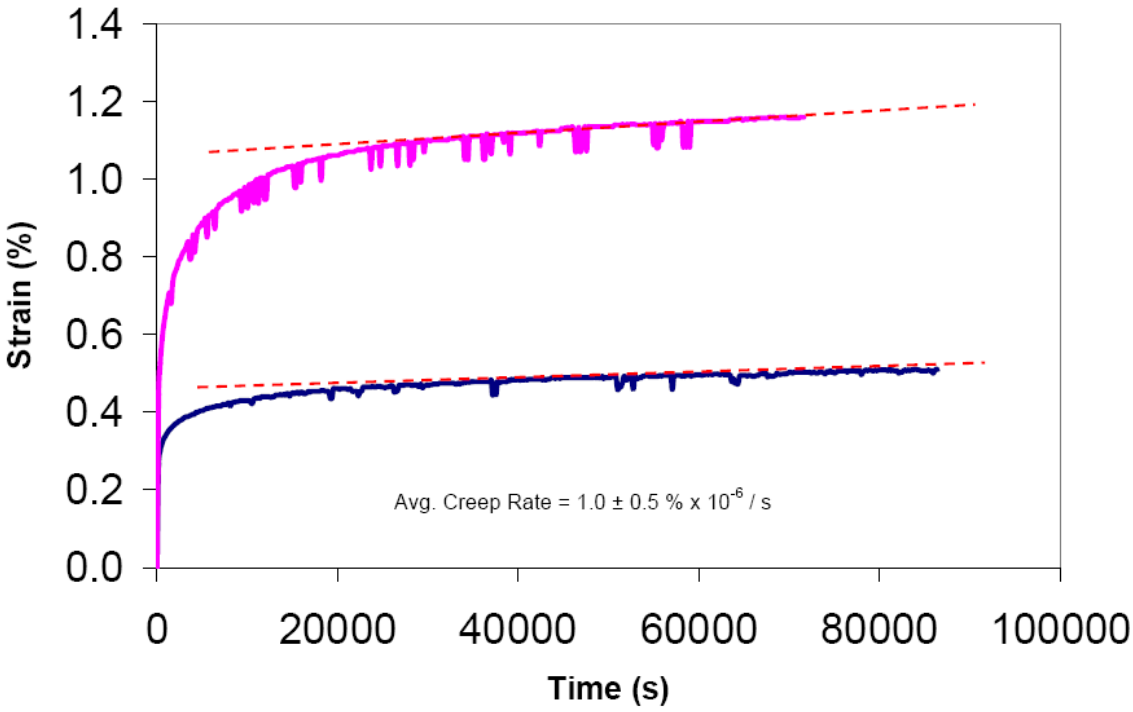

G - 67% RT-UTS

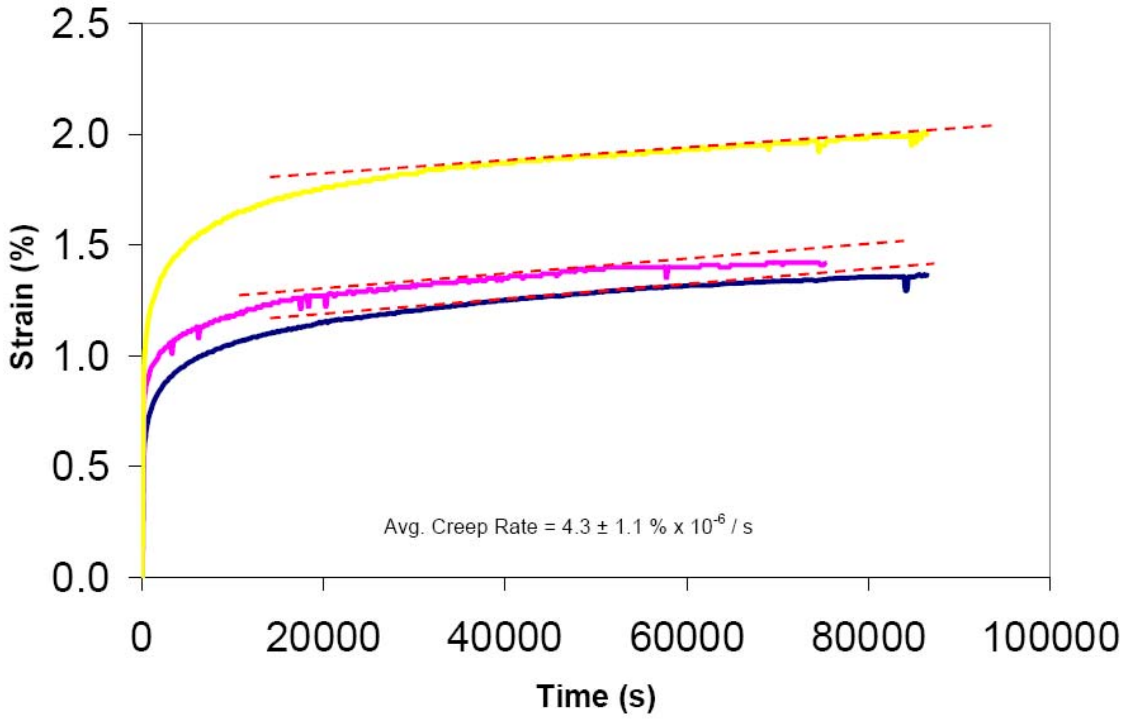

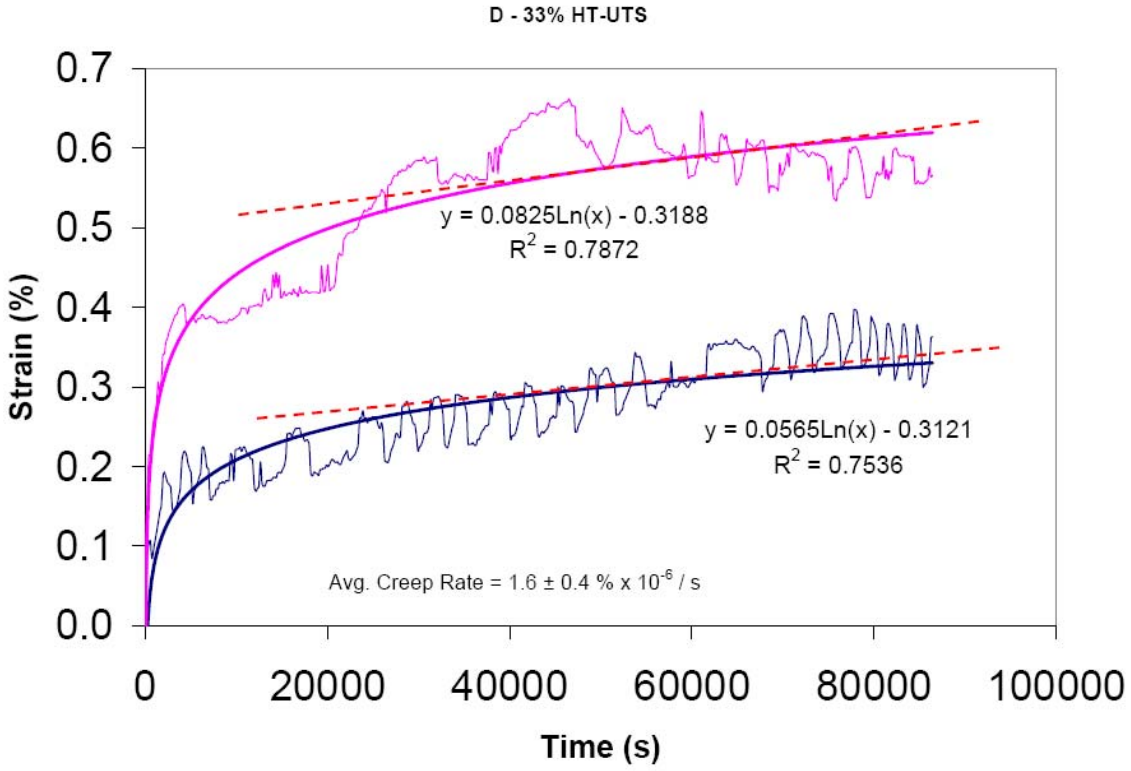
D - 33% HT-UTS
Strain (%)
Time (s)
y = 0.0825Ln(x) - 0.3188
R2 = 0.7872
y = 0.0565Ln(x) - 0.3121
R2 = 0.7536
Avg. Creep Rate = 1.6 ± 0.4 % x 10-6 / s

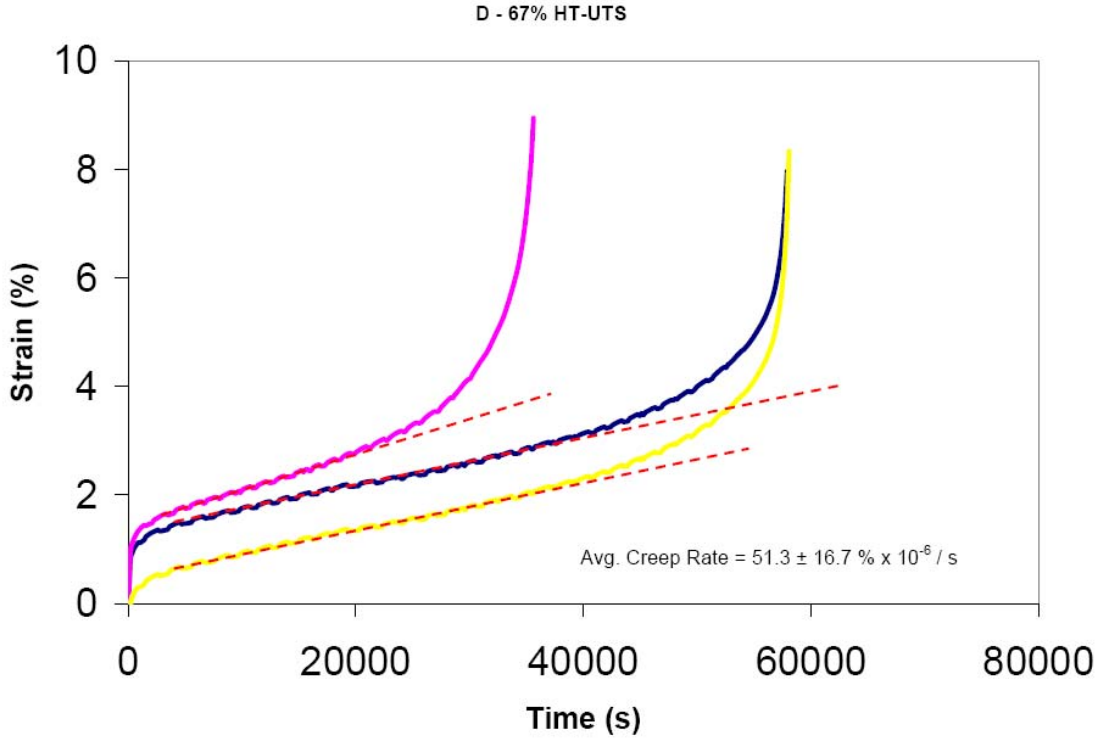
D - 67% HT-UTS
Strain (%)
Time (s)
Avg. Creep Rate = 51.3 ± 16.7 % x 10-6 / s

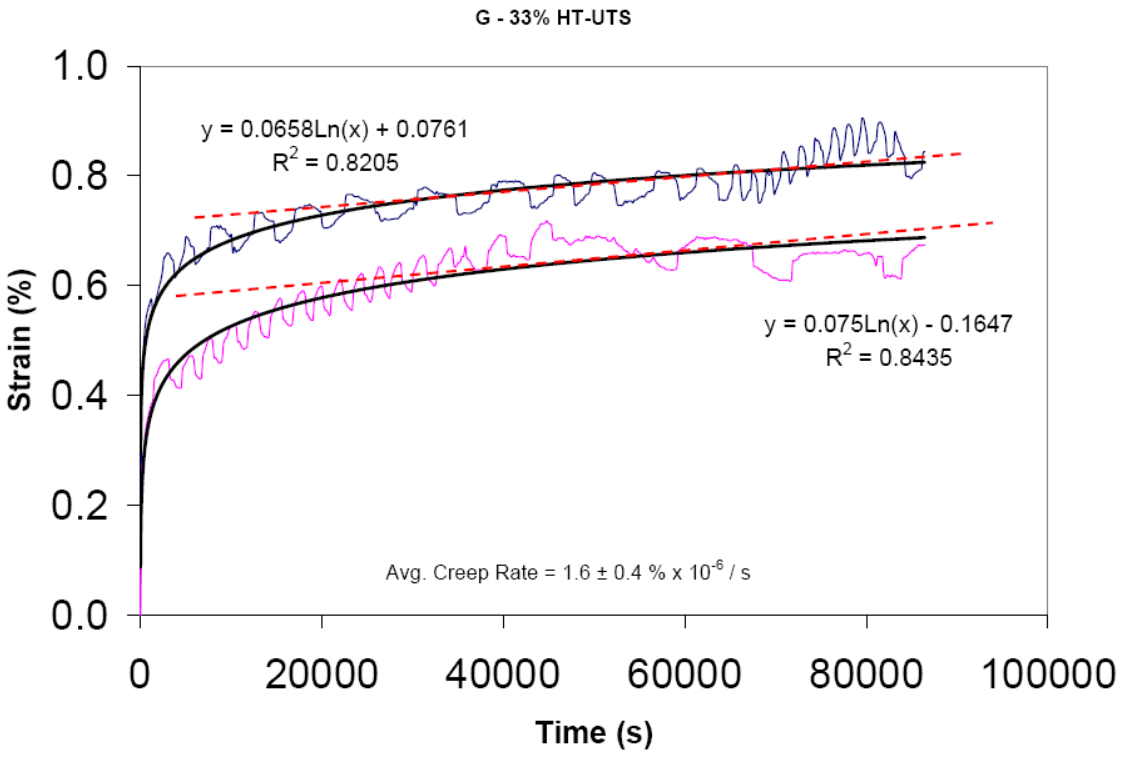
G - 33% HT-UTS
y = 0.0658Ln(x) + 0.0761
R2 = 0.8205
y = 0.075Ln(x) - 0.1647
R2 = 0.8435
Avg. Creep Rate = 1.6 ± 0.4 % x 10-6 / s
Strain (%)
Time (s)
0.0
0.2
0.4
0.6
0.8
1.0
0
20000
40000
60000
80000
100000

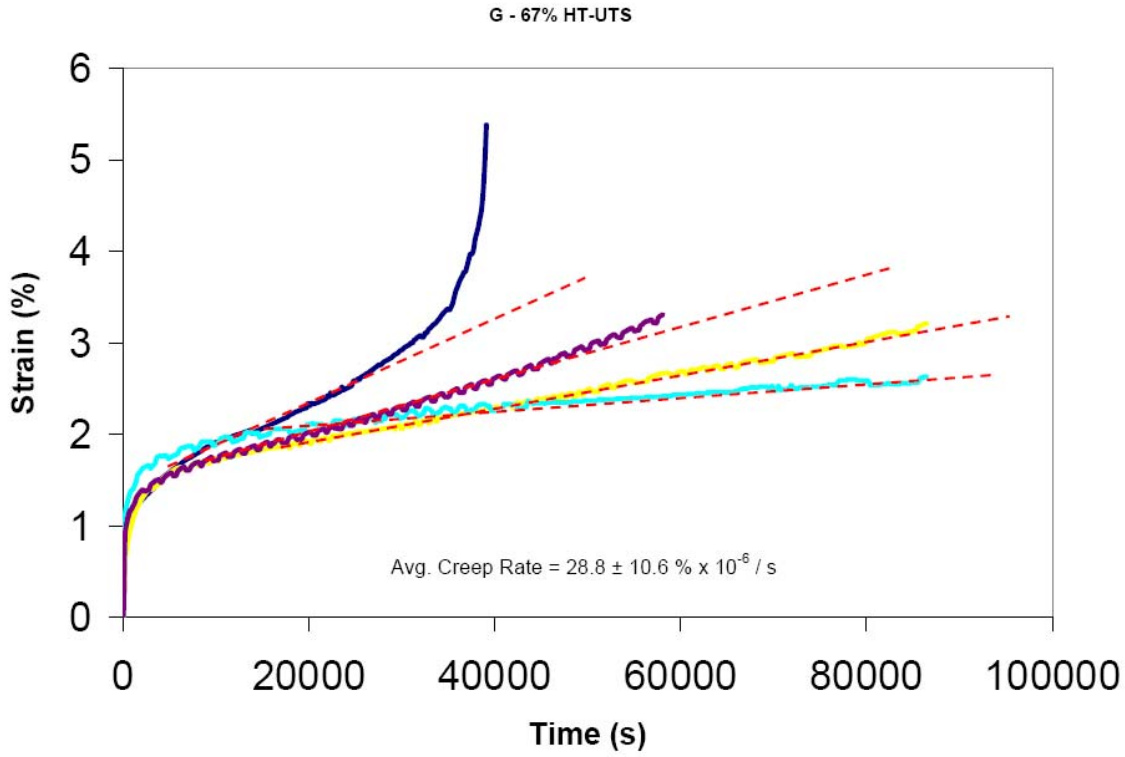
G - 67% HT-UTS
Avg. Creep Rate = 28.8 ± 10.6 % x 10-6 / s
Strain (%)
Time (s)
0
1
2
3
4
5
6
0
20000
40000
60000
80000
100000

Appendix F: X-ray Diffraction Data

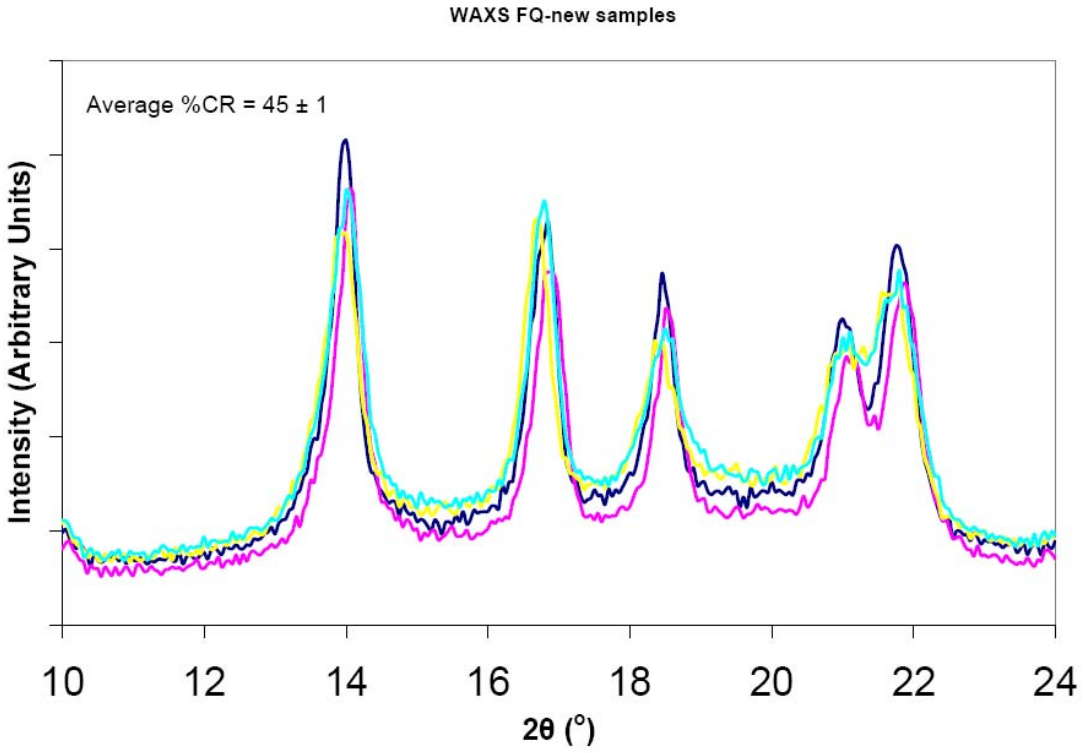

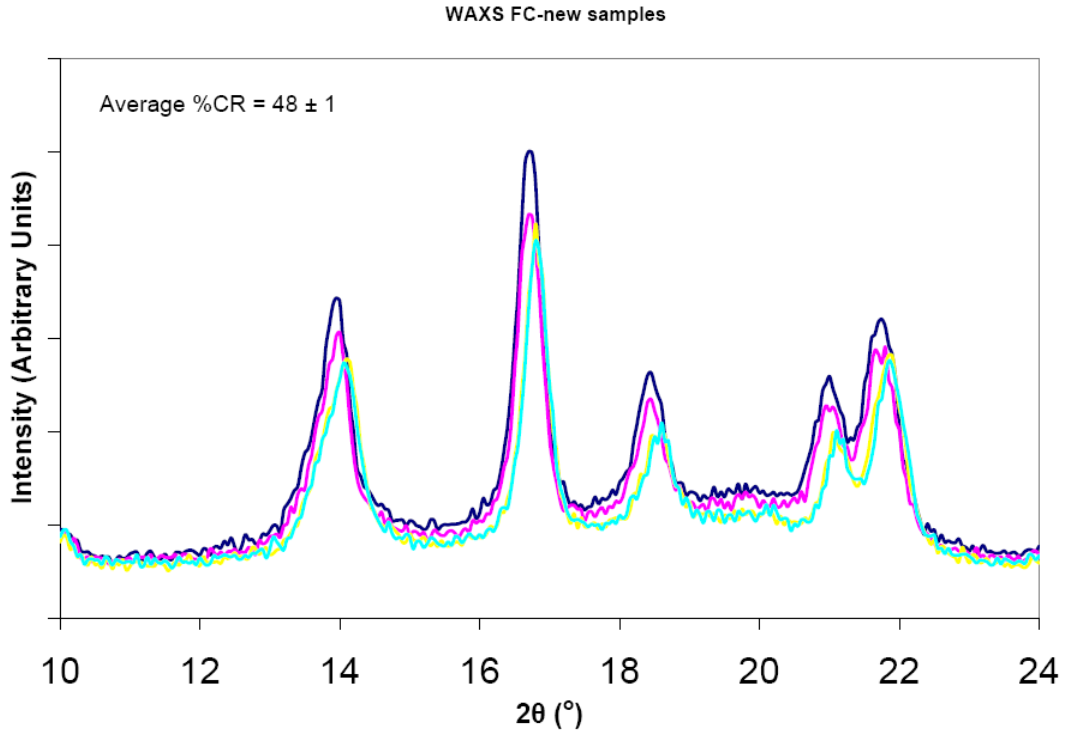

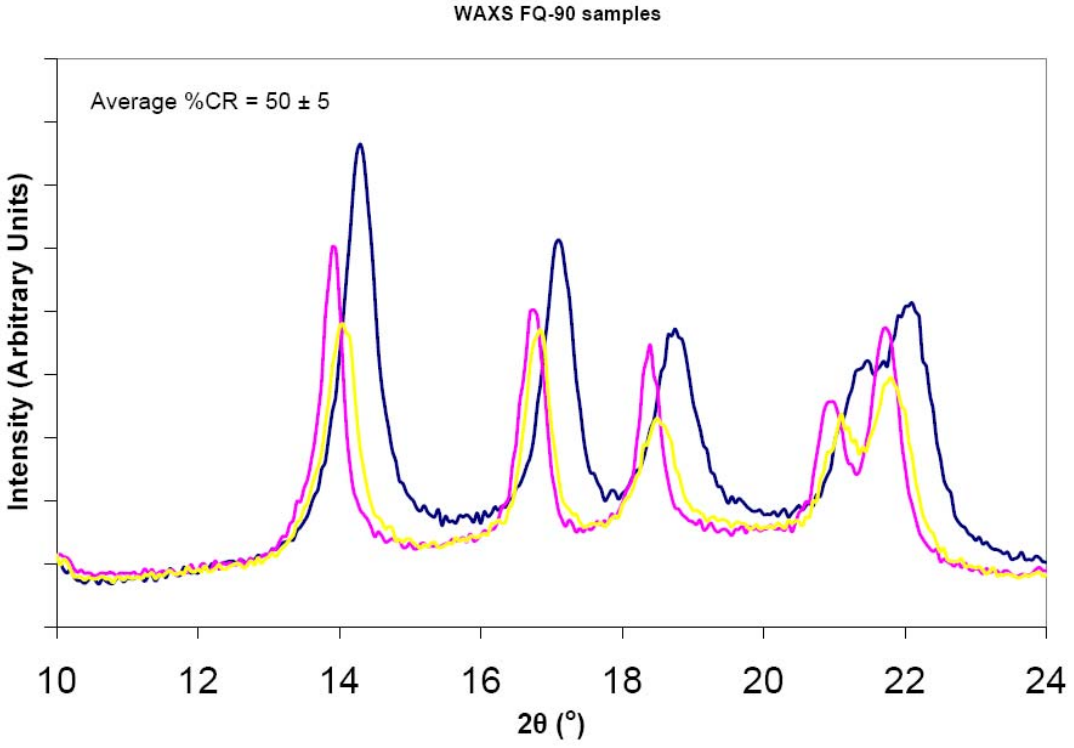
WAXS FQ-90 samples
Average %CR = 50 ± 5
Intensity (Arbitrary Units)
10
12
14
16
18
20
22
24
2θ (°)

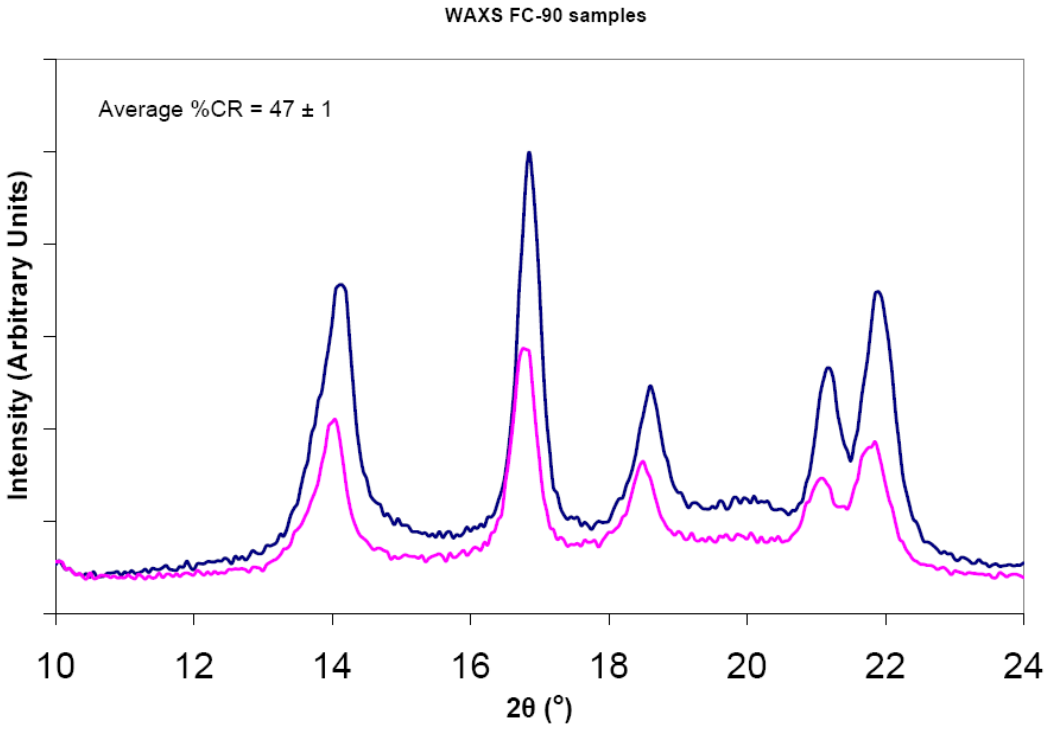
WAXS FC-90 samples
Average %CR = 47 ± 1
Intensity (Arbitrary Units)
10
12
14
16
18
20
22
24
2θ (°)

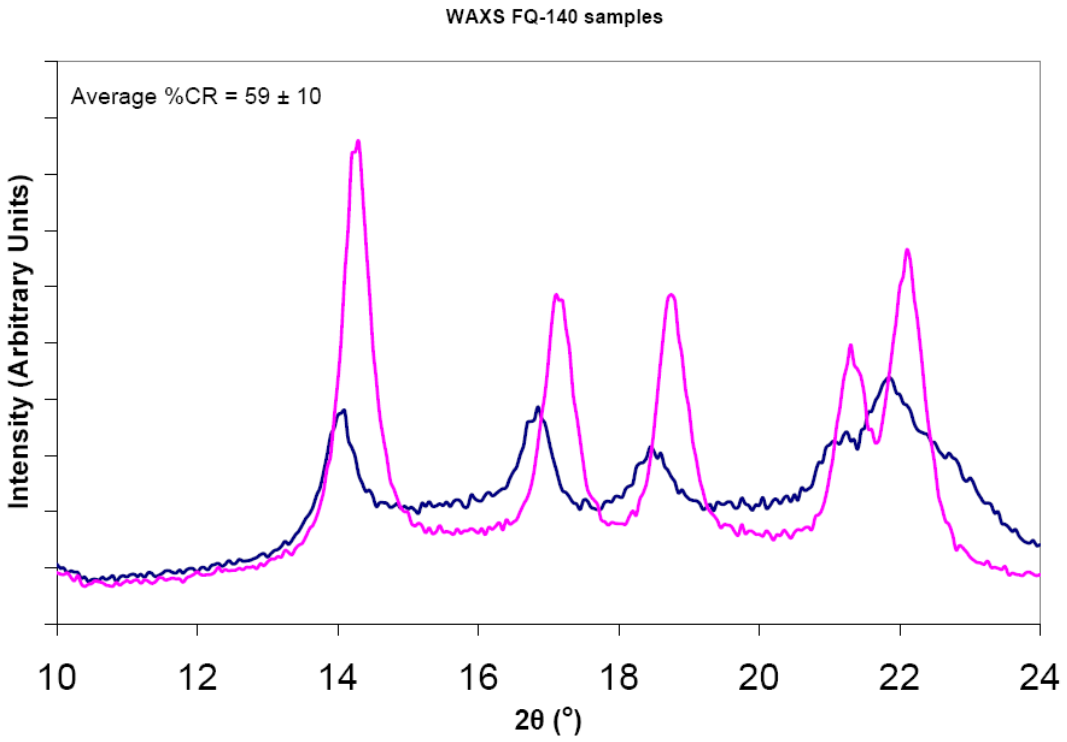
WAXS FQ-140 samples
Average %CR = 59 ± 10
Intensity (Arbitrary Units)
10
12
14
16
18
20
22
24
2θ (°)

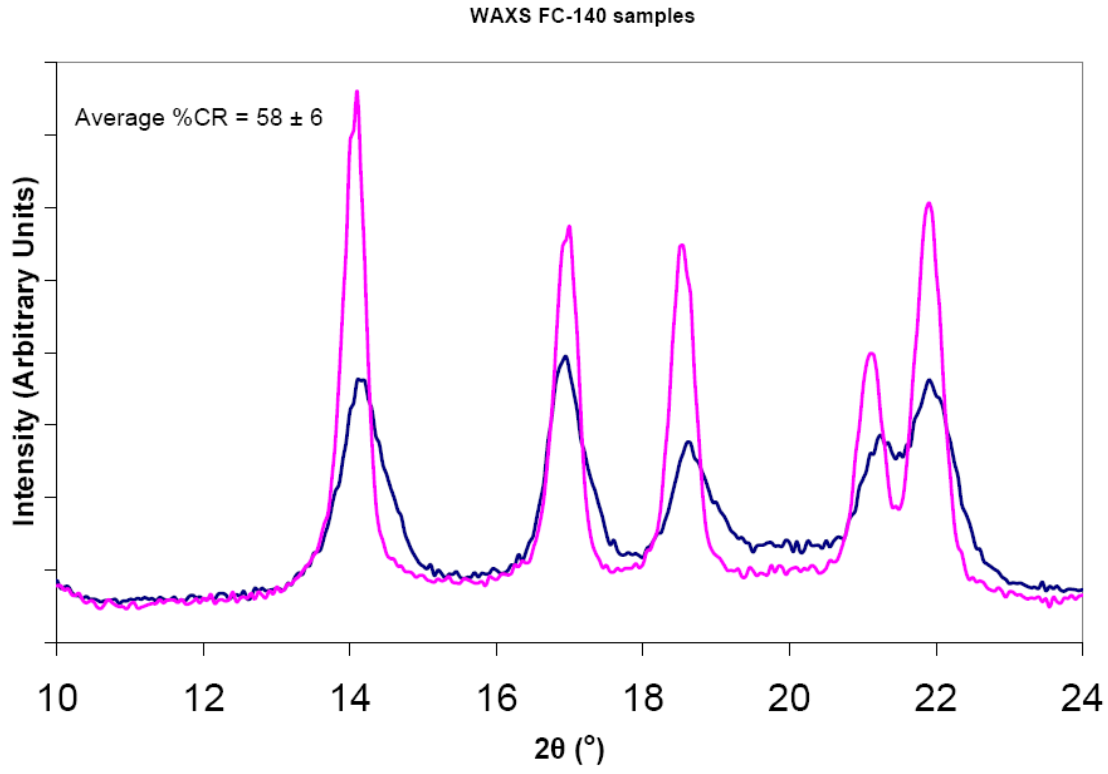
WAXS FC-140 samples
Average %CR = 58 ± 6
Intensity (Arbitrary Units)
10
12
14
16
18
20
22
24
2θ (°)

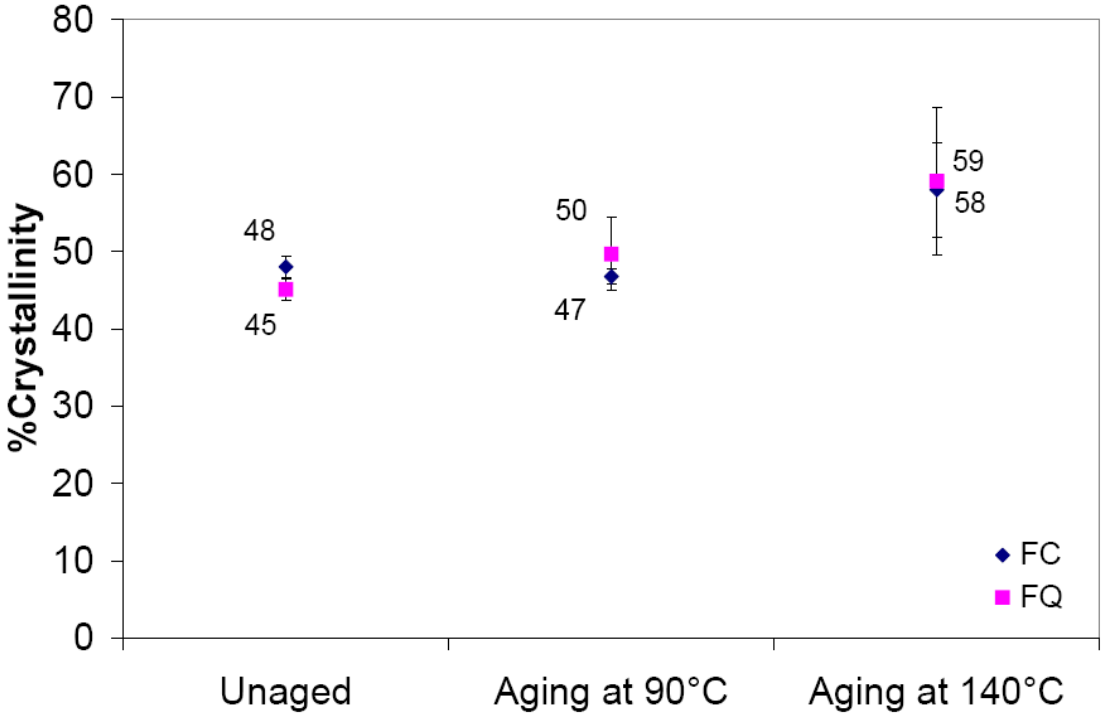
80
70
60
50
40
30
20
10
0
%Crystallinity
48
45
50
47
59
58
FC
FQ
Unaged
Aging at 90°C
Aging at 140°C

Appendix G: FTIR Data

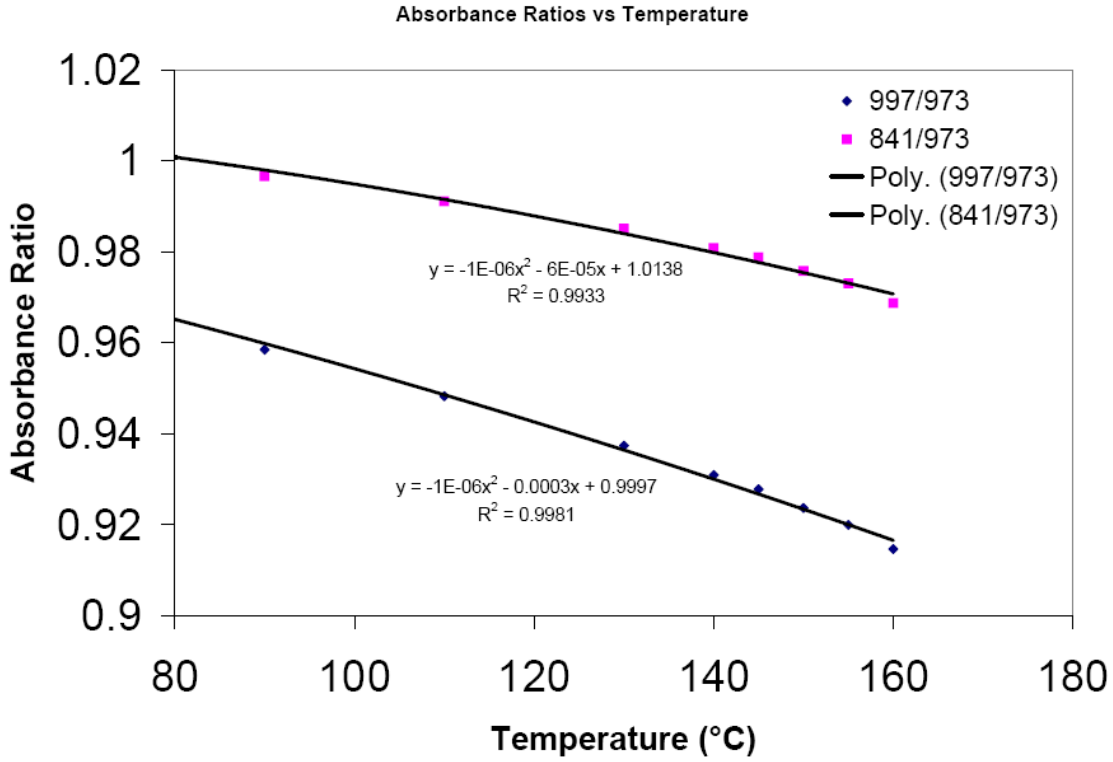

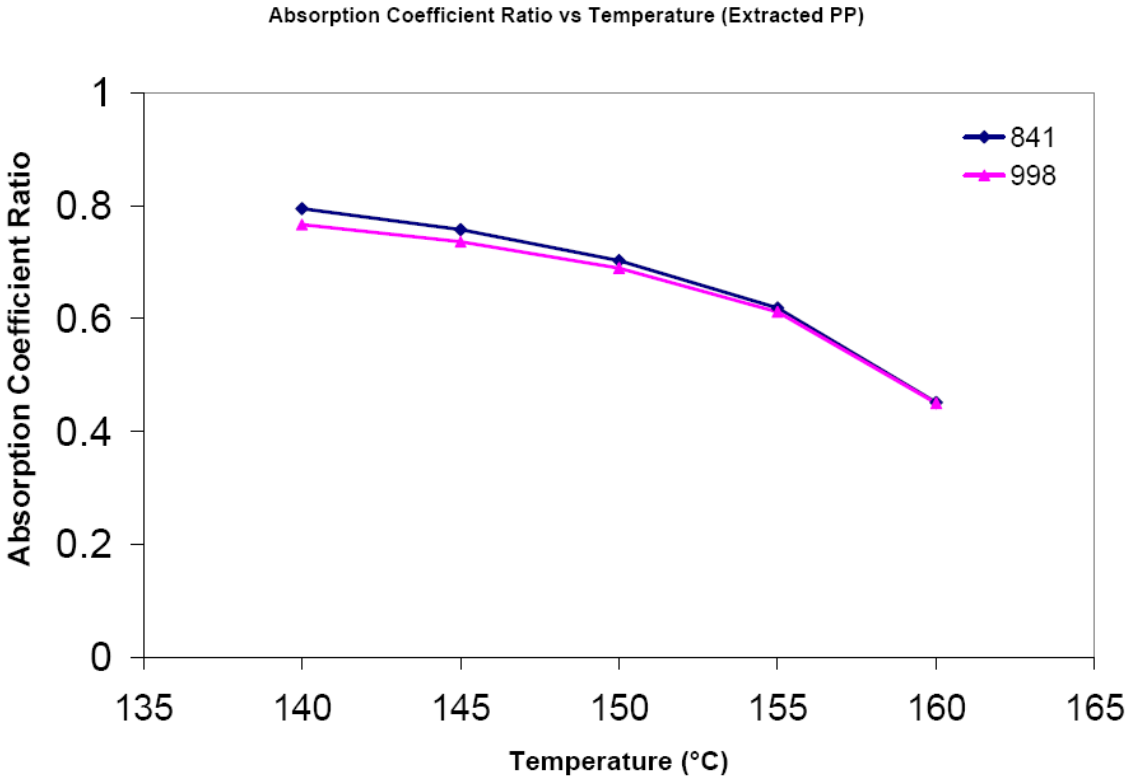

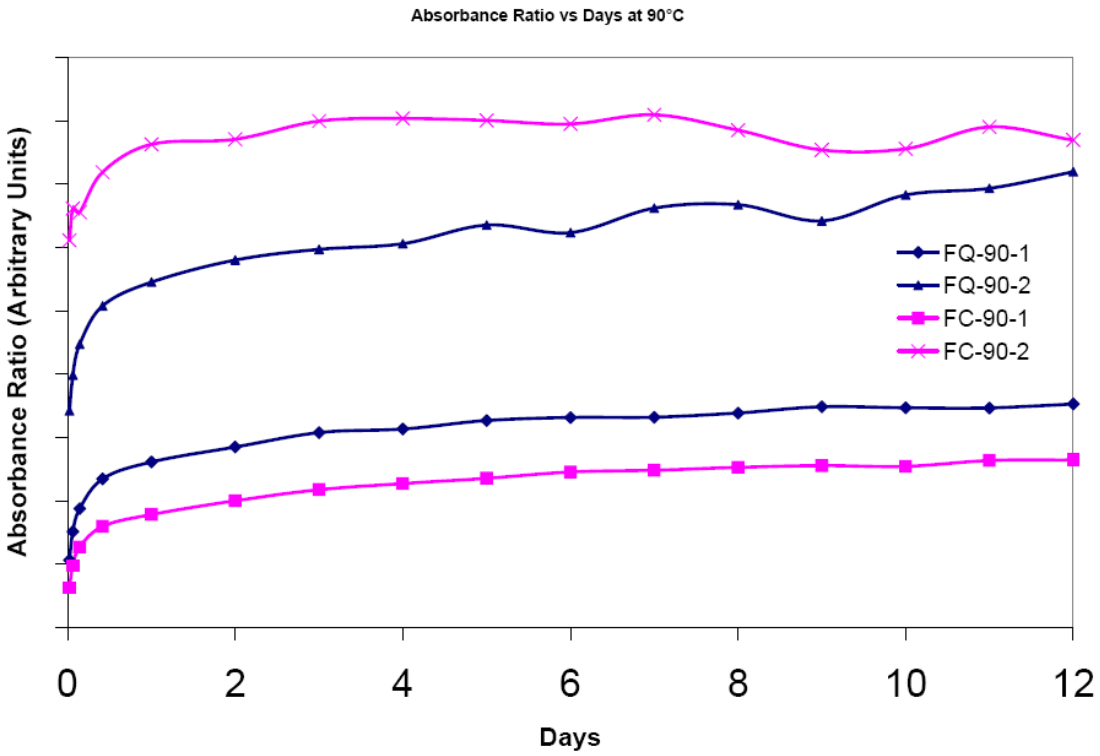
Absorbance Ratio vs Days at 90°C
Absorbance Ratio (Arbitrary Units)
FQ-90-1
FQ-90-2
FC-90-1
FC-90-2
0
2
4
6
8
10
12
Days

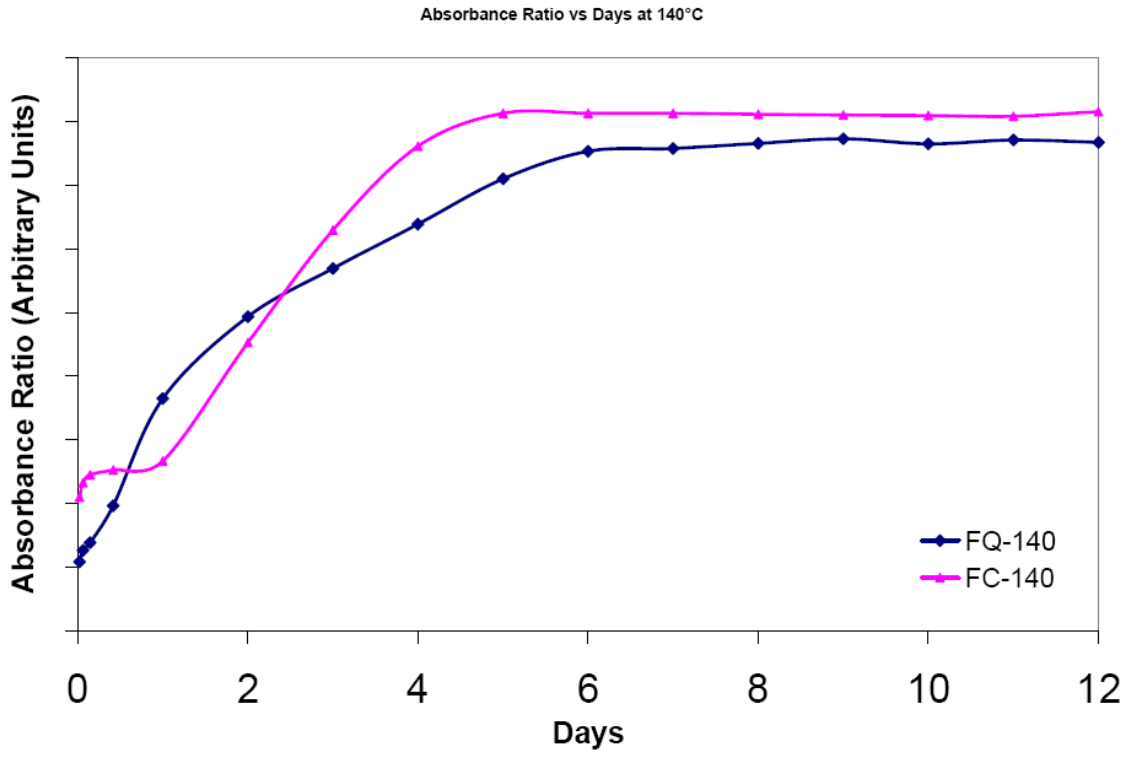
Absorbance Ratio vs Days at 140°C
Absorbance Ratio (Arbitrary Units)
FQ-140
FC-140
0
2
4
6
8
10
12
Days

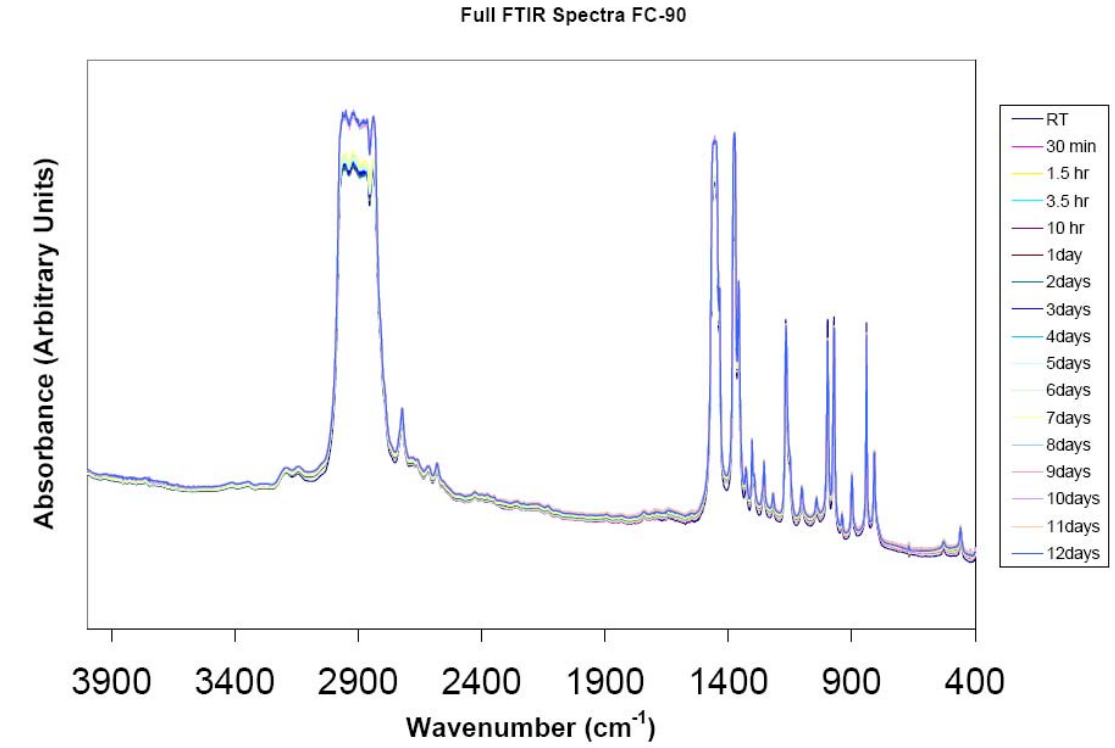
Full FTIR Spectra FC-90
Absorbance (Arbitrary Units)
RT
30 min
1.5 hr
3.5 hr
10 hr
1day
2days
3days
4days
5days
6days
7days
8days
9days
10days
11days
12days
3900
3400
2900
2400
1900
1400
900
400
Wavenumber (cm-1)

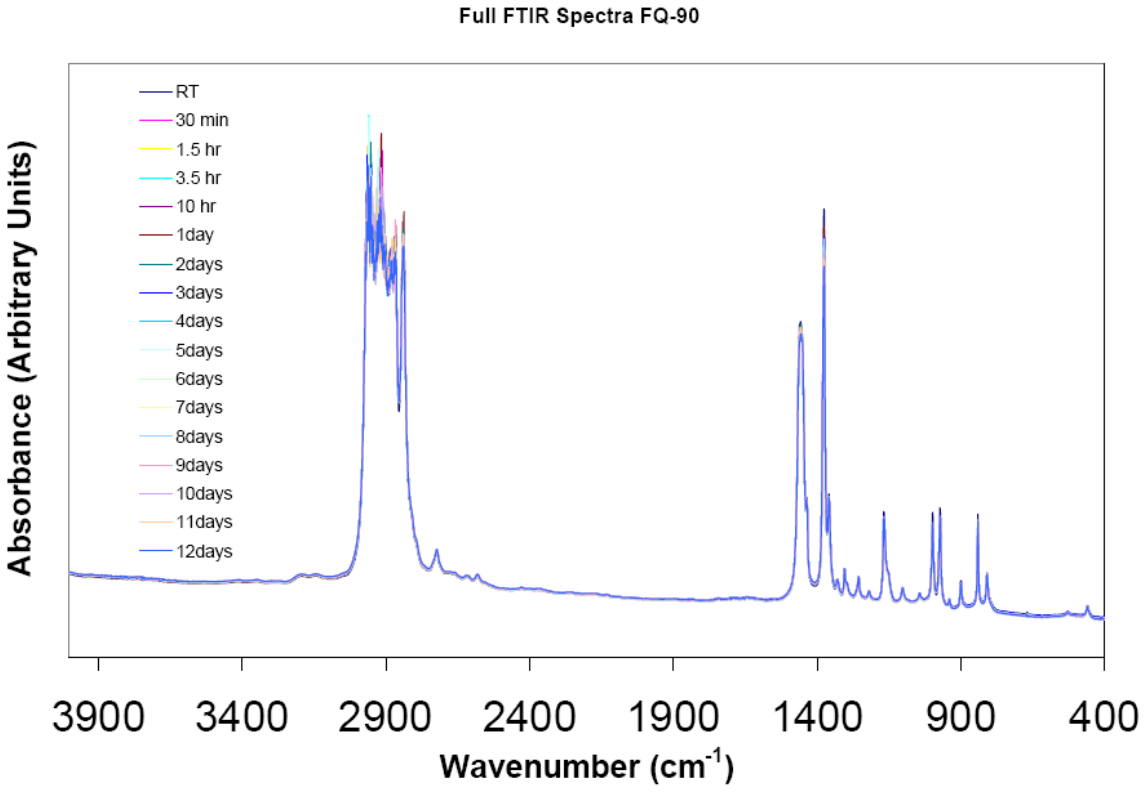
Full FTIR Spectra FQ-90
Absorbance (Arbitrary Units)
RT
30 min
1.5 hr
3.5 hr
10 hr
1day
2days
3days
4days
5days
6days
7days
8days
9days
10days
11days
12days
3900
3400
2900
2400
1900
1400
900
400
Wavenumber (cm-1)

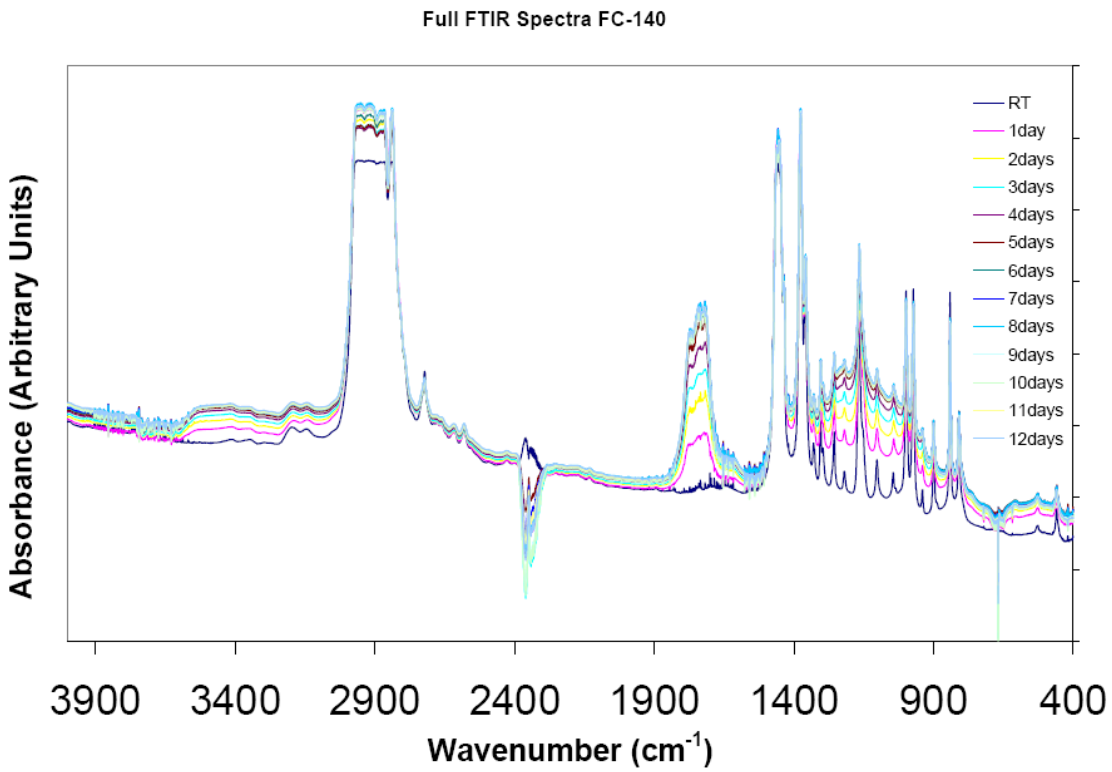
Full FTIR Spectra FC-140
Absorbance (Arbitrary Units)
RT
1day
2days
3days
4days
5days
6days
7days
8days
9days
10days
11days
12days
3900
3400
2900
2400
1900
1400
900
400
Wavenumber (cm-1)

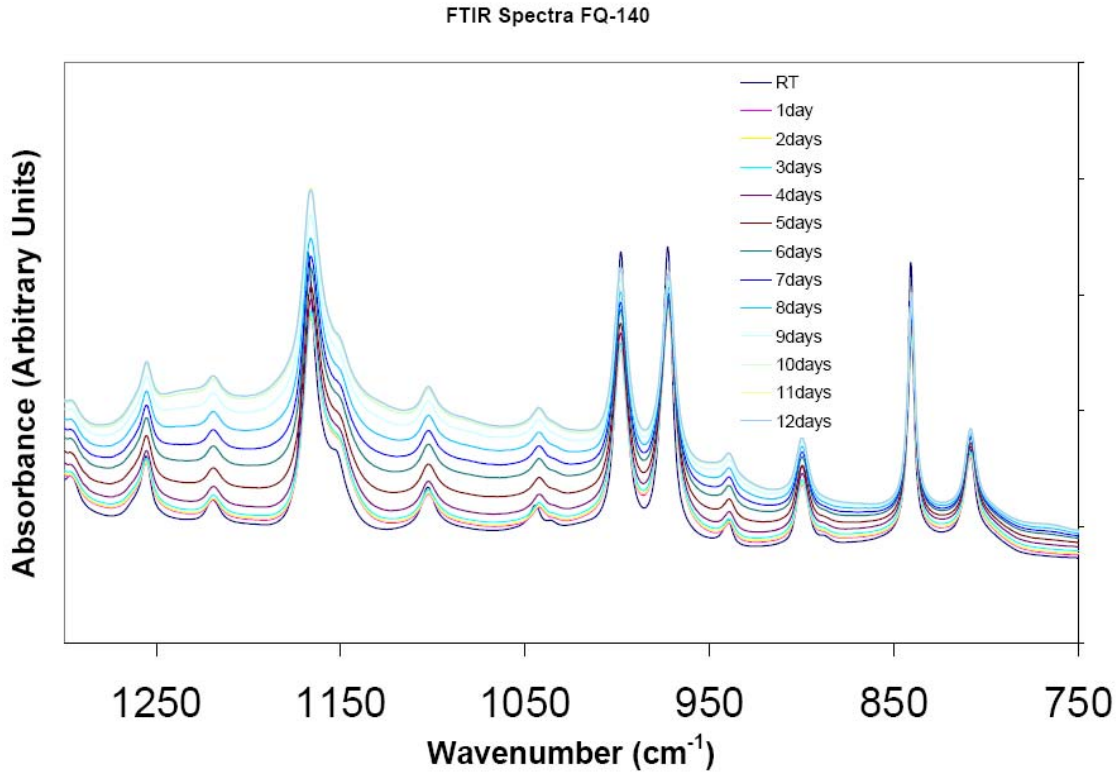
FTIR Spectra FQ-140
Absorbance (Arbitrary Units)
RT
1day
2days
3days
4days
5days
6days
7days
8days
9days
10days
11days
12days
1250
1150
1050
950
850
750
Wavenumber (cm-1)

Appendix H: DSC Data

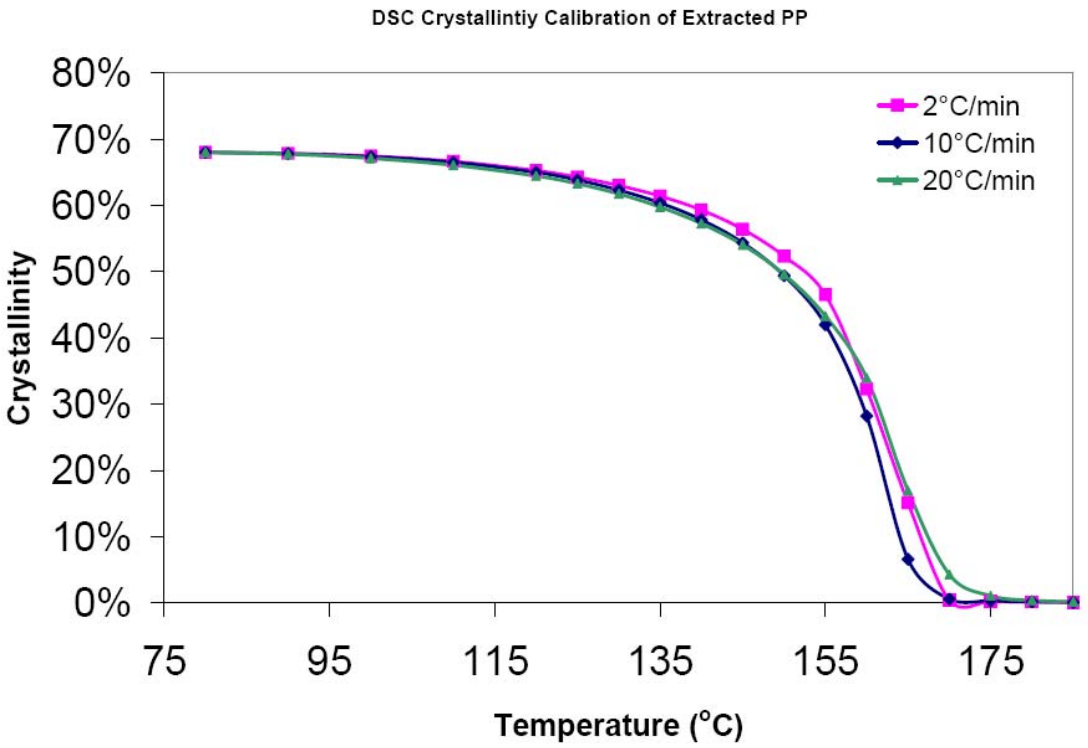

DSC results for extracted PP

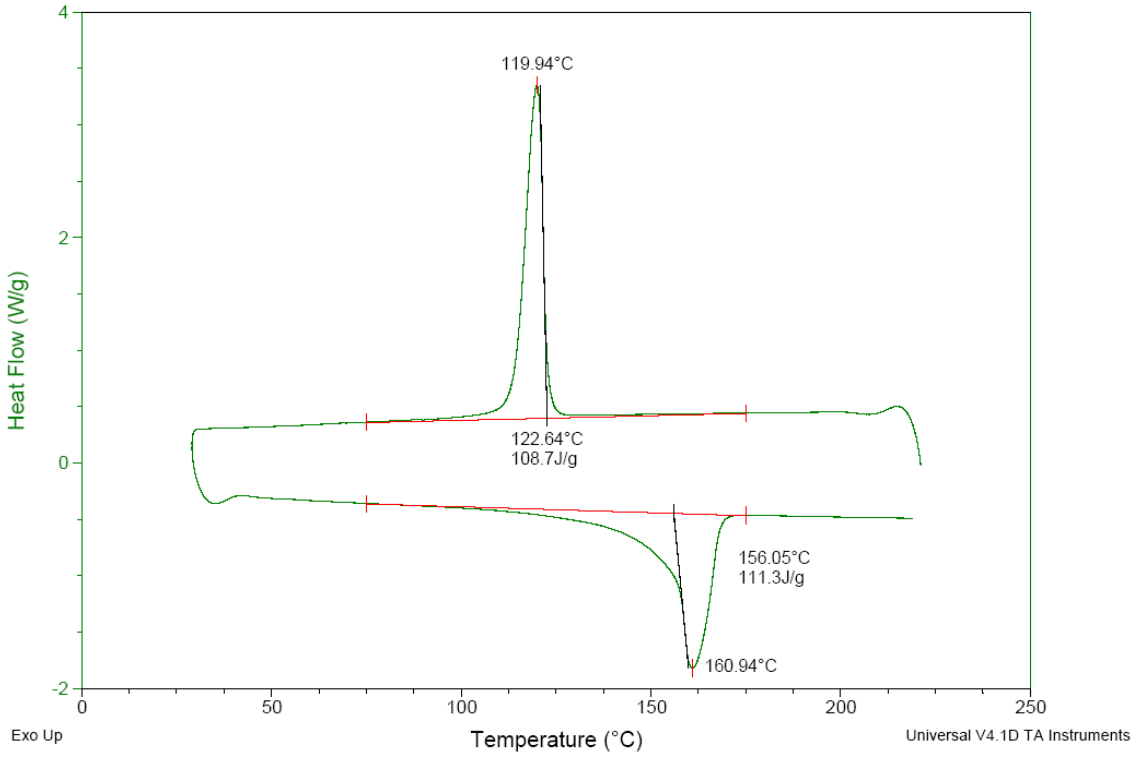

FC-unaged

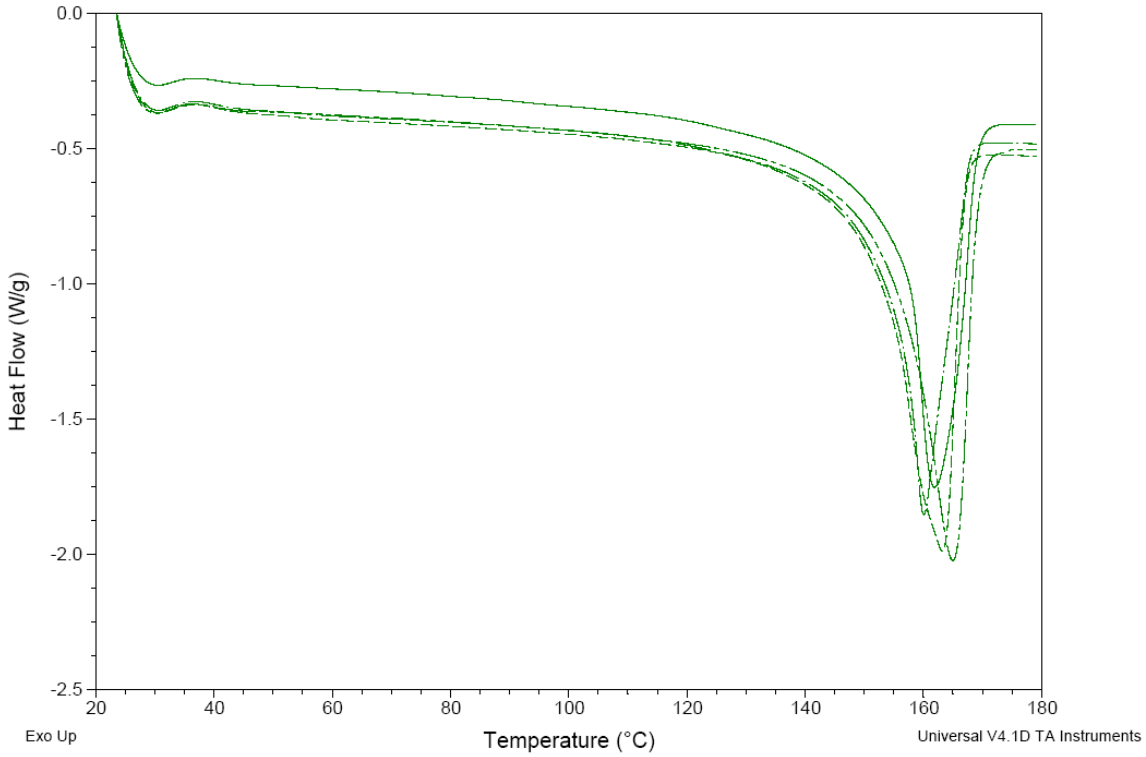

FQ-unaged

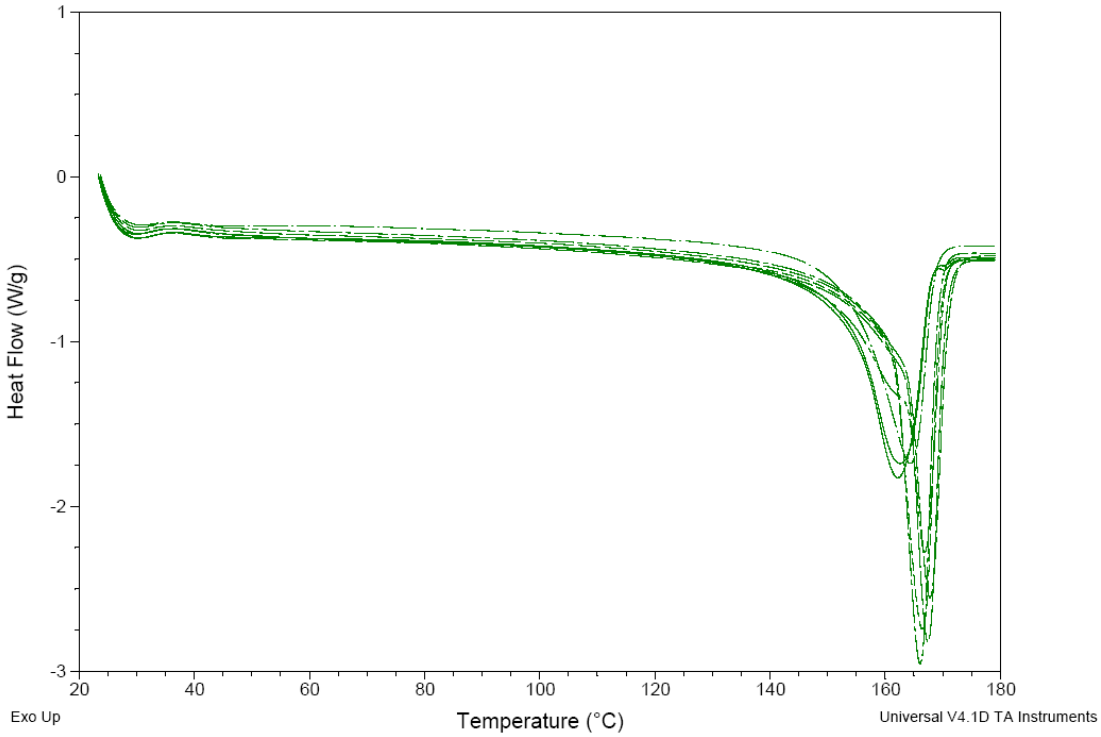

FC-90

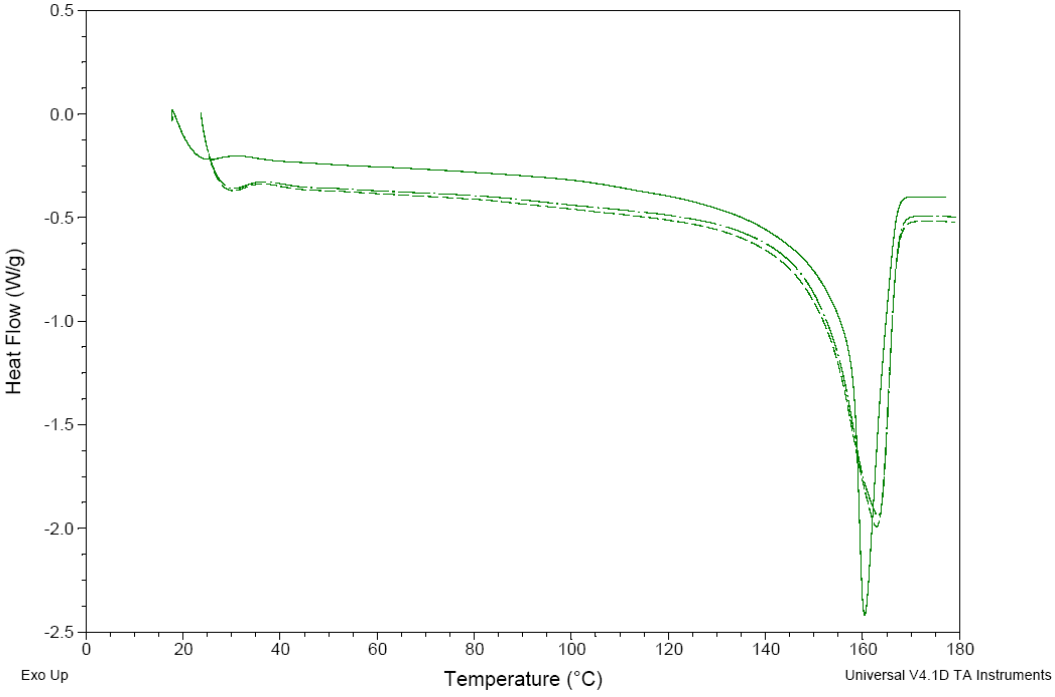
0.5
0.0
-0.5
-1.0
-1.5
-2.0
-2.5
Heat Flow (W/g)
0
20
40
60
80
100
120
140
160
180
Temperature (°C)
Exo Up
Universal V4.1D TA Instruments

FQ-90

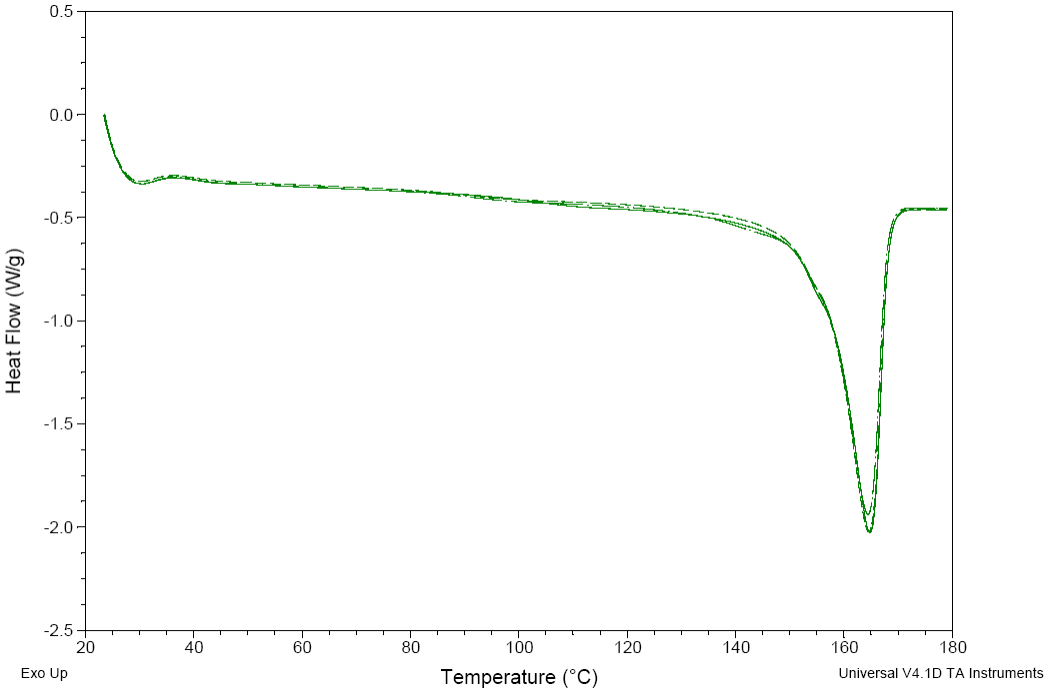
0.5
0.0
-0.5
-1.0
-1.5
-2.0
-2.5
Heat Flow (W/g)
20
40
60
80
100
120
140
160
180
Temperature (°C)
Exo Up
Universal V4.1D TA Instruments

FC-140

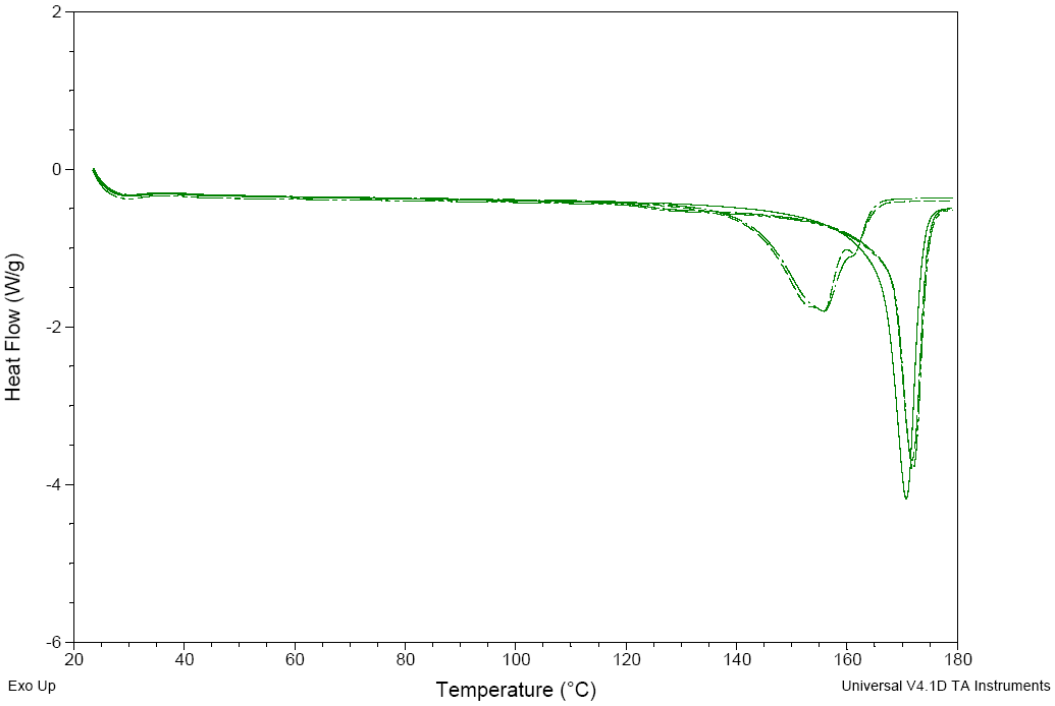
Heat Flow (W/g)
2
0
-2
-4
-6
20
40
60
80
100
120
140
160
180
Temperature (°C)
Exo Up
Universal V4.1D TA Instruments

FQ-140

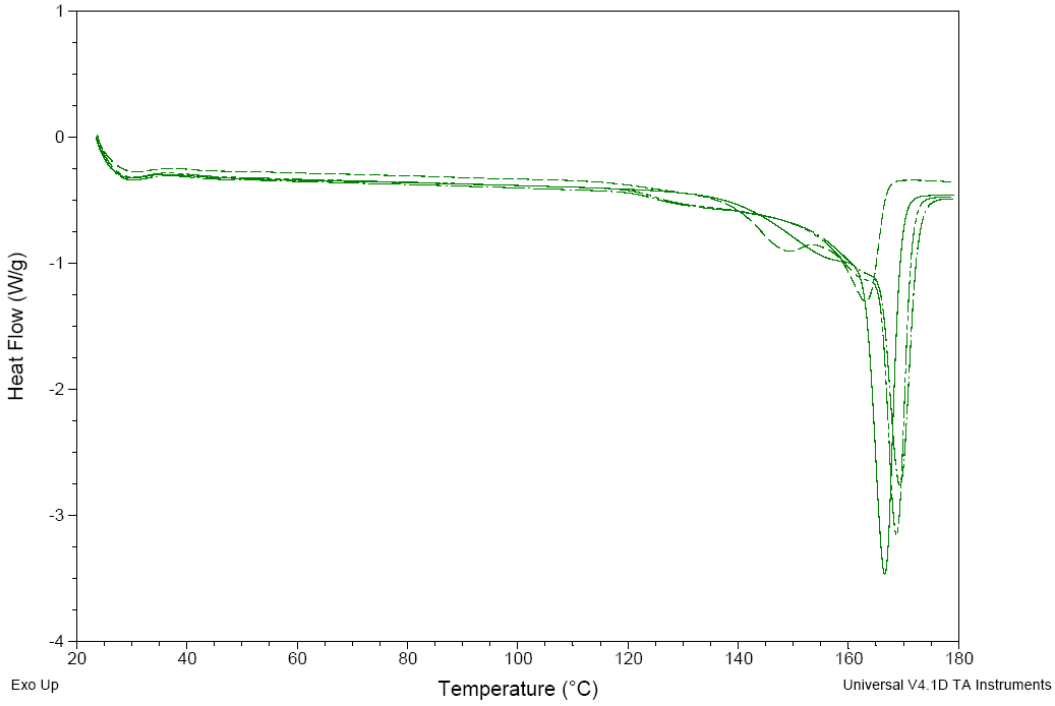
Heat Flow (W/g)
1
0
-1
-2
-3
-4
20
40
60
80
100
120
140
160
180
Temperature (°C)
Exo Up
Universal V4.1D TA Instruments

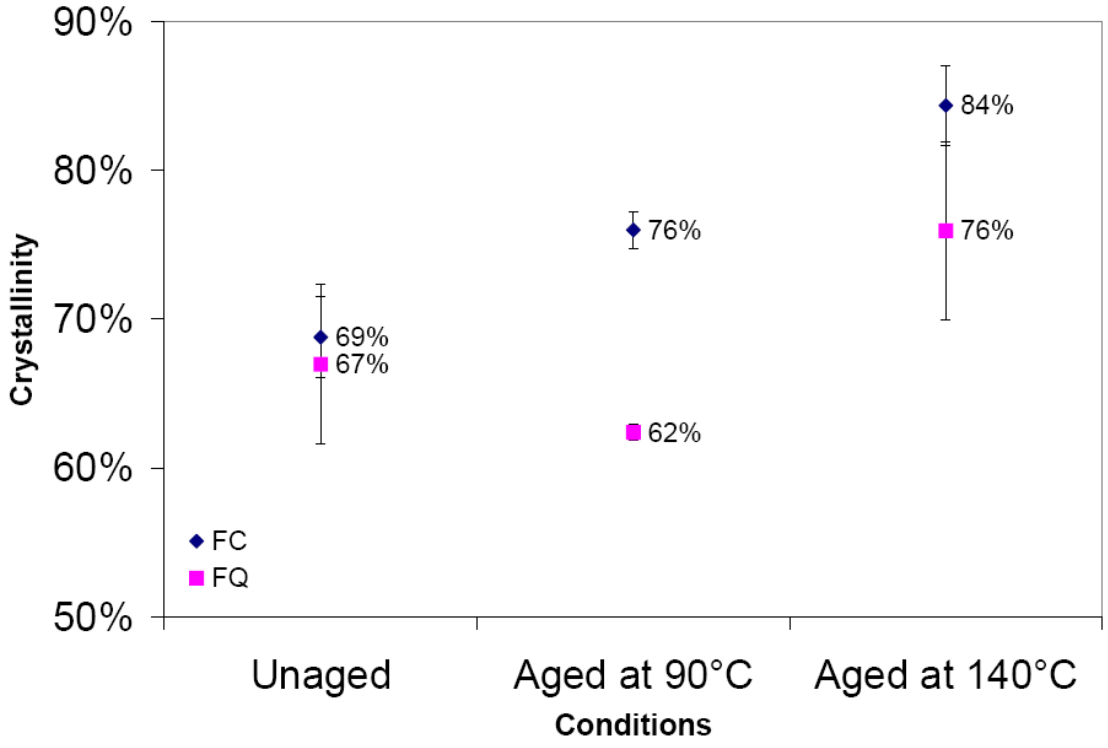
90%
80%
70%
60%
50%
Crystallinity
84%
76%
76%
69%
67%
62%
FC
FQ
Unaged
Aged at 90°C
Aged at 140°C
Conditions

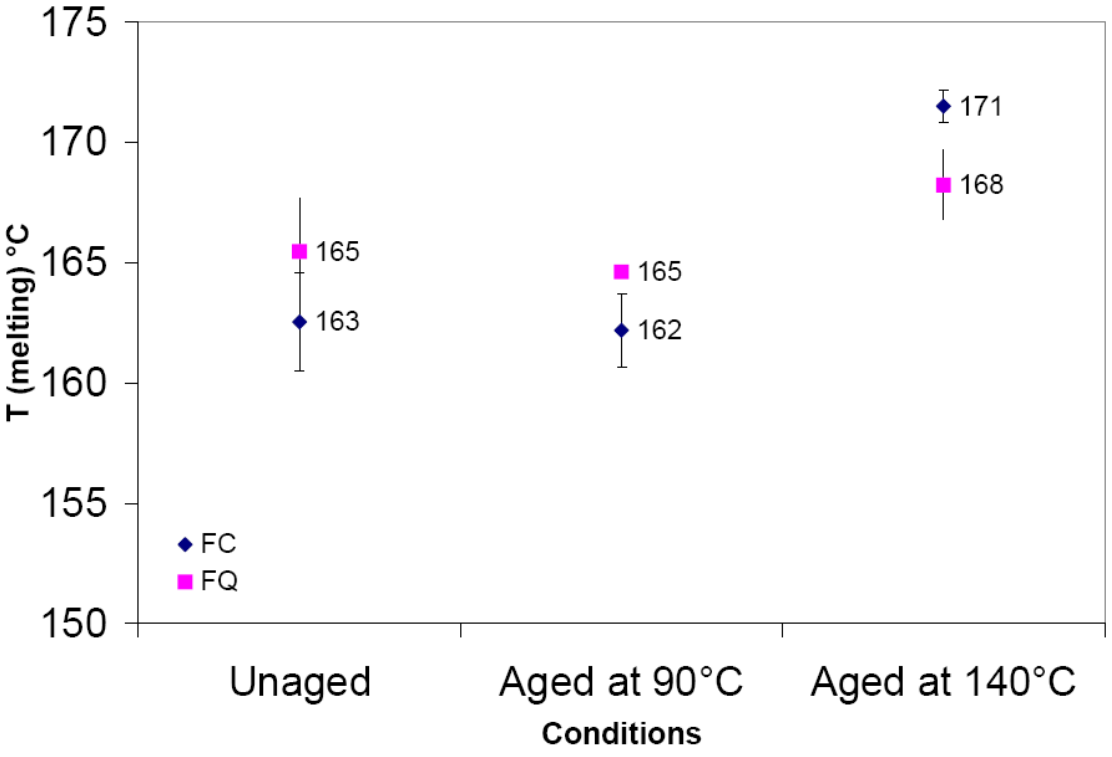
175
170
165
160
155
150
T (melting) °C
171
168
165
165
163
162
FC
FQ
Unaged
Aged at 90°C
Aged at 140°C
Conditions

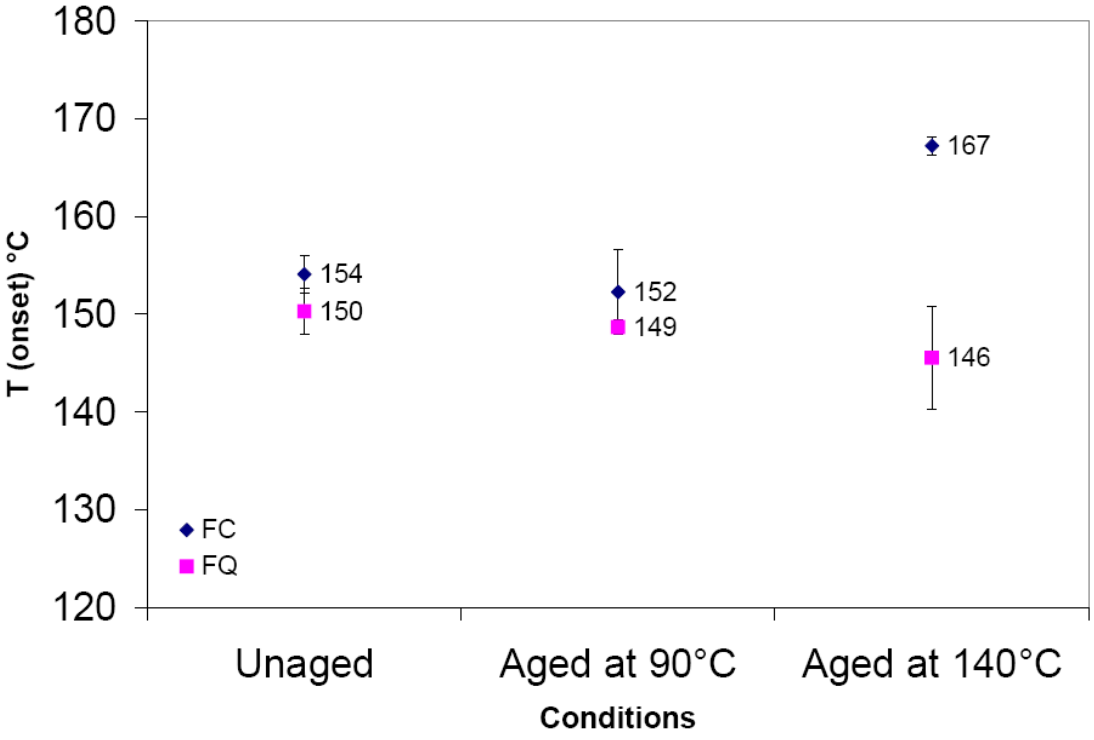
180
170
160
150
140
130
120
T (onset) °C
154
150
152
149
167
146
FC
FQ
Unaged
Aged at 90°C
Aged at 140°C
Conditions

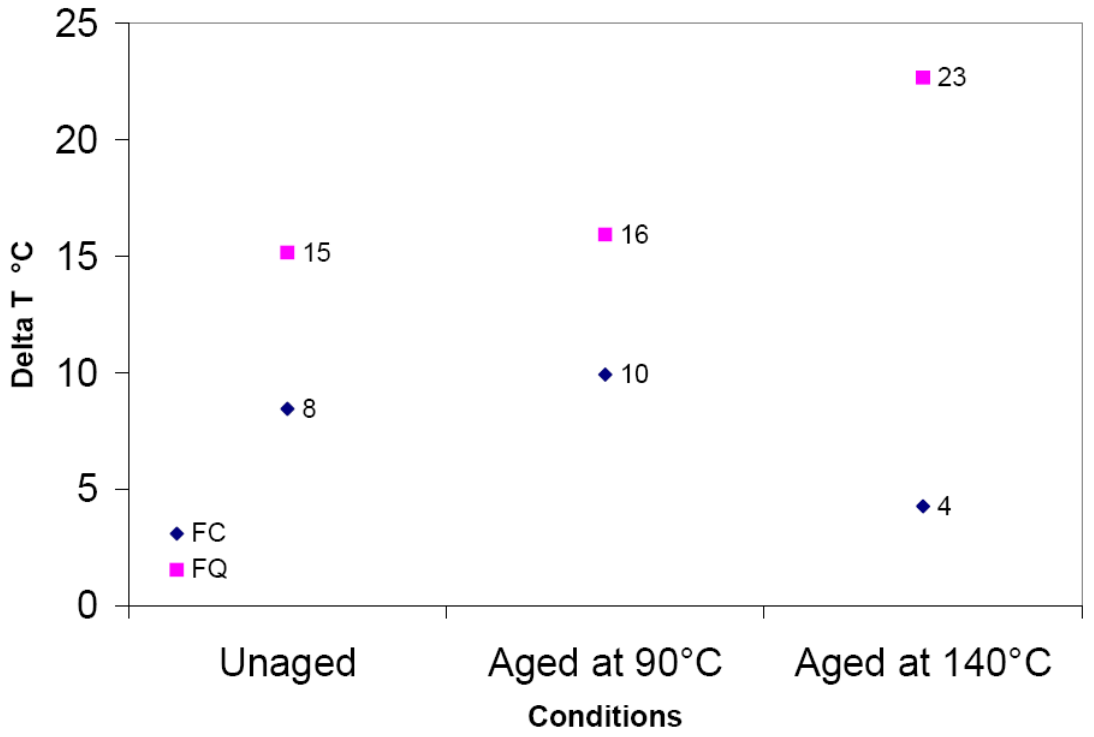
25
20
15
10
5
0
Delta T °C
15
8
16
10
23
4
FC
FQ
Unaged
Aged at 90°C
Aged at 140°C
Conditions